

Laboratoire de Physique Nucléaire et des Hautes Énergies

**Strategies for precision measurements
of the charge asymmetry of the W boson mass
at the LHC within the ATLAS experiment**

by

Florent Fayette

presented to the

Université de Paris VI – Pierre et Marie Curie

for the degree of *Docteur de l'Université Paris VI*

This Ph.D. thesis was supervised by Dr. Mieczysław Witold Krasny at the LPNHE institute in Paris and it was eventually submitted to the Université de Paris VI - Pierre et Marie Curie to obtain the degree of *Docteur de l'Université Paris VI* on January 16th. 2009 in front of a committee consisting of Prof. Michael Joyce (President of the committee), Prof. Stefan Tapprogge (Referee), Prof. Fabian Zomer (Referee), Dr. Thomas LeCompte, Dr. Gavin Salam and Dr. Mieczysław Witold Krasny.

Abstract

This thesis dissertation presents a prospect for a measurement of the charge asymmetry of the W boson mass ($M_{W^+} - M_{W^-}$) at the LHC within the ATLAS experiment. This measurement is of primordial importance for the LHC experimental program, both as a direct test of the charge sign independent coupling of the W bosons to the fermions and as a mandatory preliminary step towards the precision measurement of the charge averaged W boson mass. This last pragmatic point can be understood since the LHC specific collisions will provide unprecedented kinematics for the positive and negative channels while the SPS and Tevatron collider produced W^+ and W^- on the same footing. For that reason, the study of the asymmetries between W^+ and W^- in Drell-Yan like processes (production of single W decaying into leptons), studied to extract the properties of the W boson, is described thoroughly in this document.

Then, the prospect for a measurement of $M_{W^+} - M_{W^-}$ at the LHC is addressed in a perspective intending to decrease as much as possible the systematic errors that will inevitably comes from the misunderstanding of both phenomenological and apparatus modeling. For that matter strategies have been devised specifically for the present measurement to display robustness with respect to the main uncertainties. These strategies consist of introducing new observables along with considering specific LHC running modes and configurations of the ATLAS tracker. Eventually we show that the present (2009) precision can be improved at the LHC by a factor of 20 and argue that such a precision is beyond the reach of the standard measurement and calibration methods imported to the LHC from the Tevatron program.

Remerciements, podziękowania, acknowledgements, etc.

Mes premiers remerciements s'adressent à ceux qui ont œuvré pour que j'obtienne une bourse pour réaliser ma thèse au LPNHE, à savoir Anne-Marie Cazabat, Matteo Cacciari, Jean-Eudes Augustin, Philippe Schwemling et Mieczysław Witold Krasny mon directeur de thèse. En particulier je tiens à exprimer ma reconnaissance à Pascal Debu, Philippe Schwemling et Witold Krasny pour avoir dispensé avec parcimonie toutes injonctions pour rattraper ce léger retard que j'accusais ce qui m'aura permis de parachever ma thèse en toute quiétude. Enfin je tiens à remercier Stefan Tapprogge et Fabian Zomer pour avoir accepté d'en être les rapporteurs et pour avoir studieusement pris en considération mon travail pendant leurs vacances de Noël. Cette gratitude s'adresse par ailleurs aux autres membres du jury, Michael Joyce, Tom LeCompte, Gavin Salam et mon directeur.

Je remercie ce dernier, Mieczysław Witold Krasny, pour m'avoir offert l'opportunité de faire ma thèse avec lui et surtout pour avoir su composer, à la faveur de mes capacités et de mes aspirations, un sujet de thèse idoine à ma délicate personne. Par bien des aspects travailler sous sa direction sur le présent sujet fit largement honneur au travail de recherche tel que l'on peut se le figurer dans l'idéal. Ces remerciements ne sauraient rendre justice à ce que furent ces trois dernières années en sa compagnie si je ne devais mentionner sa sympathie, sa bienveillance et pour ne m'avoir jamais mis sous pression favorisant en cela le plaisir dans le travail à la production de résultats équivoques. Enfin l'originalité du personnage, à mi-chemin entre le diable de Tasmanie et le "road-runner", son génie ainsi que son humour ont fait de cette collaboration une expérience unique.

Just like to fire there is water, or to vodka there is miód pitny to Witold Krasny there is Wiesław Płaczek. On many aspects I consider Wiesław Płaczek as my second supervisor for all of his helps which improved the quality of my work over these last years. I learned a lot from his rigor, his infallible skills in informatics and I am indebted for all the multiple times he helped me using the WINHAC Monte Carlo. Besides I always appreciated his zen attitude and I also do not forget that most of my stays in Kraków would not have been possibly that smooth if it had not been for his attentions and his hospitality. Za wszystko dziękuję Ci polski mistrzu Zen.

I am deeply grateful to Giorgos Stavropoulos whose help and support, while fighting with Athena, allowed me to reach my first concrete results in my thesis. His broad sympathy really made of this task an agreeable moment, which, in regard of what Athena is, stands as a huge compliment.

Jestem wdzięczny Andrzejowi Siódmokowi. Indeed, Andrzej brought equilibrium to tackle the Krasny-Płaczek doublet which would have been hard to tame all by myself (especially the M.W.K. component), besides I am grateful to him for his sympathy and his hospitality in Kraków. I also do not forget Katarzyna Rejzner whose recent arrival in our team brought additional fun and more importantly allowed to decrease the amount of krasnic activity Andrzej and I used to deal with.

Je remercie les membres du groupe ATLAS du LPNHE pour leur accueil et plus précisément Frédéric Derue pour s'être montré toujours disponible pour m'aider lors de mes confrontations non-ASCII avec Athena ainsi qu'Emmanuel Busato dont les aides, même après son départ pour Clermont-Ferrand, auront grandement contribué à améliorer la qualité de mon code. Je tiens aussi à rendre hommage à Emmanuel "Mini Manu" Hornero, Jérôme "Jers" Glisse et Rui Pereira pour avoir toujours pris le temps de s'intéresser aux problèmes informatiques sur lesquels je butais. Je double mes louanges à l'endroit de Rui et Jers dont les aides en Matplotlib auront contribué à améliorer la facture de ce document. Je triple mes louanges à Mini Manu pour tout le temps qu'il m'aura accordé pour résoudre les obstacles techniques qui se sont dressés sur mon chemin. Enfin remerciements particuliers à Pietro Cavalleri, Jérémie Lellouch et Jers (une fois de plus). Pietro, gentilhomme d'Italie dedans Paris, avec qui j'ai eu l'opportunité de passer de bons moments grâce à son humour et un caractère unique. Jérémie, du groupe des zéros du LPNHE, pour nos échanges désinvoltes voire ouvertement oisifs qui, à l'aune de nos travaux, s'avèrent salutaires. Jers enfin qui, outre toutes les aides en informatique, m'aura prodigué à maintes reprises l'occasion de rire de bon cœur.

I thank the members of the ATLAS group of the Institute of Nuclear Physics in Kraków for their hospitality during my several stays amongst them, in particular Jolanta Olszowska and Janusz

Chwastowski. I am grateful to the nice fellows I met in Kraków with whom I shared nice moments especially Zofia Czyczula, Ewa Stanecka, Adam Matyja, Sebastian Sapeta, Hayk and Meri. I have also a thought for all the poles from CERN especially Justyna and Janek. Enfin de manière plus générale je rends hommage au peuple Polonais pour son accueil et son savoir-vivre. Depuis les charmantes polonaises callipyges aux vieillards voutés par les ans en passant par les vendeurs ambulants de pierogi et de vodka c'est toujours avec grande courtoisie, force délicatesse et patience non feinte que l'on m'aura considéré. Ce faisant, tous mes séjours à Cracovie, sans exception, furent autant de pauses "civilisation" qui auront émaillées les vicissitudes inhérentes à la vie parisienne.

I would like to greet the people from the CERN Standard Model forum especially, Lucia DiCiacco, Nathalie Besson, Stefan Tapprogge, Thomas Nunneneman, Maarten Boonekamp and Troels Petersen. Special thanks to Tom LeCompte for sharing his experience with a genuine vivid and communicative enthusiasm. I am also grateful to the following people with whom I had positive exchanges: David Rousseau, Andrea Dell'Acqua, Wojciech Wojcik, Paweł Brückman de Restrom, Mike Whalley, Borut Kersevan, Kristin Lohwasser, Fred Olness, Muge Karagoz Unel, Chris Hay, Ashutosh Kotwal, Mark Lancaster and Arkadiusz Weinstein.

Je suis reconnaissant à Benoit Loiseau pour son attention quant au bon déroulement de ma thèse et je l'associe aussi à ma gratitude envers Bertrand Desplanques tous deux m'ayant permis de trouver asile scientifique à Grenoble lorsque je m'étais mis en délicatesse avec une partie du milieu académique parisien. Outre le sauvetage d'un avenir potentiel dans les sciences, les explications de Bertrand Desplanques au cours de mon stage sous sa direction m'auront apportées beaucoup dans mon approche actuelle vis-à-vis de la physique des particules.

Je remercie aussi mes collègues du LPTHE: Matteo Cacciari, gran maestro di quark pesanti, pour le stage sous sa direction et pour m'avoir toujours fait profiter des ses explications limpides pendant le début de ma thèse quand mon esprit peinait à se calibrer sur le mode de pensée polonais, Gavin Salam pour ses aides efficaces et pour sa relecture de mon manuscrit enfin Bruno Machet pour sa grande bonté, son enthousiasme et toutes ces agréables discussions qui, faisant écho aux discours de mes autres mentors, m'auront permis d'élargir mon ouverture d'esprit. Enfin une mention particulière à Rédamy Perez-Ramos pour ses aides et ses encouragements.

Je m'incline devant Souad Rey, Véronique Joisin, Jocelyne Meurguey et Annick Guillotau pour leur efficacité dans l'organisation de mes déplacements comme dans d'autres tâches administratives.

Jestem wdzieczny mojej młej siostrze Ani "Pani Ruda" Kaczmarska i Mariusz Bucki whose sympathy brought me a lot during these last years especially when hustling my way through krasnic mazes or when I was feeling hyper-weak rather than electroweak. I cherish all these nice moments I shared with them in Kraków and thank them for the basics in polish they learned me, short, but yet enough to get myself into trouble.

Je rends un hommage particulier à Pascal Parneix dont la passion pour la physique et l'énergie mise à son service auront marqué une partie de mes études universitaires, pour ce stage bien sympathique passé sous sa direction ainsi que pour ses conseils et ses aides dans les moments difficiles.

Je remercie Alain "Docteur Folamour" Mazeyrat pour son soutien dans les passages à vide et salue sa dextérité qui sauva une carte mère dont la perte aurait grandement fait défaut à mon travail. Merci aussi à Jean Onésippe pour son aide, son écoute et pour avoir distillé un peu de sa grande sagesse antillaise dans mon esprit inquiet. Je suis reconnaissant à Olivier Destin pour m'avoir aidé bien des fois en C++ et en L^AT_EX avec une efficacité hors du commun. Enfin encore plus important je le remercie pour tous nos échanges passionnants, divertissants ou hilarants qui m'auront permis de m'aérer l'esprit.

Pour conclure je remercie infiniment mes parents et ma sœur pour leur soutien au cours de mes longues années d'études sans lequel je n'aurais pas pu matérialiser mes aspirations. Chciałbym także podziękować mojej młej i subtelnej Paulince za jej czułość i ciepło oraz za wszystkie spędzone razem chwile, które tak bardzo pomogły mi przetrwać trudny czas przed obroną pracy.

Contents

Introduction	11
1 Phenomenological context and motivations	13
1.1 The Standard Model in a nutshell	13
1.1.1 Overview	13
1.1.2 The theoretical background of the Standard Model: Quantum Field Theory	15
1.1.3 Quantum Electrodynamics	15
1.1.4 Quantum Chromodynamics	16
1.1.5 Electroweak interactions	17
1.1.6 Summary	18
1.2 The W mass charge asymmetry in the Standard Model	19
1.2.1 A first overview from the experimental point of view	19
1.2.2 Motivations for a measurement of the W mass charge asymmetry	20
1.3 Notations and conventions	22
1.4 Generalities on the production of W boson in Drell–Yan like processes	24
1.4.1 W decay	24
1.4.2 W in Drell–Yan-like processes at the LHC	28
1.5 An invitation to the rest of the document	41
2 The ATLAS experiment	43
2.1 The Large Hadron Collider	43
2.1.1 The collider	43
2.1.2 The LHC experiments	46
2.2 The ATLAS detector	47
2.2.1 Detector requirements	47
2.2.2 Overview of the ATLAS detector	47
2.2.3 Calorimetry	49
2.2.4 Muon system	53
2.3 The ATLAS inner detector	55
2.3.1 Description of the inner detector	55
2.3.2 Track fitting and general performances	59
2.4 The weak modes affecting the inner detector	60
2.4.1 Misalignment and definition of the weak modes	60
2.4.2 Consequences of the weak modes on the error on the W boson mass measurement	61
2.A W mass charge asymmetry and tracker misalignment in CDF II	63
2.A.1 Context of the measurement of the W mass at CDF	63
2.A.2 Description of the CDF Central Outer Tracker	64
2.A.3 Influence of tracker misalignment on the W mass charge asymmetry	64

3	The Monte Carlo event generator WINHAC	67
3.1	The Monte Carlo event generator WINHAC	67
3.1.1	Monte Carlo methods	67
3.1.2	The Monte Carlo event generator WINHAC	70
3.2	Implementation of WINHAC in the ATLAS software	72
3.2.1	Introduction	72
3.2.2	Software environment of the ATLAS experiment	72
3.2.3	Simulation and reconstruction of Monte Carlo events within ATLAS	73
3.2.4	Implementation of WINHAC inside Athena	76
3.3	Framework of the analysis	80
3.3.1	Generation framework	81
3.3.2	Analysis framework	82
3.A	Example of a WINHAC summary event	85
4	Phenomenology of W^+ and W^- in Drell–Yan like processes at the LHC	87
4.1	Context of these studies	87
4.2	Production of W^+ and W^- bosons	88
4.3	Decays of W^+ and W^- bosons	93
4.3.1	Overview in proton–anti-proton and proton–proton collisions	93
4.3.2	Proton–anti-protons collisions	96
4.3.3	Proton–proton collisions	97
4.3.4	More details on the leptons transverse momenta charge asymmetry in pp collisions	100
4.3.5	Summary on the sources of charge asymmetries in proton–proton collisions	101
4.A	Detailed description of W in Drell–Yan for $p\bar{p}$, pp and dd collisions	103
4.A.1	Observables and context of the discussion	103
4.A.2	A study of the purely sea contributions	105
4.A.3	Proton–anti-proton collisions	107
4.A.4	Proton–proton collisions	113
4.A.5	Deuteron–deuteron collisions	121
4.A.6	Transverse momentum of the (anti-)quarks for W in Drell–Yan	127
4.A.7	Amplitude of the final state charge asymmetries in function of the energy in the collision	128
5	Strategy for a reduction of the systematic errors on $M_{W^+} - M_{W^-}$	131
5.1	Measurement strategies	131
5.1.1	Event selection	131
5.1.2	Observables	133
5.1.3	The machine and the detector settings	136
5.2	The analysis method	137
5.2.1	Likelihood analysis	137
5.2.2	The MT and \mathcal{PD} event samples	138
5.2.3	Scaling distributions for quarks flavors systematics	140
5.3	Systematic error sources	141
5.3.1	Phenomenological modeling uncertainties	142
5.3.2	Experimental uncertainties	145
5.4	In search for the optimal measurement strategy	147
5.4.1	Validation of the framework and behaviour of the likelihood analysis	147
5.4.2	Reducing impact of systematic measurement errors	148
5.4.3	Reducing impact of systematic modeling errors	150
5.4.4	Two complementary strategies	153
5.A	Validation tests and miscellanea technical variations of the analysis	155
5.A.1	Details on the validation of the analysis framework	155

5.A.2	Influence on the results of some input parameters to the analysis	158
5.B	Measurement of the W mass charge asymmetry: the How Not To	161
5.C	Step-by-step interpretations of systematic errors results	163
5.C.1	Detailed tables	163
5.C.2	Detailed comments and graphics	168
Conclusion		177

Introduction

Là trois cent mille personnes trouvèrent place et bravèrent pendant plusieurs heures une température étouffante, en attendant l'arrivé du Français. De cette foule de spectateurs, un premier tiers pouvait voir et entendre; un second tiers voyait mal et n'entendait pas; quant au troisième, il ne voyait rien et n'entendait pas davantage. Ce ne fut cependant pas le moins empressé à prodiguer ses applaudissements.

De la Terre à la Lune
JULES VERNES

The actual description of the fundamental building blocks of matter and the interactions ruling them is called the Standard Model. It is believed not to be the most fundamental description but rather a phenomenological approximation for energies below the TeV scale. In this model, two types of particles are to be distinguished. First are the quarks and leptons building up the matter and, second, are the bosons that mediate the interactions among them. Of all the four known fundamental interactions –the gravitation, electromagnetic, weak and strong interactions– only the last three are now implemented within the mathematical formalism supporting the Standard Model. Amid these interactions the weak one, acting on both quarks and leptons, is mediated by the exchange of the massive neutral Z and two charged W^\pm bosons. The W^+ and W^- , which are antiparticle of each other, are the object of interest in this dissertation.

The Z boson has been observed in 1973 in the Gargamelle bubble chamber at CERN while the W^\pm bosons were observed in single production in 1983 in the UA1 detector of the Super Proton Synchrotron (SPS) $p\bar{p}$ collider, again at CERN. This discovery confirmed the Glashow–Weinberg–Salam electroweak model. Since then, the W^\pm have been studied for the last decades at the Large Electron Positron (LEP) e^+e^- collider (W^+W^- pair production) and at the Tevatron $p\bar{p}$ collider (single W production). These two experiments allowed to measure W properties such as its mass M_W or its width Γ_W . These parameters are important since they provide, when combined to other Standard Model parameters, constraints on the Standard Model. For example the masses of the W and of the top quark constrain the mass of the hypothetical Higgs boson. The specific W study of this work aims at improving the experimental value of the charge asymmetry of the W mass by studying single W production at the Large Hadron Collider (LHC). This measurement has so far not received much attention and, as a consequence, displays an accuracy 10 times larger than the one on the absolute mass M_W . With the new possibilities that the LHC pp collider should offer for the next years we considered the prospect for a drastic decrease of the experimental error on the $M_{W^+} - M_{W^-}$ value using the ATLAS multipurpose detector capabilities. The first motivation for such a measurement is to refine the confirmation of the CPT invariance principle through the direct measurement of the W^\pm masses, to complete the accurate CPT test made by observing charged μ^+ and μ^- life time decays. Other motivations will be given later. Besides, as it will be shown, the W bosons, despite the fact they will be produced with the same process as at the SPS and the Tevatron colliders, will nonetheless display original kinematics due to the nature of the colliding beams. Indeed, while W^+ and W^- are produced on the same footing in $p\bar{p}$ collision, this will not be the case anymore at the LHC. The first step of this work is to understand the W^+ and W^- kinematics in pp collisions. After, this first stage providing all cards in our hands to understand the

W properties at the LHC, the rest of this work will focus on the improvement that could be provided to the $M_{W^+} - M_{W^-}$ measurement using the ATLAS detector at the LHC. Here, rather than reusing Tevatron tactics, we devised new strategies specific to this measurement and to the LHC/ATLAS context. The philosophy for these strategies –as it will be detailed– aims at being as independent as possible of both phenomenological and experimental uncertainties, that cannot be fully controlled. Eventually, we argue that the proposed strategies, could enhance the actual accuracy on $M_{W^+} - M_{W^-}$ by a factor of ≈ 20 .

This work represents the second stage of a series of several publications aiming at providing precision measurement strategies of the electroweak parameters for the upcoming LHC era. In the same logic, next steps will provide dedicated strategies for the measurement of the absolute mass and width of the W boson.

This work is the result of three years of collaboration in a team consisting of Mieczysław Witold Krasny, Wiesław Płaczek, Andrzej Siódmok and the author. Furthermore, the technical work that took place within the ATLAS software was made possible with substantial help from Giorgos Stavropoulos.

Chapter 1

Phenomenological context and motivations

- Depuis lors, continua Aramis, je vis agréablement. J'ai commencé un poème en vers d'une syllabe ; c'est assez difficile, mais le mérite en toutes choses est dans la difficulté. La matière est galante, je vous lirai le premier chant, il a quatre cents vers et dure une minute.

- Ma foi, mon cher Aramis, dit d'Artagnan, qui détestait presque autant les vers que le latin, ajoutez au mérite de la difficulté celui de la brièveté, et vous êtes sûr au moins que votre poème aura deux mérites.

Les Trois Mousquetaires
ALEXANDRE DUMAS

This Chapter introduces the background of the present work. The first part reviews in a nutshell the Standard Model which is the present paradigm to describe the elementary particles and their interactions. Then, a parenthesis is made on the experimental setting to already provide to the reader the global vision necessary to understand the rest of the Chapter. For this purpose, the hadronic production of W bosons and how their properties are extracted from leptonic decays are reviewed. Next, motivations for the measurement of the W mass charge asymmetry are given.

The second part introduces the notations and conventions used throughout the document.

The third part describes the phenomenological formalism used to study W bosons produced in hadronic collisions and decaying into leptons, phenomenon also known as production of W in Drell–Yan-like processes. This presentation, rather than being exhaustive, emphasises the relevant kinematics needed to understand the gist of W physics in Drell–Yan-like processes and how, from such kinematics, the W properties like its mass and its width are extracted.

Finally the Chapter closes on a presentation of the rest of the document.

1.1 The Standard Model in a nutshell

1.1.1 Overview

Based on the experience that seemingly different phenomena can eventually be interpreted with the same laws, physicists came up with only four interactions to describe all known physics processes in our Universe. They are the gravitational, electromagnetic, weak and strong interactions. The electromagnetic, weak and strong interactions are described at the subatomic level by Quantum Field Theory (QFT), the theoretical framework that emerges when encompassing the features of both Special Relativity and Quantum Mechanics. In particular the weak and electromagnetic interactions are now unified in QFT into the Glashow–Weinberg–Salam electroweak theory. The description of the three interactions in QFT is called the Standard Model of elementary particles and their interactions,

Fermions	1 st generation	2 nd generation	3 rd generation	Q
Quarks	u (up)	c (charm)	t (top)	$+2/3$
	d (down)	s (strange)	b (bottom)	$-1/3$
Leptons	e^- (electron)	μ^- (muon)	τ^- (tau)	-1
	ν_e (electron neutrino)	ν_μ (muon neutrino)	ν_τ (tau neutrino)	0

Table 1.1: The three generations of quarks and leptons. Q is the electrical charge.

or simply Standard Model (SM). The “Standard” label means that it is the present day reference, which, although not believed to be the ultimate truth, is not yet contradicted by data. This amends for the term “phenomenology” used in some applications in the SM, where phenomena are described with non fundamental models and, hence, non fundamental parameters. Gravity, on the other hand, is not yet implemented in QFT, it is described by General Relativity. It mostly concerns Cosmology, that rules the behaviour of space–time geometry under the influence of massive bodies and in non-inertial frames. It explains the structure of the Universe and its components on large scales, and eventually leads to the Big Bang theory. In the Standard Model, the effects of gravity are negligible as long as the energies stay below the Planck scale ($< 10^{19}$ GeV).

Before presenting the Standard Model in more details we present an overview of the particles properties and denominations. At this stage, we already adopt natural units where $c = 1$ and $\hbar = 1$. Table 1.1 displays the elementary (*i.e.* structureless) particles building the matter. They are fermions¹ of spin $S = 1/2$ and come in two types, the quarks and the leptons, both present in three generations of doublets: this leads to six different flavours of quarks or leptons. The only thing that differentiates each generation is the masses of the particles [1]. Quarks have fractional electrical charge –with respect to the charge e of the electron– and are sensitive to all interactions. Charged leptons are sensitive to the weak and electromagnetic interactions, while neutral leptons (neutrinos) are only sensitive to the weak interaction. Interactions among all fermions are due to the exchange of elementary particles of boson type. The electromagnetic interaction is mediated by the exchange of neutral massless photons γ between all particles that have an electrical charge. The weak interaction is mediated by three massive vector bosons: the electrically charged W^+ and W^- and the electrically neutral Z . All particles bearing a weak isospin charge are sensitive to the weak interaction. The strong interaction between particles having a color charge is mediated by massless colored gluons g of eight different kinds.

The quarks and leptons were discovered on a time scale that span no less than a century. The electron was observed at the end of the 19th century [2, 3, 4] while the muon and tau were observed respectively in the thirties [5] and the seventies [6]. The electron neutrino ν_e was found in the fifties [7], the ν_μ ten years later [8] and the ν_τ after another forty years later [9]. The up, down and strange quarks were observed in hadrons in the deep inelastic electron–nucleon and neutrino–nucleon scattering experiments [10, 11]. The discovery of the charmed quark occurred in the seventies [12, 13], the bottom was discovered a few years later [14], while the top, due to its very large mass, was discovered in the nineties at the Tevatron $p\bar{p}$ collider [15, 16]. Concerning the gauge bosons, the photon was discovered with the theoretical interpretation of the photo-electric effect [17] while the W^\pm and Z bosons were isolated in $p\bar{p}$ collisions [18, 19, 20, 21]. The existence of gluons was deduced from the observation of hadronic jets generated in e^+e^- collisions at high energies [22, 23, 24].

Each particle mentioned so far has its own anti-particle with opposite quantum numbers. Anti-particles of electrically charged particles are noted with the opposite sign of the charge (*e.g.* e^+ is the

¹Fermion is the generic term used to qualify all particles whose spin is a “half-value” of the Planck constant, *i.e.* $n \frac{1}{2}$ in units of \hbar , n being an integer. Boson on the other hand qualifies particles whose spin is an integer of the Planck constant.

anti-particle of e^-) while neutral particles are noted with a bar upon them (*e.g.* $\bar{\nu}_l$ is the anti-particle of ν_l). Some particles are their own anti-particles, *e.g.* the photon and the Z boson. The rest of this section presents the main features of the Standard Model. First, a glimpse at QFT is given, then we describe the electromagnetic, strong and weak interactions in QFT.

1.1.2 The theoretical background of the Standard Model : Quantum Field Theory

The beginning of the 20th century witnessed the emergence of two revolutions in physics : Quantum Mechanics and Special Relativity. Quantum Mechanics deals with phenomena below the atomic scale while Special Relativity, based on space–time homogeneity/isotropy, describes laws of transformations between inertial frames. Exploring deeper the subatomic world, the Heisenberg principle entails that, as the length scale decreases, the momentum (energy) increases. This increase of the energy amends for the High Energy Physics (HEP) terminology used to refer to the elementary particles and their interactions. In those conditions, taking into account Special Relativity is mandatory.

The Klein–Gordon and Dirac equations were the first relativistic generalisations of the Schrödinger equation. The problem with these equations is that they have negative energies solutions which are difficult to interpret. This problem can be overcome if one considers that a negative energy solution describes an anti-particle. An anti-particle can be interpreted as a positive energy particle travelling backward in time. Besides, in this relativistic and quantum context, a solution describes a quantum field ψ whose elementary excitations are the particles. Then, the number of particles is no longer fixed and the relativistic mass–energy equivalence accounts for the annihilation/creation of pairs of particle–anti-particle. This new framework is the Quantum Field Theory.

QFT describes local interactions of supposedly point-like particles. It bears its own difficulties, with the arising of infinities, which need to be consistently taken care of in the process of renormalisation. Taking into account local Lorentz invariant QFT with the spin–statistic theorem leads to the CPT symmetry, *i.e.* the conservation the product of the charge conjugation C , parity P and time inversion T operators in any processes. In particular, CPT symmetry shows that $M_{W^+} = M_{W^-}$.

One method to quantify a field is to use the Feynman path integral. Path integral formulation of Quantum Mechanics relies on a generalisation of the least action principle of classical mechanics. It is based on the Lagrangian density from which the equations of the dynamics can be deduced. The Lagrangian density (called hereafter Lagrangian) of the field under study contains its kinetic and potential energies. Hence, the description of the dynamics of elementary particles under the influence of fundamental forces consists to formulate the right Lagrangian with: (1) the kinetic energy of the free fields of the spin- $\frac{1}{2}$ quarks/leptons and of the spin-1 bosons mediators and (2) the potential term displaying their mutual interactions and –if any– the bosonic field self-interaction terms. A term of interaction is proportional to a coupling constant, say $g_{\text{int.}}$, inherent to the interaction under study. Up to the fact that this constant is small enough, the calculus of the amplitude of probability can be developed into a perturbative expansion in powers of the coupling constant $g_{\text{int.}}$. All terms proportional to $g_{\text{int.}}^n$ in the expansion involve processes with n interaction points (vertices) between quarks/leptons and bosons. We can associate to them drawings, called Feynman diagrams. Each one entangles all processes sharing the same topological representation in momentum space.

Finally let us mention that QFT is also extensively used in condensed matter physics, in particular in many-body problems, and the interplay of ideas between this domain and HEP is very rich. With the basics features of QFT presented above we now describe the electromagnetic, strong and weak interactions.

1.1.3 Quantum Electrodynamics

The theory that describes the electromagnetic interactions in QFT is called Quantum Electrodynamics (QED). The Lagrangian of QED includes the Dirac and Maxwell Lagrangians respectively to describe the kinetic energy of, say, the free electron field ψ (its excitation are the electrons) and of the free gauge field A^μ (its excitation are the photons). It also contains an interaction term between the

photon and electron fields which is proportional to e , the charge of the electron. The charge e is linked α , the fine structure constant of QED, via $\alpha \equiv e^2/4\pi$. Since $\alpha \approx 1/137$ the expansion in power of α is feasible. Still, when taking into account Feynman diagrams with loops, *i.e.* quantum fluctuations involving particles with arbitrary four-momenta, the calculus diverges. This reflects the conflict between the locality of the interactions inherited from Special Relativity and Quantum Mechanics that allows virtual processes to have arbitrary high energies. Divergences come from terms like $\ln(\Lambda/m)$, where Λ is a temporary unphysical cut-off parameter and m the mass of the electron.

The procedure to get rid of those divergences is called renormalisation. It consists in redefining the fundamental parameters of the theory by realising that the charge e used so far is already the one resulting from all quantum loops. These e^+e^- loops affect the value of the bare charge e_0 that one would observe if there was no interaction. Expressing in a perturbative series e as a function of e_0 and Λ and, then, writing in the expression of the amplitude e_0 as a function of e allows to get rid of the divergences when $\Lambda \rightarrow +\infty$. The effect of these loops depends on the energy, for that reason a renormalisation scale energy μ_r is chosen close to a characteristic energy scale in the process. Since μ_r is arbitrary the charge must obey an equation expressing the invariance of physics with respect to μ_r . This leads to the formulation of the renormalisation equations. Eventually the e^+e^- loops screen the bare charge. Then, the charge e and mass of the electron, in our example, are no longer fundamental parameters but rather effective parameters (running coupling constants) which values depends of μ_r .

Gauge invariance is an essential tool in proving the renormalisability of a gauge theory. For QED, it appears that equations are invariant under a local transformation of the phase factor of the field ψ . The invariance of the Lagrangian under this particular transformation directly governs the properties of the electromagnetic interaction. Group theory allows to describe these properties, in the case of QED this group is $U(1)_{\text{QED}}$. Consequent to those developments, physicists tried to describe the remaining interactions with the help of gauge invariant theories, too.

1.1.4 Quantum Chromodynamics

The description of the strong interaction by a gauge theory became sensible when the elementary structure of the hadrons was discovered in lepton-hadron deep inelastic scattering (DIS) experiments. Those experiments shed light on the partons, the hypothetical constituents of the hadrons, which become quasi free at high energies. The partons are of two types, the quarks and the gluons [25, 26] and, at first, the structure of the hadrons was found to satisfy some scaling properties.

The observation of hadrons made quarks of the same flavour and spin hinted at the existence of a new quantum number attached to quarks that could eventually help to anti-symmetrise the wave functions of such hadrons, and save the Fermi exclusion principle. It was then postulated that the group describing the strong interaction is $SU(3)_c$, where c stands for color. Indeed, in analogy with the additive mixing of primary colors, quarks hold three primitive “colors” (“red”, “green” and “blue”) that, when combined, give “white” hadrons, which justifies the term of chromo in Quantum Chromodynamics (QCD), the QFT model of the strong interaction [27, 28, 29]. This group is non-abelian which pragmatically implies that the interactions carriers, the gluons, are colored and can interact among themselves, in addition to interacting with quarks. There are eight colored gluons to which we can associate the gauge field G_a^μ where $a = 1, 2, \dots, 8$.

This last property implies striking differences with respect to QED. In addition to gluon-quark vertices, equivalent to photon-lepton/quark vertices in QED, there are now three and four gluons vertices. During the renormalisation of the strong interaction coupling constant g_s , while the quarks loops screen the color charge, the gluons loops magnifies it and eventually dominate. As a consequence g_s , or equivalently $\alpha_s \equiv g_s^2/4\pi$, is a decreasing function of the renormalisation energy μ_r . This justifies *a posteriori* the asymptotic freedom hypothesis for the partons in DIS, and also, qualitatively, the confinement of quarks in hadrons. Hence, at some point, when the energy involved in a QCD process becomes small, α_s gets large which prohibits the use of perturbative calculations. The energy scale marking this frontier is of the order of 0.1 GeV. Below this limit, other techniques have to be employed

to make calculations (*e.g.* lattice QCD). Note, finally, that the change of α_s with the energy implies that the formerly observed scaling property must be violated, which was observed and formalised in particular with DGLAP equations [30, 31, 32]. Note also that the renormalisation constraints impose to have as many quarks as there are leptons which twice allowed to predict new quarks: the charm to match, with the u , d and s , the two first leptons families and eventually the top and bottom quark doublet when the tau lepton was discovered.

1.1.5 Electroweak interactions

(a) Weak interactions and the path to the electroweak model

The weak interaction was discovered in nuclear β -decay and recognised to drive as well the muon decay. The first model was a point-like interaction involving charged currents (to account for the change of flavor) and proportional to the Fermi constant G_F . The peculiarity of this interaction is that it violates parity, leading to the vector minus axial-vector ($V - A$) nature of the weak currents. Hence, weak interactions couple only left-handed particles and right-handed anti-particles.

The problem of the Fermi model is that it collapses above ≈ 300 GeV by giving inconsistent predictions. Using unitarity constraints, one can shape the form of the more fundamental model ruling the weak interactions. First, based on the previous examples of QED and QCD, the weak interaction can be assumed to be mediated by the exchange of heavy charged vector bosons. In this new context the propagator of the W boson damps the rise with energy. Assuming that the coupling strength of the W to fermions is comparable to the one of QED, one finds that the mass of the W must be around 100 GeV. Hence, due to the mass of the W the range of the weak interaction is of the order of $1/M_W$.

In addition to charged currents the theory needs neutral currents as well. Let us consider, for example, the process $e^+ e^- \rightarrow W^+ W^-$ that occurs with an exchange of a neutrino. When the W bosons are produced with longitudinal polarisation their wave functions grows linearly with the energy while the exchange of a neutrino predicts a growth quadratic with the energy. To overpass this new breakdown of unitarity a neutral boson, the Z , must take part in the process like $e^+ e^- \rightarrow Z \rightarrow W^+ W^-$ with a tri-linear coupling to the W^+ and W^- .

A consequence of this tri-linear coupling is that, now, scattering of vector bosons can be observed. In the case of $W^+ W^- \rightarrow W^+ W^-$ the amplitude of longitudinally polarised W bosons, built-up by the exchange of Z , grows as the fourth power of the energy in the center of mass of the collision. This leading divergence is canceled by introducing a quadri-linear coupling among the weak bosons. Still, unitarity is not yet restored for asymptotic energies since the amplitude still grows quadratically with the energy.

At this stage, two solutions can be envisaged. The scattering amplitude can be damped, either by introducing strong interactions between the W bosons (technicolor model), or by introducing a new particle, the scalar Higgs boson H , which interferes destructively with the exchange of weak bosons.

We have seen that the coupling strength of the weak and electromagnetic interactions are of the same order. Besides we have seen that the road to preserve unitarity is very much linked to the handling of longitudinally polarised W bosons. We now give a brief presentation of the electroweak model that unifies electromagnetic and weak interactions.

(b) The electroweak model

Since weak interactions couple only left particles and right anti-particles, finding a gauge theory to cope with this implies that all elementary particles have to be considered, in a first approximation, to be massless. The path to the electroweak model can be presented in two steps. In the first step, the Glashow–Weinberg–Salam (GWS) model [33, 34, 35] unifies the weak and electromagnetic interactions up to the approximation that all quarks, leptons and vector bosons are massless, QCD can be added along to the GWS model, still with massless particles. The second step describes the

mechanism that allows massive particles without explicitly breaking the gauge invariance constructed earlier. This is the Brout–Engler–Higgs–Kibble mechanism [36, 37, 38].

The fact that elementary fermions were found in doublets and the desire to unify the weak and electromagnetic interactions in a gauge invariant theory led to the gauge groups $SU(2)_L \otimes U(1)_Y$.

The $SU(2)_L$ takes into account the fact that left-handed fermions are found in weak isospin doublet, *i.e.* $I = 1/2$ which, for the conventionally used third component, means $I_3 = \pm 1/2$, while right-handed fermions are found in singlets. Let us note also that the left-handed quarks eigenstates in weak interactions differ from the mass eigenstates; the convention tends to write down the lower isospin states q' as linear combinations of the eigenstate masses q , like $q'_i = \sum_j V_{ij} q_j$, where i and j are the flavors of the quarks and the elements V_{ij} are the elements of the Cabibbo–Kobayashi–Maskawa (CKM) [39, 40] 3×3 matrix. The non-abelian properties of the $SU(2)$ group ensures that some mediators of the interaction will have a charge and then will be assimilable to the W bosons. At this stage, there are 3 fields, $W^{1,\mu}$, $W^{2,\mu}$ and $W^{3,\mu}$ that couples to particles with a weak isospin with a coupling constant g .

The group $U(1)_Y$, although different from $U(1)_{\text{QED}}$, is chosen so that, eventually, some of its components will give back QED. It governs the interaction of weakly hypercharged particles Y coupled to a gauge field B^μ via a coupling constant g' .

In this context one imposes the electric charge Q of a particle to be linked to the weak isospin and hypercharge via the Gell-Mann–Nishijima equation: $Q = \frac{1}{2}Y + I_3$. Things can then be recast in terms of electric charge to purposely make the W bosons appear; from the weak hypercharge and isospin terms we end up with three terms respectively displaying positively, negatively and neutrally charged currents. In this new basis the W bosons fields are linear combinations of the $W^{1,\mu}$ and $W^{2,\mu}$. We are left with a neutral term involving the gauge fields B^μ and $W^{3,\mu}$. These fields, though, are not yet the photon and the Z . In fact, the latter appear to be admixtures of B^μ and $W^{3,\mu}$. The angle that governs this mixture is called the Weinberg angle Θ_W . Weak and electromagnetic interactions are now unified and described by three parameters: how they mix via Θ_W and their individual coupling strength G_F and α .

Like mentioned previously QCD can be added such that three gauge theories finally account for the three interactions, *i.e.* $SU(3)_c \otimes SU(2)_L \otimes U(1)_Y$. Nonetheless this model presents a few flaws. The problem of the unitarity above 300 GeV is partially fixed by introducing massive vector bosons but the unitarity still breaks down around 1 TeV in $W^+ W^- \rightarrow W^+ W^-$, where the W are polarised longitudinally. Last but not least, some elementary particles are massive but if one enters mass terms explicitly in the equations the gauge invariance is broken. To keep the gauge invariance properties of the GWS model and take into account the masses a mechanism that spontaneously breaks the symmetry of the solutions had to be devised.

The solution was directly inspired by condensed matter physics, more precisely, from superconductivity where photons can become massive due to the non-symmetric fundamental state of the scalar field ($S = 0$) describing electrons pairs. Here, the electroweak symmetry breaking (ESB) is realised by adding to the previous model a Higgs scalar field which, to respect $SU(2)_L \otimes U(1)_Y$, comes as a weak isospin doublet with an hypercharge. A part of the potential for the Higgs field is chosen so that the vacuum energy is degenerate. This complex Higgs doublet makes a total of four degrees of freedom. Three of these degrees mix with the W^\pm and Z bosons and provide them with a third longitudinal spin state which makes them massive while the remaining one becomes the massive Higgs boson. The fermions acquire their masses via Yukawa couplings with the Higgs field. The Higgs boson is the last missing piece of the present day formulation of the Standard Model. If it exists and if it perturbatively interacts, its experimental observation will validate the Standard Model.

1.1.6 Summary

We briefly presented the quantum and relativistic framework for the dynamics of the quarks and leptons sensitive to the electromagnetic, weak and strong interactions, as well as how massive particles gain their masses dynamically by interacting with the Higgs scalar field. The Standard Model has a

highly predictive power in its actual form but its main problem still lies in the understanding of the origin and nature of the masses of the particles. Although the ESB mechanism accounts for them while respecting the gauge invariance, its addition is mainly *ad hoc*.

This summary of the Standard Model did not had the pretension to be exhaustive. In particular, the wide variety of experiments, such as hadron–hadron, lepton–nucleon or electron–positron colliders, that provided essential results, were not credited to keep this presentation as short as possible. As a consequence the reader is invited to refer to classical textbooks with more details and references to historical papers: for QFT/SM in order of accessibility Refs. [41, 42, 43, 44, 45], for details in QCD Ref. [46] and in the Electroweak Model Ref. [47] for example.

1.2 The W mass charge asymmetry in the Standard Model

1.2.1 A first overview from the experimental point of view

The present work takes place in the context of collider physics, more specifically within the Large Hadron Collider (LHC) that should accelerate in a large ring counter-rotating hadrons –most of the time protons– and make them collide at several interaction points with an energy \sqrt{S} in the center of mass of $\sqrt{S} = 14$ TeV. The observation of the particles emerging from these hadronic collisions is achieved by several detectors located in the vicinity of the interaction points. Among them is the ATLAS detector whose capabilities were used in this analysis. The LHC and the ATLAS detector will be described in more details in the next Chapter. Also, worth mentioning, is the Tevatron which, for the last decades before the LHC, has been the largest circular accelerator. The Tevatron collider accelerates counter rotating protons and anti-protons at energies in the center of mass of $\sqrt{S} \approx 2$ TeV.

Amid all the difficulties entering such experimental analysis, two are to be noticed. The first, inherent to high energy physics, is that most of the exotic particles cannot be observed directly due to their short life time but are rather detected indirectly from the observations of their decays displaying specific kinematics. The second difficulty, specific to hadronic processes, is that from the theoretical point of view physicists speak in terms of quarks and gluons but from the experimental point of view only hadrons and their respective decays –if any– can be observed. When colliding hadrons this last problem is unavoidable due to the nature of the initial state.

In hadronic collisions the extraction of the W and Z bosons properties are made studying their leptonic decays which display a distinguishable signal due to the high energy leptons in the final state. This, in particular, allows to get rid of the problems inherent to QCD in the final state. Let us remark the decay into the tau channel is not considered as the short life time of the latter makes it not “directly” observable in a detector.

In the case of the Z boson, where $Z \rightarrow l^+ l^-$, things are simple as the direct observation of the two charged leptons gives access, via their invariant mass $m_{l^+l^-}^2$, to the invariant mass of the Z . In the case of the W the presence of a neutrino in the final state complicates things a lot more. Indeed, because the neutrino does not interact with any part of the detector its kinematics can be only deduced from the overall missing energy for a given event, which will never be as precise as a direct measurement. Multipurpose detectors instruments are more precise in the transverse direction of the beam axis, since this is where interesting physics with high p_T particles occur. The presence of the beam-pipe leaves the very forward region less hermetic in term of calorimetry, forbidding eventually to measure the longitudinal component of the neutrino. This leaves then only the transverse momenta of the two leptons to extract the W boson mass. As it will be shown in this Chapter, the shapes of these transverse momenta depends on W properties such as its mass M_W and its width Γ_W . Nonetheless, because here we cannot access any Lorentz invariant quantities, the kinematics of the W boson and of the leptons in the W rest frame needs to be known with accuracy to model precisely enough the observed kinematics of the leptons in the laboratory frame. Hence the extraction of the W properties proves to be a real challenge from both phenomenological and experimental point of views.

Channel	M_W [GeV]	$M_{W^+} - M_{W^-}$ [GeV]	Year
$W \rightarrow l \nu_l$	79.910 ± 0.390	-0.190 ± 0.580	1990,1991 [52, 53]
$W \rightarrow \mu \nu_\mu$	80.310 ± 0.243	0.549 ± 0.416	
$W \rightarrow e \nu_e$	80.490 ± 0.227	0.700 ± 0.290	1995 [54, 55]
$W \rightarrow l \nu_l$	80.410 ± 0.180	0.625 ± 0.240	
$W \rightarrow \mu \nu_\mu$	80.352 ± 0.060	0.286 ± 0.152	
$W \rightarrow e \nu_e$	80.477 ± 0.062	0.257 ± 0.117	2007 [56, 51]
$W \rightarrow l \nu_l$	80.413 ± 0.048	\times	

Table 1.2: Sum up of the measured values of M_W with the CDF detector for the last decades (1990 \rightarrow 2007). Each of result is obtained for the considered collected data in each publication, *i.e.* with no combinations with previous results from CDF or other experiments. The two references next to the year indicate: (1) the results and (2) the detailed W mass analysis. The errors are the one obtained when adding up quadratically the statistical and systematic errors.

1.2.2 Motivations for a measurement of the W mass charge asymmetry

As demonstrated by Gerhard Lüders and Wolfgang Pauli [48], any Lorentz-invariant quantum field theory obeying the principle of locality must be CPT -invariant. For theories with spontaneous symmetry breaking, the requirement of the Lorentz-invariance concerns both the interactions of the fields and the vacuum properties. In CPT -invariant quantum field theories, the masses of the particles and their antiparticles are equal.

The Standard Model is CPT -invariant. In this model, the W^+ and W^- bosons are constructed as each own antiparticle, which couple to leptons with precisely the same $SU(2)$ strength g_W . The hypothesis of the exact equality of their masses is pivotal for the present understanding of the electroweak sector of the Standard Model. It is rarely put in doubt even by those who consider the CPT invariant Standard Model as only a transient model of particle interactions. However, from a purely experimental perspective, even such a basic assumption must be checked experimentally to the highest achievable precision.

The most precise, indirect experimental constraint on equality of the W^+ and W^- masses can be derived from the measurements of the life time asymmetries of positively and negatively charged muons [49, 50, 1]. These measurements, if interpreted within the Standard Model framework, verify the equality of the masses of the W^+ and W^- bosons to the precision of 1.6 MeV. Such a precision cannot be reached with direct measurements of their mass difference. The experimental uncertainty of the directly measured mass difference from the first CDF run and reported by the Particle Data Group [1] is $M_{W^+} - M_{W^-} = -190 \pm 580$ MeV, *i.e.* about 400 times higher. More recently the CDF collaboration [51] measured $M_{W^+} - M_{W^-}$ to be 257 ± 117 MeV in the electron decay channel and 286 ± 136 MeV in the muon decay channel. The Table 1.2 sums up the measured values at CDF for the last decades for both M_W and $M_{W^+} - M_{W^-}$ at the time being. Note that in this thesis the experimental measurement will be focused on CDF results since up to this day it is the only collaboration that published experimental values for $M_{W^+} - M_{W^-}$.

These measurements provide to this date the best model independent verification of the equality of the masses of the two charge states of the W boson. They are compatible with the charge symmetry hypothesis. It is worth stressing, that the present precision of the direct measurement of the charge averaged mass of the W boson derived from the combination of LEP and Tevatron results and under the assumption that $M_{W^+} = M_{W^-}$ is $M_W = 80.398 \pm 0.025$ GeV. It is better by a factor 10 than the precision of the direct individual measurements of the masses of its charged states.

In top of the obligatory precision test of the CPT -invariance of the spontaneously broken gauge

theory with *a priori* unknown vacuum properties, we are interested to measure $M_{W^+} - M_{W^-}$ at the LHC for the following three reasons. Firstly, we wish to constrain the extensions of the Standard Model in which the effective coupling of the Higgs particle(s) to the W boson depends upon its charge. Secondly, contrary to the Tevatron case, the measurement of the charge averaged mass at the LHC cannot be dissociated from, and must be preceded by the measurement of the masses of the W boson charge states. Therefore, any effort to improve the precision of the direct measurement of the charge averaged mass of the W boson and, as a consequence, the indirect constraint on the mass of the Standard Model Higgs boson, must be, in our view, preceded by a precise understanding of the W boson charge asymmetries. Thirdly, we would like to measure the W boson polarisation asymmetries at the LHC. Within the Standard Model framework the charge asymmetries provide an important indirect access to the polarisation asymmetries. This is a direct consequence of both the CP conservation in the gauge boson sector and the purely $(V - A)$ -type of the conjugation (C) and parity (P) violating coupling of the W bosons to fermions. Any new phenomena contributing to the W boson polarisation asymmetries at the LHC must thus be reflected in the observed charge asymmetries.

The optimal strategies for measuring the charge averaged mass of the W boson and for measuring directly the masses of its charge eigenstates are bound to be different. Moreover, the optimal strategies are bound to be different at the LHC than at the Tevatron.

At the Tevatron, the nature of the colliding beam makes it so the production of W^+ is the same than W^- up to a CP transformation. Then, producing equal numbers of the W^+ and W^- bosons, the measurement strategy was optimised to achieve the best precision for the charge averaged mass of the W boson. For example, the CDF collaboration [51] traded off the requirement of the precise relative control of the detector response to positive and negative particles over the full detector fiducial volume, for a weaker requirement of a precise relative control of charge averaged biases of the detector response in the left and right sides of the detector. Such a strategy has provided the best up to date measurement of the charge averaged W boson mass, but large measurement errors of the charge dependent W boson masses as seen above in Table 1.2. More detailed explanations on this experimental development are given in Chapter 2 Appendix 2.A.

If not constrained by the beam transfer systems, the best dedicated, bias-free strategy of measuring of $M_{W^+} - M_{W^-}$ in proton–anti-proton colliders would be rather straightforward. It would boil down to collide, for a fraction of time, the direction interchanged beams of protons and anti-protons, associated with a simultaneous change of the sign of the solenoidal B -field in the detector fiducial volume. Such a measurement strategy cannot be realised at the Tevatron leaving to the LHC collider the task of improving the measurement precision.

The statistical precision of the future measurements of the W boson properties at the LHC will be largely superior to the one reached at the Tevatron. Indeed, where this error was of $\delta_{M_W}^{(\text{stat.})} = 34 \text{ MeV}$ at the Tevatron for an integrated luminosity L of 200 pb^{-1} [51] at the LHC, for the same measurement, in just one year of pp collisions at low luminosity ($L = 10 \text{ fb}^{-1}$) the statistical error should approximately reach $\delta_{M_W}^{(\text{stat.})} \approx 5 \text{ MeV}$. On the other hand, it will be difficult to reach comparable or smaller systematic errors. At the Tevatron they equalise to the statistical error, *i.e.* $\delta_{M_W}^{(\text{sys.})} = 34 \text{ MeV}$ while at the LHC the primary goal is, to constrain the hypothesised Higgs mass, to reach $\delta_{M_W}^{(\text{sys.})} = 15 \text{ MeV}$. The measurements of the W boson mass and its charge asymmetry can no longer be factorised and optimised independently. The flavour structure of the LHC beam particles will have to be controlled with a significantly better precision at the LHC than at the Tevatron. While being of limited importance for the M_W measurement at the Tevatron, the present knowledge of the momentum distribution asymmetries of: (1) the up and down valence quarks and (2) of the strange and charm quarks in the proton will limit significantly the measurement precision. The ‘standard candles’, indispensable for precise experimental control of the reconstructed lepton momentum scale – the Z bosons and other ‘onia’ resonances – will be less powerful for proton–proton collisions than for the net zero charge proton–anti-proton collisions. Last but not least, the extrapolation of the strong interaction effects

measured in the Z boson production processes to the processes of W boson production will be more ambiguous due to an increased contribution of the bottom and charmed quarks.

Earlier studies of the prospects of the charge averaged W boson mass measurement by the CMS [57] and by the ATLAS [58] collaborations ignored the above LHC collider specific effects and arrived at rather optimistic estimates of the achievable measurement precision at the LHC. In our view, in order to improve the precision of the Tevatron experiments, both for the average and for the charge dependent masses of the W boson, some novel, dedicated strategies, adapted to the LHC environment must be developed. Such strategies will have to employ full capacities of the collider and of the detectors in the aim to reduce the impact of the theoretical, phenomenological and measurement uncertainties on the precision of the W boson mass measurement at the LHC.

1.3 Notations and conventions

In this section notations and conventions used through out the rest of the document are introduced.

Let us remind to the reader that to simplify analytic expressions the natural unit convention $c = 1$ and $\hbar = 1$ is adopted. In this notation energies, masses and momenta are all expressed in electron-Volt (eV). Nonetheless, although every MKSA units can be expressed in powers of eV, cross sections –noted σ – are expressed in powers of barns, where $1 \text{ barn} \equiv 10^{-28} \text{ m}^2$. Especially, unless stated otherwise, all differential cross sections $d\sigma/da$ for a scalar observable a produced in this work are all normalised to $\text{nb}/[A]$, A being the dimension of the observable a .

Both Cartesian and cylindrical coordinate basis are considered in the inertia laboratory frame. They are defined already with respect to the experimental apparatus. The interaction point, located in the center of the ATLAS detector, corresponds to the origin of both coordinate systems. In the Cartesian basis, colliding hadrons move along the z axis, $+y$ points upward and $+x$ to the center of the LHC accelerating ring. In the cylindrical basis, r is the radius in the $x - y$ plane, ϕ the azimuthal angle with respect to the $+x$ direction, and θ the polar angle with respect to the $+z$ direction. Unit vectors along these different directions are noted \vec{e}_i where i can stands for x , y , z , r or ϕ . The components of a vector observable \vec{b} along the axis i is noted b_i . All angles are expressed in radians unless stated otherwise.

To define the most relevant kinematics variables to collider physics we consider the example of a particle which four-momentum, energy, momentum and absolute momentum are noted respectively p , E , \vec{p} and $|\vec{p}|$. The four-momentum of a particle in its co-variant representation and in the Cartesian basis writes

$$p = \begin{pmatrix} E \\ \vec{p} \end{pmatrix} = \begin{pmatrix} E \\ p_x \\ p_y \\ p_z \end{pmatrix}, \quad (1.1)$$

where the energy E and the momentum \vec{p} of the particle are related to its invariant mass m by the relation $E^2 = \vec{p}^2 + m^2$. The form of Eq. (1.1) implies the same conventions for the time and space components of any other kind of four-vectors. The helicity λ of a particle is defined by the projection of its spin \vec{S} against the axis pointing in the same direction than the momentum of the particle \vec{p} , that is analytically

$$\lambda \equiv \vec{S} \cdot \frac{\vec{p}}{|\vec{p}|}. \quad (1.2)$$

The transverse component p_T in the $r - \phi$ plane of the vector \vec{p} is defined by

$$p_T \equiv \sqrt{p_x^2 + p_y^2}. \quad (1.3)$$

In that notation transverse energies and missing transverse energies are written E_T and \cancel{E}_T . In ATLAS, and other multipurpose detectors, the central tracking sub-detector bathes in a solenoidal magnetic field $\vec{B} = |\vec{B}|\vec{e}_z$. In this context, the transverse curvature ρ_T , defined as the projection of a particle track on the $r - \phi$ plane, is related to the particle's transverse momentum via

$$\rho_T \equiv 1/p_T. \quad (1.4)$$

A particle kinematics can be unequivocally described by its azimuth ϕ , its transverse momentum p_T and its rapidity y defined by

$$y \equiv \frac{1}{2} \ln \left(\frac{E + p_z}{E - p_z} \right). \quad (1.5)$$

The rapidity is additive under Lorentz transformations along the z axis. For massless/ultra-relativistic particles the rapidity equals the pseudo-rapidity η which is related to the particle polar coordinate by the following relation

$$\eta \equiv -\ln(\tan(\theta/2)). \quad (1.6)$$

Finally to understand more deeply some important physics aspects it is better to consider them in the W Rest Frame (WRF) rather than in the laboratory frame (LAB) where fundamental dynamical patterns are blurred by the add-up of the effects of the W boosts. Variables considered in the WRF are labeled with a $*$ superscript while the one with no particular sign are to be considered in the laboratory frame. More details on relativistic kinematics can be found in Ref. [1].

Another useful variable that will be extensively used is the charge asymmetry, which, for a scalar a , is noted $\text{Asym}^{(+,-)}(a)$ and defined like

$$\text{Asym}^{(+,-)}(a) \equiv \frac{d\sigma^+/da - d\sigma^-/da}{d\sigma^+/da + d\sigma^-/da}, \quad (1.7)$$

where the $+$ and $-$ refers to the electrical charge of the particle under consideration. Finally when the electrical charge is not made explicit it means we consider indifferently both positive and negative particles, *i.e.* hereafter $W \equiv W^\pm$ and $l \equiv l^\pm$.

Different levels of understanding for the observables are considered, respectively the “true”, the “smeared” and the “reconstructed” levels. The true level, also called particle or generator level, refers to the phenomenological prediction of a model or, to be more precise, to the best emulation a given Monte Carlo simulation can produce. The smeared level refers to the true level convoluted with the finite resolution of a detector. For an observable a , the link between the smeared distribution $\text{Smear}(a)$ and the true one $\text{True}(a)$ is

$$\text{Smear}(a) \equiv \int dt \text{True}(t - a) \text{Res}(t; a), \quad (1.8)$$

where $\text{Res}(t; a)$ is the function governing the response of the detector to an input of value t for the observable a . Here, the general resolution performances of a detector will be usually given using rough Gaussian parametrisation

$$\text{Res}(t; a) = \frac{1}{\sqrt{2\pi}\sigma_a} e^{(-t^2/2\sigma_a^2)}, \quad (1.9)$$

where the variance σ_a characterises the resolution of the detector for the observable a of the considered particle. Finally the collected data suffer from additional degradations coming from misalignment, miscalibration, limited accuracy of algorithms, *etc.* All those effects concur to give in the end a reconstructed observable deviating from the smeared value a perfect detector would provide. From the purely experimental point of view only the reconstructed level is relevant but the intermediate levels are used for both pedagogical and pragmatic purposes.

1.4 Generalities on the production of W boson in Drell–Yan like processes

This section starts with a short presentation of the decay of both unpolarised and polarised spins states of a real W boson which leads to the computation of its width Γ_W . These derivations will prove to be useful afterward and it allows as well to remind some basics related to the electroweak interaction. After, the whole process hadron – hadron $\rightarrow W \rightarrow l \nu_l$ is presented. The goal is to give an intuitive comprehension of the kinematics relevant to the W production. Among these kinematics is the charged lepton transverse momentum that is used in the present document for extracting the mass of the W .

1.4.1 W decay

(a) Unpolarised W bosons

The case of the leptonic decay of an unpolarised W boson is considered through the example of

$$W^-(P) \rightarrow l^-(p_1) \bar{\nu}_l(p_2), \quad (1.10)$$

where P , p_1 and p_2 are respectively the four-momenta of the W^- boson, of the charged lepton l^- and of the anti-neutrino $\bar{\nu}_l$. This process in the first perturbation order (Born level) is made of one Feynman diagram (Fig. 1.1). Here, and in all other Feynman diagrams, the time flow goes from the left to the right.

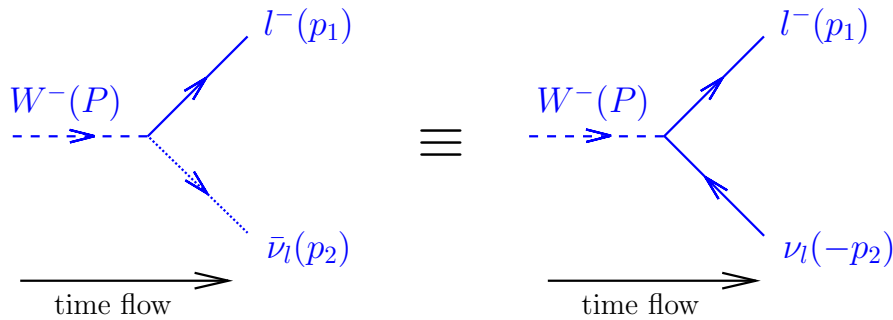


Figure 1.1: Feynman diagram of the leptonic decay of a W boson at the Born level. The diagram on the right represents the conventional way to handle anti-particles in perturbative calculation (see text for more details).

The leptonic decay can be of any type (electronic, muonic or tau) since all leptons can be considered to be massless. Indeed, in the W Rest Frame (WRF) each charged lepton have an energy of the order of $E_l \sim M_W/2 \approx 40 \text{ GeV}$, hence the charged leptons have a Lorentz β factor of $\beta = 0.999 \dots \sim 1$ making out of them ultra-relativistic particles². The amplitude of probability of this process is

$$\mathcal{M}_\lambda = -i \frac{g}{\sqrt{2}} \varepsilon_\mu^\lambda(P) \bar{u}(p_1) \gamma^\mu \frac{1}{2}(1 - \gamma^5) v(p_2). \quad (1.11)$$

In this last equation, the weak force is embedded in the strength $g/\sqrt{2}$ that couples particles sensible to the weak interaction and by the nature of this coupling represented by the co-variant bi-linear term $\gamma^\mu \frac{1}{2}(1 - \gamma^5)$ of Vector–Axial ($V - A$) form. The coupling constant $g/\sqrt{2}$ is usually expressed as a function of the Fermi constant G_F that was formerly used when modeling weak interactions as contact interactions when occurring at energies scales much lower than M_W . For historical reasons they are linked through the relation

$$\frac{G_F}{\sqrt{2}} \equiv \frac{g^2}{8 M_W^2}. \quad (1.12)$$

²In fact for the case of the τ , taking into account its mass eventually leads after computation to affect the W width at the level of 0.1%, but we consider this to be negligible in the context of our discussion.

The W^- polarisation state of helicity λ is represented by the four-vector $\varepsilon_\mu^\lambda(P)$, $\bar{u}(p_1)$ is the spinor of l^- and $v(p_2)$ that of ν_l . We use here the convention which tends to consider that anti-fermions going forward in time can be treated on the algebraic level as fermions going backward in time. The spinors of backward traveling time fermions are noted $v(k) \equiv u(-k)$ for convenience. Let us note in the $V - A$ term the operator $\frac{1}{2}(1 - \gamma^5)$ which, applied to a spinor u , projects only its left-handed component u_L

$$\frac{1}{2}(1 - \gamma^5) u = u_L, \quad (1.13)$$

while the operator $\frac{1}{2}(1 + \gamma^5)$ projects the right component of the latter

$$\frac{1}{2}(1 + \gamma^5) u = u_R. \quad (1.14)$$

In other words, the presence of the $V - A$ term in the current couples only left-handed fermions and right-handed anti-fermions in electroweak interactions.

Usual “diracologic” calculus techniques allow to calculate $\overline{|\mathcal{M}_\lambda|^2}$, which corresponds to the Lorentz co-variant expression of the squared amplitude summed and averaged with respect to all possible spins states for the W and leptons. The differential decay rate writes in the WRF

$$d\Gamma = \frac{1}{2M_W} \overline{|\mathcal{M}_\lambda|^2} d\text{Lips}, \quad (1.15)$$

where $d\text{Lips}$, the Lorentz invariant phase space assuring energy-momentum conservation, can be reduced here to

$$d\text{Lips} = \frac{1}{128\pi^2} \delta(E_l^* - M_W/2) dE_l^* d\Omega_l^*, \quad (1.16)$$

where the energy E_l^* and solid angle Ω_l^* are those of the charged lepton. After the integration over the whole accessible phase space to the particles, the partial width $\Gamma(W \rightarrow l\nu_l)$ of this process reads

$$\Gamma(W \rightarrow l\nu_l) = \frac{G_F}{\sqrt{2}} \frac{M_W^3}{6\pi}, \quad (1.17)$$

$$\equiv \Gamma_W^0, \quad (1.18)$$

which is a Lorentz scalar. The result is the same when considering the case of the W^+ decay. The reader willing to have further details on the previous development or how to undergo such perturbative calculation, can go to classic references in particle physics/quantum field theory such as Refs. [59, 45].

This first order expression for the partial width allows to calculate the total width Γ_W of the W^+ or the W^- . The W can decay into leptons or into a pair of quark–anti-quark that in turn decay to observable hadrons with a probability of one

$$\Gamma_W = \Gamma(W \rightarrow \text{leptons}) + \Gamma(W \rightarrow \text{hadrons}). \quad (1.19)$$

For the leptonic decay, in the ultra-relativistic approximation assumed so far, the width is simply

$$\Gamma(W \rightarrow \text{leptons}) = \Gamma(W \rightarrow e\nu_e) + \Gamma(W \rightarrow \mu\nu_\mu) + \Gamma(W \rightarrow \tau\nu_\tau), \quad (1.20)$$

$$= 3\Gamma_W^0. \quad (1.21)$$

For the hadronic decay, the calculus is similar to the one for the leptons except that here: (1) CKM matrix element intervene and mix the quarks flavors and (2) in top of summing/averaging on the quarks spin states the sum and average on their color charge states need to be done as well. The W can decay into all quarks flavors but the top which is forbidden by energy conservation since $m_t > M_W$. The quarks possess masses such that they can be treated like the charged leptons as ultra-relativistic particles. Then studying $W \rightarrow q\bar{q}' \rightarrow \text{hadrons}$ gives for the partial width

$$\Gamma_W(W \rightarrow \text{hadrons}) = N_c |V_{qq'}|^2 \Gamma_W^0, \quad (1.22)$$

where $N_c = 3$ is the color number, $V_{qq'}$ the element of the CKM matrix governing the mixing angle between flavors q and q' . Summing over all quarks flavors in Eq. (1.22) gives

$$\sum_{q \bar{q}'} |V_{qq'}|^2 = \sum_q \underbrace{\sum_{\bar{q}'} |V_{qq'}|^2}_{=1}, \quad (1.23)$$

where the sum on q' of the squared CKM elements translates the unitarity of the CKM matrix and where \sum_q is restricted to u and s flavors since the decay to the top is forbidden. Then in this context

$$\Gamma(W \rightarrow \text{hadrons}) = 2 N_c \Gamma_W^0. \quad (1.24)$$

Adding both leptonic and hadronic parts gives eventually in the Born level approximation

$$\Gamma_W = (3 + 2 N_c) \frac{G_F}{\sqrt{2}} \frac{M_W^3}{6\pi}, \quad (1.25)$$

where Γ_W^0 has been replaced by its explicit form. Adding QCD corrections in quarks decays transforms the latter expression to

$$\Gamma_W = \left(3 + 2 N_c \left[1 + \frac{\alpha_s(M_W)}{\pi} \right] \right) \frac{G_F}{\sqrt{2}} \frac{M_W^3}{6\pi}, \quad (1.26)$$

where $\alpha_s (\equiv g_s^2/4\pi)$ is evaluated at the energy scale imposed by the W mass. Following those developments it is assumed in the rest of this thesis that $\Gamma_{W^+} = \Gamma_{W^-}$.

(b) Polarised W bosons

Considering the leptonic decay of a real W boson with a specific polarisation state proves to be very helpful to understand the angular decay behaviour of the quarks or leptons. The polarisation states of the two transverses ($\lambda = \pm 1$) and the one longitudinal mode $\lambda = 0$ of a W of momentum $\vec{p}_W = p_W \vec{e}_z$ can be expressed in the laboratory frame like

$$\varepsilon^{(\lambda=\pm 1)} = \mp \frac{1}{\sqrt{2}} \begin{pmatrix} 0 \\ 1 \\ \pm i \\ 0 \end{pmatrix}, \quad \varepsilon^{(\lambda=0)} = \frac{1}{M_W} \begin{pmatrix} |\vec{p}_W| \\ 0 \\ 0 \\ E_W \end{pmatrix}. \quad (1.27)$$

Transverse polarisation states. The example of the leptonic decay of a W^- is again considered, for a polarisation state of $\lambda = +1$. Substituting the expression of $\varepsilon^{(\lambda=+1)}$ in Eq. (1.11) gives the probability amplitude for $W^-(\lambda = +1) \rightarrow l^- \bar{\nu}_l$. This amplitude squared and averaged on the leptons spins, gives the term $|\mathcal{M}_{W^-(\lambda=+1)}|^2$ from which the differential decay width, in the WRF is

$$\frac{d\Gamma}{d \cos \theta_{W,l}^*} \propto |\mathcal{M}_{W^-(\lambda=+1)}|^2. \quad (1.28)$$

Developing that expression gives, in the end, an angular dependency of

$$\frac{d\Gamma}{d \cos \theta_{W,l}^*} \propto (1 - \cos \theta_{W,l}^*)^2, \quad (1.29)$$

where the angle $\theta_{W,l}^*$ is defined like

$$\cos \theta_{W,l}^* \equiv \frac{\vec{p}_W \cdot \vec{p}_l^*}{|\vec{p}_W| |\vec{p}_l^*|}. \quad (1.30)$$

The angular dependency in Eq. (1.29) is an important key for understanding the leptons kinematics in the W decay. It can actually be understood without going to refined calculations but using only the helicity conservation rules in the high energy limit imposed on the leptons by the mass of the W . As it was seen previously the electroweak interactions couples only left-handed fermions and right-handed anti-fermions. In the high energy limit chirality and helicity becomes the same, which means that the helicity is a conserved quantum number and only negative (positive) helicity fermions (anti-fermions) are involved. This explain why sometime in the literature, as a shortcut, but only in the high energy limit, negative helicities states are referred to as “left” and positive states as “right”.

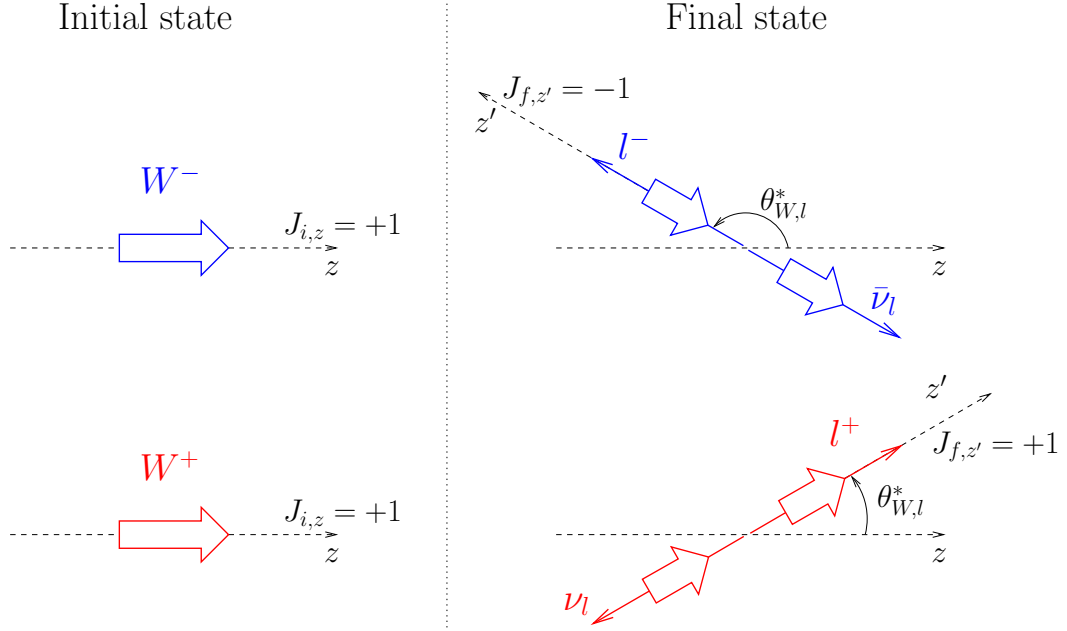


Figure 1.2: Representation in the WRF of the leptonic decay of a positive helicity W^- boson (up) and W^+ boson (down).

Now the previous example is treated from the helicity conservation point of view. The decay $W^- \rightarrow l \bar{\nu}_l$ is depicted in the WRF in the upper part of Fig. 1.2. The convention for the axis is the following. In the initial state the $+z$ direction is parallel to the direction of the momentum of the W in the laboratory frame while the $+z'$ direction points to the direction of the decaying charged lepton in the final state. In that context, the decay proceeds from an initial W state with $J_{i,z} = +1$ to a final leptonic state with $J_{f,z'} = -1$ and in both cases the system holds a total spin of $J = 1$, thus the amplitudes are proportional to the rotation matrices, it reads

$$d_{J_{f,z'}, J_{i,z}}^J(\theta_{W,l}^*) \equiv \langle J, J_{f,z'} | e^{-i\theta_{W,l}^* J_y} | J, J_{i,z} \rangle, \quad (1.31)$$

which expressions for commonly used spins are tabulated in many places, *e.g.* Ref. [1], then

$$\frac{d\Gamma}{d \cos \theta_{W,l}^*} \propto |d_{-1,1}^1(\theta_{W,l}^*)|^2, \quad (1.32)$$

$$\propto (1 - \cos \theta_{W,l}^*)^2. \quad (1.33)$$

Thus the most privileged configuration is the one where the initial and final spin projection $J_{i,z}$ and $J_{f,z'}$ are aligned, while on the other hand the configuration where the l^- would be emitted such that $z' = +z$ would be totally forbidden by helicity conservation.

The case of the decay of the W^+ can be deduced using the same kind of argument except this time the charged lepton is “right” and the neutrino is “left” as shown in the lower part of Fig. 1.2, the angular dependency is then

$$\frac{d\Gamma}{d\cos\theta_{W,l}^*} \propto |d_{1,1}^1(\theta_{W,l}^*)|^2, \quad (1.34)$$

$$\propto (1 + \cos\theta_{W,l}^*)^2. \quad (1.35)$$

Longitudinal polarisations state. For the decay of a W possessing a longitudinal polarisation state a detailed calculus can be carried out using the expression of $\varepsilon^{(\lambda=0)}$ with $p_W = 0$ and $E_W = M_W$ in the WRF. Instead of doing so the angular dependency, that really matters, can be unraveled using again rotations matrices

$$\frac{d\Gamma}{d\cos\theta_{W,l}^*} \propto |d_{\pm 1,0}^1(\theta_{W,l}^*)|^2 \quad (1.36)$$

$$\propto \sin^2\theta_{W,l}^*. \quad (1.37)$$

In this equation $J_{f,z'} = -1$ in the case of a W^- decay and $+1$ for the one of a W^+ . Here there are no differences in the angular decay between the positive and negative channels.

Sum up for the decay of polarised W . The previous derivations can be generalised to include in the formulae both the W boson charge Q and helicity λ

$$\frac{d\Gamma_{W \rightarrow l\nu_l}}{d\cos\theta_{W,l}^*} \propto (1 + \lambda Q \cos\theta_{W,l}^*)^2, \quad (1.38)$$

$$\frac{d\Gamma_{W \rightarrow l\nu_l}}{d\cos\theta_{W,l}^*} \propto \sin^2\theta_{W,l}^*. \quad (1.39)$$

The sign in front of $\cos\theta_{W,l}^*$ can be deduced easily each time by deducing which direction is privileged for the charged lepton from helicity conservation arguments point of view.

1.4.2 W in Drell–Yan-like processes at the LHC

The Drell–Yan [60] processes were originally defined, in hadron–hadron collisions within the parton model, before identifying partons with quarks and later on, with gluons. In these processes, a pair of partons, the hypothesised building blocks of nucleons, collide and annihilate giving in the final state a high invariant mass lepton pair l^+l^- . Within QCD, this partonic reaction proved to be achieved at first order, by the quark–anti-quark annihilation via $q\bar{q}' \rightarrow \gamma^*/Z \rightarrow l^+l^-$. The main features of the formalism describing Drell–Yan survived to the rise of the QCD up to a few refinements. Still, for historical reasons even though the whole present discussion takes place within QCD the term parton is still used and refers to quarks or gluons.

By extension the production of high invariant mass $l\nu_l$ pair through the production of an intermediate W boson is referred to as “Drell–Yan like processes”, or –for convenience– Drell–Yan. Below reminders of the treatment of W boson production in Drell–Yan is given. Let us remark that the formalism described is applicable to the original Drell–Yan and to a wide variety of over hard scattering processes including jet and heavy flavour production. Further general details on this topic can be found in Refs. [61, 46, 62].

(a) Overview

The production of a W in Drell–Yan can be written

$$H_A(P_A) H_B(P_B) \rightarrow W X \rightarrow l(p_1) \nu_l(p_2) X. \quad (1.40)$$

The associated Feynman like representation of this process is shown in Fig. 1.3, where H_A and H_B are hadrons of four-momenta P_A and P_B accelerated by the collider bringing a total energy \sqrt{S} in the center of mass. The collision produces a pair of leptons $(l, \nu_l) \equiv \{(l^-, \bar{\nu}_l), (l^+, \nu_l)\}$ of four-momenta p_1 and p_2 . The other particles produced in this collision noted X are not considered at all. The derivations that follow are applicable to the decay in the τ channel, nonetheless the analysis being restricted to the electronic and muonic decays, throughout the whole document $l \equiv \{e, \mu\}$ unless stated otherwise.

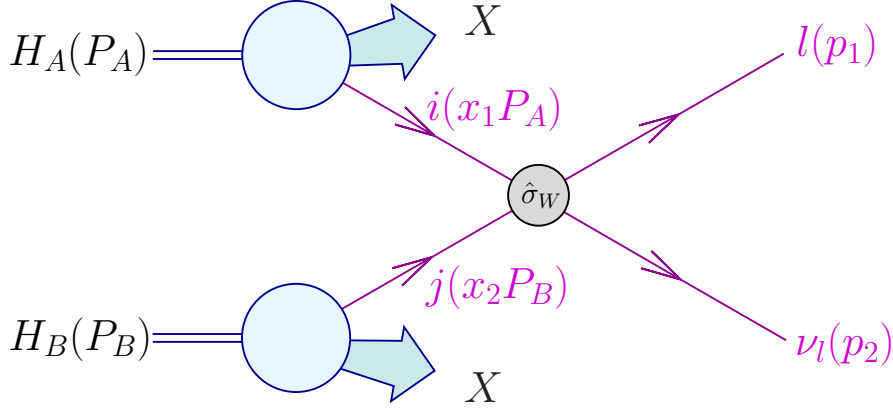


Figure 1.3: Feynman like diagram, *i.e.* in momentum-space time-ordered fashion, of the process $H_A(P_A) H_B(P_B) \rightarrow W \rightarrow l(p_1) \nu_l(p_2)$. X represents all the particles in the collision but the W boson and its leptonic decay.

The hadronic cross section $d^4\sigma_{ij}(S)$ for a given point of the quarks and leptons phase space, $d^4\Phi \equiv dx_1 dx_2 dp_1 dp_2$, and for a particular collision of partons i and j can be expressed using the factorisation “theorem” like

$$\frac{d^4\sigma_{ij}(S)}{dx_1 dx_2 dp_1 dp_2} = f_i^A(x_1, \mu_f) f_j^B(x_2, \mu_f) d^2\hat{\sigma}_{ij}(x_1 x_2 S, p_1, p_2, \mu_r), \quad (1.41)$$

that is as the product of the partonic cross section $d^2\hat{\sigma}_{ij}$ and the parton distributions functions (PDFs) f_i^A and f_j^B .

The PDFs are the density probabilities $f_i^A(x_1)$ and $f_j^B(x_2)$ for two partons i and j , to carry before their hard scatter fractions x_1 and x_2 ($0 < x_{1,2} < 1$) of the four-momenta of the hadrons they respectively income from. Purely theoretical derivation of PDFs are not computable as their description falls in the non perturbative regime of QCD where α_s is too large, therefore they are extracted from global fits to data from processes such deep inelastic scattering, Drell–Yan and jet production at the available energy range fixed by colliders. The implementation of QED and QCD radiative corrections from quarks in the initial state are universal, *i.e.* independent from the process. These corrections contain mass singularities that can be factorised and absorbed in a redefinition (renormalisation) of the PDFs. The singularities are removed in the observable cross section while the PDFs becomes dependent of a factorisation scale μ_f controlled by the DGLAP evolution equations [30, 31, 32]. This scale is to be identified –for example– to a typical scale of the process, like the transverse momentum or in the present case by the mass of the resonance $\mu_f = M_W$.

The partonic cross section $d^2\hat{\sigma}_{ij}$ corresponds to the probability that the partons i and j , of four-momenta $x_1 P_A$ and $x_2 P_B$, collide and create a W resonance of mass $m_W = \sqrt{x_1 x_2 S}$ which in turn decays into leptons l and ν_l respectively of four-momenta p_1 and p_2 . The hard scattering occurs at such energies that partons can be seen as free, *i.e.* α_s is small. This allows to calculate the cross section using perturbation theory. Up to a given energy scale higher order Feynman diagrams are not directly computed but accounted by factorising their effect in the value of the constant α_s . This renormalisation scale is the one of the virtual resonance, which means here $\mu_r = M_W$. The total

partonic cross section is then developed in power of $\alpha_s(M_W)/(2\pi)$

$$\hat{\sigma}_{ij} = \hat{\sigma}_{ij}^{(0)} + \frac{\alpha_s(M_W)}{2\pi} \hat{\sigma}_{ij}^{(1)} + \left(\frac{\alpha_s(M_W)}{2\pi}\right)^2 \hat{\sigma}_{ij}^{(2)} + \mathcal{O}(\alpha_s^3). \quad (1.42)$$

In this equation the first term of this series is the leading-order (LO), usually called the Born level, the second the next-to-leading order (NLO) correction of order α_s and so on the third term adds up next-to-next-to-leading order (NNLO) corrections of order α_s^2 . The last term contains all corrections above α_s^2 . In practice only the first corrections are brought to a calculus as the number of Feynman diagrams increase rapidly when going to higher order corrections. Let us remark that a correction term of order (k) is to be implicitly apprehended as $\hat{\sigma}_{ij}^{(k)} \equiv \hat{\sigma}_{ij}^{(k)} \delta_{ij}^{(k)}$ where

$$\begin{aligned} \delta_{ij}^{(k)} &= 1 && \text{if the } ij \text{ collision contribute to } \hat{\sigma}_{ij}^{(k)}, \\ \delta_{ij}^{(k)} &= 0 && \text{if the } ij \text{ collision do not contribute to } \hat{\sigma}_{ij}^{(k)}. \end{aligned}$$

The total hadronic cross section is then deduced by embracing all available corrections to the partonic cross section and by successively integrating Eq. (1.41) over the accessible phase space to the leptons and partons. This means in the latter case integrating over all possibles x_1 and x_2 , but also by summing over all possible partonic collisions, which gives eventually

$$\sigma(S) = \sum_{i,j} \int_0^1 dx_1 \int_0^1 dx_2 f_i^A(x_1, \mu_f) f_j^B(x_2, \mu_f) \hat{\sigma}_{ij}(x_1 x_2 S, \mu_r). \quad (1.43)$$

From the experimentalist pragmatic point of view the matter of importance is to understand the kinematics of the leptons and how the W properties can be extracted from them. Hence, in what follows, basics on the partonic cross section and on the PDFs are reminded with emphasis on the kinematics aspects rather than the dynamical issues. After that, an overview of the relevant kinematics in W production is given.

(b) Partonic level

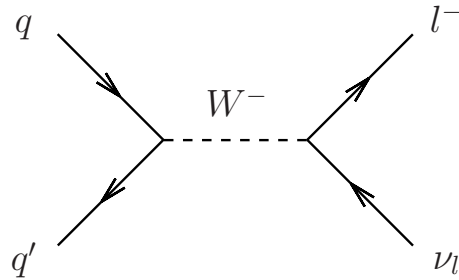


Figure 1.4: Feynman diagram for the production of a W in $q\bar{q}' \rightarrow W^- \rightarrow l^- \bar{\nu}_l$ at the Born level.

The production of a W at the Born level is made through quark–anti-quark annihilation, which is illustrated here for the case of a W^- and noted

$$q(k_1) \bar{q}'(k_2) \rightarrow W^- \rightarrow l^-(p_1) \bar{\nu}_l(p_2), \quad (1.44)$$

where the four-momenta of the particles have been put into brackets. This process, described by one Feynman diagram (Fig. 1.4), has an amplitude of probability expressed as

$$\mathcal{M} = i \left[\frac{g}{\sqrt{2}} V_{q\bar{q}'} \bar{v}(k_2) \gamma^\mu \frac{1}{2}(1 - \gamma^5) u(k_1) \right] \left\{ \frac{1}{\hat{s} - M_W^2 + i M_W \Gamma_W} \right\} \left[\frac{g}{\sqrt{2}} \bar{u}(p_1) \gamma_\mu \frac{1}{2}(1 - \gamma^5) v(p_2) \right]. \quad (1.45)$$

The pending expression for the process $q\bar{q}' \rightarrow W^+ \rightarrow l^+ \nu_l$ is obtained by doing the substitution $k_1 \leftrightarrow k_2$ and $p_1 \leftrightarrow p_2$ in this last equation. Let us note that in the case where $\hat{s} \ll M_W^2$, that is for a low energy in the collision, the propagator of order $\sim 1/M_W^2$ makes us rediscover the historical coupling constant $G_F/\sqrt{2}$ from the Fermi model.

At Born level all partons have a purely longitudinal motion, which means that in the present convention, the quark and anti-quark momenta are expressed in the Cartesian coordinate basis like

$$k_1 = \frac{\sqrt{\hat{s}}}{2} \begin{pmatrix} 1 \\ 0 \\ 0 \\ 1 \end{pmatrix}, \quad k_2 = \frac{\sqrt{\hat{s}}}{2} \begin{pmatrix} 1 \\ 0 \\ 0 \\ -1 \end{pmatrix}. \quad (1.46)$$

The total partonic cross section $\hat{\sigma}^{(0)}(q\bar{q}' \rightarrow W \rightarrow l\nu_l) \equiv \hat{\sigma}$ deduced from Eq. 1.45 reads

$$\hat{\sigma}(\hat{s}) = \frac{4}{3\pi} \frac{|V_{q\bar{q}'}|^2}{s_q s_{\bar{q}'} N_c} \left(\frac{M_W^2 G_F}{\sqrt{2}} \right)^2 \frac{\hat{s}}{(\hat{s} - M_W^2)^2 + M_W^2 \Gamma_W^2}, \quad (1.47)$$

where s_q and $s_{\bar{q}'}$ are the spins of the quark and of the anti-quark. The previous formula is correct as well in the case of a W^+ production. The variable \hat{s} belongs to a set of three others invariant Lorentz scalars, known as the Mandelstam variables, and is defined by

$$\hat{s} \equiv (k_1 + k_2)^2 = (p_1 + p_2)^2, \quad (1.48)$$

$$\equiv m_W^2, \quad (1.49)$$

where the last line makes the link with the invariant mass m_W of the off-shell W . The fraction in Eq. (1.47) depending of \hat{s} reveals the Breit-Wigner resonant behaviour of the W , that is a peaked distribution centered on M_W and whose width is controlled by Γ_W . It means a W can be produced at any mass, as high or low as possible, but the probability this happens gets smaller and smaller as m_W is far from the central value M_W of the peak like as shown on Fig. 1.5.

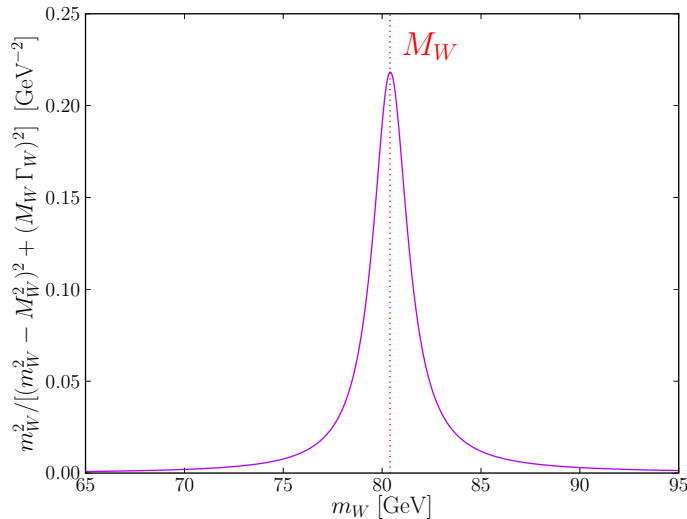


Figure 1.5: Breit-Wigner behaviour of the off-shell W mass.

The NLO corrections of $\mathcal{O}(\alpha_s)$ comes from the three following contributions in which γ^* represents a virtual photon: (a) virtual gluon corrections to the LO $q\bar{q}' \rightarrow \gamma^* g$, (b) real gluon corrections

$qg \rightarrow \gamma^* q$ and (c) quark/anti-quark gluon scattering $qg \rightarrow \gamma^* q$, or $\bar{q}'g \rightarrow \gamma^* \bar{q}'$. The Feynman diagrams associated to these corrections are displayed in Fig. 1.6 (a), (b) and in (c) for the case of quark gluon scattering only.

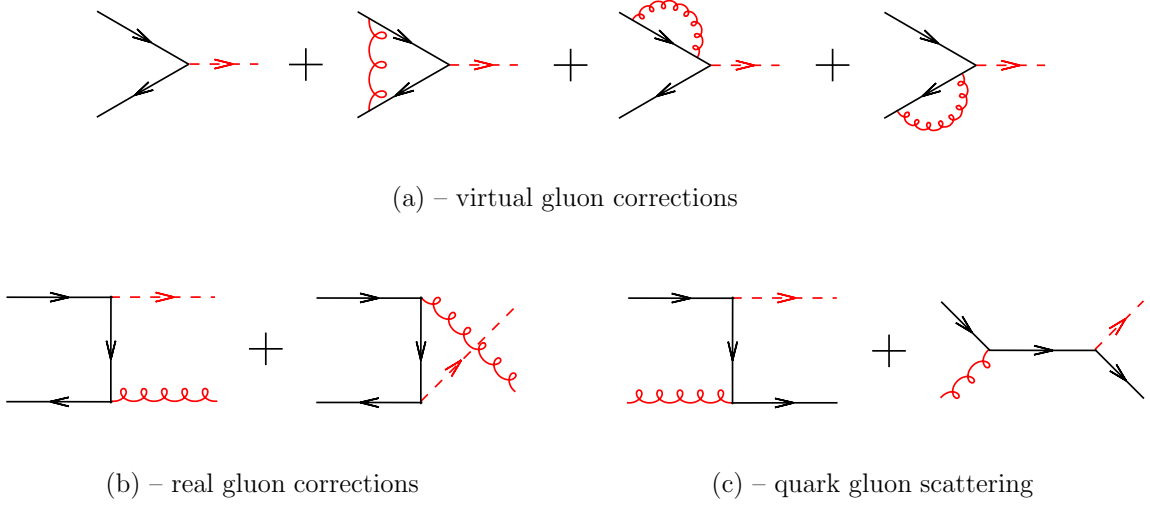


Figure 1.6: The leading- and next-to-leading-order Feynman diagrams for W in Drell–Yan like.

In top of QCD corrections are electroweak radiative corrections briefly mentioned below. The $\mathcal{O}(\alpha)$ EW radiative corrections to the W in Drell–Yan can be divided in a gauge invariant way into three parts: the initial state radiation (ISR), the initial-final state interferences (non factorisable corrections) and the final state radiation (FSR). The leading ISR (mass singular) QED corrections can be absorbed as stated previously into the PDFs. The non factorisable corrections are negligible in resonant W boson production [63]. On the contrary, the FSR corrections affect considerably various W observables among which is the transverse momentum of the charged lepton whose shape is primordial for the extraction of the M_W . For example in Ref. [64], the final state photonic correction was approximated and lead to a shift in the value of M_W of 50 – 150 MeV for the Tevatron collisions at that time. The development of these electroweak NLO corrections is beyond the scope of our discussion, the reader interested to have more details on this particular topic can look at Refs. [63, 65].

Coming back to the LO, before the phase space integration the differential partonic cross section can be written as a function of $\theta_{W,l}^*$,

$$\frac{d\hat{\sigma}}{d\cos\theta_{W,l}^*} = \frac{3}{8} \hat{\sigma}(\hat{s}) (1 + \lambda Q \cos\theta_{W,l}^*)^2, \quad (1.50)$$

the angular dependency can be traced back from the derivations made in Eq. (1.38), and where in the present context the polarisation λ of the W is ruled by the following inequality between the fractions of momenta x_1 and x_2 the partons bears before the collision

$$x_1 > x_2 \Rightarrow \lambda = +1, \quad (1.51)$$

$$x_1 < x_2 \Rightarrow \lambda = -1. \quad (1.52)$$

Note that at the LO there are no production of W of longitudinal polarisation state due to the absence of a transverse momentum of the W and in the massless quark approximation. Nonetheless, from the algebraic point of view, rather than the W , the quarks and leptons are the objects we manipulate, hence in the continuity of the present calculus Eq. (1.50) writes in function of $\theta_{q,l}^*$ –the angle between the charged lepton and the quark q momenta– like

$$\frac{d\hat{\sigma}}{d\cos\theta_{q,l}^*} = \frac{3}{8} \hat{\sigma}(\hat{s}) (1 - Q \cos\theta_{q,l}^*)^2. \quad (1.53)$$

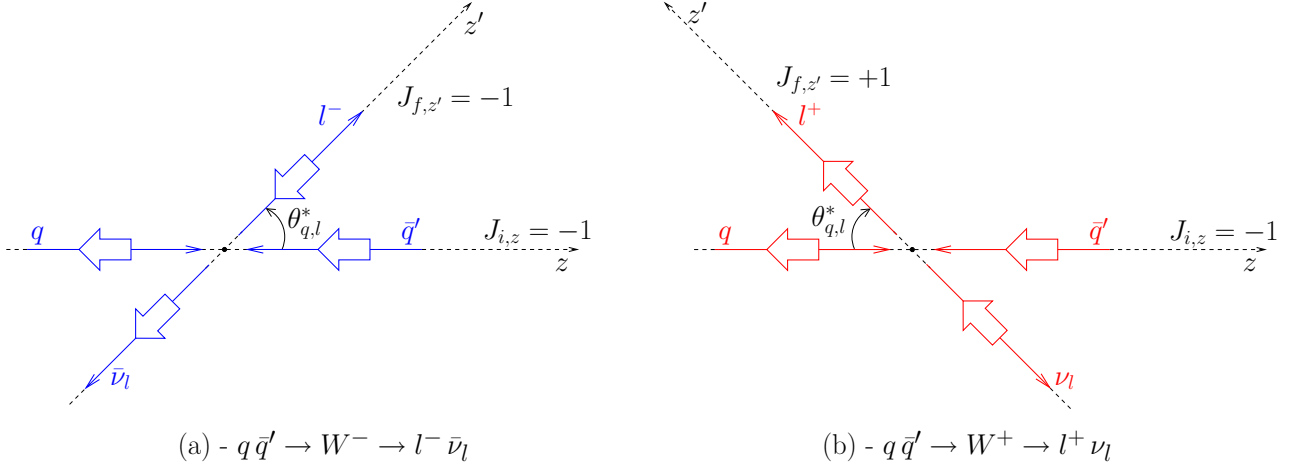


Figure 1.7: Favored opening angle between the quark q and the charged lepton l in the WRF for the production of a W^- (a) and W^+ (b).

The angular dependency can be found out quickly using the rotations matrices techniques. Figure 1.7 actually gives the hint for the privileged angular decay configuration constrained by helicity conservation, for both W^- and W^+ cases. For example in the case of $q \bar{q}' \rightarrow W^- \rightarrow l^- \bar{\nu}_l$, using rotation matrices techniques with the help Fig. 1.7.(a) gives

$$\frac{d\hat{\sigma}}{d\cos\theta_{q,l}^*} \propto |d_{-1,-1}^1(\theta_{W,l}^*)|^2, \quad (1.54)$$

$$\propto (1 + \cos\theta_{W,l}^*)^2. \quad (1.55)$$

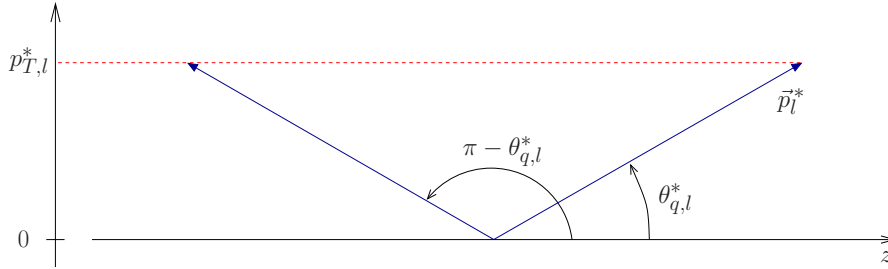


Figure 1.8: Representation of the two angular configurations that can produce the same transverse momentum for the charged lepton.

Based on Eq. (1.53) the partonic cross section can be expressed as a function of the transverse momentum of the charged lepton in the WRF $p_{T,l}^*$. This function will be useful later to understand the behaviour of the charged lepton p_T in the laboratory frame. The change of variable is done by summing the two angular configurations giving the same $p_{T,l}^*$ as shown on Fig. 1.8. The analytical derivation writes

$$\frac{d\hat{\sigma}}{dp_{T,l}^*} = \left(\left. \frac{d\hat{\sigma}}{d\cos\theta_{q,l}^*} \right|_{\theta_{q,l}^*} + \left. \frac{d\hat{\sigma}}{d\cos\theta_{q,l}^*} \right|_{\pi-\theta_{q,l}^*} \right) \times \left| \frac{d\cos\theta_{q,l}^*}{dp_{T,l}^*} \right| \quad (1.56)$$

which gives finally

$$\frac{d\hat{\sigma}}{dp_{T,l}^*} = 6 \frac{\hat{\sigma}(\hat{s})}{\hat{s}} \frac{p_{T,l}^* \left(1 - 2p_{T,l}^{*2}/\hat{s}\right)}{\sqrt{1 - 4p_{T,l}^{*2}/\hat{s}}} \quad (1.57)$$

From the jacobian $|d \cos \theta_{q,l}^*/d p_{T,l}^*|$ arise a term whose denominator shows a singularity when $p_{T,l}^* = \sqrt{\hat{s}}/2$. This singularity is visible in Fig. 1.9 that represents the $p_{T,l}^*$ distribution and for that reason it is called the jacobian peak.

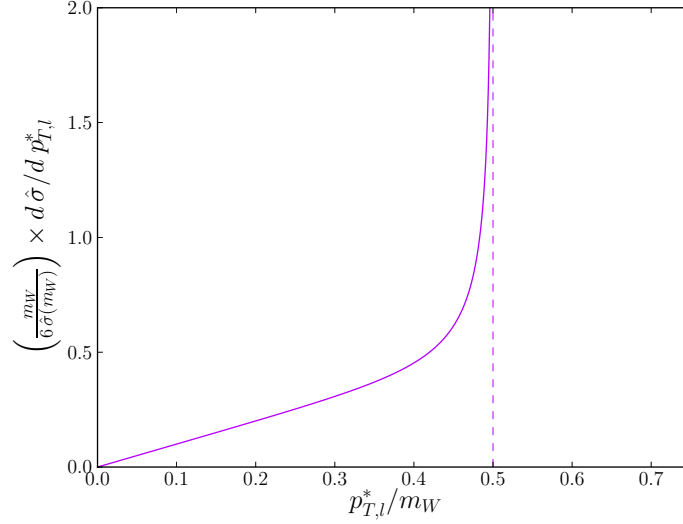


Figure 1.9: Transverse momentum of the charged lepton in the W rest frame.

This means this peak will eventually be visible at the hadronic level but will be smoothed when integrating over all possible masses for the W . Still, because the $p_{T,l}^*$ distribution is weighted by $\hat{\sigma}(\hat{s})$ only the contributions for which the invariant mass is such that $m_W \approx M_W$ will be preponderant (cf. Fig. 1.5). Therefore a peak is to be expected around $p_{T,l}^* \approx M_W/2$ its smoothness being a direct consequence of the width Γ_W .

The jacobian peak in the $p_{T,l}^*$ distribution can be understood from a more intuitive geometric point of view that consists to project the momenta of the charged lepton on the $r - \phi$ transverse plane like shown in Fig. 1.10 where an isotropic decay of the charged lepton has been adopted for representation practicability. As as can be seen the rise of the $p_{T,l}^*$ is a direct consequence of the $\sin \theta_{q,l}^*$ function entering the projection $p_{T,l}^* \equiv p_l^* \sin \theta_{q,l}^*$.

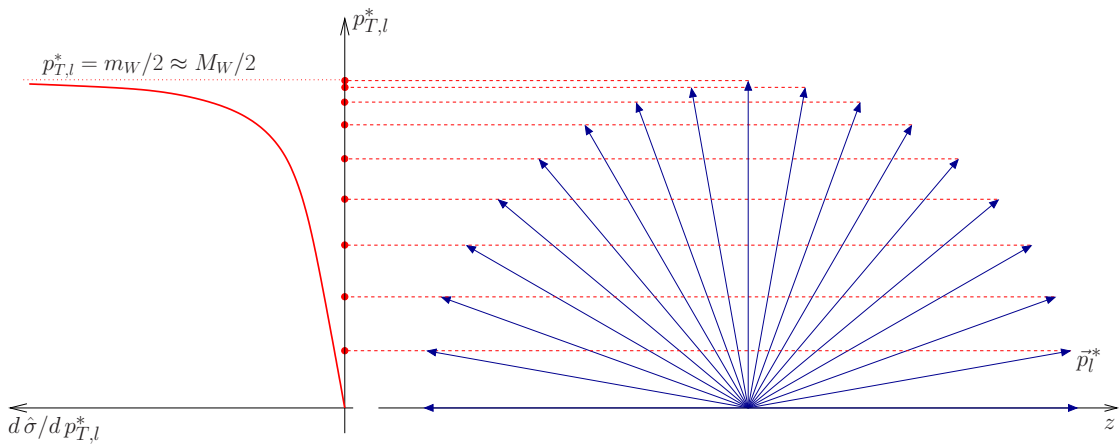


Figure 1.10: Schematic drawing giving a geometric intuition to apprehend the jacobian peak of the $p_{T,l}^*$ distribution.

(c) Behaviour of the parton distribution functions

Here the PDFs behaviour in function of x are reminded because of their strong influence on the kinematics of the W and in consequence on the leptons. The quantity $f_a^p(x)$ represents the probability to have a parton of type a in a proton having a fraction of the four-momentum of the latter comprised between x and $x + dx$. Figure 1.11 represents the PDFs extracted from the set CTEQ6.1M [66] used in this analysis.

Two type of partons can be distinguished in a proton, the valence (v) quarks and the sea (s) quarks. The valence quarks –bound by the strong interaction– are the elementary particles conferring to the proton its properties. The sea quarks arise as a consequence of the short-time fluctuation of the wave function of the proton. As described in relativistic quantum physics particles can create and annihilate, which translates in the present case that valence quarks/gluons radiate gluons which in turn can split again in gluon or pairs of quark–anti-quark. A way to look at those distributions is to consider that a probing particle impinging on the proton can resolve in the transverse direction its smaller building blocks as better as it possess a high energy. Indeed, using optics vocabulary, to a probe of momentum p we can associate an intrinsic wave-length $\lambda = 1/p$ which is most likely to diffract with pattern of the same wave-length. Bearing this fictitious probe in mind the behaviour of each flavours are recaptured.

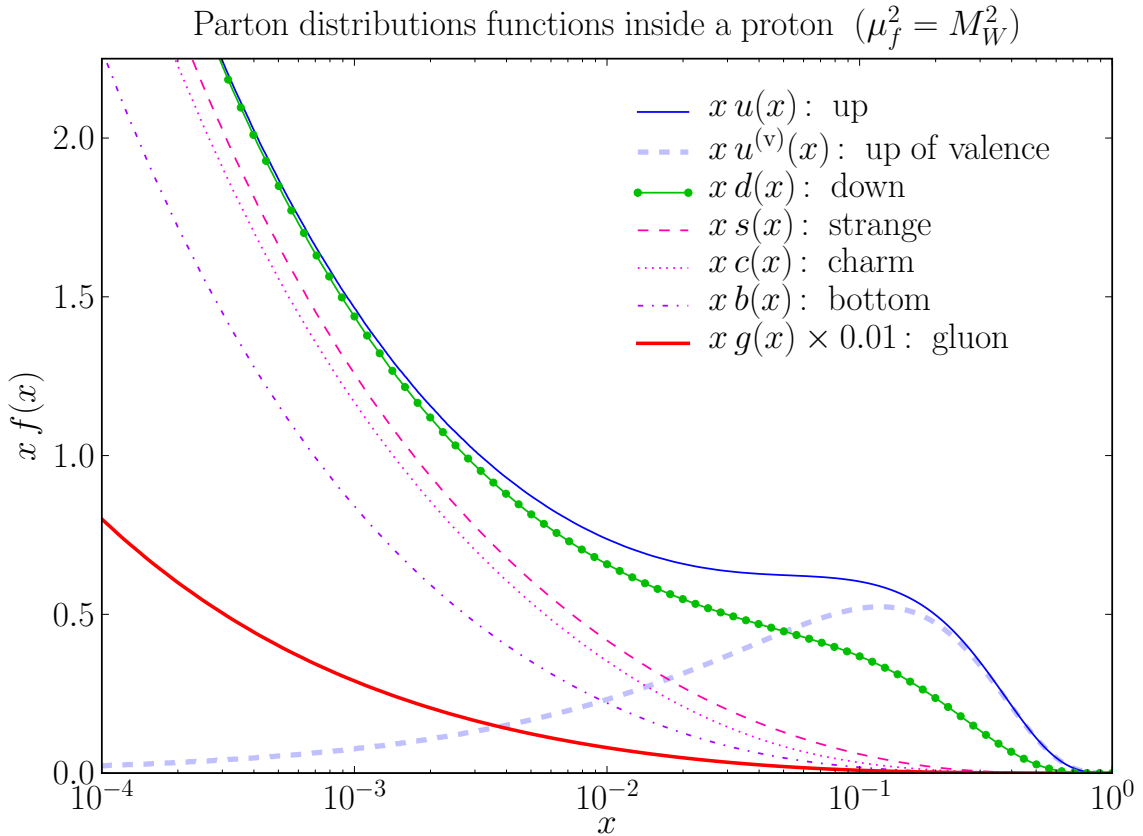


Figure 1.11: CTEQ6.1M parton distributions functions for the quarks and gluons.

The up and down quarks are predominant compared to any other flavors which means that as we would expect a probe will most likely hit a u or a d in proton. Near $x \rightarrow 1$ the bumps reflect the high probability to hit a valence u or d quarks. In Fig. 1.11 the valence contribution for the case of the up quark is shown. Thus, the rise of the probability at low x is due to the sea contributions starting from 0 at $x = 1$ and increases as $x \rightarrow 0$. The behaviour at small- x is the consequence that probe

starts to resolve more and more of de-localised sea quarks. The \bar{u} and \bar{d} behaviour can be directly deduced from the removal of the valence bump present for the u and d flavors. Let us stress that even though the masses of the u and d quarks are very close for $x < 10^{-4}$ we observe that $\bar{u} < \bar{d}$.

The patterns in the strange, charm and bottom quarks can be understood from the previous explanations for the up and down quarks of the sea. For a given x the probability to observe a given flavour decreases as the quark mass increase. Indeed, it is harder to create virtual pairs of heavy quarks compared to lighter quarks given the same amount of energy explaining why $s(x) > c(x) > b(x)$. Concerning the top flavour the energies scales we are working with are far too small to resolve any top quarks hence, $t(x) = 0$. The distributions of the \bar{s} , \bar{c} and \bar{b} are exactly the same in a first approximation. For example, only very recently the strange quark asymmetry has been implemented in some PDF set. Such corrections are not present in the CTEQ6.1M set that was used in this work, then later on $q^{(s)}(x) = \bar{q}^{(s)}(x)$.

Finally there is the gluon contribution that needed to be divided to a factor of 100 to be scaled to the frame.

(d) Hadronic level at the improved leading order

Higher order corrections are necessary to get rid in the cross section as much as possible of the dependency from the unphysical renormalisation and factorisation scales due to the perturbation expansion truncation. Nonetheless, the comprehension of the main features of the W and leptons kinematics can be done studying just an improved leading-order description of the phenomenon, and when necessary, use higher order corrections to pin-point a particular effect in a given phase-space domain.

This improved LO, considered in the rest of this Chapter, is defined by taking the LO expressions of the partonic cross section convoluted with the remormalised PDFs and by taking part of the radiation of the partons in the initial state. Due to momentum conservation, the radiation of gluons and photons off partons provide a realistic picture in which quarks produce a W with a non zero transverse motion. Note that by “part of the radiation” we mean that emission of real gluons and photons are taken into account but without embracing all other virtual loop corrections belonging to the same order in α_s or α . In this scheme, Fig. 1.12 represents an example of such initial state radiation for a particular event.

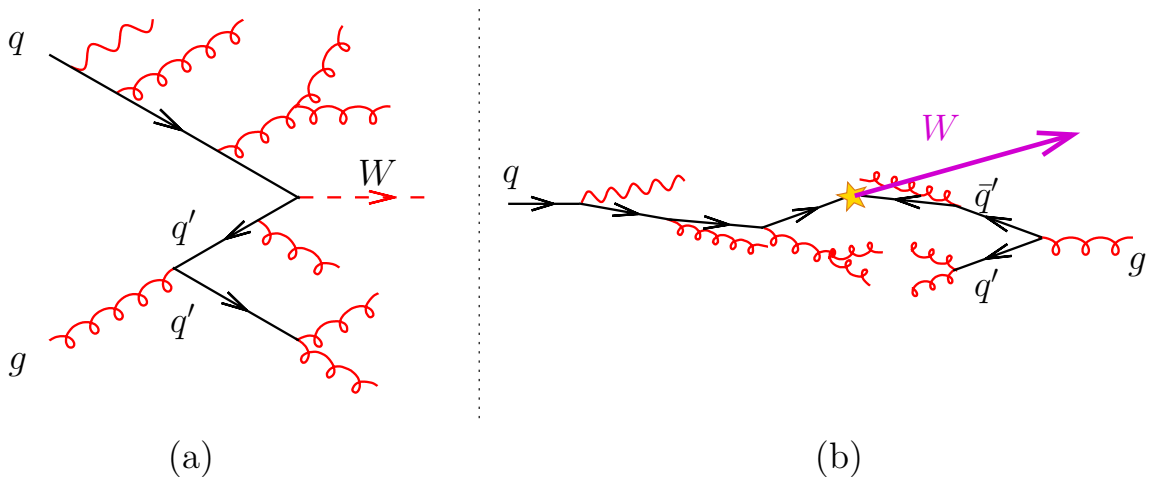


Figure 1.12: Example of the emission of real gluons and photons from the initial state partons in a Feynman-like representation (a) and in the associated \bar{x} -space representation (b).

Before going any further common variables and conventions are reminded. Usually, switching to a second set of variables (τ, y_W) equivalent to (x_1, x_2) proves to be useful. This change of variables

is defined by

$$\tau \equiv x_1 x_2, \quad (1.58)$$

$$y_W \equiv \frac{1}{2} \ln \left(\frac{E_W + p_{z,W}}{E_W - p_{z,W}} \right), \quad (1.59)$$

At leading order, using the expressions of the quark and anti-quark momenta from Eqs. (1.46) gives for the rapidity the expression

$$y_W = \frac{1}{2} \ln(x_1/x_2), \quad (1.60)$$

which for x_1 and x_2 when expressed in function of τ and y_W give the following expressions

$$x_1 = \sqrt{\tau} \exp(y_W), \quad (1.61)$$

$$x_2 = \sqrt{\tau} \exp(-y_W). \quad (1.62)$$

To get rough estimations, in top of relying on LO expressions, the “narrow width approximation” is commonly used, it is defined assuming $\Gamma_W/M_W \ll 1 \Rightarrow \Gamma_W = 0$, the consequences for the mass and τ being then

$$\Gamma_W = 0 \Rightarrow m_W = M_W, \quad (1.63)$$

$$\Gamma_W = 0 \Rightarrow \tau = \frac{M_W}{\sqrt{S}} \approx 6 \times 10^{-3}, \quad (1.64)$$

where for reminder $\sqrt{S} = 14$ TeV in the case of pp collisions at the LHC. The numerical value in the last equality gives an idea of the percentage of the total energy \sqrt{S} needed to produce a W . In this approximation the partonic cross section at LO can be expressed with a Dirac function. The Breit–Wigner term in Eq. (1.47) becomes³

$$\lim_{\Gamma_W \rightarrow 0} \frac{1}{(\hat{s} - M_W^2)^2 + (M_W \Gamma_W)^2} = \frac{\pi}{M_W \Gamma_W} \delta(\hat{s} - M_W^2), \quad (1.65)$$

that is any dependency from \hat{s} vanishes, the partonic cross section is a constant which is non null only if the energy of the partons in the center of mass exactly equals M_W .

The gist of the W and leptons kinematics are illustrated below with the process $W \rightarrow l \nu_l$, that is merging both positive and negative channels and looking at the W and leptons kinematics. The Monte Carlo used to produce these preliminaries pedagogical histograms is WINHAC which will be described with more details in Chapter 3. All Monte Carlo predictions in this document are, unless stated otherwise, produced using WINHAC. The derivations presented below will serves as a base to understand later on with more refinement the production of W for each electrical charge channel separately.

Rapidity of the W boson. In the improved LO picture the rapidity approximately equals the LO expression Eq. (1.60), that is $y_W \approx \ln(x_1/x_2)$. This form translates an unbalance between the fractions x_1 and x_2 , and explains why the rapidity is strongly correlated to the PDFs. To the leading order approximation we add the one of the narrow width, in that context the x_1 and x_2 fractions entering the PDFs now reads

$$\sum_{i,j} f_i^A(x_1) f_j^B(x_2) \approx \sum_{i,j} f_i^A \left(\frac{M_W}{\sqrt{S}} e^{y_W} \right) f_j^B \left(\frac{M_W}{\sqrt{S}} e^{-y_W} \right). \quad (1.66)$$

The pattern of the rapidity distribution can be devised only from the previous expression, the weight from the partonic cross section being just a multiplicative factor.

³For reminder the Cauchy-Lorentz function $\mathcal{L}(x; x_0, \varepsilon) = \frac{1}{\pi} \frac{\varepsilon}{(x-x_0)^2 + \varepsilon^2}$ tends to a Dirac distribution $\delta(x - x_0)$ as ε reaches zero with positive values.

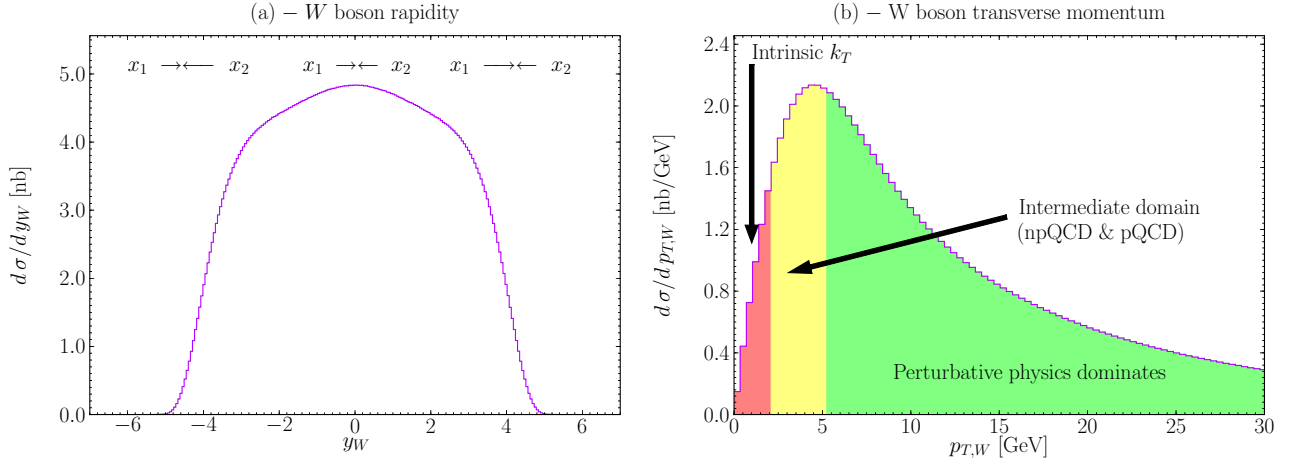


Figure 1.13: General features of a the W rapidity (a) and transverse momentum (b) in Drell–Yan at the improved LO order. The “intermediate” domain in $p_{T,W}$ is ruled by both non-perturbative and perturbative QCD (npQCD & pQCD).

The range for the rapidity can be deduced using the constraints on x_1 and x_2

$$0 < x_{1,2} < 1 \quad \Rightarrow \quad |y_{W,\max}| \approx \ln \left(\frac{\sqrt{S}}{M_W} \right), \quad (1.67)$$

which means a higher energy in the collision provides more kinematic energy to the W while its mass M_W reduces this kinematic energy. Replacing in Eq. (1.67) M_W and \sqrt{S} by their values one find that at the LHC the rapidity range is approximately $|y_{W,\max}| \approx 5$ as displayed in Fig. 1.13.

The W rapidity distribution tends to zero when $|y_W| \rightarrow 5$ because one of the fraction x is necessarily tending to 1 and as seen previously $f(x \rightarrow 1) \rightarrow 0$. Considering, in a first approximation, that x fractions are of the order of $x \sim M_W/\sqrt{S}$ one find that in average $x_{\text{LHC}} \sim 6 \times 10^{-3}$ while for the Tevatron energies $x_{\text{Teva.}} \sim 4 \times 10^{-2}$. This shows how the energy in the LHC collisions will make small- x contributions predominant with respect to the one of the Tevatron.

In the region $y_W \approx 0$, the form of the rapidity seen in Eq. (1.60) indicates that $x_1 \approx x_2$, which happens for sea quarks most of the time. Indeed, substituting in Eqs. (1.61–1.62) $M_W/\sqrt{S} \sim 6 \times 10^{-3}$ and $y_W = 0$ gives $x_{1,2} \approx 6 \times 10^{-3}$. For these values of x the probability of having a valence quark is small, most contributions comes from sea quarks.

On the other hand, in the forward rapidity region, there must be an important unbalance between x_1 and x_2 . In an extreme case scenario, this condition is fulfilled when a quark bears an important fraction x_{high} while the other one possesses a very small fraction x_{low} , which is most probably occurring when a valence quark and a low energy sea quark collide. This can be shown using rough values, substituting again in Eqs. (1.61–1.62) $M_W/\sqrt{S} \approx 6 \times 10^{-3}$ and $|y_W| \approx 4$ gives, $x_{\text{high}} \approx 0.3$ and $x_{\text{low}} \approx 10^{-4}$. The fall of the rapidity, occurring at $y_W \approx 3$, is then a consequence of the fall of the valence quarks PDFs densities as $x \rightarrow 1$.

Let us remark that the impossibility to measure the neutrino longitudinal component $p_{z,\nu}$ implies that while trying to resolve it using the other measurable kinematics one ends up with an equation of second degree in $p_{z,\nu}$ with two solutions leading in turn to two ambiguous solutions for y_W . Nonetheless, even if the problem is not solvable on an event-per-event basis, some solution based on the whole data event allows to partly overpass the problem in the narrow-width approximation [67].

Transverse momentum of W boson. The distribution of $p_{T,W}$ (Fig. 1.13.(b)) in this improved LO picture is the consequence of three main effects. First is the perturbative emission of real gluons and quark/anti-quark gluon scattering (Fig. 1.6.(b,c)) which dominates at high p_T . As p_T decreases

the spectrum is governed by the re-summation of leading-logs, then finally below $p_{T,W} \approx 2 \text{ GeV}$ the intrinsic transverse momentum of partons inside the proton dominates.

Since the intrinsic k_T of partons modeling enters our analysis more details are given below. This intrinsic k_T can be initially apprehended as the consequence of the Heisenberg uncertainty principle applied to the confinement of the partons in a finite volume of the order of a Fermi. Still, a quick calculus shows this effect cannot totally account for the observed data and this initial k_T is nowadays depending on the energy involved in the collider. Assuming a simple factorisation of this effect from the longitudinal motion ruled by the PDFs the expression of the latter necessary to the cross section calculus can be accounted doing the following substitution

$$f(x) \rightarrow h(\vec{k}_T) f(x), \quad (1.68)$$

where $h(\vec{k}_T)$ is the density of probability for a parton to have a transverse momentum of \vec{k}_T . Modeled with a Gaussian distribution it can reads:

$$h(\vec{k}_T) = \frac{b}{\pi} \exp(-b k_T^2), \quad (1.69)$$

where the average value of k_T noted $\langle k_T \rangle$ is $\langle k_T \rangle = \sqrt{\pi/(4b)}$. This values needs to be estimated for a particular collider to match to the data. In the case of the Tevatron energies it is estimated to be of $\langle k_T \rangle \sim 2.2 \text{ GeV}$ and should be higher at the LHC.

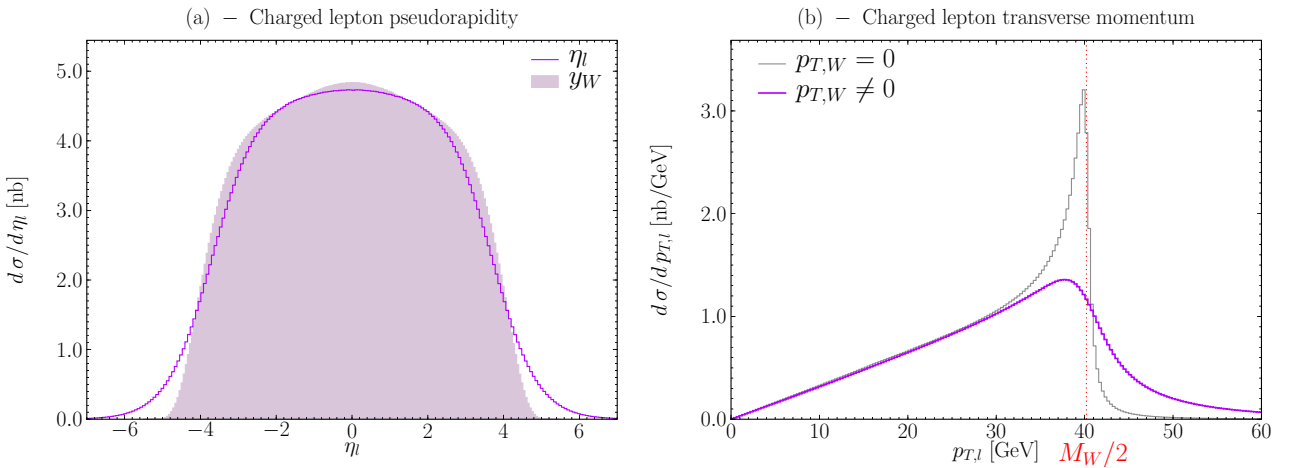


Figure 1.14: General features of the charged lepton pseudo-rapidity (c) and transverse momentum (b) in Drell–Yan at the improved LO order. In the case of $p_{T,l}$ both LO and improved LO are shown.

Pseudo-rapidity of the charged lepton. The pseudo-rapidity of the charged lepton is obtained by adding to its intrinsic rapidity y_l^* in the WRF the rapidity of the W , it reads at LO

$$\eta_l = y_W + y_l^*. \quad (1.70)$$

The rapidity of the W , as shown previously, is related to the energy in the collision and the mass of the W while the intrinsic rapidity y_l^* is a consequence of the angular decay governed by the $V - A$ coupling. Indeed, still at LO, y_l^* takes the form

$$y_l^* = \frac{1}{2} \ln \left(\frac{1 + \cos \theta_{W,l}^*}{1 - \cos \theta_{W,l}^*} \right). \quad (1.71)$$

The estimation of the contribution of the intrinsic rapidity of the lepton to the total pseudo-rapidity can be evaluated roughly. We make the assumption that in average there is as much charged leptons

spreading the fundamental y_W distribution that narrowing it, which can be formalised stating there is as much $\langle \cos \theta_{W,l}^* \rangle \approx 1/2$ than $\langle \cos \theta_{W,l}^* \rangle \approx -1/2$. Substituting these averaged values of $\cos \theta_{W,l}^*$ in Eq. (1.71) gives $\langle y_l^* \rangle = \pm 0.6$, *i.e.* $|\langle y_l^* \rangle| < |\langle y_W \rangle|$. Then, the main pattern of the η_l distribution is mostly inherited from the one present in the y_W distribution. This explains why η_l distribution covers sensibly the same range than y_W as can be seen in Fig. 1.14.(c). Because the W rapidity cannot be measured the η_l distribution is used as a substitute and proves particularly useful in the PDFs study. More details on that topic in the context of the ATLAS experiment can be found in Ref. [68].

To be completely honest here, and tease the reader's curiosity, the assumption that spreading and narrowing behaviour of the η_l distribution occurs in the same proportions is more or less verified at the Tevatron but it will not be the case at the LHC. In the latter case the y_{l+}^* tends to narrow the inner y_W spectrum while the y_{l-}^* spreads the latter. Then, the previous calculus is justified since both charge being merged the narrowing and spreading compensate each other and also because $\langle y_l^* \rangle < \langle y_W \rangle$.

Transverse momentum of the charged lepton. The distribution for the transverse momentum of the charged lepton at the hadronic level is directly linked to the one at the partonic level. At leading order, $p_{T,W} = 0$ which implies $p_{T,l} = p_{T,l}^*$. Then a jacobian peak around $\approx M_W/2$ is visible, its smearing coming from contributions in which $m_W \approx M_W$. Contributions displaying a value m_W too far from the central value M_W are, as it was shown in Eq.(1.57) highly improbable. Then, the $p_{T,l}$ distribution which is observable in a detector presents a jacobian peak which position allows to deduce the value of M_W .

Things gets more complicated when going to a more realistic scenario where the W possesses a transverse motion. To understand that the relative angle between $p_{T,W}$ and $p_{T,l}^*$ in the $r - \phi$ plane noted $\cos \phi_{W,l}^*$ is considered. The sign of $\cos \phi_{W,l}^*$ give rise to ambivalent behaviour for $p_{T,l}$. In the first case, where $\cos \phi_{W,l}^* > 0$, $p_{T,W}$ is such that the total Lorentz boost based from \vec{p}_W increase the value of $p_{T,l}$. In such events then $p_{T,l}$ are shifted to higher values, to the right of the Jacobian peak. On the contrary, in $(\cos \phi_{W,l}^* < 0)$ -cases $p_{T,l}$ are decreased, that is shifted to the left of the Jacobian peak.

Figure 1.14.(b) shows how much the transverse momentum of the W smears the sharpness of the Jacobian peak. That means that the extraction, from the bare $p_{T,l}$ distribution, of M_W with a Monte Carlo imply a refined implementation of the $p_{T,W}$.

Let us note also that the smearing of the jacobian peak being partially due to the W width the tail of the distribution beyond $\approx M_W/2$ can be used to measure Γ_W . This is however beyond the scope of the present document. The reader interested in this topic can consult Refs. [61, 46] for example.

Transverse momentum of the neutrino. The transverse momentum distribution of the neutrino displays the very same features than the one of the charged lepton. Still from the experimental point of view, it is very different as p_{T,ν_l} can be deduced only from the missing transverse energy given by the entire response of the calorimetry of a detector. For that reason p_{T,ν_l} is preferentially noted $\cancel{p}_{T,\nu}$ or \cancel{E}_T . The calibration of the missing transverse energy needs at least a few years, and even after that it cannot compete with the study of the charged lepton, indeed as can be seen in Table 1.3 the CDF II results [51] shows large systematic errors on M_W when using the $\cancel{p}_{T,\nu}$ distribution.

Transverse mass of the lepton pair. The transverse mass was suggested in Refs. [69, 70] to provide an alternative to measure the mass and width of the W boson. It consists of calculating the invariant mass $m_{T,l\nu_l}$ the lepton pair would have if $p_{z,l}$ and $p_{z,\nu}$ would be null. For that reason it is

called the transverse mass⁴ is defined like

$$m_{T,l\nu_l} \equiv \sqrt{(p_{T,l} + p_{T,\nu_l})^2 - (\vec{p}_{T,l} + \vec{p}_{T,\nu_l})^2}, \quad (1.72)$$

$$= \sqrt{2p_l p_{\nu_l} (1 - \cos \phi_{l\nu_l})}. \quad (1.73)$$

Now since the transverse momenta of both leptons enter as a product the influence of $p_{T,W}$ upon $p_{T,l}$ is counterbalanced by the opposite effect upon p_{T,ν_l} . At LO in the WRF both leptons transverse momenta are equal, a purely longitudinal boost does not affect these values, hence $p_{T,l} = p_{T,\nu_l}$ and $\cos \phi_{l\nu_l} = 0$ which gives for the transverse mass the $m_{T,l\nu_l} = 2p_{T,l}$, explaining why in this case the jacobian peak is located at M_W .

Figure 1.15 represents the $p_{T,l}$ and $m_{T,l\nu_l}$ distributions for three different steps in the simulation of W in Drell–Yan inside ATLAS [71]. Note that in each step trigger and acceptance cuts were made according to the ATLAS requirements, in particular $p_{T,l}$ and \cancel{E}_T cuts can be clearly distinguished looking at the low p_T region of the histograms, for further details see Ref. [71]. The first case considered is the true level, that is the prediction from the Monte Carlo at pure leading order where $p_{T,W} = 0$. Both $p_{T,l}$ and $m_{T,l\nu_l}$ jacobian peaks are sharp. When adding up QCD corrections in the initial state the jacobian peak of $p_{T,l}$ is very smeared by $p_{T,W} \neq 0$, while $m_{T,l\nu_l}$ still displays a sharp jacobian peak. The last step consists to pass the latter event generations to a simulation of the ATLAS detector. The good resolution for the charged lepton does not change a lot, while the bad resolution for \cancel{E}_T smears a lot the jacobian peak of $m_{T,l\nu_l}$.

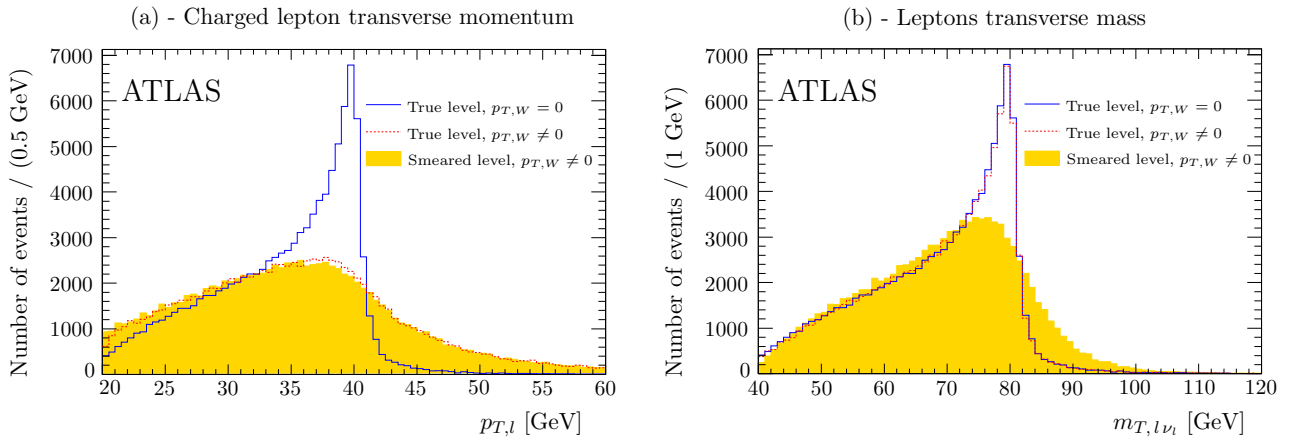


Figure 1.15: Transverse momentum of the lepton (a) and of the transverse mass (b) at the true level for $p_{T,W} = 0$, $p_{T,W} \neq 0$ and at the smeared level with $p_{T,W} \neq 0$ based on the ATLAS detector resolution [Data extracted from [71]].

1.5 An invitation to the rest of the document

Up to now, the motivation and the general context for a measurement of the W charge asymmetry $M_{W^+} - M_{W^-}$ within the Standard Model paradigm have been described. Now the outline of the rest of the document is presented through a short description of each Chapter aims and content.

Chapter 2 presents the experimental context in which this measurement can be achieved, that is at the LHC and more precisely with the ATLAS detector. Especially, the emphasis is made on the ATLAS tracker since the analysis was restricted using this sub-detector capabilities. Some highlights are made on the deformations of the tracker that should increase the systematic errors on $M_{W^+} - M_{W^-}$.

⁴This definition of the transverse mass should not be confused with the one introduced sometimes in relativistic kinematics and defined as $m_T^2 \equiv m^2 + p_T^2$, like for example in the *Kinematic* review in Ref. [1].

Distribution	$M_W \pm \delta_{M_W}^{(\text{stat.})} \pm \delta_{M_W}^{(\text{sys.})}$ [GeV]
$m_{T,e\nu_e}$	$80.493 \pm 0.048 \pm 0.039$
$p_{T,e}$	$80.451 \pm 0.058 \pm 0.045$
\cancel{p}_{T,ν_e}	$80.473 \pm 0.057 \pm 0.054$
$m_{T,\mu\nu_\mu}$	$80.349 \pm 0.054 \pm 0.027$
$p_{T,\mu}$	$80.321 \pm 0.066 \pm 0.040$
\cancel{p}_{T,ν_μ}	$80.396 \pm 0.066 \pm 0.046$

Table 1.3: CDF II results for the mass of the W [51] for the electronic and muonic channel using the transverse mass, charged lepton and neutrino transverse distributions. The statistical error is noted $\delta_{M_W}^{(\text{stat.})}$ and the systematic error $\delta_{M_W}^{(\text{sys.})}$.

Chapter 3 presents the tools that were used or implemented to carry out our analysis to evaluate the ATLAS potential to measure $M_{W^+} - M_{W^-}$. It almost exclusively treats about the Monte Carlo event generator WINHAC. The physics inside it is described along with the tools implemented downstream for the stand-alone analysis that was made. The Chapter describes as well the work done to include this Monte Carlo event generator inside the ATLAS software environment.

Chapter 4 presents the detailed work that was done to understand the kinematics of the W^+ and W^- at the LHC made necessary for the prospect of the measurement of $M_{W^+} - M_{W^-}$ but as well as for our other ongoing effort made on W properties extraction such as M_W [72, 73] or Γ_W [74]. Actually we consider this Chapter to be of interest for every physicist working on the W production in Drell–Yan at the LHC, for ATLAS, CMS and even LHC***b*** detectors.

Chapter 5 presents dedicated strategies to measure $M_{W^+} - M_{W^-}$ and their qualitative evaluation. After a short introduction of the general experimental context (trigger, acceptance, background, *etc.*) the analysis strategies devised to measure the W boson mass charge asymmetry. The strategies were specifically designed for this measurement to get rid as much as possible of the dependency from both Monte Carlo and apparatus imperfections to decrease the impact of systematic errors on $M_{W^+} - M_{W^-}$.

A Conclusion closes the document by summing up the results obtained with the proposed methods and, by taking a step backward, localise the importance of the present work amid the ongoing effort on precision measurements of the W boson properties at the LHC.

Chapter 2

The ATLAS experiment

Atlas: “Where is he ? Where is your titan ?! I will show him sorrow! I will show him pain ! I will show him Atlas ! I am the champion this city, this land, this orb needs.”

Superman #677 - In The SHADOW Of ATLAS (August 2008)

The Large Hadron Collider (LHC) [75, 76, 77, 78, 79] will be the largest circular accelerator of hadrons ever build providing unprecedented energy and luminosity. It is buried $\approx 100 - 150$ m underground within the CERN [80] facility near Geneva. This accelerator was designed to fulfill the increasing needs to probe ever smaller lengths scales to unravel the nature of the interactions of elementary particles. For that purpose the LHC accelerates in its ring counter rotating bunches of hadrons at ultra relativistic speed and collide them in four distinct points. The particles produced during these collisions are studied using one or several detectors built in the vicinity of each of the four interaction points. Among them is ATLAS [81, 82] a general purpose detector.

In this chapter, two of the most fundamentals collider parameters from the physicist point of view, *i.e.* the energy in the center of mass and the luminosity, are reminded in the LHC context. Then, the ATLAS detector is presented by reviewing the geometry and technology implemented within each of its sub-detectors: the tracker, the calorimeters and the muon spectrometer. Especially the tracker, which performances are used in this work, is described with more details. Some emphasis are made on the aspects relevant to the measurement of $M_{W^+} - M_{W^-}$ through the observation of the process hadron – hadron $\rightarrow W \rightarrow l \nu_l$ where l for reminder stands for $l \equiv \{e, \mu\}$.

2.1 The Large Hadron Collider

2.1.1 The collider

The need to produce physics resonances of ever higher masses at noticeable rates within colliders requires higher energy \sqrt{S} in the center of mass of the collision as well as higher luminosity \mathcal{L} . The importance of synchrotron radiation in e^+/e^- collisions is such that it proved to be prohibitive above LEP [83] energies to use circular collider. Then, the idea of studying non e^+e^- collisions using the LEP tunnel began to be studied in 1984 [84] and at the time the LEP collider shutdown in 2000, the project of colliding hadrons was decided [75]. So far hadron–hadron colliders were designed for $p\bar{p}$ collisions like at the SPS or the Tevatron colliders. Above 3 TeV the cross sections for pp and $p\bar{p}$ collisions are comparable but for the latter case the luminosity would have been inferior to a factor 100 at the LHC due to the difficulty to produce anti-protons. On the other hand collisions of particles holding the same charge impose *a priori* to have two independent rings having magnets of opposite polarity with separate cryostat which would have turned out to be more expensive. For the LHC a special two-in-one dipole magnet was conceived in the aim to be more economic and compact. Thus,

pp collisions being more easily achievable and less costly it was the chosen option. The LHC will as well make collisions of heavy positively charged ions.

From the physics point of view the most striking difference between hadron–hadron and e^+e^- collisions is that in the primer case the colliding particles are composite and gives for each inelastic process of interest to the physicists an important number of other particles. Hence, the LHC is primarily designed for discoveries rather than for precision measurements, still, its high center of mass energy and luminosity combined to the detectors performances should allow precision measurements. Another consequence of the hadrons composition is that partons participating in an inelastic scattering borrow only part of the whole disposable energy \sqrt{S} . For the case of W production in Drell–Yan we have seen in Eq. (1.64) that in average $\approx 0.6\%$ of \sqrt{S} is used.

Fig. 2.1 shows the different parts entering each superconducting magnet dipole that were assembled along the 27 km circumference of the LHC ring. Each proton beams are moving in opposite directions inside each of the two main dipole aperture beam-pipe. The dipole generates a magnetic field of 8.33 T to maintain the protons beams along the ring circumference, other magnets are present to focus and correct any deviations of the beams.

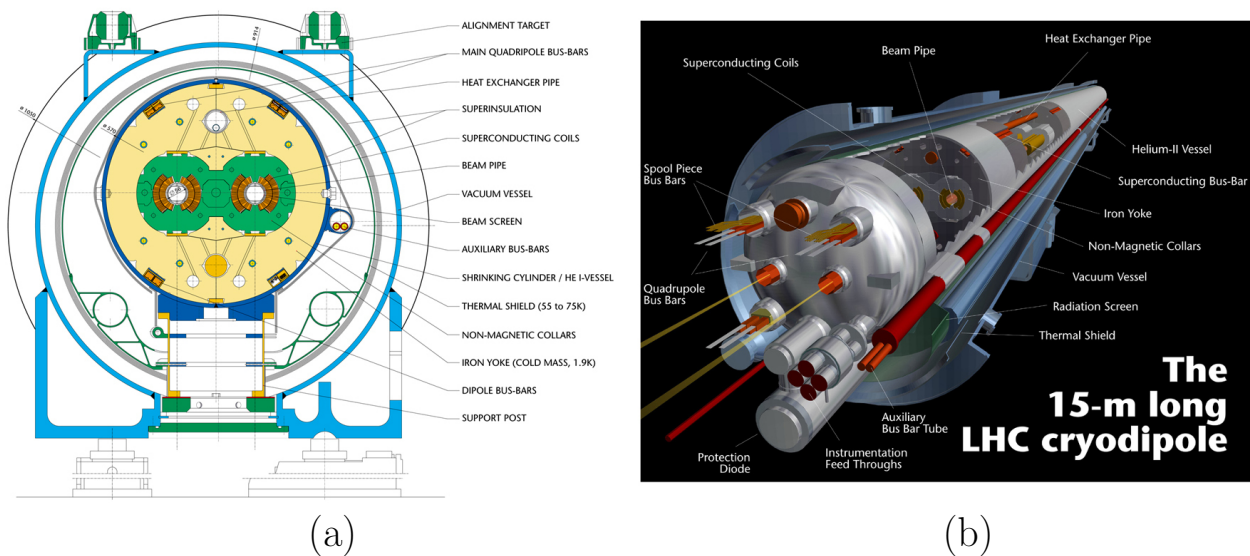


Figure 2.1: The LHC superconducting magnet cross section (a) and in a 3D rendition (b) [©CERN Geneva].

The different steps of the protons acceleration and injection inside the LHC ring are shown in Fig. 2.2. The proton beams, split in bunches of oblate volume, are successively accelerated by the LINAC2, the BOOSTER, the PS and the SPS accelerators. The SPS injects proton bunches of 450 GeV in the LHC superconducting magnet, half moving in one direction and the over half in the opposite direction. Each proton in a bunch has an energy of $E_p = 7$ TeV providing a total energy in the center of mass of $\sqrt{S} = 14$ TeV. The total pp cross section $\sigma_{pp}^{\text{tot.}}$ and its inelastic part $\sigma_{pp,\text{inel.}}^{\text{tot.}}$ are approximately equals to

$$\sigma_{pp}^{\text{tot.}} \approx 100 \text{ mb}, \quad (2.1)$$

$$\sigma_{pp,\text{inel.}}^{\text{tot.}} \approx 80 \text{ mb}. \quad (2.2)$$

The volume of a proton bunch can be defined using Gaussian functions which full widths at half maximum are, with respect to the z -axis along which protons move, of $\sigma_T = 15 \mu\text{m}$ in the transverse direction and $\sigma_z = 5.6 \text{ cm}$ in the longitudinal direction. Each bunch, composed of an order of $\sim 10^{11}$ protons, are separated by a time lapse of 25 ns (7.5 m).

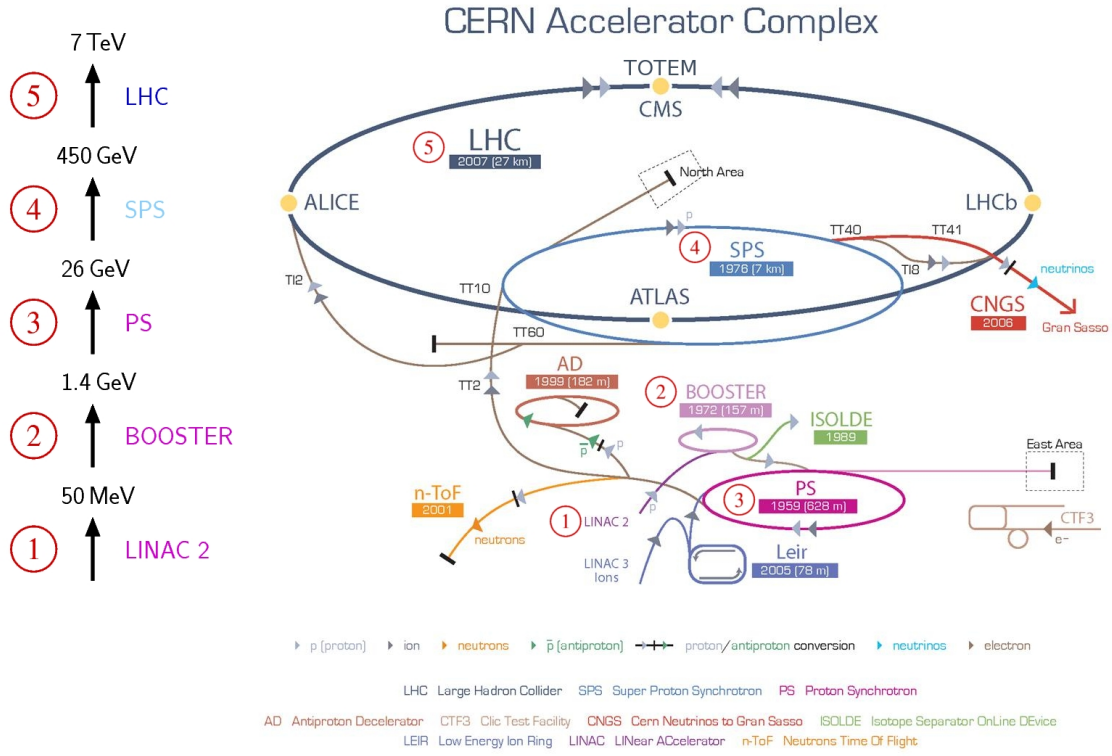


Figure 2.2: Representation of the different steps, within the CERN accelerator complex, necessary to inject protons in the LHC ring [Figure adapted from CERN-DI-0606052 ©CERN Geneva].

The luminosity \mathcal{L} is defined at the LHC like

$$\mathcal{L} = \frac{N_p^2 k_b f \gamma}{4\pi \varepsilon_n \beta^*} F, \quad (2.3)$$

where N_p is the number of protons per bunch, k_b the number of bunches, f the revolution frequency around the ring, γ the relativistic Lorentz factor related to the proton velocity ($\gamma \approx 7500$), ε_n the normalised emittance and β^* the beta function at the interaction point. The factor $F \approx 0.9$ accounts for the reduction of interaction numbers due to the full crossing angle θ_c and other characteristics of the beam configuration, it reads :

$$F = 1 / \sqrt{1 + \left(\frac{\theta_c \sigma_z}{2 \sqrt{\varepsilon_n \beta^*}} \right)^2}. \quad (2.4)$$

The number of produced inclusive events $N_{\text{events}}^{(\text{incl.})}$ for a process with an inclusive cross section σ_{process} over a time lapse $\Delta t = t_2 - t_1$ is related to the integrated luminosity L over Δt via

$$N_{\text{events}}^{(\text{incl.})} = \sigma_{\text{process}} L \quad \text{with} \quad L \equiv \int_{t_1}^{t_2} \mathcal{L} dt, \quad (2.5)$$

The nominal luminosity of the LHC, expressed in several convenient unit should reach :

$$\mathcal{L}_{\text{high}} = 10^{34} \text{ cm}^{-2} \text{ s}^{-1} = 10^7 \text{ mb}^{-1} \text{ s}^{-1} = 10^{-5} \text{ fb}^{-1} \text{ s}^{-1} = 10 \text{ nb}^{-1} \text{ s}^{-1}. \quad (2.6)$$

Based on Eqs (2.1,2.2), this gives a frequency of ~ 1 GHz of produced events among which inelastic events occur at the rate of 0.8 GHz. This will eventually lead each event of interest to be accompanied

by an average of 20 inelastic events also referred to as the “pile-up”. For this reason the LHC will use during the first three years a lower luminosity $\mathcal{L}_{\text{low}} = \mathcal{L}_{\text{high}}/10$ for which the smaller pile-up (≈ 2 events) will allow physicists to understand first the detectors before exploiting them at the design luminosity.

Most of the analysis in this work are considered for one year of LHC data taking at low luminosity, which, due to technical reasons, was assumed to be of the order of 10^7 s. Thus, one year of data taking in ATLAS at low luminosity implies an integrated low luminosity of

$$L_{\text{low}}^{1\text{year}} = 10 \text{ fb}^{-1} = 10^7 \text{ nb}^{-1}. \quad (2.7)$$

the choice for unit being cast on nb as the W inclusive/cut cross sections are of this order.

The LHC ring is planned to accelerate and collide heavy ions as well. For the purpose of our measurement strategy the possibility of having run programs with light ions have been considered. In such a context the total energy of 7 TeV for the accelerated hadron is shared between the different nucleons building it. The energy E_{nucleon} of a nucleon belonging to an hadron of mass A and charge Z is

$$E_{\text{nucleon}} = \frac{Z}{A} \times 7 \text{ [TeV]}. \quad (2.8)$$

Considering the collision of two hadrons 1 and 2 respectively of masses A_1 and A_2 the nucleon–nucleon ($n_1 n_2$) center of mass energy is $\sqrt{S_{n_1 n_2}} = E_{n_1} + E_{n_2}$ where the energies E_{n_1} and E_{n_2} of each nucleon are computed using Eq. (2.8). Concerning the luminosity, it should be possible in the most optimistic case scenario to reach $L_{A_1 A_2} = L_{pp}/A_1 A_2$, L_{pp} corresponding to the standard integrated luminosity for pp collisions. In the present study, using these rules for the case of dd collisions that were occasionally considered, gives

$$E_{\text{nucleon}} = 3.5 \text{ TeV}, \quad (2.9)$$

$$L_{dd} = L_{pp}/4. \quad (2.10)$$

To sum up for pp and dd collisions, the nucleons energies and the integrated luminosity for one year at low luminosity are

$$pp : L_{pp} = 10.0 \text{ fb}^{-1}, \quad E_{\text{nucleon}} = 7.0 \text{ TeV} \quad (\Rightarrow E_p = 7 \text{ TeV}), \quad (2.11)$$

$$dd : L_{dd} = 2.50 \text{ fb}^{-1}, \quad E_{\text{nucleon}} = 3.5 \text{ TeV} \quad (\Rightarrow E_d = 7 \text{ TeV}). \quad (2.12)$$

A number of produced events related to a process is computed using Eq. (2.5).

2.1.2 The LHC experiments

The detectors layout around the LHC ring is shown in Fig. 2.2. The actual approved experiments are: Alice, ATLAS, CMS, LHCb, LHCf and TOTEM.

ATLAS (A Toroidal LHC ApparatuS) and CMS [85] (Compact Muon Solenoid) are two detectors made for general studies of the physics at the LHC, *i.e.* refine the Standard Model parameters, confirm/infirm the existence of the Higgs boson and study new physics signatures (hypothesised BSM models, new signatures). Both can measure the signatures of high p_T objects such as e , γ , μ , τ , jets, b -jets, missing transverse energy \cancel{E}_T , etc.

Alice [86] (A Large Ion Collider Experiment) has been created to study lead ions collisions to possibly materialise a state of matter known as quark–gluon plasma, which may have existed soon after the Big Bang.

LHCb [87] (Large Hadron Collider beauty) is dedicated to the study of b quarks decays in hadrons to understand the mechanism of CP violation that could explain the matter/anti-matter asymmetry in the Universe.

The LHCf [88] (Large Hadron Collider forward) experiment uses forward particles created in collisions as a source to simulate cosmic rays in laboratory conditions.

TOTEM [89] (TOTal Elastic and diffractive cross section Measurement) will measure the general properties of pp collisions such as the total cross section and the luminosity.

2.2 The ATLAS detector

2.2.1 Detector requirements

The ATLAS detector was designed in function of the expected physics signatures, the high energies involved in the hadrons collisions and the high luminosity context present at the LHC. This imposed high constraints over the detector performances, size and trigger system. Assuming an operation life of ten years or so the detecting devices and their associated electronics must stand high radiation due to the important particles fluxes. The other problem is that in average each inelastic scattering of interest that triggers the apparatus is accompanied by usually ≈ 20 other non-interesting inelastic events. To decrease as much as possible this pile-up impact the detector needs, using a highly efficient trigger, to provide a precise and fast detector response. Also the detector needs a high granularity to lift as much as possible overlapping ambiguities between the processes of interest and the pile-up.

The size of the ATLAS detector is directly related to the \sim TeV energy scale of the produced particles which needs to be contained. For example, electrons of 1 TeV are absorbed by 30 radiation length (X_0), pions of 1 TeV by 11 absorption length (λ) and measuring momenta of muons of 1 TeV needs bending power of several Tm. Another reason for the size of the ATLAS detector is the choice made for the magnetic field which, contrary to CMS, is separated in two pieces. The first one (solenoid) used by the inner tracking detector allows a good charged particle momentum resolution and reconstruction efficiency while the muons –not stopped by the calorimetry– have their momenta resolved by large magnets generating a toroidal over a large range of momenta.

Turning now to the events signatures, ATLAS needs to identify extremely rare events, some as low as representing 10^{-14} of the total pp cross section. In the LHC context, lepton identification is challenging due to the high QCD background (*e.g.* the electrons jet ratio is $e^\pm/\text{jet} \sim 10^{-5}$) and Higgs/BSM hypothesised signatures constrained strongly each sub-detectors performances.

These general requirements reminded, we give an overview of the ATLAS detector.

2.2.2 Overview of the ATLAS detector

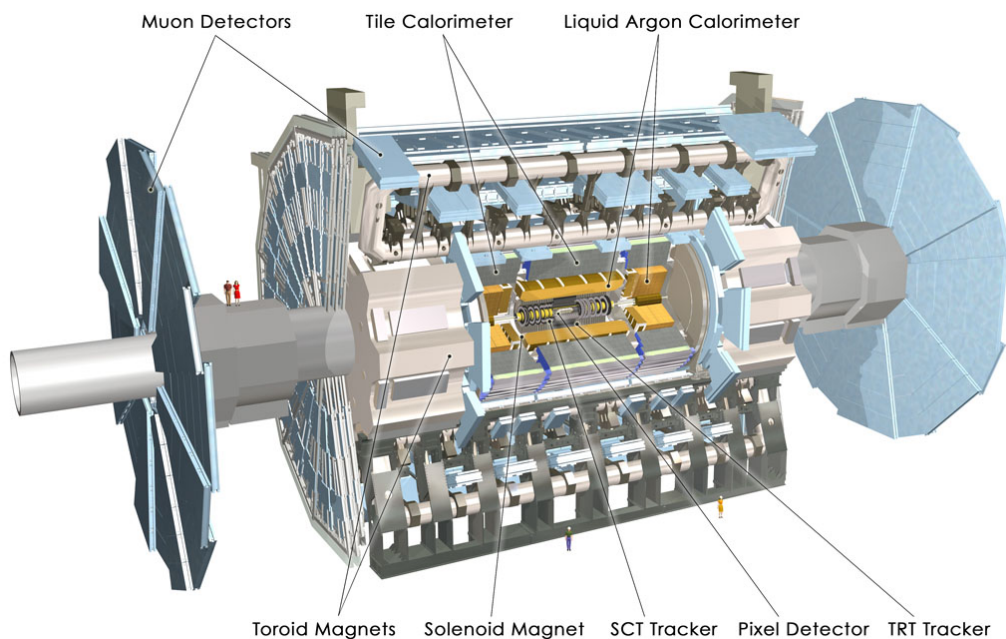


Figure 2.3: Overview of the ATLAS detector [CERN-GE-0803012 © CERN Geneva].

Detector. The ATLAS detector is nominally forward-backward symmetric with respect to the interaction point. The sub-detectors layout follows basic rules common to all hadronic colliders. Starting from the beam-pipe one can find a tracking device, then electromagnetic and hadronic calorimeters and finally a detector for muons. The inner tracker and the muon spectrometer are immersed in magnetic fields generated respectively by a thin superconducting solenoid and three large superconducting toroidal magnets. This general setup can be seen in Fig. 2.3.

Each sub-detector is composed mainly of three pieces, a barrel for high p_T particles and two end-caps located symmetrically from the interaction point to optimise the solid angle coverage. Usually, the transition regions between the barrels and the end-caps, also called the transition region, are used to pass the power cables and the readout cables of the devices.

First, the tracker, also referred to as the Inner Detector (ID), bathes in a 2 T magnetic field generated by a surrounding solenoidal magnet. It is made of semi-conductor silicon vertex detectors in the inner layers (pixel and semi-conductor tracker) and of straw trackers in its outer part. Charged particles, as they pass each layer, leave measurable hits that allow to reconstruct their trajectories and creation points (vertex) while their transverse momenta are deduced from their tracks deflection by the magnetic field.

After comes the sampling calorimeters made of alternate layers of absorbers and active detector medium. First is the electromagnetic (EM) calorimeter made of lead (absorber) and liquid argon (LAr) for the active medium. It measures with a high granularity and excellent performances in energy and position resolution the electrons and photons. The hadronic calorimeter measures the energy of hadrons and QCD jets. It is made in the barrel of steel plates (absorber) and scintillator-tiles (active detector medium), in the end-cap both tile and LAr calorimeters are used.

Around the hadronic calorimeter is the muon spectrometer bathing in the air-core toroid magnetic field. The high bending power of the magnetic field provides an excellent muon momentum resolution using three layers of high precision tracking chambers to detect the muon passage. Muons properties are measured using drift tubes and multiwire chambers. The spectrometer uses as well other chambers relying on cathode-plate and multi-wire chambers to trigger for high p_T muons events. The muon detector defines the overall size of ATLAS which is ≈ 20 m of diameter and ≈ 45 m long. The total weight of the detector reaches ≈ 7000 tons.

Trigger. The harvest of the data measured by those sub-detectors is achieved using a fast trigger. The trigger system selects events displaying interesting signatures among the plethora of events produced at the rate of ~ 1 GHz at nominal luminosity. For the first time the collected statistic for large scale processes such as W or Z production will be limited by the bandwidth and read out systems rather than by the produced events. The trigger is split into three Levels (L), L1, L2 and the event filter, the two last one being referred to as the high-level trigger. Each level refines the decision outgoing from the precedent level and, if necessary, apply additional selection criteria.

The L1 trigger treats subsets from each sub-detector information, it scans for high transverse momentum muons, electrons, photons, jets, τ leptons decaying into hadrons as well as large missing and total transverse energies. It also spots in each event to regions of interests defined as regions within the detector displaying interesting features. The decision to accept/reject an event is made within $2.5 \mu\text{s}$ and decreases the rate of incoming events to ~ 75 kHz. The L2 trigger reduces within ~ 40 ms the events rate to ~ 3.5 kHz based on full data information within the regions of interested input by L1. The last stage of the event selection, made by the event filter, reduces the rate of events to ~ 200 Hz. This step, lasting ~ 4 s, is carried out offline using analysis procedure and supply an event of size 1.3 Megabyte.

Already at this point we mention few trigger information relevant for both selection and analysis of W properties from Drell–Yan production. More details will be given on these topics later on. Among few other requirements, the trigger should be activated for isolated electrons/muons with high p_T threshold of the order of $p_{T,l} > 20 - 25$ GeV while the data from such events should be studied in the range $30 \text{ GeV} < p_{T,l} < 50 \text{ GeV}$.

Forward detectors. Also worth mentioning are three smaller detectors in the forward region associated to ATLAS. From the interaction point, at ± 17 m is LUCID (LUminosity measurement using Čerenkov Integrating Detector), at ± 140 m is ZDC (Zero-Degree Calorimeter) and at ± 240 m is ALFA (Absolute Luminosity For ATLAS) LUCID and ALFA roles are to determine the luminosity delivered to ATLAS and ZDC to have a key role to determine the centrality of heavy ions collisions.

Figure 2.4 concludes this overview by recapturing the interactions of some particles with the different sub-detectors.

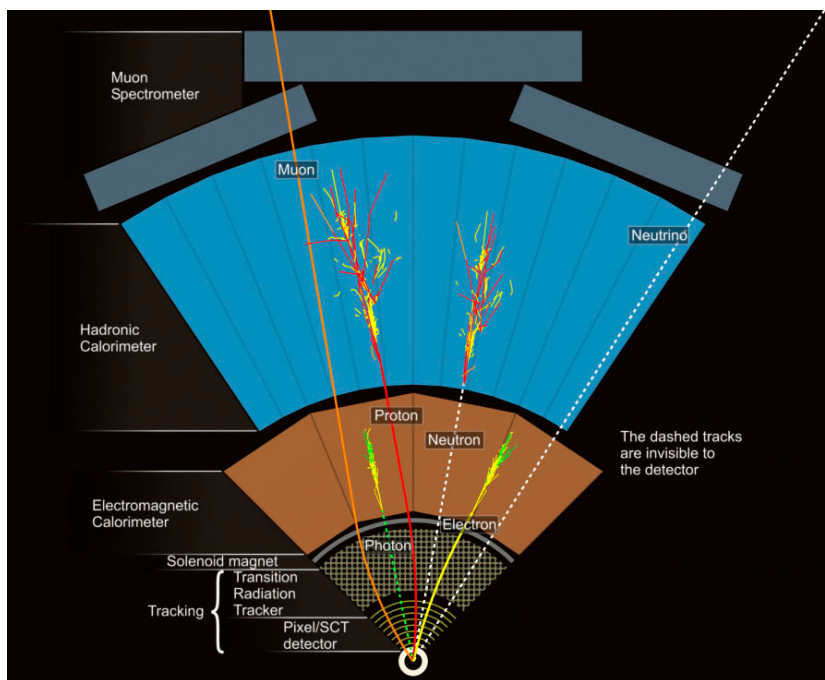


Figure 2.4: Overview of some particles passage through the ATLAS tracker, electromagnetic calorimeter, hadronic calorimeter and eventually through the first layers of the muon spectrometer. Toroidal magnets located at higher radii are not visible in this picture [CERN-GE-0803022 ©CERN Geneva].

The rest of the Chapter presents the technology and geometry of each ATLAS sub-detectors. First the calorimeters and muon spectrometer are presented. In top of a general description, the link of their role on the measurement of W in Drell–Yan is mentioned mostly from the trigger point of view since the tracker, so far, does not have any trigger on its own. Hence the electromagnetic calorimeter and muon spectrometer trigger efficiencies for events displaying respectively isolated high p_T electrons and muons are cited. These kind of studies associates as well \cancel{E}_T due to the final state neutrino. However, since in the present analysis the latter is not taken into account, the \cancel{E}_T trigger is not considered to be relevant although its influence on the results was controlled. More details will be given in Chapter 5. In the second and final part, a detailed description of the inner detector is given. In what follows, dimensions of devices are given by their radial(longitudinal) extensions $r(L)$ and their absolute pseudo-rapidity acceptance $|\eta|$.

2.2.3 Calorimetry

Both electromagnetic calorimeter (EMC) and hadronic calorimeter (HC) geometry, technology and performances are reviewed. Their set up can be seen in Figs. 2.5 and 2.8.

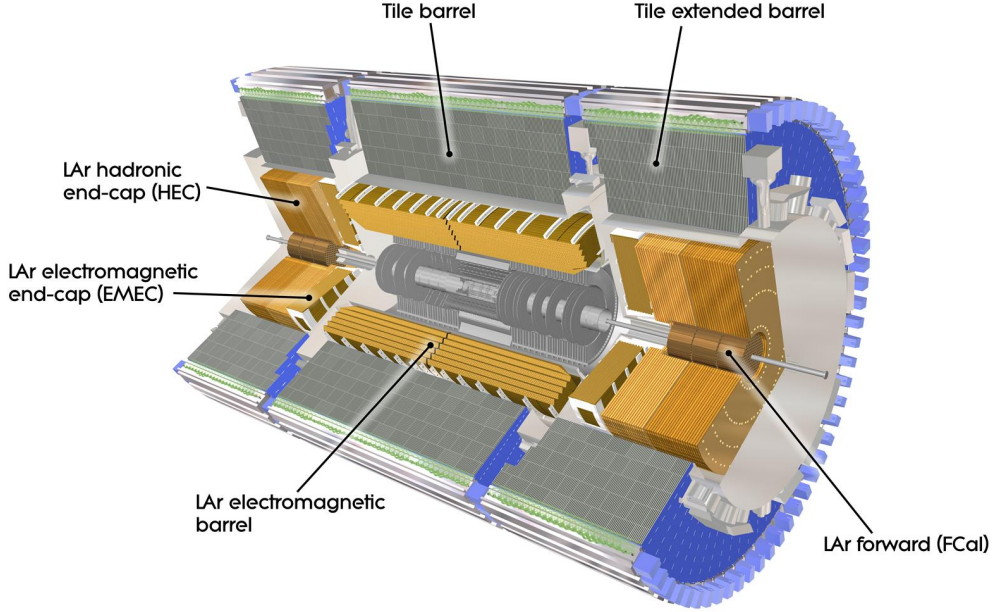


Figure 2.5: Overview of the ATLAS calorimetry. Near the beam-pipe the tracker is visible, surrounding it is the EM calorimeter and beyond the hadronic calorimeter. Both barrel and end-caps elements are displayed. [CERN-GE-0803015 © CERN Geneva].

(a) Electromagnetic calorimeter

Technology. The EMC [90, 91] is made of accordion shaped layers of lead plates-kapton electrodes bathing in liquid argon as depicted in Fig. 2.6. The accordion geometry, symmetric in ϕ , presents a full and crack-free azimuthal coverage. The readout of the high voltage electrodes are maintained at equal distance from two lead sheets using honeycomb spacers. A high energy electron or photon as it passes through an absorber loses energy respectively via bremsstrahlung $e^\pm \rightarrow e^\pm \gamma$ or pair production $\gamma \rightarrow e^+e^-$. These produced particles in their turn interact with the other absorbers creating a shower of particles. Particles from this shower excite liquid argon from which ionised electrons –as they drift to the electrode– allow to find eventually the shape and the total energy yielded by the incoming electron/photon.

Geometry. The barrel ($1.25 \text{ m} < r < 2.25 \text{ m}$, $L = 6.4 \text{ m}$, $|\eta| < 1.475$, $\geq 22 X_0$) is made of two identical half-barrels with the accordion waves running in the r axis. Both are stored with the solenoid in the same cryostat.

The two end-caps ($330 \text{ mm} < r < 2098 \text{ mm}$, $L = 63 \text{ cm}$, $1.375 < |\eta| < 3.2$, $\geq 24 X_0$) are stored with the hadronic end-caps and forward calorimeters in the same cryostat. Here the waves of the accordion are parallel to the z axis. Each end-caps are mechanically split into two coaxial wheels in an approximately projective geometry at $|\eta| = 2.5$. The external wheel end-cap ($1.375 < |\eta| < 2.5$) together with the barrel provide precision measurements with a granularity of the cells of the order of $\Delta\eta \times \Delta\phi \sim 0.025 \times 0.025$. Liquid argon presamplers are implemented upstream of both the barrel and external wheel end-cap in the aim to correct for the loss of energy of the electrons and photons before they enter the calorimetry.

Performances. For tracker based studies the energy E of electrons measured in the EMC enters as references to tracker measurement through the ratio $E_{e^\pm}^{(\text{EMC})}/p_{e^\pm}^{(\text{ID})} \equiv E/p$. The intrinsic energy

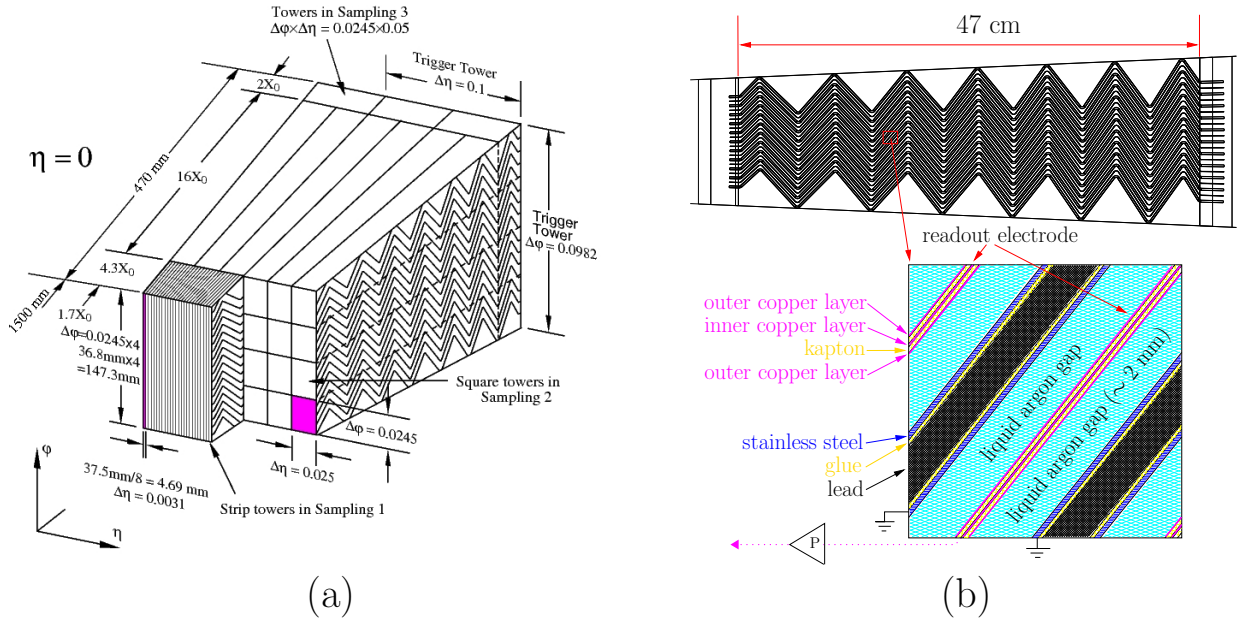


Figure 2.6: Schematic view of an EMC barrel module (a) [90] and detailed view of the accordion structure (b) [Figures adapted from [91]].

resolution in the barrel was found, using test-beams [92], to be for a Gaussian fit resolution

$$\frac{\sigma_E}{E^{(\text{true})}} = \frac{0.1}{\sqrt{E^{(\text{true})}}} \oplus 0.0017. \quad (2.13)$$

In the previous equation E is expressed in GeV, the (true) labels refers to the true level and the \oplus symbol means that the two terms are added in quadrature.

Trigger on electrons. The trigger on electrons should not affect the data used in the analysis. Indeed, simulation (Fig. 2.7) shows that the efficiency for electrons with a threshold of $p_{T,e} = 20\text{ GeV}$ reach the Efficiency=1 plateau already for 40 GeV where the data enters our analysis. This behaviour is expected to be the same for separated positrons and electrons selection.

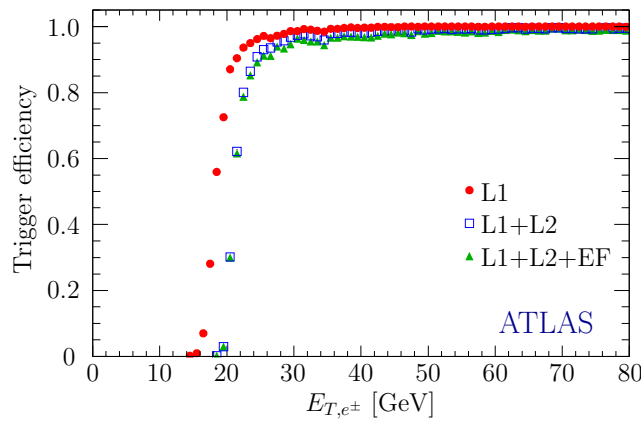


Figure 2.7: Simulation on ATLAS electron trigger efficiency for $p_{T,e} = 20\text{ GeV}$ [Taken in [93]].

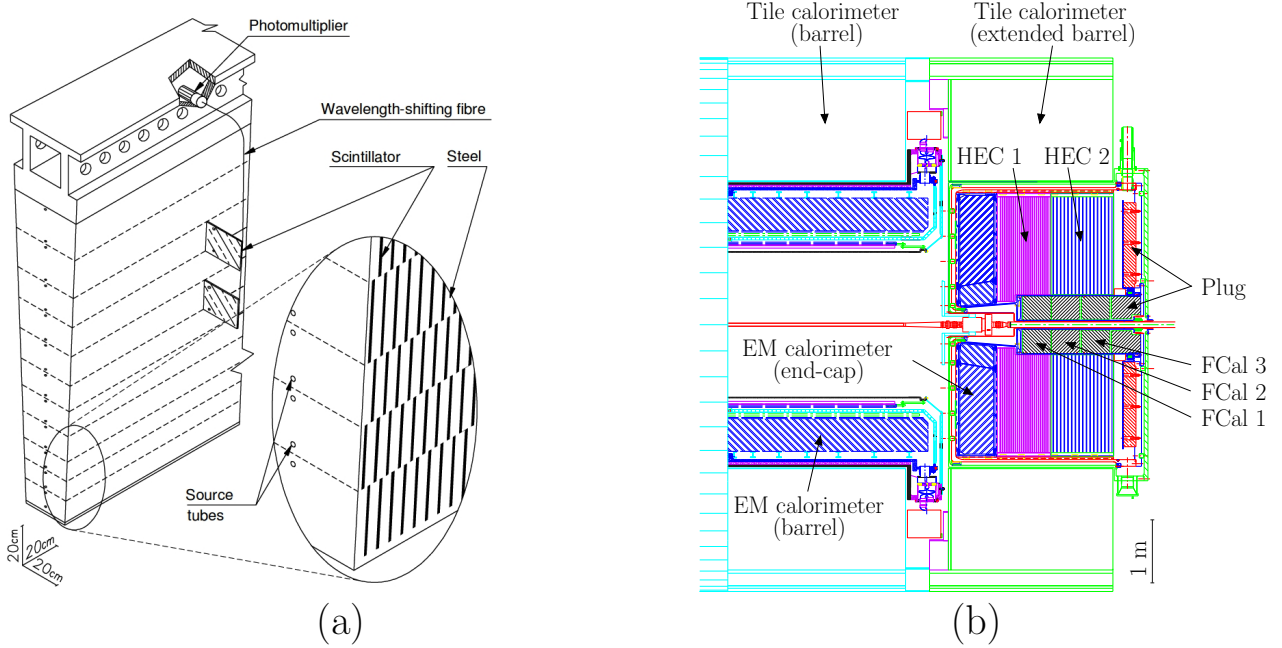


Figure 2.8: Schematic representations of the tile calorimeter geometry with its structure with its optical readout in (a) and of the electromagnetic/hadronic end-caps and forward calorimeters in (b) [Fig.(a) taken in [82], Fig.(b) adapted from [90]].

(b) Hadronic calorimeter

Technology. The hadronic calorimeter [90, 94] uses both LAr and scintillators tiles technology.

The tile calorimeter is used in the barrel. It is a sampling calorimeter made of alternate layers of steel plates (absorbers) and scintillating tiles (active medium) orthogonal to the z axis (Fig. 2.8.(a)). Ionising objects (hadrons or jets) as they pass through the tiles induce the production of ultra-violet scintillation light which is converted to visible light by wavelength-shifting fibres. The fibres are grouped together and coupled to photo-multipliers. Just like for the EM calorimeter the shape and energy of the object is measured as the object yields all its energy in form a shower.

Sampling calorimeter made of flat copper plates (absorber) and LAr (active medium) are used for the end-cap calorimeter while the forward calorimeter uses both LAr in association with copper and tungsten (absorbers).

Geometry. The tile calorimeter ($2.28 \text{ m} < r < 4.25 \text{ m}$, $|\eta| < 1.7$, $\geq 7.4 \lambda$) is made of one barrel ($L = 5.8 \text{ m}$, $|\eta| < 1.0$) and two extended barrels ($L = 2.6 \text{ m}$, $0.8 < |\eta| < 1.7$).

In the forward pseudo-rapidity the hadronic end-cap (HEC) and forward calorimeter (FCal) are implemented to enhance the hermetic confinement of the produced particles to refine the measurement of \cancel{E}_T (Fig. 2.8.b). The end-cap calorimeter ($r < 2030 \text{ mm}$, $L = 1818 \text{ mm}$, $1.5 < |\eta| < 3.2$) is split in a front wheel (HEC 1: $372 - 475 \text{ mm} < r < 2030 \text{ mm}$) and a rear wheel (HEC 2: $475 \text{ mm} < r < 2030 \text{ mm}$).

The forward calorimeter ($3.1 < |\eta| < 4.9$) measures the energy of the intense particles flux in this forward region, it is divided in three layers of equal length, first an electromagnetic and then two hadronic calorimeters. It relies on copper-LAr in the first layer (FCal 1) for electromagnetic calorimetry and on tungsten-LAr in the two last hadronic calorimeters (FCal 2 & 3).

The granularity in the barrel and extended barrels is of the order of $\Delta\eta \times \Delta\phi \sim 0.1 \times 0.1$ and of $\Delta\eta \times \Delta\phi \sim 0.2 \times 0.2$ in the forward calorimeters.

2.2.4 Muon system

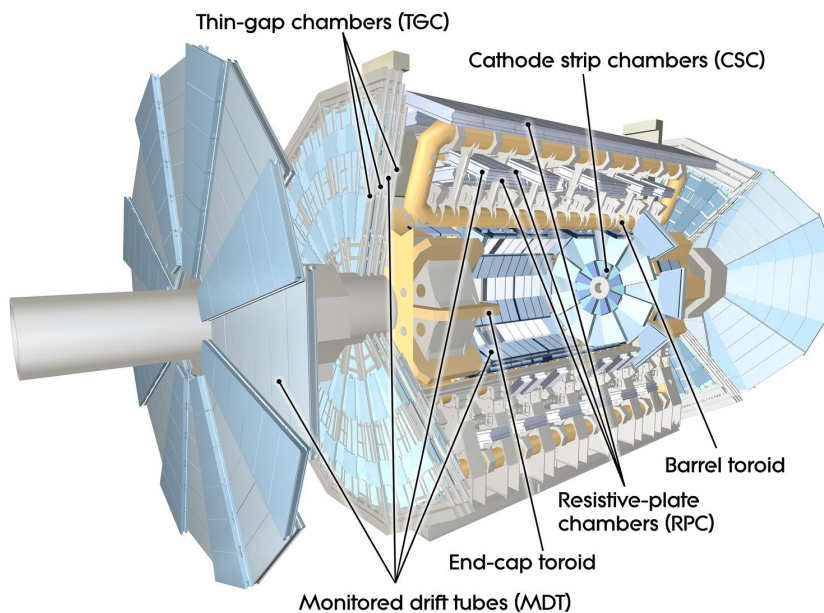


Figure 2.9: Overview of the ATLAS muon spectrometer [CERN-GE-0803017 © CERN Geneva].

The muon precision tracking instruments and the toroidal magnet are reviewed. Information on the muon triggering relevant to the present analysis is given as well. An overview of the muon spectrometer can be seen in Fig. 2.9.

Technology. The bending of the muons is done in the $r - z$ plan by a toroidal field which strength can reach 3 T in the barrel and 6 T in the end-cap. Nonetheless, the magnetic field bending power is characterised rather by its integral over the track length inside the tracking volume $BL \equiv \int \vec{B} \cdot d\vec{l}$ [T m], where $d\vec{l}$ is an infinitesimal track portion. Large values of BL are necessary to make precise measurements of ~ 1 TeV muon tracks.

Over most of the pseudo-rapidity range, precise measurement of the track coordinates in the principal bending direction is provided by Monitored Drift Tubes (MDT). As muons pass through a pressurized gas mixture filling the tubes, ionised electrons drift to the anode wire. The radius of the particle passage in the tube is deduced using space drift-time relation. Eventually, all collected radii give the muon track as shown in Fig. 2.10.(a).

For larger pseudo-rapidity, Cathode Strip Chambers (CSC), which are multiwire proportional chambers with cathodes segmented into strips, are used due to their higher rate capability and time resolution. Both cathodes are segmented. The one with strips orthogonal to the direction of the wires measure the precision coordinate, while the other with strips parallels to the wires provides the transverse coordinate. The position of the track is deduced by interpolating the charged induced among adjacent strips (Fig. 2.10.(b)).

The trigger chambers use Resistive Plate Chambers (RPC) in the barrel and Thin Gap Chambers (TGC) in the end-cap. In top of their triggering primer role, these chambers provides second coordinate measures in the bending plane $r - z$ to cross check the ones from the MDTs.

Geometry. The magnetic field is generated in the barrel using three large air-core toroidal magnet ($9.4 \text{ m} < r < 20.1 \text{ m}$, $L = 25.3 \text{ m}$, $|\eta| < 1.4$, $BL = 1.5 - 5.5 \text{ T m}$), each of them composed by eight coils arranged radially and symmetrically around the z axis. In the end-cap two smaller magnets ($1.65 \text{ m} < r < 10.7 \text{ m}$, $L = 5 \text{ m}$, $1.6 < |\eta| < 2.7$, $BL = 1.0 - 7.5 \text{ T m}$) are inserted into both ends

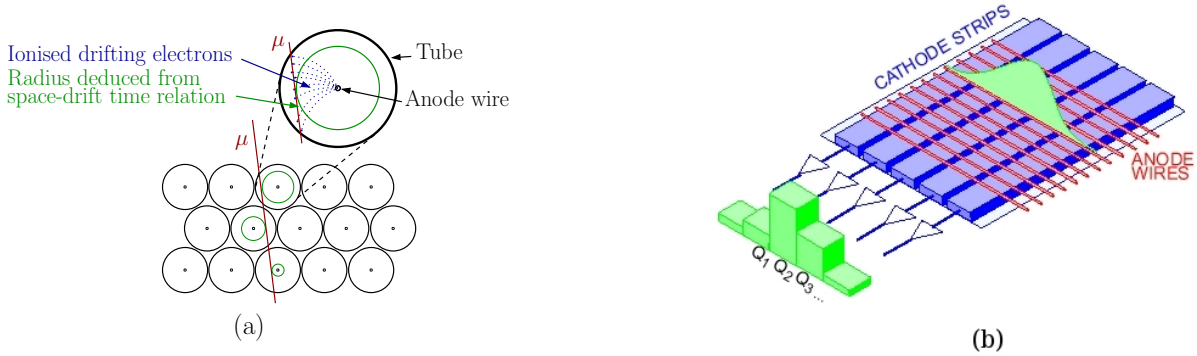


Figure 2.10: Principle of operation for MDT (a) and CSC devices (b) [Figure (b) taken in [82]].

of the barrel toroid. In the transition region ($1.4 < |\eta| < 1.6$), tracks deflection are done by a combination of both barrel and end-caps magnet field.

MDTs configuration follow a projective geometry and display a ϕ orientation of the wires in both barrel and end-cap. In the barrel, MDT chambers are arranged in three concentric cylindrical shells ($|\eta| < 2.0$) around the beam axis at radii of approximately 5 m, 7.5 m and 10 m. In the end-cap they are confined inside large wheels ($|\eta| < 2.7$) perpendicular to the z axis at $z \approx 7.4$ m, 10.8 m, 14 m and 21 m. CSCs ($2.0 < |\eta| < 2.7$) are arranged in wheels with approximate radial orientation of the wires. RPCs and TGCs are respectively used in the barrel ($|\eta| < 1.05$) and in the end-caps ($1.05 < |\eta| < 2.7$), their implementation based on the one of the MDT and CSC modules. There are in total three layers of RPCs in the barrel and three layers of TGCs in the end-cap.

Trigger on muons. Again, like for the electron the muon trigger efficiencies has already reached a plateau at 40 GeV where the data starts to enter the analysis (Fig. 2.11). Still here, contrary to the EMC, some asymmetries can arise between μ^+ and μ^- due to the toroidal topology of the magnetic field which, for a given side of the detector, is in-bending for a charge and out-bending for the opposite charge. Nonetheless such effect should be mostly insignificant with respect to other apparatus limitations.

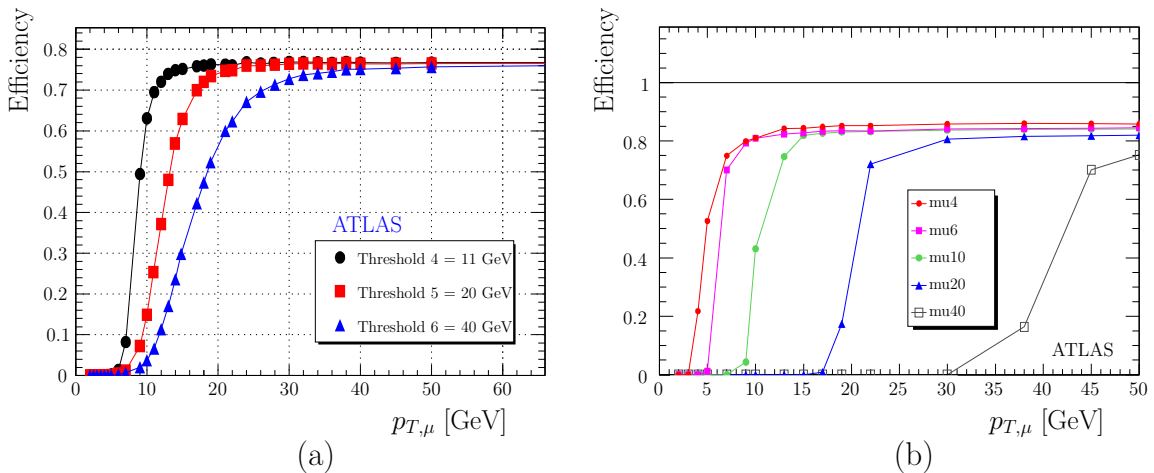


Figure 2.11: L1 barrel efficiency (a) and event filter efficiencies with the MuId algorithm (b) for several $p_{T,\mu}$ thresholds [Histograms extracted from [95]].

2.3 The ATLAS inner detector

2.3.1 Description of the inner detector

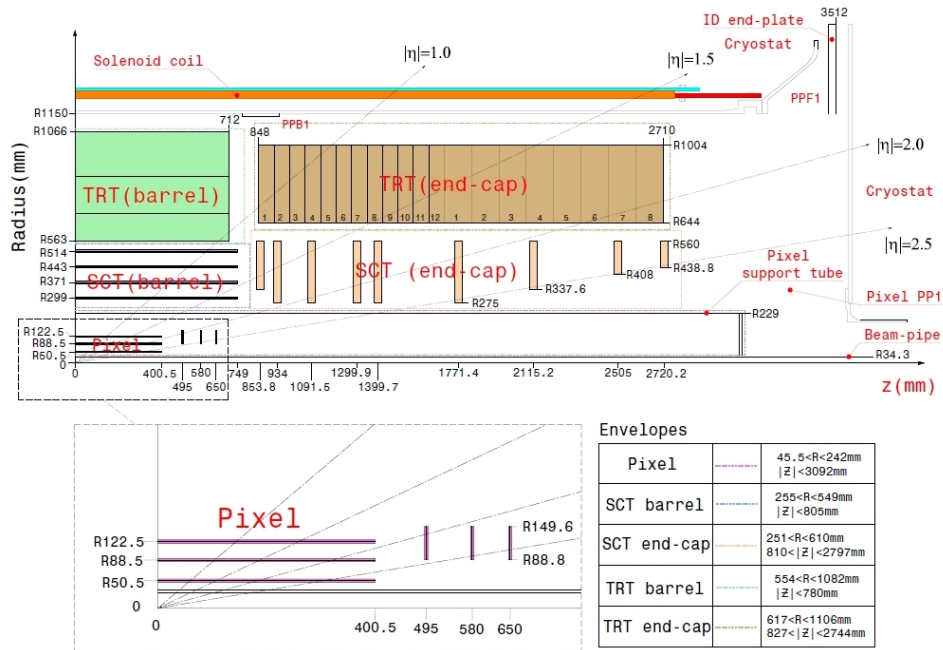


Figure 2.12: Longitudinal cross section of the ATLAS tracker [Figure taken from [82]].

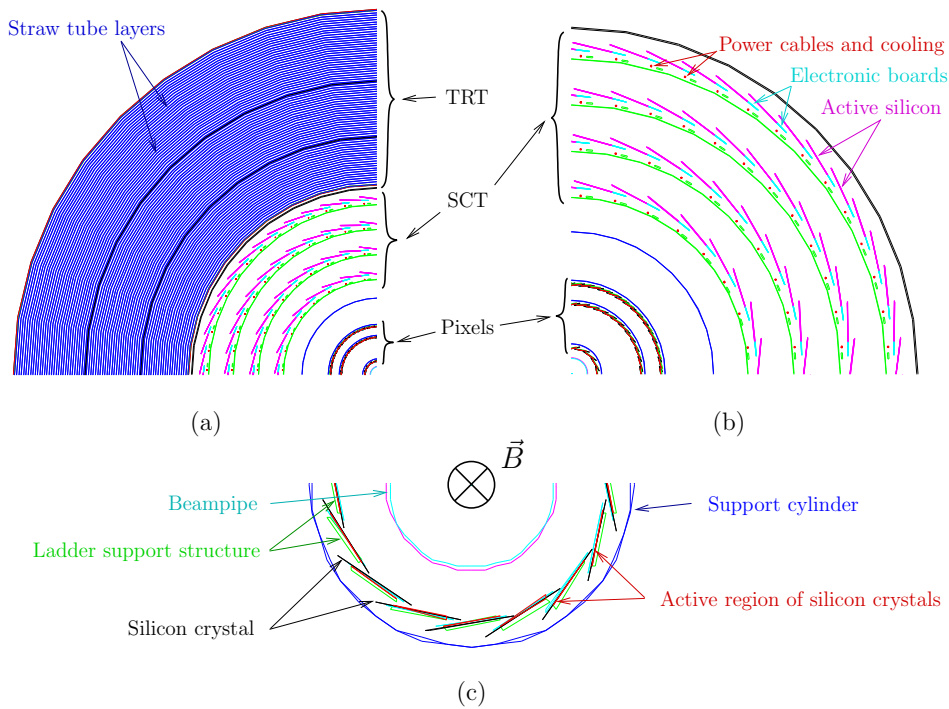


Figure 2.13: Radial cross section of the ATLAS tracker precision region, showing the three detectors (a), a zoom on the SCT and pixel detector (b) and finally a zoom on the first layer of the pixel detector with the the direction of the magnetic field \vec{B} in (c) [Figures adapted from [96]].

The ATLAS inner detector [96, 97, 98] pixel, SCT and TRT elements along with the central solenoid are described below. Their implementation is displayed with details on Figs. 2.12 and 2.13. Since the analysis strategy to decrease systematic errors relies on the possibility to invert the magnetic field of the solenoid, mentions on the drift of charge carriers in the modules were found worth to be noticed.

The Inner Detector is designed to provide a fine pattern recognition, an excellent momentum resolution and both primary and secondary vertex measurements for charged particles tracks displaying $p_T > 0.5 \text{ GeV}$ and within the pseudo-rapidity range $|\eta| < 2.5$. This is achieved by using three independent but complementary sub-detectors. At inner radii, high-resolution pattern recognition performances are done by discrete space-points from silicon pixel layers and stereo pairs of silicon micro-strip (SCT) layers. At larger radii the Transition Radiation Tracker (TRT), made of gaseous proportional counters embedded in radiator material, allows continuous track following. Each track leaves at least 7 hits in the precision tracking (pixel and SCT) and an average of 30 hits in the TRT.

The central solenoid with the pixel, SCT and TRT detectors are now described.

(a) Central solenoid

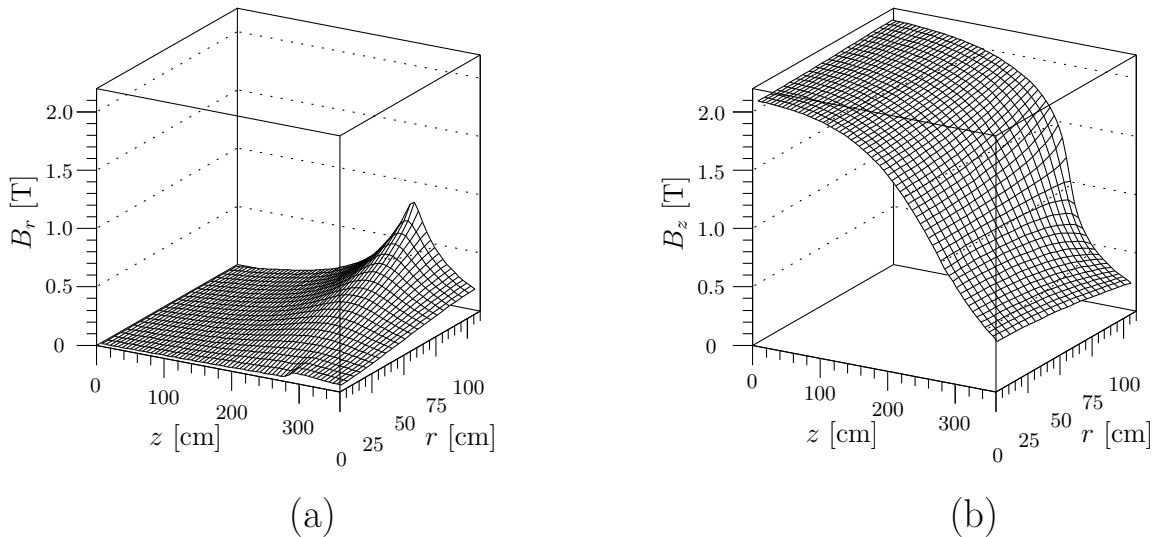


Figure 2.14: Mapping of the radial (a) and longitudinal (b) components of the magnetic field generated by the central solenoid [Taken in [99]].

The solenoid coil, surrounding the tracker, generates a magnetic field to bend the tracks of charged particles emerging from the interaction point allowing, with the tracker instruments, to identify and measure their transverse momenta.

The solenoid coil [100] ($1.23 \text{ m} < r < 1.28 \text{ m}$, $L = 5.8 \text{ m}$) provides a magnetic field

$$\vec{B} = B_r \vec{e}_r + B_z \vec{e}_z. \quad (2.14)$$

In that equation, B_z is the main component of the field and the radial component B_r , optimally null at $z = 0$, grows with $|z|$ due to border effects and the influence of iron in the tile calorimeter (Fig. 2.14). Charged particles are bent predominantly in the $r - \phi$ plane with bending powers of 2 T m at $\eta = 0$ decreasing to 0.5 T m at $|\eta| < 2.5$. Besides, since the solenoid length is shorter than the tracker the field inhomogeneities in the forward region need to be accounted using a field map in both simulation and reconstruction.

One aspect in the present study relies on the capability of inverting the magnetic field of the solenoid which, although not programmed so far, is possible as stated in Ref. [100]. The consequences of this operation, from the physics analysis point of view, will be discussed in the analysis in Chapter 5.

(b) Pixel detector

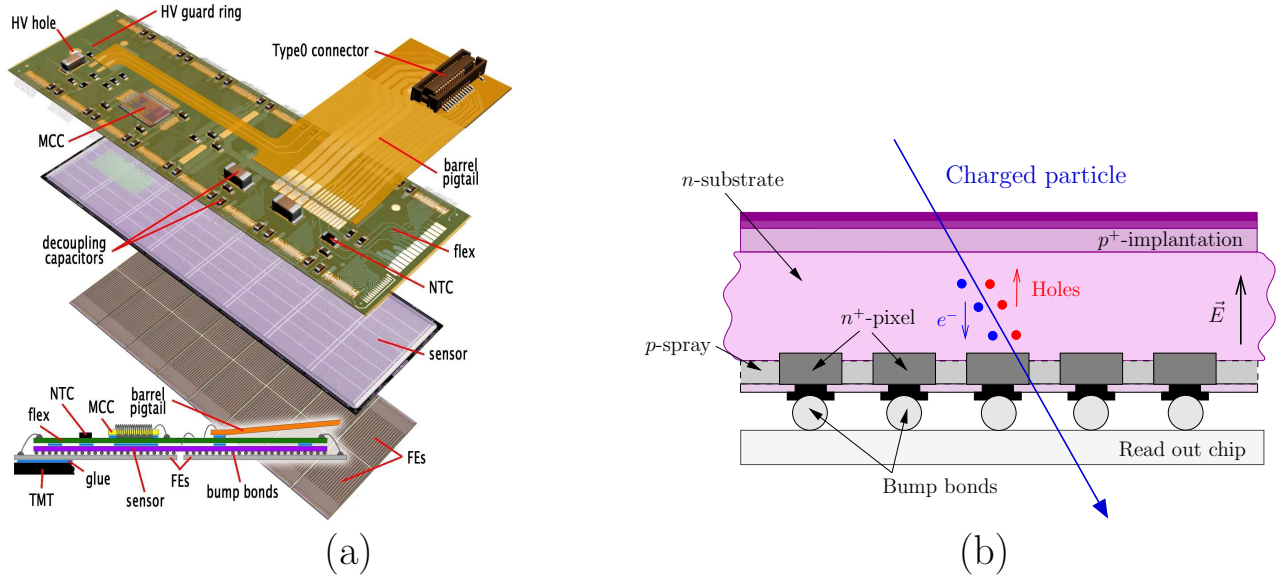


Figure 2.15: Pixel module structure of the ATLAS tracker (a) and principle of operation (b) [(a) taken in [82]].

The measurements from the pixel detector [97] are fundamental as they provide information on charged particles before they yield energy to the apparatus. Silicon detectors are used to provide fine vertexes information with high granularity [101]. The cells are made, as shown on Fig. 2.15.(a), using silicon sensor layers of size width \times length = $50 \times 400 \mu\text{m}^2$ segmented in both width and length to provide the pixel information. Incoming charged particles ionise pairs of electrons/holes in the silicon. The bias voltage applied in the silicon makes electrons drift to the n^+ -side readouts. Bump bonds transmit the collected charge to the front end electronic allowing to decipher which pixel was hit (Fig. 2.15.(b)).

Pixels modules –all identical in design– are dispatched between a central and two forwards parts. The central part is made of three concentric cylinders and the forward one are made each of three disks orthogonal to the z axis. This provide for each particle track 3 hits.

In the central barrel, as can be seen in Fig. 2.13.(b), modules are tilted in ϕ with respect to the tangent position. This tilt provides an overlap of the active area of the modules in the ϕ -direction which enhance the hermetic confinement of particles. It also ensures a better spatial resolution via the alignment of the effective charge drift –induced by the \vec{B} field via Lorentz force– direction with the particle trajectory [102] as seen in Fig. 2.16.

Layers are segmented like $r\Delta\phi \times \Delta z = 10 \mu\text{m} \times 115 \mu\text{m}$. In the forward barrel, that same segmentation correspondence is $r\Delta\phi \times \Delta r = 10 \mu\text{m} \times 115 \mu\text{m}$.

(c) Semi-Conductor tracker

The SCT [97, 103] is based upon silicon micro-strip detector. Each module is made of two silicon sensor layers segmented in strips put back to back and rotated by 40 mrad to enhance the z measurement (Fig. 2.17.(a)). The principle of operation is similar to pixel detector modules. Here the holes drift to the strips while the electrons drift to the back of the sensor. The strips are read out by a front-end chip, which measures the induction signal of the drifting holes/electrons pairs. Especially as shown on Fig. 2.17.(b) the Lorentz drift in each layer are working in opposite directions. The position of the hit is averaged offline from the two sides hit positions. The active area is width \times length = $61.6 \times 62 \text{mm}^2$ and the modules are segmented in both width and length.

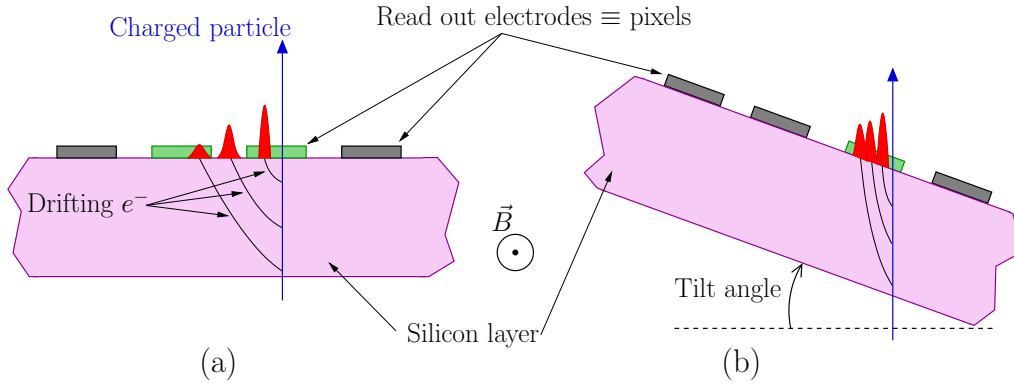


Figure 2.16: Schematic representation –simplified with respect to Fig. 2.15.(b)– of the electrons drift in a barrel pixel module with no tilt (a) and with a tilt (b) that aligns the charge drift carriers direction with the one of the charged particle. The drift trajectories are not straight lines since the electric field is not constant in the depleted region, for more details see for example Ref. [102].

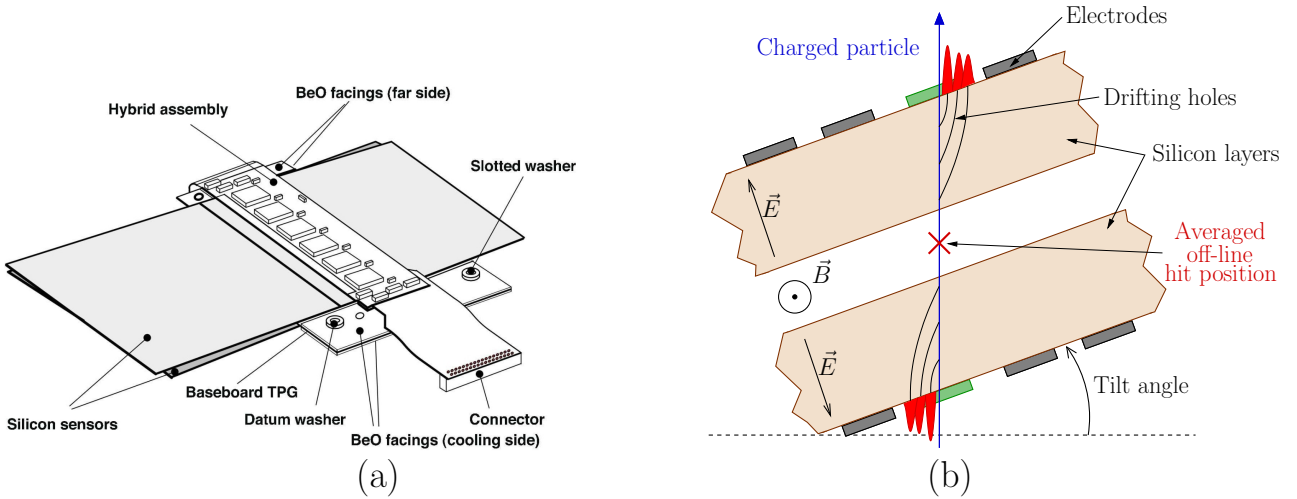


Figure 2.17: SCT module structure (a) and principle of operation (b) [(a) taken in [82]].

The layout is made of four layers in the barrel and of nine disks in the end-cap orthogonal to the z direction. In the barrel modules are slightly tilted from the tangent position (Fig. 2.13.(b)) for the same reasons than for the pixel detector. The segmentation in the barrel is $r\Delta\phi \times \Delta z = 580 \mu\text{m} \times 17 \mu\text{m}$. In the end-cap, modules are also mounted to display some overlap and the corresponding segmentation is of $r\Delta\phi \times \Delta r = 580 \mu\text{m} \times 17 \mu\text{m}$.

(d) Transition radiation tracker

The TRT [97] assures continuous tracking as well as electrons identification. Even if it is not as precise as the silicon trackers its long lever arm plays an important role in the momentum resolution.

The TRT is made of layers of gas filled straws interleaved with transition radiation material. A charged particle passing through the straw ionise the electrons of the gas mixture (Fig. 2.18.(b)). A large potential difference is applied between the straw wall and the wire. The anode wire collects the energy of the ionised electrons (Fig. 2.18.(b)). Also, charged particles as they pass trough materials of different dielectric constant (radiator \rightarrow straw) radiate photons proportionally to their Lorentz γ factor. Part of the gas mixture in the straw is sensitive to photons and in consequence this ionisation energy adds up to the collection of the one induced by the incoming particle. The threshold for a

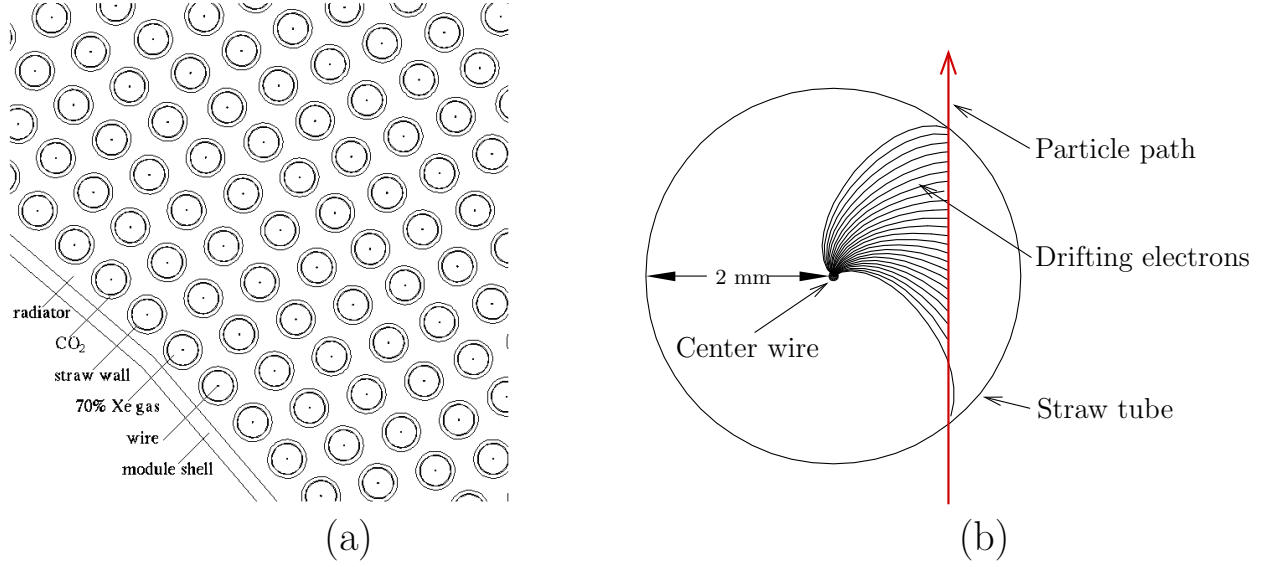


Figure 2.18: TRT tubes assembly (a) and principle of operation of one tube (b) [(a) taken and (b) adapted in/from [96]].

significant radiation ($\gamma \sim 1000$), depends then on the mass of the particle and help to identify electrons amid other heavier charged particles. The TRT only provides information in $r\Delta\phi$ with an accuracy of $130 \mu\text{m}$.

In the barrel the straws are parallel to the z axis and arranged in three cylindrical rings. In each end-cap the wires are aligned to the radial direction and arranged in three sets of identical and independent wheels. Again the precise dimensions and pseudo-rapidity coverage can be seen in Figs. 2.12.

2.3.2 Track fitting and general performances

The track fitting is realised in three stages. First the raw data from the pixel/SCT and TRT detectors are respectively converted into clusters and calibrated circles. The SCT clusters are converted to space-points using a combination of the cluster from both sides of SCT modules (cf. Fig. 2.17.(b)). Then comes the track finding stage where algorithms [104, 96] essentially follow pattern recognition starting from the innermost pixel layers and goes outwards to the TRT. These algorithms, based on Kalman filter techniques [105] and Global- χ^2 [106], perform recognition of helices among the hits in the tracker. In the final stage primary vertexes are resolved. Also tracking information from the muon spectrometer is used as well to enhance the data on muons. In the present work the expected stand-alone performances of the tracker are used exclusively.

The ID performances in p_T , θ and ϕ can be parametrised using Gaussian functions (cf. Ref. [99] § 3.3.1.6) where, up to the approximation the material and the solenoid field are uniform in r writes

$$\sigma_{1/p_T} = 3.6 \times 10^{-4} \oplus \frac{1.3 \times 10^{-2}}{p_T^{(\text{true})} \sqrt{\sin \theta^{(\text{true})}}} \quad [\text{GeV}^{-1}], \quad (2.15)$$

$$\sigma_{\cotan \theta} = 0.7 \times 10^{-3} \oplus \frac{2.0 \times 10^{-3}}{p_T^{(\text{true})} \sin^{3/2} \theta^{(\text{true})}}, \quad (2.16)$$

$$\sigma_{\phi} = 0.075 \times 10^{-3} \oplus \frac{1.8 \times 10^{-3}}{p_T^{(\text{true})} \sqrt{\sin \theta^{(\text{true})}}} \quad [\text{rad}]. \quad (2.17)$$

where $p_T^{(\text{true})}$ are in GeV and (true) superscript means a kinematic is considered at the generator level.

2.4 The weak modes affecting the inner detector

2.4.1 Misalignment and definition of the weak modes

The tracker is build into an *a priori* perfect “blue-print” configuration, but in reality modules assembly differs from such an ideal picture due to mounting limitations, mechanical stress, temperature variations, sagging due to gravity, *etc.* Since the tracker relies on the relative hits positions to measure the particles momenta and vertexes these small misalignment spoil the relevancy of reconstructed tracks. Since the module positions cannot be touched after their assembly modules misalignment are accounted by performing a mapping of the detector shape and module positions to correct the collected data. This procedure is called the alignment. Since some of the constraints on the tracker are time dependent this alignment survey must be continually updated.

The alignment of the tracker is realised using two kind of methods: hardware-based and track-based methods. Hardware methods make *in situ* measurement of the shape of the support structure and its change over time. Track based alignment requires, using the least squares principle, that the measurements in the detector are consistent with the assumed track model, *i.e.* follows the expected track trajectory in the given \vec{B} field and the scattering is consistent with the known amount of material.

Still, despite these surveys some deformations are such that the fitted track even if being relevant from the tracking algorithm point of view –*i.e.* an helix is recognised– nonetheless deviates from the real track. These deformations can be –in a first approximation– represented by a set of 9 simple and independent distortions called the weak modes [107], parametrised using global deformations on the tracker. Due to the symmetry of the problem, the parametrisation is made in the cylindrical coordinate system, hence the combination of deformations in r , ϕ and z directions folded with Δr , $\Delta\phi$ and Δz variations gives 9 weak modes. The total misalignment of the tracker is a combination of these 9 modes gathered in Fig. 2.19.

More details on the alignment and weak modes can be found in Refs. [107, 108, 71].

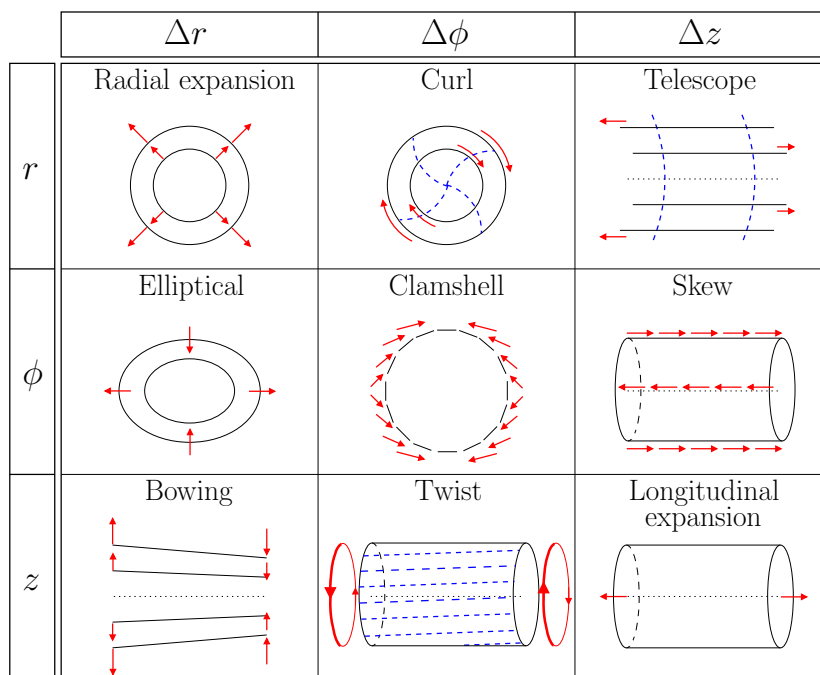


Figure 2.19: Weak modes affecting at the first order the alignment of the tracker. The arrows represent the constraints modules are submitted to and the dashed lines emphasise the consequences when not obvious to visualise.

2.4.2 Consequences of the weak modes on the error on the W boson mass measurement

Curl and twists modes are responsible for limitations on the precision on the W mass determination at CDF II [109]. In CDF II systematic errors on M_W are of the same order than the statistical errors, *i.e.* $\delta_{M_W}^{(\text{stat.})} = \delta_{M_W}^{(\text{sys.})} = 34 \text{ MeV}$ while at the LHC statistical errors will be of the order of 5 MeV already for one year at low luminosity. For that reason the weak modes have to be addressed more thoroughly within ATLAS in regard of the difficulties encountered in the CDF II tracker (cf. Appendix 2.A). For example, considering again our interest in W production, a requested precision of 25 MeV for the measurement of the M_W constrains track parameters and momentum uncertainties. For that purpose the degradation of the high p_T tracks parameters due to misalignment have to be smaller than 20% while the systematic uncertainty on the momentum resolution needs to be smaller than 0.1% [99, 110].

Here the focus is made on the predominant modes increasing the error of $M_{W^+} - M_{W^-}$. Like it will be explained thoroughly in Chapter 4 the present work is based on the knowledge of the transverse momenta $p_{T,l}$ of charged leptons decaying from single W bosons. Hence the attention is cast on modes affecting the reconstruction of positive and negative transverse tracks. Modes involving Δz deformations are not considered as they do not degrade the resolution of $p_{T,l}$, this leaves Δr and $\Delta\phi$ modes which are discussed below. Two kind of biases are considered, the ones biasing the positive and negative charged particles tracks curvatures in the same direction (coherent biases) and the one affecting them in opposite directions (incoherent biases) the latter being the most important source of errors for $M_{W^+} - M_{W^-}$. In what follows no values are estimated, only the relative qualitative amplitudes between coherent and incoherent biases.

The modes amplitudes biases are noted ε and tagged using the 2×2 matrix form displayed in Fig. 2.19, *i.e.* using the notation r or $\Delta r \rightarrow 1$, ϕ or $\Delta\phi \rightarrow 2$ and z or $\Delta z \rightarrow 2$. The sign of a scalar a is noted $\text{sg}_a \equiv a/|a|$.

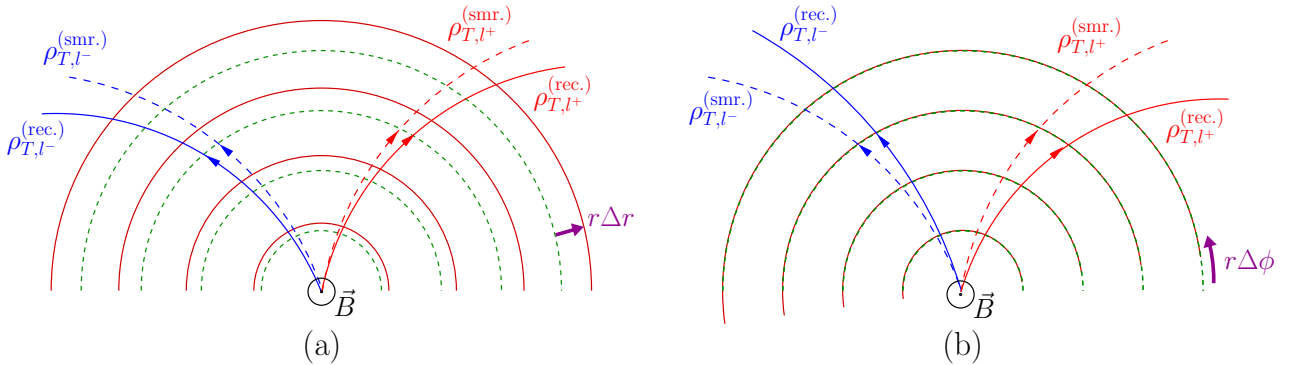


Figure 2.20: Consequences of the radial expansion (a) and curling (b) distortions on the positively and negatively charged particles reconstructed tracks. In both cases, tracks of the same curvature, *i.e.* $\rho_{T,l^+}^{(\text{smr.})} = \rho_{T,l^-}^{(\text{smr.})}$, are considered.

(a) Δr modes

$r\Delta r$: radial. The radial expansion ($r\Delta r > 0$) and contraction ($r\Delta r < 0$) infer coherent biases. This is shown in Fig. 2.20.(a) in the case of a radial expansion while starting with smeared curvatures of the same values $\rho_{T,l^+}^{(\text{smr.})} = \rho_{T,l^-}^{(\text{smr.})}$. The reconstructed curvatures can be written in the first order of a perturbation expansion in the parameter $\varepsilon_{11}(\propto \text{sg}_{\Delta r})$ that governs the radial expansion/contraction

amplitude :

$$\rho_{T,l^+}^{(\text{rec.})} = \rho_{T,l^+}^{(\text{smr.})} (1 + \varepsilon_{11}), \quad (2.18)$$

$$\rho_{T,l^-}^{(\text{rec.})} = \rho_{T,l^-}^{(\text{smr.})} (1 + \varepsilon_{11}). \quad (2.19)$$

$\phi\Delta r$: elliptical. For this mode, the effect of the gravity will most likely flatten the tracker as depicted in Fig. 2.19. In the region where the nominal radius of the tracker is larger ($\Delta r > 0$) positive and negative particle tracks curvature are overestimated. On the contrary tracks are getting more straight in regions where the tracker's nominal radius decreases ($\Delta r < 0$). Eventually these two effects should compensate each other and leave a residual coherent bias such that $\varepsilon_{21} < \varepsilon_{11}$.

$z\Delta r$: bowing. Here, for a given z coordinate positive and negative reconstructed tracks will be more straight (bent) if the tracker is expanding (contracting) with respect to its nominal radius. Biases coming from expansions are counter balanced by the one arising from contractions. The final bias from the bowing should be a residue from the averaging of these two opposite constraints. In any of those cases, again, the coherent bias should verify $\varepsilon_{31} < \varepsilon_{11}$.

(b) $\Delta\phi$ modes

$r\Delta\phi$: curling. The curling of the tracker gives incoherent biases. Figure 2.20.(b) shows it in the case where $\text{sg}_{\Delta\phi} > 0$ and with smeared curvatures are of the same values $\rho_{T,l^+}^{(\text{smr.})} = \rho_{T,l^-}^{(\text{smr.})}$. The curling acts on the curvature like $\rho_{T,l}^{(\text{smr.})} \rightarrow \rho_{T,l}^{(\text{smr.})} + \delta_{\text{curl}}$ where δ_{curl} is the bias induced by the curl. For small enough values of δ_{curl} we assume –to keep the same parametrisation used up to now– that the reconstructed curvatures can be written in the first order of a perturbation expansion in the parameter governing the curl amplitude $\varepsilon_{12}(\propto \text{sg}_{\Delta\phi})$:

$$\rho_{T,l^+}^{(\text{rec.})} = \rho_{T,l^+}^{(\text{smr.})} (1 + \varepsilon_{12}), \quad (2.20)$$

$$\rho_{T,l^-}^{(\text{rec.})} = \rho_{T,l^-}^{(\text{smr.})} (1 - \varepsilon_{12}). \quad (2.21)$$

$\phi\Delta\phi$: clam-shell. This mode is unlikely to affect any component of the inner tracker [111].

$z\Delta\phi$: twist. To illustrate the twist, a rotation of the tracker $\Delta\phi < 0$ of the left side and of $\Delta\phi > 0$ on the right side are considered. Based on the understanding of the curl mode, on the left side positive tracks are believed to be more bent while negative tracks are believed to be more straight. On the right side this effect is reversed. Just like for the bowing, antagonists modes of the same amplitudes cancel each other. Eventually the most important twist should contribute with a term like $\varepsilon_{32} < \varepsilon_{12}$.

(c) Global effect of the 6 previous modes

In conclusion, the reconstructed positively and negatively charged tracks should be biased like

$$\rho_{T,l^+}^{(\text{rec.})} = \rho_{T,l^+}^{(\text{smr.})} (1 + \varepsilon_{\Delta r} + \varepsilon_{\Delta\phi}), \quad (2.22)$$

$$\rho_{T,l^-}^{(\text{rec.})} = \rho_{T,l^-}^{(\text{smr.})} (1 + \varepsilon_{\Delta r} - \varepsilon_{\Delta\phi}), \quad (2.23)$$

where $\varepsilon_{\Delta r}$ and $\varepsilon_{\Delta\phi}$ are respectively the global coherent bias from Δr and $\Delta\phi$ modes, *i.e.*

$$\varepsilon_{\Delta r} = \varepsilon_{11} + \varepsilon_{21} + \varepsilon_{31}, \quad (2.24)$$

$$\varepsilon_{\Delta\phi} = \varepsilon_{22} + \varepsilon_{32}. \quad (2.25)$$

Again, let us repeat that only qualitative estimations are made here. This is justified as in our work these biases will be implemented with large worst case scenario values to improve the robustness of our proposed analysis scheme.

2.A W mass charge asymmetry and tracker misalignment in CDF II

(About the difficulties to measure M_W because of tracker misalignment)

“You all remember how during your studies you were taught a solid could be described by only six degrees of freedom. Well. Forget about it. It’s crap.”

CTEQ-MCnet Summer School 2008 - Standard Model lectures

TOM LECOMPTE

2.A.1 Context of the measurement of the W mass at CDF

The CDF detector used in Tevatron Run II, labeled CDF II [109], is a multipurpose detector nominally forward-backward symmetric with respect to the interaction point where protons and anti-protons collide at a center of mass energy of $\sqrt{S} = 1.96$ TeV. It is made, starting from the beam-pipe, of an inner tracker bathing in a 1.4 T solenoidal magnetic field, an electromagnetic calorimeter followed by a hadronic calorimeter to contain and measure respectively the energies of electrons/photons and hadrons. Finally a muon spectrometer surrounds the previous apparatus to measure the properties of muons. The data is read-out on-line using the decisions of a three level trigger system.

The measurement of M_W [51, 56] in CDF II is achieved using the tracker data for the muons and both tracker and electromagnetic calorimeter data for electrons. The acceptance and resolutions for central electrons and muons are the same which means both channels enter with the same weight in the analysis.

The extraction of M_W is addressed via the usual observables such as $p_{T,l}$, $m_{T,l\nu_l}$ and $\cancel{p}_{T,l}$ and via muon and electronic decays of the W . Along all these information the difference between the masses of the positive and negative W bosons is estimated as a mean of consistency check. Actually this last measurement is not to be apprehended as a real attempt to measure $M_{W^+} - M_{W^-}$. Rather than that it has to be understood that the measurement is entirely focused on M_W and that the effects responsible for the low precision on $M_{W^+} - M_{W^-}$ were at no time addressed by the authors as long as it does not have a major role for the determination of M_W . Both M_W and $M_{W^+} - M_{W^-}$ CDF results for these last years, as seen in Table 1.2, are recaptured here :

Channel	M_W [GeV]	$M_{W^+} - M_{W^-}$ [GeV]	Year
$W \rightarrow l \nu_l$	79.910 ± 0.390	-0.190 ± 0.580	1990,1991 [52, 53]
$W \rightarrow \mu \nu_\mu$	80.310 ± 0.243	0.549 ± 0.416	
$W \rightarrow e \nu_e$	80.490 ± 0.227	0.700 ± 0.290	1995 [54, 55]
$W \rightarrow l \nu_l$	80.410 ± 0.180	0.625 ± 0.240	
$W \rightarrow \mu \nu_\mu$	80.352 ± 0.060	0.286 ± 0.152	
$W \rightarrow e \nu_e$	80.477 ± 0.062	0.257 ± 0.117	2007 [56, 51]
$W \rightarrow l \nu_l$	80.413 ± 0.048	\times	

The question one might ask is how come the absolute mass is measured with an error of ≈ 40 MeV then ? The trick is that incoherent biases are at work between the positively and negatively charged particle tracks and they get drastically reduced when both charges are merged.

The next subsection describes briefly the CDF II central outer tracker used for the W measurement. After that a recapitulation of how the tracker misalignment affects charged particles curvature is made. This shows how the experience from Tevatron physicists guided us to address, aware of the LHC/ATLAS original features, the relevant weak modes for a future dedicated measurement of $M_{W^+} - M_{W^-}$ in ATLAS. It also explains why so far all experimental measurements of $M_{W^+} - M_{W^-}$ display such a low accuracy.

2.A.2 Description of the CDF Central Outer Tracker

The CDF configuration is such that we borrow for its description the same conventions adopted for ATLAS (cf. § 1.3). The CDF II uses silicon at lower radii and drift tubes technologies afterward. The silicon detector is not detailed since its data was not used for the determination of M_W .

Around the silicon tracker is an open-cell drift chamber, the COT [112] which span the radial range $40 \text{ cm} < r < 137 \text{ cm}$ and extend longitudinally for $|z| < 155 \text{ cm}$ ($|\eta| \approx 0.1$).

The COT, as displayed in Fig. 2.21.(a) is made of eight concentric “super-layers” separated in azimuth into cells. Each cell, as shown in Fig. 2.21.(b), is made of sense wires and potential wires immersed in an ambient gas mixture. Ionised electrons from the passage of high energy charged particles drift under the influence of the electrostatic field to the sense wires and yield their energy which allow to decipher the particle hit position. The sense wires are attached at each extremities to end-plates which hold them into a string position. The tilt angle of the cells aims to make it so the ionised electrons travels approximately in azimuth to the sense wires under the combined influence of the solenoid magnetic field and of the local electrostatic field. Let us note that the cells move from their nominal geometry under the influence of gravity which makes field sheets and wires sag. This eventually implies that the sense wires deflect toward a particular field sheet. To decrease this effect a support rod at $z = 0$ connects the sense wires at the center of the detector.

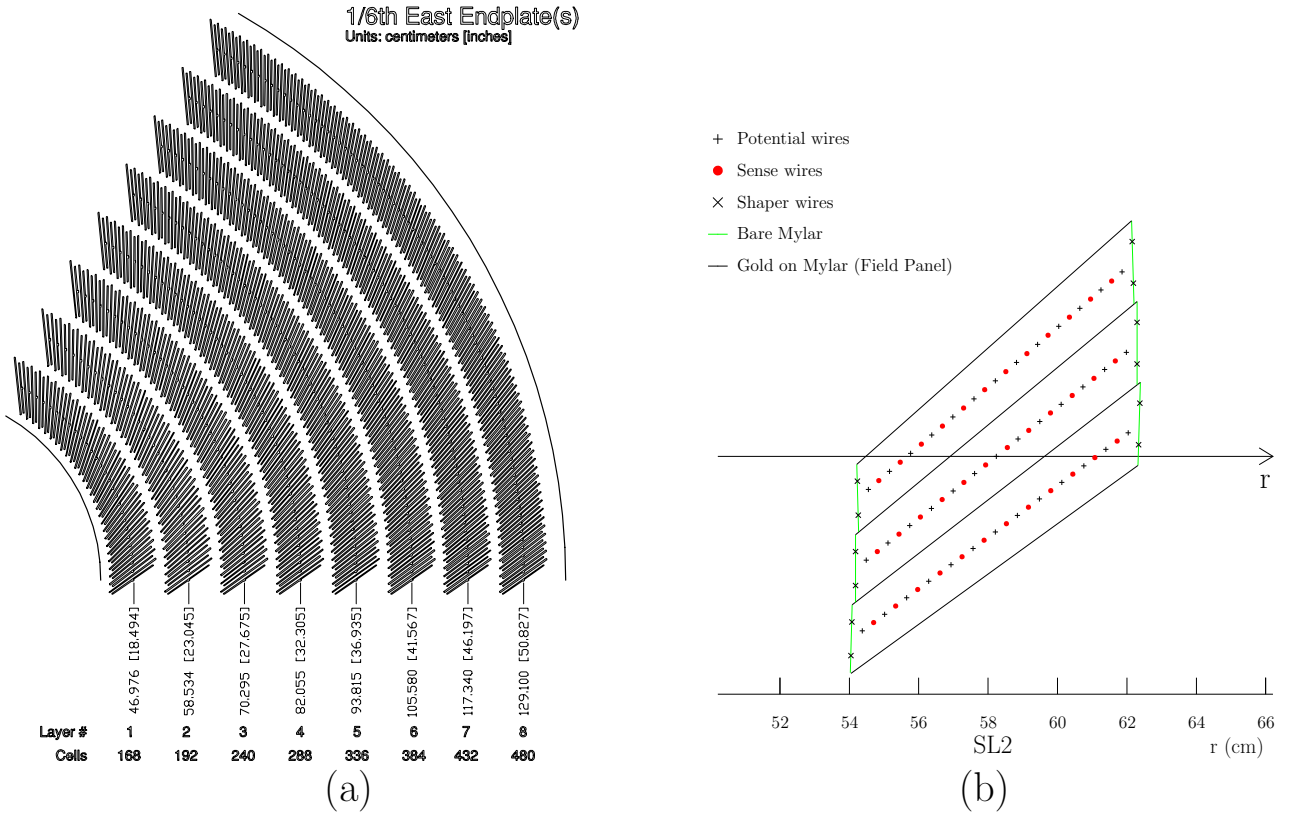


Figure 2.21: Structure of the CDF II central outer tracker [Taken in [109]].

2.A.3 Influence of tracker misalignment on the W mass charge asymmetry

We adopt in the rest of this Appendix the conventions of Ref. [51] to address the curvature c of a charged particle track in the $r - \phi$ plane. It is defined like

$$c \equiv q/(2R), \quad (2.26)$$

where q is the charge of the particle and R is the radius of the track in the $r - \phi$ plan. Charged leptons have their transverse momenta deduced from c which is measured by the hits left in the COT. For that purpose the position of the cells needs to be determined precisely to have a good accuracy for the momentum scale. The calibration of this momentum scale is determined starting with the *a priori* position of the cells. Then *in situ* measures correct for the electrostatic and gravity sag biases, cosmic ray muon data allow to add up *in situ* corrections and finally track based corrections are applied using data calibration. For these last corrections first comes the study $W \rightarrow e\nu$ to reduce relative curvatures biases between positive and negative particles and finally absolute scale data calibration using J/ψ , Υ and Z bosons decays to $\mu^+\mu^-$.

The reconstructed track curvature c_r can be expressed as a function of the true curvature c_t in a Taylor expansion around zero which is justified by the high p_T of the charged leptons of interest ($c_t \approx 0.02 - 0.03$). It reads

$$c_r = \varepsilon_1 + (1 + \varepsilon_2) c_t + \varepsilon_3 c_t^2 + \varepsilon_4 c_t^3 + \dots, \quad (2.27)$$

which now allows us to consider the case of two positively and negatively charged leptons respectively of curvatures $c_{r,+}$ and $c_{r,-}$, having the same true transverse momentum (*i.e.* $c_{t,-} = -c_{t,+}$). Their reconstructed tracks are written

$$c_{r,+} = \varepsilon_1 + (1 + \varepsilon_2) c_{t,+} + \varepsilon_3 c_{t,+}^2 + \varepsilon_4 c_{t,+}^3 + \dots, \quad (2.28)$$

$$c_{r,-} = \varepsilon_1 - (1 + \varepsilon_2) c_{t,+} + \varepsilon_3 c_{t,+}^2 - \varepsilon_4 c_{t,+}^3 + \dots, \quad (2.29)$$

Now, remembering the goal is to eventually merge positive and negative channels for the extraction of M_W , flipping the sign of the curvature in Eq. (2.29) (*i.e.* $c_{r,-} \rightarrow -c_{r,-}$) to get rid of the charge sign and averaging this new expression with Eq. (2.28) gives an average track curvature

$$\frac{1}{2}(c_{r,+} - c_{r,-}) = (1 + \varepsilon_2) c_{t,+} + \varepsilon_4 c_{t,+}^3. \quad (2.30)$$

With that development we see all terms of even power of c_t are cancelled when averaging, the term linear in c_t scales the true curvature and is deduced from momentum calibration. The term $\varepsilon_4 c_{t,+}^3$ is the first one to affect the determination of M_W but it can be neglected because of the high transverse momentum of the leptons. On the other hand, the direct average of the signed curvatures (Eqs. (2.28–2.29)) that should ideally be equal to zero, leads to constraints on ε_1 , indeed

$$\frac{1}{2}(c_{r,+} + c_{r,-}) \equiv \varepsilon_1 + \varepsilon_3 c_{t,+}^2 + \dots, \quad (2.31)$$

$$\approx \varepsilon_1, \quad (2.32)$$

where in the last line higher order terms are neglected compared to ε_1 and because as we saw they are not worth to be considered for a measurement of M_W . Then, ε_1 is constrained using data calibration since the relative difference between $(E/p)_{e^+} - (E/p)_{e^-}$ should be zero in the absence of misalignment. The parametrisation of Eq. (2.32) can be written like

$$\frac{1}{2}(c_{r,+} + c_{r,-}) = a_0 + a_1 \cotan \theta + a_2 \cotan^2 \theta + b_1 \sin(\phi + 0.1) + b_3 \sin(3\phi + 0.5), \quad (2.33)$$

where the terms a_0 , a_1 and a_2 can be interpreted as distortions of the COT.

Figure 2.22 illustrates these distortions as a function of the more intuitive θ observable. Using the vocabulary of weak modes (cf. § 2.4), the term in a_0 corresponds to a curl of the tracker while the term a_1 corresponds to a twist between the left and right end-plates. The term proportional to a_2 goes beyond the first order approximation of the weak modes and is characteristic of the COT construction, it corresponds to a curl of second order where the left and right end-plates are being rotated in the same ϕ direction but the center of the tracker is maintained to its original position by the support rod. The terms in b_1 and b_3 corresponds to mis-measurements of the beam position.

Figure 2.23 shows now the tracker misalignment consequences on $(E/p)_{e^+} - (E/p)_{e^-}$ before and after corrections in function of $\cotan \theta$.

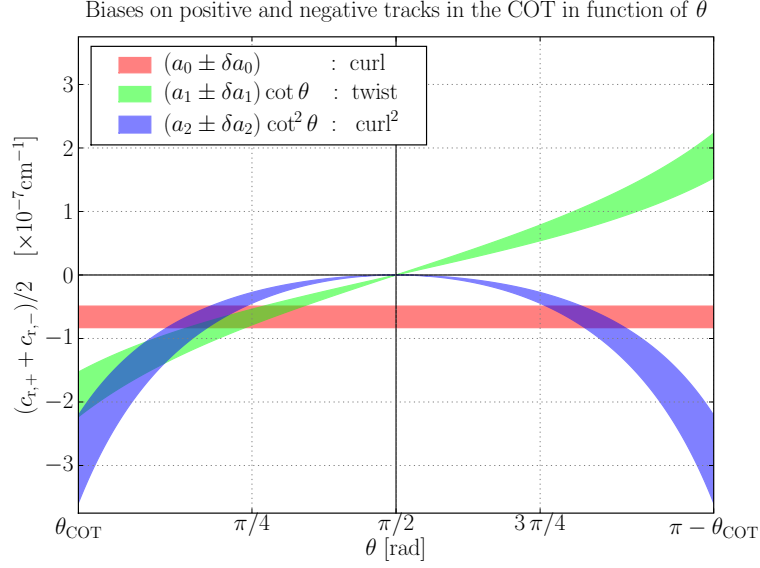


Figure 2.22: Representation of the spatial distortion of the CDF II COT in function of θ .

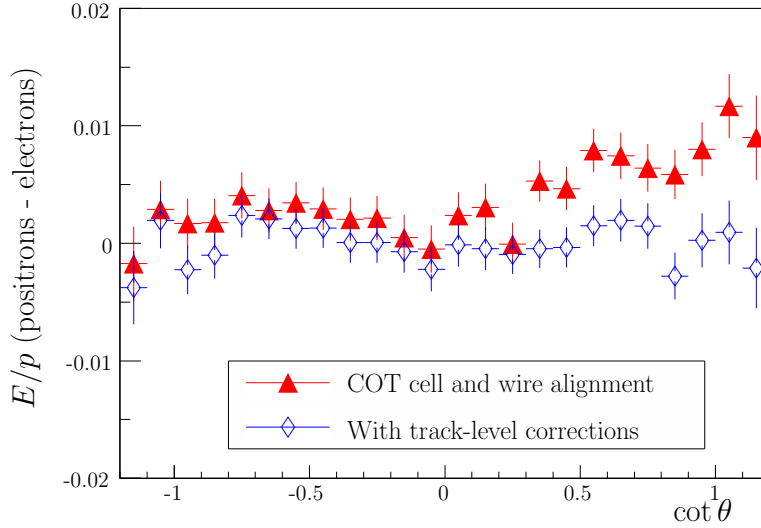


Figure 2.23: $(E/p)_{e^+} - (E/p)_{e^-}$ in function of $\cot \theta$ before and after corrections [Taken in [109]].

In conclusion, this measurement dedicated to extract M_W merges both W^+ and W^- measurement which gives data where half of the tracks are biased in one direction and the over half of the same amount but in the opposite direction. Eventually all those corrections lead to a precision on tracker momentum resolution of $\Delta p/p \approx -1.50 \times 10^{-3}$ which in turn leads for all $p_{T,l}$, $m_{T,l\nu_l}$ and \cancel{p}_{T,ν_l} fits to a systematic error of 17 MeV for the measurement of M_W . But, when performing fit analysis for separated W^+ and W^- the curl distortion (a_0 and a_2) give rise as it was seen in the core the Chapter to incoherent biases between the positively and negatively charged tracks curvature responsible for the important difference of the order of $\approx 2\sigma$. From that experience we can state that the LHC capabilities and a dedicated measurement strategy should considerably improve the accuracy on the value $M_{W^+} - M_{W^-}$.

Chapter 3

The Monte Carlo event generator WINHAC

veillant
doutant
roulant
brillant et méditant
avant de s'arrêter
à quelque point dernier qui le sacre

Toute Pensée emets un Coup de Dés
Un coup de dés jamais n'abolira le hasard
STÉPHANE MALLARMÉ

So far a description of the theoretical and experimental context in which the prospect for a measurement of $M_{W^+} - M_{W^-}$ have been given. This Chapter describes the tools that were used for that purpose, which consist mostly of a description of the Monte Carlo event generator WINHAC used to simulate the production of W bosons in Drell–Yan. The other tools entering in the generation and the analysis steps are also described briefly.

This Chapter is divided into three parts. The first one, after reminding the gist of Monte Carlo methods, describes the physics implemented inside WINHAC. The second part presents the work done within this thesis to implement WINHAC inside the ATLAS software. The reader interested only in the physics thread can skip this technical part in a first reading. Indeed, to the use of the full and refine ATLAS software, a lighter framework was preferred to make the studies presented in Chapter 4 and 5. This personal framework is eventually presented in the third part of the Chapter.

3.1 The Monte Carlo event generator WINHAC

3.1.1 Monte Carlo methods

Monte Carlo (MC) methods [113] provide in high energy physics efficient solutions to deal with numerical integration and, due to their very stochastic nature, to simulate inelastic scatterings for both phenomenological and experimental specific needs. The principles of MC procedure is reviewed in a nutshell.

(a) Principle of Monte Carlo methods.

Starting with one dimension, the numerical integration of a function f between a and b can be recast as the product of the integration range $b - a$ by the average of the integrand over it, that is

$$I = \int_a^b f(x) dx, \quad (3.1)$$

$$= (b - a) \langle f \rangle_{a,b}. \quad (3.2)$$

This last expression can be approximated using a discrete number of points N within the range $[a, b]$, giving then

$$I \approx I_N \equiv (b - a) \times \frac{1}{N} \sum_{i=1}^N f(x_i). \quad (3.3)$$

Two types of methods can be distinguished to evaluate I_N . The first one consists essentially to slice regularly the integration range, these are called numerical quadratures. A broad range of refinements exist to increase the accuracy and convergence speed of the result (see *e.g.* [114]). Among them let us mention the trapezium and the Simpson rules which accuracies in one dimension are respectively converging like $\propto 1/N^2$ and $\propto 1/N^4$. The second approach consists to pick up N random points in $[a, b]$ to approximate $\langle f \rangle_{a,b}$. This is the principle of Monte Carlo procedure, which in the one dimension case display a convergence $\propto 1/\sqrt{N}$.

When the dimension of the integral increases to a higher dimension, say d , quadrature integration methods become very cumbersome as the integration volume, or phase space to already adopt physics vocabulary, needs to be split into N^d bits. Thus, the trapezium and Simpson methods converge now like $\propto 1/N^{2/d}$ and $\propto 1/N^{4/d}$ whereas for the MC integration by still picking up N random points in the phase space keeps a convergence $\propto 1/\sqrt{N}$. Then, Monte Carlo may be slow but their speed convergence is independent of the dimension of the integral.

Since at the LHC the typical number of produced particles in an inelastic scattering is of the order of $n \sim 1,000$ it implies a dimension $d = 3^n - 4$ where the subtraction of 4 to the degrees of freedom is a consequence of the energy/momentum conservation.

(b) Monte Carlo in High Energy Physics.

Coming back to high energy physics, estimating the probability of occurrence of a LHC reaction $A + B \rightarrow C + D$ demands the computation of its cross section which can be roughly written

$$\sigma = \int_{d=3^n-4} \left(\frac{d\sigma}{d\Phi} \right) d\Phi, \quad (3.4)$$

where $d\Phi$ is an infinitesimal element of the phase space of the process and $d\sigma/d\Phi$ is calculated with perturbative QCD/EW/BSM along with the relevant and available higher corrections depending on the nature of the process. Let us emphasise that here, picking up a random element $d\Phi$ corresponds to a particular physical configuration for the event, that is four-momenta of the colliding partons, of the decaying particles as well as other partons and photons which have been radiated. Hence, the record of these random $d\Phi$ elements, in top of helping to compute σ , represents a collection of events which can be kept and used to plot afterward any desired distribution for an observable a in the form $d\sigma/da$. Note this would not be possible with quadrature procedures where from the start the calculus should be aimed to resolve a particular distribution. This collected events are referred to as “weighted events” as they are indeed weighted by the theoretical prediction $d\sigma/d\Phi$ associated to their production.

Nonetheless, these weighted events are not a simulation of real physics processes. Indeed in nature a physical event do not come with the information whether it is frequent or rare, only harvesting large enough data allows to see it. Still, from the simulation of weighted events a simple trick can be

used to emulate the outcome of unweighted events, that is events with a weight of 1. The principle is the following. In a local region of phase space a maximum MAX is determined for the integrand, *i.e.* $\text{MAX} > d\sigma/d\Phi$. When a weighted event is generated a random number r is drawn in the range $[0, 1]$ then

- If $r < (d\sigma/d\Phi)/\text{MAX}$ the event is accepted with a weight of 1.
- If $r > (d\sigma/d\Phi)/\text{MAX}$ the event is simply rejected.

This rejection method allows to produce events with the same frequency of occurrence than in reality. Histograms produced with weighted and unweighted events are the same in the asymptotic limit $N \rightarrow +\infty$ (in practice when N is large enough so the Central Limit Theorem can be applied). Let us note this trick is possible because the integrand is positive definite which is true only at LO in QCD, the QCD NLO treatment becomes then very delicate, *e.g.* Ref. [115].

Monte Carlo event generators opens, from the experimentalist point of view, a wide range of possibilities. During the generation, acceptance cuts as well as detector smearing on the generator predictions can be applied which justify their extensive use in both R&D prospects and real data analysis.

Also, worth mentioning is the generation of random numbers. It is impossible for an algorithm to generate random numbers since, by definition, its behaviour is deterministic by essence. Hence random numbers are in fact sequence of pseudo-random numbers outgoing small algorithms. The quality of these sequence of number comes from their periodicity –the time it takes to repeat the series– and some short-range correlations between the generated numbers (see *e.g.* Ref. [116]). To better emulate the non correlation between several simulated data, different long sequences can be generated using different seeds in the algorithm initialisation. In the rest, for convenience, the term random is used instead of pseudo-random.

We can distinguish two types of Monte Carlo, the one using the MC technique only for integration and the other which profit of MC properties to simulate physics processes. The latter are referred to as “event generator” or simply “generators”.

Another way to classify Monte Carlo, from the physics point of view this times, is to look at their domain of applications. On the one hand stands a few general purpose MC that possess a wide range of inelastic scattering ($2 \rightarrow 2$ or $2 \rightarrow 3$) implemented for both SM and some BSM processes. They also provide the radiation of photons from leptons and photons/gluons from quarks (called in that context QCD “parton shower”), the hadronisation of jets, decays of unstable particles and the underlying event. The most frequently used general purpose MC are PYTHIA [117, 118, 119], Herwig++ [120, 121] and Sherpa [122, 123]. The other category are MC focused on specific processes but that embrace more corrections at the level of the hard process ($2 \rightarrow n$) compared to the general purpose MC. To obtain eventually physical events just like the one we observe in experiments they are interfaced to general purpose MC. These tools are quite numerous and span large domains of physics, this can go from standard processes with higher QCD/EW corrections to the supply of corrections to existing MC events such as higher QED radiation in the final state like PHOTOS [124, 125, 126] or management of τ or Higgs decays done respectively by TAUOLA [127, 128, 129] and HDECAY [130].

The refinements brought to the art of MC integration and event generation in High Energy Physics goes far beyond the short overview made here. Among them is the variance reduction to improve convergence speed, the handling of singularities in the integrand, and the delicate issue to generate events at NLO in QCD. All those points and many others are addressed in dedicated documents.

There is, so far, no classic textbooks on the use of MC techniques in high energy physics. Nonetheless, the reader eager to learn more on the subject is invited to look at the thesis of Michael Seymour [131] where one chapter provides a short yet thorough description of the matter. Other relevant sources are the presentations given by Monte Carlo experts in conferences (see *e.g.* [132, 133, 134, 135, 136]).

(c) Weakness of Monte Carlo methods.

So far Monte Carlo methods have been promoted as the best tools one can work with in experimental high energy physics. Nonetheless, to be completely objective some light is cast on a few of their weaknesses.

The use of Monte Carlo simulation are safe when it comes to pragmatic application. To illustrate this let us consider the example of nuclear safety where the control of the behaviour of a nuclear facility relies on Monte Carlo simulations. In no case the underlying model implemented have to be perfect, as long as it sticks to physical measurements. Then, using phenomenological models altogether with empirical laws are correct as long as the intended goal –the control of the facility– is assured.

In high energy physics the aim is different. MC generators are introduced to simulate known processes but as well to help unravel possible deviations in paradigm models or even discover brand new processes. Now the actual models are far from being perfect, large parts describing inelastic scatterings are modeled by non perturbative QCD, which relies on complex –and sometime empirical– parametrisation (*e.g.* hadronisation). This poses a problem for the relevancy of an experimental analysis.

The awareness of these imperfection’s acted as an incentive in the present work to come up with analysis strategies which had to adapt to a given measurement to get as much as independent from MC imperfections. Also, in a first step, rather than using several Monte Carlo the choice for a deeper understanding of the used tool, WINHAC was adopted this being justified by the latter strategy to make an analysis.

To conclude with this parenthesis, some quotations on this particular topic. The first one is extracted from a talk by J.D. Bjorken [137] as noted by Torbjörn Sjöstrand in [115]

“The Monte Carlo simulation has become the major means of visualization of not only detector performance but also of physics phenomena. So far so good. But it often happens that the physics simulations provided by the Monte Carlo generators carry the authority of data itself. They look like data and feel like data, and if one is not careful they are accepted as if they were data.”

The second one is from the authors of PYTHIA who warn the users about the traps one can fall into

You must be very careful when you formulate the questions: any ambiguities will corrupt the reply you get. And you must be even more careful not to misinterpret the answers; in particular not to pick the interpretation that suits you before considering the alternatives. Finally [...] the current authors might unwittingly let a bug free in the program PYTHIA.

In conclusion a warning from the authors of Ref. [138]

Monte Carlo event generators are complicated programs that will almost inevitably contain bugs, incorrect assumptions and ill-chosen parameters. It is therefore vital that a user does not take any results at face value. As a minimum at least two completely independent programs should be used in any physics studies.

3.1.2 The Monte Carlo event generator WINHAC

The main tool that used in the present study is the Monte Carlo event generator WINHAC [139, 140, 141, 142]. It has been developed in FORTRAN 77 (F77) by Wiesław Płaczek and Stanisław Jadach from the Cracow theoretical group which holds a leading role in term of electroweak radiative corrections in Monte Carlo.

WINHAC is dedicated to precision description of the charged-current Drell–Yan process. It has been thoroughly tested and cross-checked with independent calculations [139, 140, 143, 142]. This MC program has already been used in previous studies of experimental prospects for exploring the

electroweak symmetry breaking mechanism [144], in our ongoing effort for precision measurement of the Standard Model parameters at the LHC within the ATLAS experiment [145, 146, 72, 74].

At the time of the redaction of this dissertation, the most recent version of WINHAC is release 1.30 [147]. It features the exclusive Yennie–Frautschi–Suura exponentiation [148] of QED effects, *i.e.* the radiation of n photons in the final state

$$q + \bar{q}' \rightarrow W^\pm \rightarrow l^\pm + \bar{\nu}_l^{(-)} + \gamma_1 + \gamma_2 + \cdots + \gamma_n, \quad (3.5)$$

with $n = \{0, 1, \dots\}$, also referred to as multi-photon radiation. It also includes $\mathcal{O}(\alpha)$ electroweak corrections for the full charged-current Drell–Yan process at the parton level, for more details see Ref. [142]. This parton-level process is convoluted with the parton distribution functions (PDFs) provided by the LHAPDF package [149] which includes a large set of recent PDF parametrisation by several groups. WINHAC is also interfaced with the PYTHIA 6.4 [117] MC event generator for the QCD/QED initial-state parton shower as well as for the hadronisation. Technical detail, PYTHIA and WINHAC are accessing to LHAPDF density functions through the LHAGLUE interface –present in LHAPDF– which mimics the procedure that was used formerly to use PDFLIB [150] the ancestor of LHAPDF. Several type of collisions are made available: proton–proton, proton–anti-proton, proton–ion, ion–ion, where each ion beam is defined by its charge number Z , atomic number A and energy in the center of mass. For $Z > 2$, the nuclear shadowing effects from Refs. [151, 152] can be optionally switched on.

The parton-level matrix elements are calculated numerically from spin amplitudes [139]. This allows for studies of any spin effects in the charged-current Drell–Yan process. In fact, WINHAC provides options for generation of processes with pure transversely or pure longitudinally polarised W bosons at the Born level.

In addition to the charged-current Drell–Yan process, WINHAC includes the neutral-current Drell–Yan process (with $\gamma^* + Z$ bosons in the intermediate state), however at the Born level only. For precision description of this latter process, similar to the former one, a dedicated MC event generator called ZINHAC [153] is being developed in C++ by Wiesław Płaczek and Andrzej Siódmok. In the future, these twin MC generators can be used for precision studies/analyses of the Drell–Yan processes including the QED/EW corrections.

The generation of random numbers in WINHAC is achieved using different classic algorithms. The one used for our work is RANMAR [154, 155] which displays a periodicity of 2^{144} .

For this study version 1.23 of WINHAC has been used which for all aspects investigated and adopted strategies is equivalent to the latest version. They differ in description of QED/EW corrections but these have not been included in the present work. In Appendix 3.A an example of a WINHAC summary event is given.

As conclusion, in Table 3.1 we stress the place of WINHAC with respect to multi-purpose and a few specialised Monte Carlo that can produce W or Z in Drell–Yan. In this table MC event generator (Event Gen.) are distinguished from the one using only MC as a mean of integration (Histograms). As it can be seen there is up to this date (2009) no Monte Carlo which hold QCD and EW corrections at the same level of detail.

Hence so far, Monte Carlo are usually combined to simulate with the closest possible accuracy the physics observables needed to be confronted to the data. For example the extraction of M_W for the CDF II run [51] is made using the following Monte Carlo

- $p_{T,W}$ is simulated with ResBos [166] and making cross checks with DYRAD [173] W +jet simulation.
- The photon radiation corrections in the final state are made by WGRAD [63] and correct the $p_{T,l}$, $m_{T,l\nu_l}$ and \not{p}_{T,ν_l} distributions from ResBos.
- The background to $W \rightarrow e\nu_e$ ($W \rightarrow \tau\nu_\tau$ and $Z/\gamma^* \rightarrow e^+e^-$) and to $W \rightarrow \mu\nu_\mu$ ($W \rightarrow \tau\nu_\tau$ and $Z/\gamma^* \rightarrow e^+e^-$) are simulated using PYTHIA v 6.129 and passed to a GEANT-based full simulation of the detector.

Monte Carlo	Refs.	Process	QCD	EW	Type
WINHAC	[139, 147]	W	PDF(x), impr. LO	$\mathcal{O}(\alpha)$ +QED FSR	Event Gen.
HORACE	[156, 157]	W, Z	PDF(x), impr. LO	$\mathcal{O}(\alpha)$ +QED PS	Event Gen.
PYTHIA	[117, 119]	W, Z	PDF(x), impr. LO	LO	Event Gen.
HERWIG	[158, 159]	W, Z	PDF(x, p_T), impr. LO	LO	Event Gen.
Herwig++	[120, 121]	W, Z	PDF(x, p_T), NLO	LO	Event Gen.
Sherpa	[122, 123]	W, Z	PDF(x, p_T), impr. LO	LO	Event Gen.
MC@NLO	[160, 161]	W, Z	parton shower, NLO	LO	Event Gen.
AcerMC	[162, 163]	W, Z	PDF(x), LO	LO	Event Gen.
ResBos-A	[164, 165]	W, Z	PDF(x, p_T), NLO	FS $\mathcal{O}(\alpha)$	Histograms
ResBos	[166, 167]	W, Z	PDF(x, p_T), NLO	LO	Histograms
WGRAD	[63, 168]	W	PDF(x), LO	$\mathcal{O}(\alpha)$	Histograms
ZGRAD2	[169, 170]	Z	PDF(x), LO	$\mathcal{O}(\alpha)$	Histograms
SANC	[171, 172]	W, Z	PDF(x), LO	$\mathcal{O}(\alpha)$	Histograms

Table 3.1: Overview of some Monte Carlo capable of simulating single W or Z production in hadronic colliders. The quoted references corresponds to, first, the main reference and second to the software homepage for further references and details on the Monte Carlo.

3.2 Implementation of WINHAC in the ATLAS software

3.2.1 Introduction

This part of the Chapter covers the work achieved in the context of this thesis to implement WINHAC in the ATLAS software environment.

As seen previously each detector needs, for both R&D and data analysis, to have at its disposition different Monte Carlo event generators to simulate the physics to be studied. Their implementation needs to follow codified rules, just like any other tools in the experiment software, for clarity's sake. On the one hand most event generators obey to custom rules and conventions and can be implemented in any programming language like F77, C/C++, *etc.* On the other, for convenience reasons, experiments software environment relies on automated skeletons that treat all the present generators with the same manner. For instance, Monte Carlo events needs, among many other things, to be smeared to simulate the particle interactions with the material of the detector. This simulation takes as input a standard data format which is completely blind to the generator that produced it. This example gives an idea of how a generator needs to fulfill a few requirements imposed by the experiment.

This section is divided as follow. After an overview of the main features of Athena [174], the software environment of ATLAS, follows a description of the context in which WINHAC was introduced, that is in the simulation and reconstruction chain of the Monte Carlo events inside ATLAS. The section ends on the implementation of WINHAC and the validation of this work.

3.2.2 Software environment of the ATLAS experiment

To better visualise the context of our discussion a brief overview of the software environment ATLAS relies on is given.

First of all, let us note the quantity of events selected by ATLAS together with the data outgoing their analysis should represents each year a volume of information of the order of 10 Peta-byte¹. Hence to overcome this challenge ATLAS had to aim for a highly decentralised storage and data

¹1 Peta $\equiv 10^{15}$.

management. This system obeys to a certain hierarchy where tasks are split into facilities called Tiers which principal activities are recaptured below.

Although it will not be emphasised later on let us note that one of the philosophy in the use of Tiers prescribes, for obvious safety reasons, to make a least one back up of each data batch. The first data processing occurs at CERN in the unique Tier-0 facility where raw data are saved and reconstructed into ESD, AOD and TAG formats which description are gathered at the end of § 3.2.3. This first data batch are shared among Tiers-1, of the order of ten all other the world. The tenth of these raw data are stored to give new ESD, AOD and TAG. Tiers-1 need to provide good accessibility for the data they store as well as the necessary capacity to analyse them. Tiers-2 provide work related to the calibration, the simulation and the analysis. Finally Tiers-3 are made of local sources in each institute necessary to store custom data (*e.g.* ntuple) and act as well as access points to upstream Tiers. More details on the precise role of each Tier are given in Ref. [174]. This decentralisation of data processing and storage is provided by the Grid which allows to make out of the ATLAS software a virtual facility split between several calculators spread throughout the world.

The informatics environment of ATLAS is called Athena [174, 175]. Athena is an evolved version of the Gaudi [176, 177] framework developed initially by the LHCb [87] experiment and is now common to both ATLAS and LHCb projects. Amid the important features of Athena is the clear separation between the data and the algorithms as well as between transient data (in memory) and persistent (in file) data. The processing of the data for data selection, event simulation, reconstruction and analysis is governed by Athena. Athena is object oriented (OO). Its structure is build mainly in C++, uses extensively the ROOT System [178, 179] with some tools written in FORTRAN 77 or Java while the user interacts with Athena via Python.

3.2.3 Simulation and reconstruction of Monte Carlo events within ATLAS

Here we give a description of the different steps that allow, starting from Monte Carlo events or from real data, to reach reconstructed data. The first overview and the details that follow can be grasped looking at Fig. 3.1. Let us remind more details on the data type mentioned are compiled at the end of this section.

(a) Overview of the simulation and of the reconstruction

Starting with the real data. The event filter –the last process of the ATLAS trigger– provides as outputs raw data in byte stream format, *i.e.* sequence of 1/0. These information are then converted to objects, the Raw Data Object (RDO) transmitted in turn to reconstruction algorithms. Before describing the reconstruction chain, let us come back to the stages the simulated data must follow. In the first step physical events are produced by Monte Carlo event generators, at this stage acceptance cuts can be applied on some observables such as p_T , η , \cancel{E}_T , *etc.* These events, as seen previously in § 1.3, are labelled “truth events” or “generator level” data. They are transmitted to algorithms that simulate their passage in the ATLAS detector. This step is by far the most CPU time consuming. The output are hits, that can be merged with pile-up events, the latter receiving a special treatment. After comes the digitisation which goal is to emulate the electronic read-out chain of the several sub-detectors of ATLAS. This gives eventually simulated RDO. The simulation step finished the reconstruction chain is over-viewed.

Even though RDO are oriented object they are nonetheless raw data. Also the goal of the reconstruction, as its name indicates, consists to reconstruct objects containing only relevant information for a physic analysis.

Finally let us mention the fast simulation of the detector. Since the simulation part is very time consuming most experiments have tools with an approximated but faster simulation of the detector. In ATLAS, this fast simulation is called Atlfast [180, 181, 182]. It shortcuts all simulation chain steps, that is from the particles four-momentum outgoing the generator it directly gives reconstructed data.

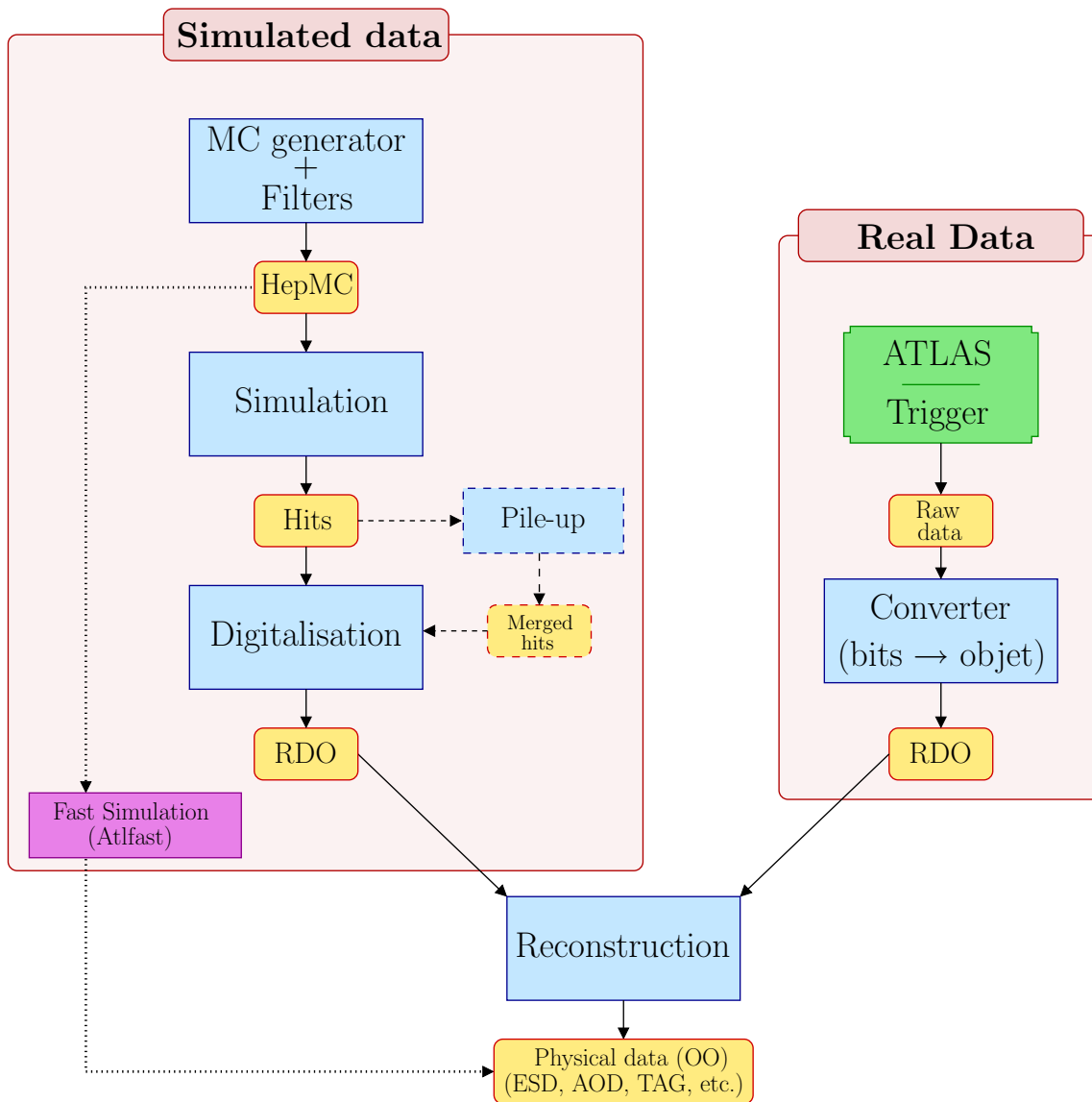


Figure 3.1: Schematic representation of the simulation (Monte Carlo data) and reconstruction of both Monte Carlo and real data. The add-up of the pile-up (box with dashed borders) is an optional step.

In the rest complementary information on the simulation and reconstruction chains are given. For each step the emphasis is made first on physics aspects and then on technical aspects. For further details on all technical aspects related to the Athena framework the reader is sent back to the ATLAS Computing TDR [174] and to the on-line workbook [175].

(b) The simulation chain

Generation. The physics motivation being already known we move on directly to technical aspects with more emphasis with respect to other steps since the work for implementing WINHAC occurred at this stage.

Inserting a MC within ATLAS consists to write inside Athena a C++ interface calling the algorithms of the generator within its original libraries. Those instances are roughly :

- The initialisation, which essentially switches on the MC generator algorithms, read the input parameters, *etc.*
- The event loop in which the MC generate events.

- The finalisation where algorithms are shut down and the data are saved.

These three steps are realised for all the generators within Athena via the inheritance of the methods of the class `GenzModule`.

Concerning the libraries of the stand-alone code they are stored outside of the Athena framework in AFS or in the GENSER (GENerator SERVICE) repository. The goal would be eventually to maintain all generators libraries by the GENSER LCG project [183] which would provide validated libraries for the needs of both theoreticians and experiments associated to the LHC.

The random numbers in Athena are provided by the use of the Athena Random Generator Service which uses RanecuEngine [154] maintained by CLHEP [184].

The parton distributions functions are provided by the LHAPDF package [149].

The output for the events is in the HepMC [185] format that records information related to each event. The HepMC format possess an infinite number of entries, the storage of the matrix density in each vertexes, the flow pattern (*e.g.* color) and their follow up, the record of the used random numbers along with an arbitrary number of statistical weight that can be associated to each event. This tool developed in C++ by ATLAS members has become the standard for the record of high energy event and is now maintained by CLHEP.

Simulation. The goal of the simulation stage is to simulate the passage of particles generated by the MC within the sub-detectors of ATLAS, *i.e.* energy deposit in the calorimetry and tracks left in both inner tracker and muon spectrometer.

This task is made by GEANT 4 [186, 187]. GEANT model the geometry and composition of the ATLAS detector, and simulate the physical process occurring as particles pass through each cells. Hits record information related to the position, yielded energies, identifications of activated elements, *etc.* For the pile-up Athena provides a stock of simulated pile-up and select for each event one random set and optionally merges it to the process simulated upstream.

Digitisation. Hits need to be converted into an output of the same format with the one provided by the ATLAS detector for real data. For that purpose matters such as the propagation of charges (*e.g.* in the tracker or in the LAr) and of light (*e.g.* in the tiles of the hadronic calorimeter) as well as the response of the read out electronic needs to be emulated.

Contrary to the previous steps these tasks are very specific to the detector and cannot be accomplished without the physicist directly involved with the assembly and testing of each ATLAS specific sub-detectors. This step provides output in RDO format. Let us note all Monte Carlo truth information, kept so far for cross check, are removed from simulated RDO so that they exactly look like the format of the real data selected by the ATLAS trigger.

(c) Reconstruction of physic events

The goal of the reconstruction is to devise from raw data the vital information necessary to perform an analysis. To be more specific information related to photons, electrons, muons, taus, K^0 , jets, \cancel{E}_T , primary vertexes, *etc.* These collected data from each sub-detector are combined to optimally reconstruct four-momenta for the widest range of momentum, pseudo-rapidity and whatever value of the luminosity, all of that with the less background for particle identification.

The reconstruction is split in several steps depicted in Fig. 3.2. In a first stage is the individual reconstruction of the data outgoing the sub-detectors (tracking and calorimetry) then comes the combined reconstruction which corresponds to the beginning of particle identification. An example of this step has been given for the case of the inner detector tracks reconstruction in Chapter 2 § 2.3.2. The output of this procedure are in ESD format.

In the second stage the preparation to the analysis starts with more complex reconstructed objects (*e.g.* b -tagging) and with a reduction of the data to the AOD format.

Finally data are tagged with the use of TAG files created from the AOD.

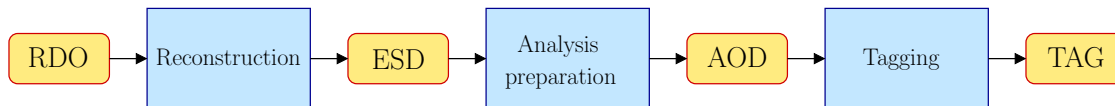


Figure 3.2: Schematic representation of the steps of the data reconstruction. Boxes with sharp edges represent algorithms while the rounded boxes represents data.

(d) Sum up of the different data format

As seen previously different data format exist at different stages of the simulation and reconstruction chain. The list below makes a summary of the one mentioned earlier.

Raw data. These are the data provided by the event filter, the last stage of the ATLAS trigger, and are written in byte stream format. Each file contains the information related to a run and each event, delivered at a frequency of 200 Hz, should weight 1.6 Mb. This data format, contrary to the one that follow, is not object oriented.

Raw Data Object (RDO). The RDO is essentially an oriented object (C++) representation of the byte stream information from the raw data.

HepMC. Format holding generator level information coming from MC generators, that is a purely theoretical information.

Hits. Format carrying recording real interactions of simulated particles with the detector. Hits carry information like position, energy deposit, identifier of the active element, *etc.* after simulating the theoretical events in the ATLAS detector.

Event Summary Data (ESD). These files contain reconstructed information necessary to deduce the identification of particles, the track refitting, the jet calibration, *etc.* The goal of this format is to avoid to access to raw data for every study out of the calibration context or of the re-reconstruction. Those files are written in POOL ROOT format [178, 179] with an average size of 500 Kb per event.

Analysis Object Data (AOD). These POOL ROOT files are derived from ESD. They contain physical objects with information relevant to an analysis. It is on this format that in the long run most physical studies should be based upon. Each even takes a size on disk of the order of 100 Kb.

TAG. These files are created in the goal to identify and select produced data. They contain information on the data batches, each event occupy a size of 100 Kb.

For conclusion several tests that were carried in this work to validate the implementation of the WINHAC interface are based on the CBNT (ComBined NTuple) format which hold data in Trees and leaves ROOT format.

3.2.4 Implementation of WINHAC inside Athena

(a) The Winhac_i interface

In this part we present Winhac_i, the interface between WINHAC and Athena. This work has been made in collaboration with Giorgos Stavropoulos to make of WINHAC an ATLAS approved Monte Carlo event generator used for the production of event samples as reported in Ref. [71].

The requirements from the Athena framework imposed to switch to its own random generator and to the use of the LHAPDF libraries since in the version of WINHAC used at that time (v 1.21) PDFLIB was still use. The feedback to the authors allowed the code to evolve in later releases to use of LHAPDF as the default option (v 1.22 and upper). Finally always at the time of this implementation the LHAPDF package did not provided nuclear corrections necessary when studying ion-ion collisions. Again to fulfill our needs the maintainer of the LHAPDF code included nuclear corrections (LHAPDF v5r2 and above) in the same way they were called so far via the LHAGLUE interface.

WINHAC is an event generator dedicated to a particular process. Nonetheless it was not implemented like many others MC using the “Les Houches” format [188] whose procedure consists to provide to a general purpose Monte Carlo a hard process to dress-up its kinematics with the QED/parton showers, hadronisation, decays, *etc.* As specified before, WINHAC uses PYTHIA parton shower and hadronisation scheme for its purpose and this specificity was kept in the interface. This is justified for example by the fact that the parton shower in the initial state should eventually be replaced by one made by the authors. To stick with the ATLAS standards an additional interface was written to overwrite the hard-coded PYTHIA options in WINHAC by the default values imposed in Athena.

(b) Validation of the implementation

This section describes essential results obtained to validate Winhac.i. In what follows all Monte Carlo which are referred to are used within the Athena framework. First, tuned comparisons at the generator level were achieved with well validated MC. The goal of these tests were to improve the interfacing of WINHAC from both technical and physical point of view. Complements on this work are available through the reports brought to the CERN forum [189, 190].

Tuned comparisons at the generator level. Tuned comparisons were achieved, *i.e.* using the same input parameters in the Monte Carlo, successively to confront WINHAC to PYTHIA and then to PYTHIA+PHOTOS for $W \rightarrow \mu \nu_\mu$ with a statistic of 100,000 events. PYTHIA parameters were tuned with the one used to the WINHAC default this being justified since at that time overwriting the hard-coded PYTHIA parameters used in WINHAC by the Athena defaults had not yet been though through.

The first test, versus PYTHIA, is set up at the Born level with, for only higher corrections, the QCD and QED parton shower in the initial state. This imply that both data due to the structure of WINHAC are perfectly similar from both physical/technical point of view, indeed in both cases the parton shower was done by PYTHIA 6.403.

In Fig. 3.3 are respectively represented the rapidity and transverse momentum of the W and the pseudo-rapidity and transverse momentum of the charged leptons. The validation using $p_{T,W}$ is important as its distribution turns out to be very sensible from the parton shower and from the intrinsic k_T of partons (cf. Chapter 1 and Fig. 1.13.(b)). In PYTHIA this meant to take for these runs a Gaussian distribution for k_T which corresponds to use the value MSTP(91)=1 with $\langle k_T \rangle = 1$ GeV that latter corresponding to the switch PARP(91)=1. Another point, no multiple interactions were used (MSTP(81)=0). For further details on the physical and technical aspects of these parameters see Ref. [117]. As expected the data from both generator agree within the statistical limit.

For the second test WINHAC was used by adding up to the previous setting QED multi-photon radiation. On the other side to emulate higher QED radiation in PYTHIA the former set up was plugged to the PHOTOS [124, 125, 126] generator which added QED corrections in the final state of the events. In both cases, WINHAC and PYTHIA+PHOTOS, a common value was used to cut on the energies of soft photons at the level of the analysis, that is $E_\gamma > 500$ MeV. In Fig. 3.4, the number of radiated photons are represented with the total energy of these photons. Below are represented the transverse momenta of the hardest and second hardest photons defined respectively as, for a given

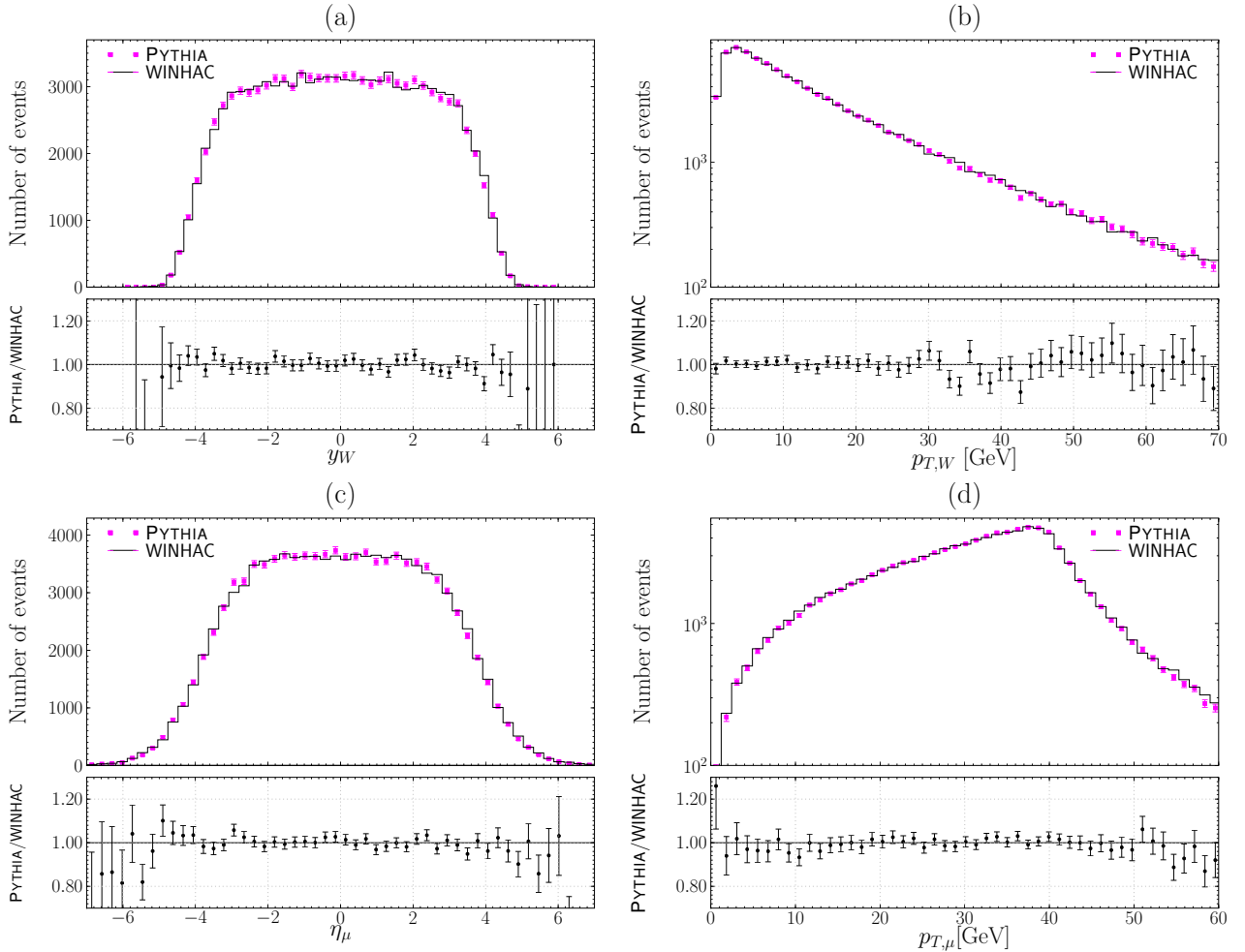


Figure 3.3: Tuned comparison between PYTHIA and WINHAC within the Athena software, displaying y_W (a), $p_{T,W}$ (b), η_l (c) and $p_{T,l}$ (d) distributions. The lower frames in each plot displays refined comparison in the ratio $PYTHIA/WINHAC$.

event, the photon with the highest p_T and the second highest p_T . Although the statistic is quite small for the histograms related to photons one can see there is a good agreement within the statistical error.

Some discrepancies were observed though while looking at the transverse mass. In Fig. 3.5 the $m_{T,\mu\nu\mu}$ distribution is represented for both the first validation set up and the present one. One can see in the latter case from the ratio frame that after the jacobian peak WINHAC displays a slight shift to higher p_T with respect to PYTHIA(+PHOTOS). These discrepancies can be amended by the fact that here WINHAC and PHOTOS do not treat QED radiation on the same footing. Indeed, PHOTOS do not take into account cases where the one or several photon are emitted by the W boson as well as the interference this creates with other diagrams where the charged lepton radiates photon(s).

Simulation and reconstruction tests. The last test consisted to pass WINHAC events through the whole simulation and reconstruction chain. Tests were passed with success respectively for $W \rightarrow e\nu_e, \mu\nu_\mu, l\nu_l$ each time with a statistic of 1,000 events using acceptance cuts of $p_{T,l} > 20$ GeV and $|\eta_l| < 2.5$. The low statistic is justified because of the long time it takes to simulate events. In each case the data was obtained in ESD, AOD and CBNT format.

Fig. 3.6 presents respectively comparisons between the generator and reconstructed data for the transverse momentum and pseudo-rapidity of the muon. The reconstruction was made using the MOORE algorithm [191] that reconstructs tracks in the muon spectrometer.

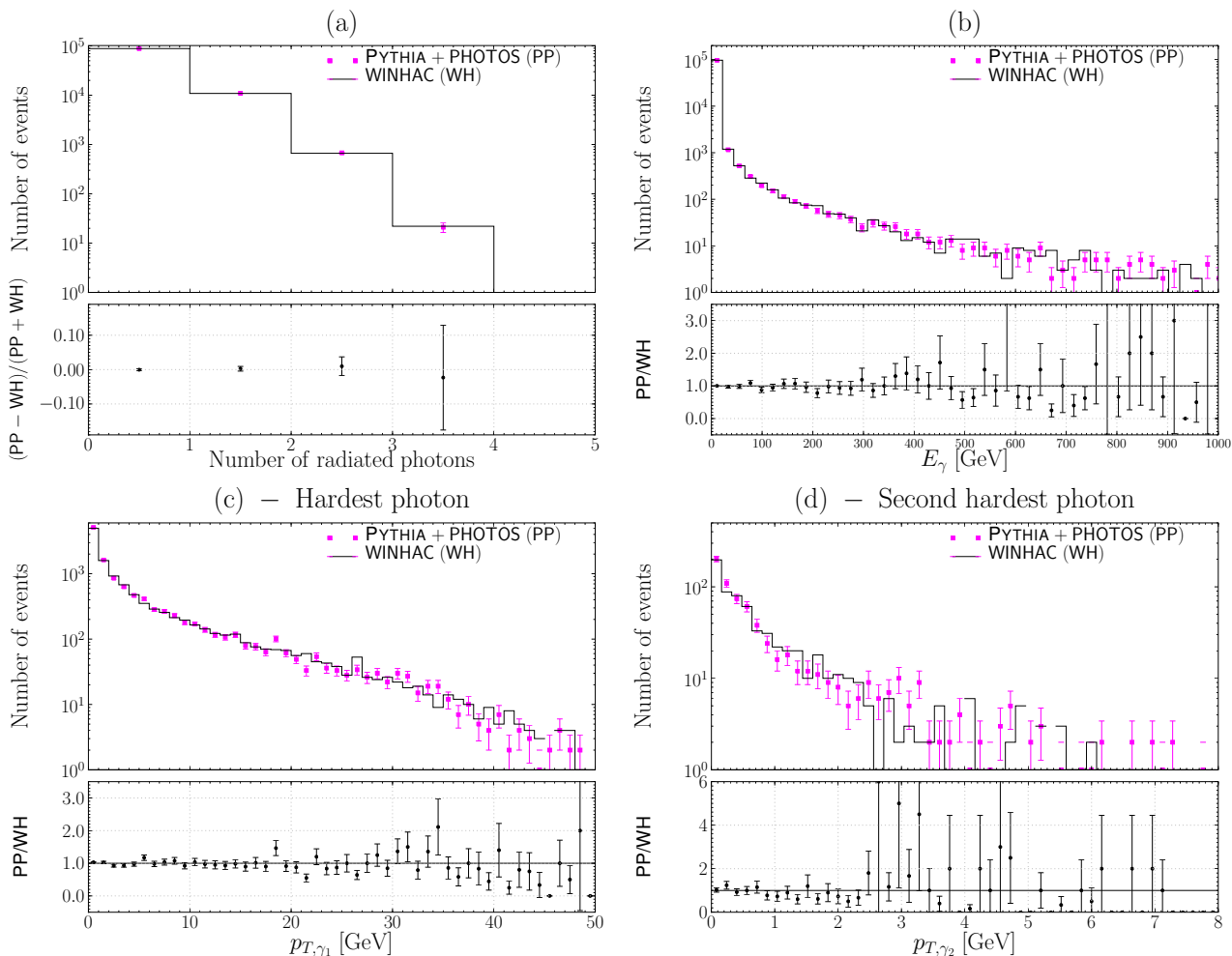


Figure 3.4: Tuned comparison between PYTHIA+PHOTOS and WINHAC showing the number of radiated photons (a), the total energy of the radiated photons (b), the transverse momentum of the first hardest photons (c) and second hardest photons (d).

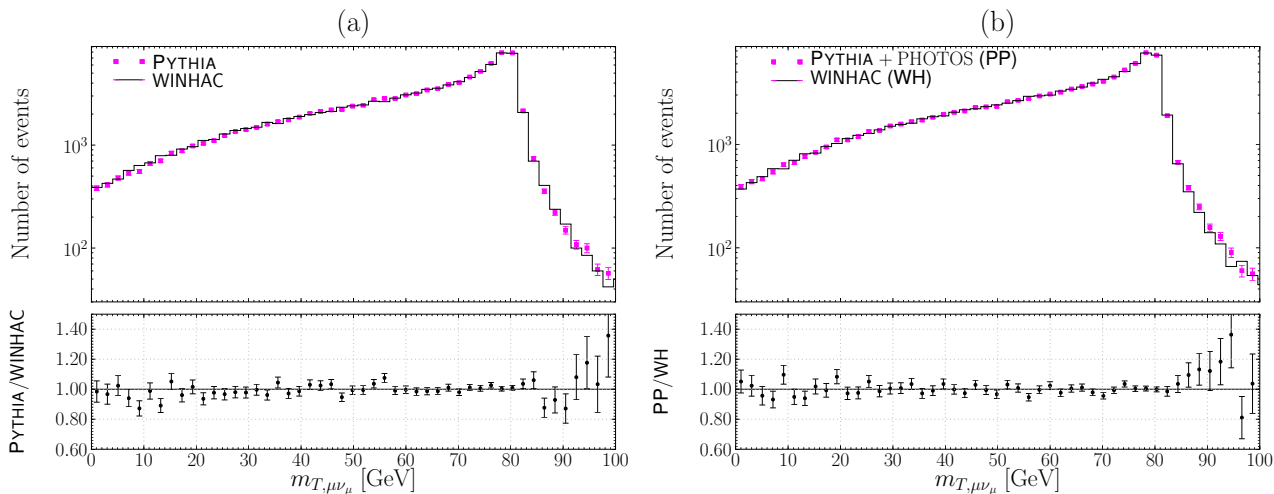


Figure 3.5: Tuned comparison based on the leptons transverse mass for PYTHIA versus WINHAC at the Born level (a) and PYTHIA+PHOTOS versus WINHAC at the Born+multi-photon QED radiation (b).

N_γ	PYTHIA+PHOTOS	WINHAC
0	88374	88440
1	10927	10874
2	677	664
3	21	22

Table 3.2: Number of radiated photons N_γ from WINHAC and PYTHIA+PHOTOS simulations.

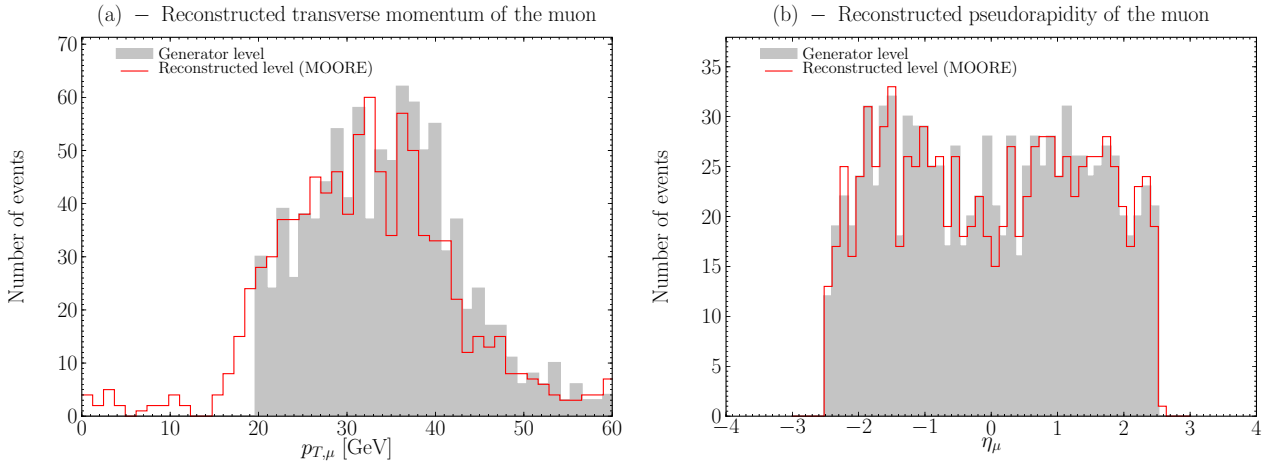


Figure 3.6: WINHAC muon kinematics at the generator and reconstructed level for the transverse momentum (a) and the pseudo-rapidity (b). The acceptance cuts applied at the generation level are: $p_{T,\mu} > 20$ GeV and $|\eta_\mu| < 2.5$.

3.3 Framework of the analysis

Like explained in the introduction of this Chapter, rather than going to the refined –but heavy– framework described above a simpler and more pragmatic approach was adopted. In this approach, the simulation of the detector for the analysis is achieved using Gaussian resolution to emulate the inner detector resolution. The reason for that is that the statistic that needed to be generated is too huge to be passed through the whole simulation and reconstruction chain of the ATLAS detector. Actually, analysis with real data are based on the same principle where instead of taking the whole simulation for the detector a tuned fast simulation is used for all Monte Carlo simulation. This is for example the strategy used by CDF II for the measurement of M_W [51].

The last argument becomes more tangible when looking quantitatively at the present analysis requirements. Studies were made for an integrated luminosity of 10 fb^{-1} which means an order of $\sim 1.1 \times 10^8 W^+$ and $\sim 0.8 \times 10^8 W^-$. In order to optimise the strategy to measure their masses, generation and simulation of $\mathcal{O}(100)$ event samples was required. These samples correspond to specific biases in the detector response, or in the theoretical (phenomenological) modeling of the W -boson production processes. In addition, a large number of unbiased event samples, for variable values of the masses of the W^+ and W^- bosons, was simulated. For an assessment of the impact of the systematic biases on the overall measurement precision each of the above event sample must contains at least 10^8 events in order to match the systematic and the statistical measurement precision.

The presented analysis is then based on a total sample of $\mathcal{O}(10^{10})$ W boson events. Generating, simulating and handling such a large event sample within reasonable limits of the storage space and computing power is challenging. Indeed, if we consider in the simplest case scenario where the gist of the event² would be recorded in double precision, this should require ≈ 500 bytes for each event

² That is the four-momenta, types and genealogy of each particle entering in the hard process (~ 10 particles per

summaries, which leads eventually to store a Terabyte of data on disk. Besides, even though one can compute an accurate experimental simulation using GEANT, the treatment of hundreds of millions of events would be prohibitive. The computing of the desired histograms on a dedicated farm, using a fast simulation, takes 1–2 days to get all the necessary event samples.

A short descriptions of both generation and analysis framework are given below.

3.3.1 Generation framework

In that state of mind, the generation is made using the WINHAC event generator in stand-alone mode. An overview of the main features of the generation framework is represented in Fig. 3.7. For convenience the generation framework interfaced to WINHAC was also written in FORTRAN 77. This framework takes as input the physics parameters necessary for the initialisation and the running of WINHAC. During this initialisation the observables of interest are booked. Then in the generation loop, for each event, standard calling instances to WINHAC implemented by its authors allow to access basics quantities such as four-momentum, particles type, *etc.* from which observables of interest can be calculated. For practical reasons all analysis were made using weighted events since it is faster. At this stage, cuts or smearing to emulate the ATLAS detector resolution can be optionally applied. Eventually each observable fills the corresponding histogram and at the end of the generation the histograms are written in ASCII files along with the cross section of the process. Already at this stage histograms are normalised to nb according to the conventions stated in Chapter 1 § 1.3.

On our road to an experimental investigation a preliminary step consisted to look only at the generator level predictions with only optional phase-space cuts to put the spot on a particular behaviour. This is presented in the next Chapter. Then the more realistic experimental analysis for $M_{W^+} - M_{W^-}$ was made using some acceptance cuts related to the ATLAS performances and the smearing of the data was computed according to Eqs. (2.15–2.16) from § 2.3.2. This step us presented in Chapter 5.

Let us note that in both cases, sometimes, changes of the original PDFs predictions needed to be done. Still, for both security and practical reasons the LHAPDF package was not touched. Instead an interface was written which lures WINHAC and PYTHIA to use custom values instead of the original ones. The subroutines that needed to be substituted to the use of the original ones are of the number of three and belong to the LHAGLUE interface written to mimic the old-fashion way to call PDFs from the PDFLIB package. These three subroutines which PYTHIA and WINHAC depend on are briefly described. The first one –the most fundamental– is STRUCTM which gives for a given PDF set at fraction x and scale μ_f^2 the parton density functions in the output form $x f_i(x, \mu_f^2)$, where i is such that

$$i = \{g, d, \bar{d}, u, \bar{u}, \overset{(-)}{s}, \overset{(-)}{c}, \overset{(-)}{b}\},$$

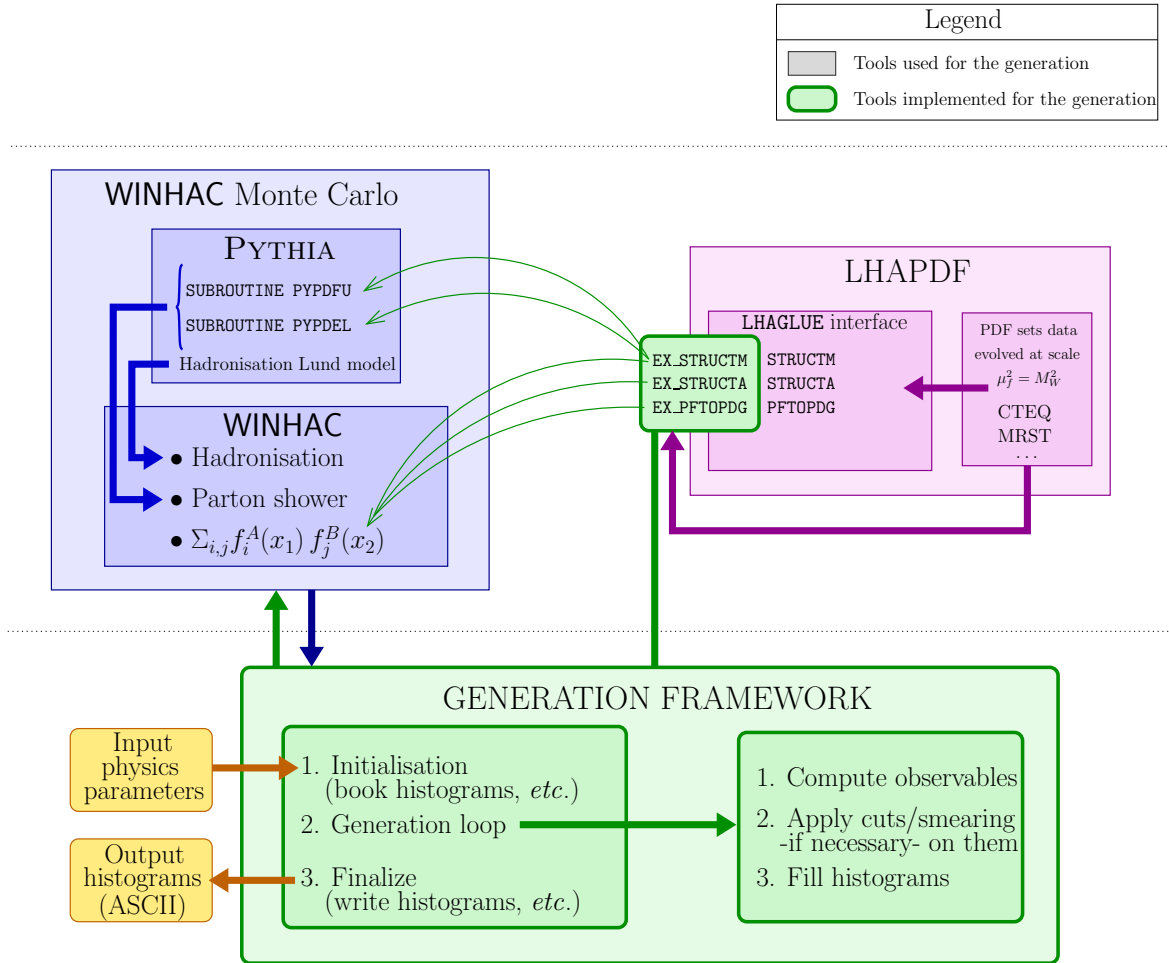
with, for reminder, $q^{(s)} = \bar{q}^{(s)}$, where (s) means sea for s , c and b flavors. The two other subroutines, used exclusively by WINHAC, are PFTOPDG and STRUCTA and both rely on the output from STRUCTM. PFTOPDG provides the flavors in a one dimensional array which indexes, ranging from -6 to 6, are associated to the conventional ID number given to partons (see Ref. [1], Monte Carlo particle numbering scheme section). STRUCTA adds to the predictions of STRUCTM nuclear shadowing effects in the aim to compute the PDFs for a hadron of mass A .

To these subroutines are substituted our custom copies

- EX_STRUCTM
- EX_PFTOPDG
- EX_STRUCTA

the structure of the two last one are unchanged, they are just relying on EX_STRUCTM instead of the original subroutine. Then, any changes in the density functions are made by playing with the output values of EX_STRUCTM.

event).



Input physics parameters

1. Initialisation (book histograms, etc.)
2. Generation loop
3. Finalize (write histograms, etc.)

1. Compute observables
2. Apply cuts/smearing -if necessary- on them
3. Fill histograms

Output histograms (ASCII)

Figure 3.7: Generation framework schematic representation. The round boxes are the code implemented to carry the analysis.

Let us remark that in Fig. 3.7 only the main features are given and in no case the whole chain of subroutine calling concatenation as it will eventually become obsolete as both F77 versions of WINHAC and PYTHIA will be replaced to C++ versions. Slight details were given for only PYTHIA since this Monte Carlo being extensively used its subroutines are more familiar in the high energy physics community.

3.3.2 Analysis framework

Here we describe the methods that were used to perform all kind of histograms and/or analysis from the WINHAC event generations present in this document and in our ongoing studies [72, 74]. This histograms/analysis framework is represented schematically on Fig. 3.8.

The framework is made of a central set of functions written in C++ and gathered in one *.cxx file and its associated header file *.h. This framework relies on C++ and STL (Standard Template Libraries) classes and also on ROOT classes [178, 179] from version 5.14. The ROOT classes and methods that are used essentially to handle one-dimensional double precision histograms containers TH1D and other methods inherent to this class which allow the user to perform basic operations on and between histograms. ROOT is also called to display histograms and related analysis results using the class TApp. Histograms are then displayed using the canvas class TCanvas, stored inside *.root files

(using the `TFile` class) and postscript files for later browsing. Each step of the histograms/analysis consists always to the same principle which is to write a C++ program to reach a given goal with the help of calls of functions from our framework.

Now, further details are given on the treatment of data in a chronological order. In a first step, all the ASCII histograms obtained from the generation and sharing the same input parameters are converted to TH1D objects and stored in `*.root` files whose names are based on the main physical input parameters.

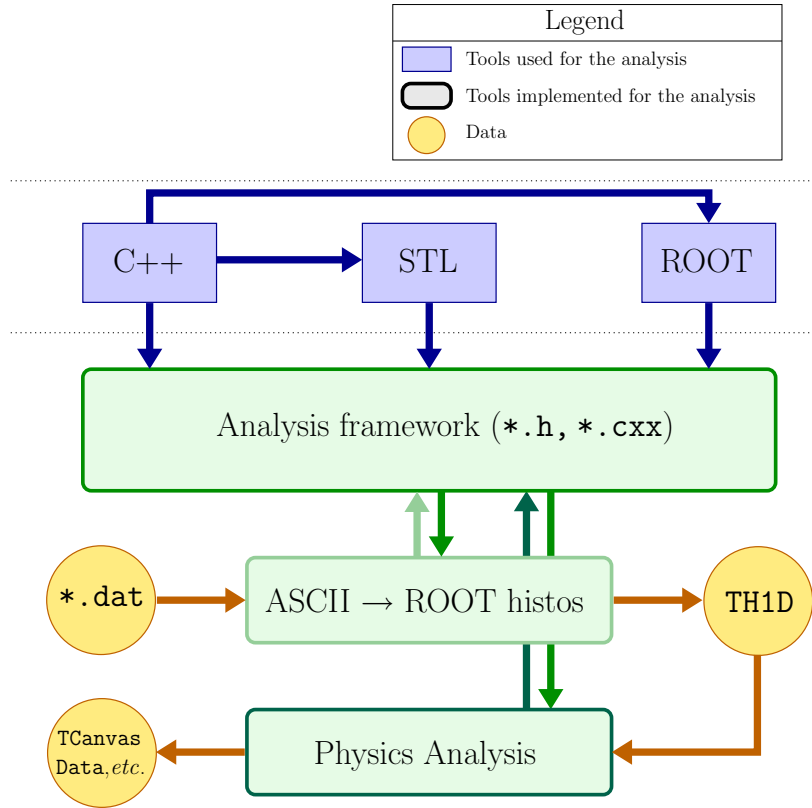


Figure 3.8: Analysis framework schematic representation.

In a second intermediate step –not represented in Fig. 3.8– the newly created histograms are read from the `*.root` files they are stored in and displayed as `TCanvas` for visual cross-check. Those canvas are saved in `*.root` and postscript files to allow visual control for safety.

Finally the last step consists to produce the desired results that is fine histograms or an analysis. The first procedure was used extensively to understand the asymmetries in the mechanisms of production between W^+ and W^- . For that purpose in top of drawing the two $(d\sigma^+/da)$ and $(d\sigma^-/da)$ distributions related to the observable a , another frame was drawn in the canvas to display discrepancies between them. Optionally the difference, the ratio, or the charge asymmetry (Eq. (1.7)) of the two distributions was computed the latter being preferred due to the nature of the present work. This kind of analysis are presented in the next Chapter.

Concerning the physics analysis it involved to perform likelihood studies between a main (M) and N -templates event samples distributions which n^{th} . template is labeled $T^{(n)}$. This will be explained thoroughly in Chapter 5 here only the technical principle is described. It is very basic though, the main/templates distributions are read out from their respective `*.root` files and using dedicated functions of the framework a likelihood analysis is performed between each couple $\{M, T^{(n)}\}$ couple. The main histograms and all templates are displayed along with the likelihood results in canvas and saved in `*.root`.

Chapter 4

Phenomenology of W^+ and W^- in Drell–Yan like processes at the LHC

Super Skrull Warrior: “I have trained my entire life to face you.”

Black Panther: “Then you have already lost. For I have trained my entire life to face the unknown.”

Black Panther #39 - See Wakanda and Die (September 2008)

This Chapter presents the phenomenology of the W^+ and W^- bosons production in Drell–Yan processes at the LHC. This preliminary work is mandatory before addressing any kind of study related to the extraction of the W boson properties. Indeed, the LHC in top of supplying unprecedented luminosity and energy in collisions will provide –due to the nature of the colliding beams– original kinematics with respect to the one inherent to $p\bar{p}$ collisions studied exhaustively for these last decades at the SPS and Tevatron colliders. These original LHC features demand to start with basics understanding before addressing a more complete analysis prospect.

The Chapter is divided as follow. In a short introduction the context of the studies is described from both physics and technical point of view. Then comes the phenomenological understanding of the W^+ and W^- bosons production in Drell–Yan, first by looking at the production of W and then at the whole process by studying the properties of the decaying charged leptons.

Let us stress that before reaching the refined understanding presented here more thorough analysis were done using complementary distributions, different physical input parameters, for specific domains of the phase-space, *etc.* Nonetheless, to keep the discussion as clear as possible in the core of the Chapter all these exhaustive studies are compiled in Appendix 4.A.

4.1 Context of these studies

The most relevant kinematics to the W in Drell–Yan are reviewed at the generator level, that is looking only at the purely phenomenological level.

Among all the observables/pseudo-observables that entered in our study only a few were kept in the core of the Chapter. They are of two categories. First are the pseudo-observables characterising the W boson properties, its rapidity y_W and transverse momentum $p_{T,W}$. Then are the observables characterising the charged lepton properties, its pseudo-rapidity η_l and transverse momentum $p_{T,l}$ that allows to study the whole process. The definitions of these quantities and the information they hold for W in Drell–Yan have been over-viewed in Chapter 1 § 1.4.2.(d) for the case of a charge blind study. Here, based on this previous overview a fine study of the positive and negative channel is considered.

The type of collisions considered are: $p\bar{p}$, pp and dd . The $p\bar{p}$ collision scheme is considered as a reference since in that case the production of W^+ and W^- are on the same footing and the

Collider	$\sigma_{(\text{incl.})}^+$ [nb]	$\sigma_{(\text{incl.})}^-$ [nb]	$\sigma_{(\text{incl.})}^\pm$ [nb]
$p\bar{p}$	17.4	17.4	34.4
pp	19.8	14.7	34.5
dd	32.5	32.4	64.9

Table 4.1: Inclusive hadronic cross sections $\sigma_{(\text{incl.})}^+$, $\sigma_{(\text{incl.})}^-$ and $\sigma_{(\text{incl.})}^\pm$ respectively for the W^+ , W^- and W in Drell–Yan with $\sqrt{S} = 14$ TeV for $p\bar{p}$ and pp collisions and $\sqrt{S}_{n_1 n_2} = 7$ TeV in the $n_1 n_2$ nucleon–nucleon center of mass energy for dd collisions (computed by WINHAC).

characteristics of the kinematics are well known from the experience gathered from SPS and Tevatron colliders. Standard LHC pp collisions are analysed as well with isoscalar beams collisions on the example of deuteron–deuteron (dd) targets which is justified for both pedagogical means and because the strategy prospect in the next Chapter relies on such a scheme. The nucleon–nucleon center of mass energy \sqrt{S} is of 14 TeV for $p\bar{p}$ and pp collisions and of 7 TeV for dd collisions according to the expected LHC capabilities (cf. Eqs. (2.11–2.12)). The choice of 14 TeV in the center of mass energy for $p\bar{p}$ is justified by the wish to put the energy scales and accessible phase space to the particles on the same footing as the one for pp collisions to stress the differences between these two collision schemes. The total hadronic cross sections corresponding to these collisions and computed by WINHAC are gathered in Table 4.1.

Now details are given on the material presented below from a more technical point of view. All the histograms were produced using the WINHAC Monte Carlo event generator at the truth level within improved leading order defined from the physics point of view in Chapter 1 §1.4.2.(d) and from a Monte Carlo point of view in Chapter 3 §3.1.2. A common statistic of 200 millions weighted events were used for each W^+ and W^- channel and for all type of collisions. The decay of the W bosons was opened to both electronic and muonic channels. Every histograms were generated with 200 bins and for visual convenience this former binning was reduced later on at the analysis level when necessarily. The remaining input parameters of importance for the generation are :

- $M_W = 80.403$ GeV, $\Gamma_W = 2.141$ GeV with the fixed-width scheme in the W boson propagator.
- The partons intrinsic k_T are modeled by the PYTHIA Gaussian scheme (cf. Ref. [117]) with $\langle k_T \rangle = 4$ GeV.
- PDF set : CTEQ6.1M [66].

Let us remind the conventions used for the coordinate systems and the definitions of the common kinematics are gathered in Chapter 1 §1.3. In this context, $p\bar{p}$ collisions are defined in the Cartesian basis, with the proton moving in the $+z$ direction while the anti-proton moves in the $-z$ direction. In what follows the discrepancies between the positive and negative channels predictions are scrutinised using the charge asymmetry (Eq. (1.7)).

4.2 Production of W^+ and W^- bosons

In this Section the W boson production mechanism is discussed via the analysis of the W boson rapidity y_W and transverse momentum $p_{T,W}$. Figure 4.1 presents the latter distributions for W^+ and W^- bosons, as well as their associated charge asymmetries in $p\bar{p}$ and pp collisions.

Our observation starts with the well known $p\bar{p}$ kinematics. Let us remind the W^+ and W^- bosons are produced with the same dynamics due to the nature of the colliding beams. Indeed, the same amount of matter and antimatter are available to produce a W^+ or a W^- . The most visible difference between the two processes occurs at the spatial level because the proton and anti-protons are always impinging respectively from the $+z$ and $-z$ directions. Thus the kinematics between the W^+ and W^- event samples differ only from a mirror reflection with respect to the $r-\phi$ plane passing

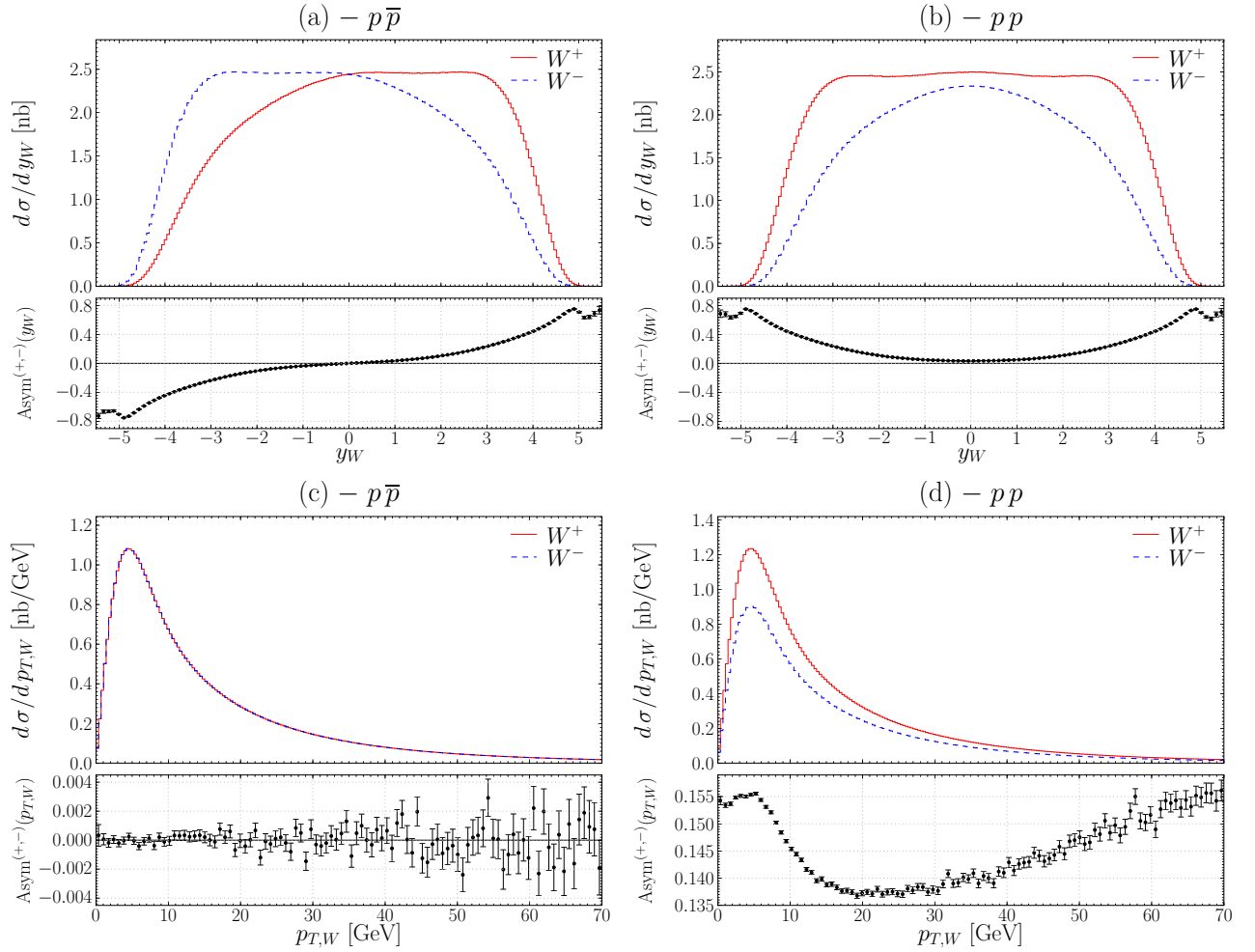


Figure 4.1: The rapidity and transverse momentum distributions of the W bosons with their associated charge asymmetries for $p\bar{p}$ (a, c) and pp (b, d) collisions.

by the origin. More explicitly, to each phase space configuration of amplitude of probability \mathcal{M} for the W^+ boson corresponds another phase space configuration for the W^- in which $\theta_{W^-} = \pi - \theta_{W^+}$ and that has the exact same amplitude. The evidence for this behaviour can be seen already for the W bosons longitudinal component when looking at the rapidity (Fig. 4.1.(a)) where one can see the W^+ and W^- distributions are the same up to a vertical flip with respect to the $y_W = 0$ origin. Concerning the W^+ and W^- transverse momenta the symmetry is such that it makes no differences between the two channels when projecting on the $r - \phi$ plane as shown in Fig. 4.1.(c). From the point of view of a M_W extraction the important thing is that $p_{T,W}$ distributions are independent of the W boson charge which means the leptons, as it will be confirmed, undergo the same boosts.

Now Figures 4.1.(b) and (d) show the corresponding distributions for pp collisions. Here both rapidity distributions are symmetric with respect to $y_W = 0$ which is the consequence of the identical nature of the colliding targets. The shapes of the spectra are different for the W^+ and W^- bosons which reflects the difference in the valence u and d quark content and properties in a proton. The y_W distribution for the W^+ boson is higher and wider with respect to the one for the W^- boson. First let us note there are twice as many valence u quarks as valence d quarks explaining the higher differential cross section for W^+ . Besides, u quarks carry, in average, a higher fraction x of the parent proton momentum (cf. Fig. 1.11), which, assuming y_W respects to a good approximation the LO expression of Eq. (1.60), implies that W^+ are more likely to have a higher absolute values rapidity. This explains the wider behaviour of $d\sigma^+/dy_W$ compared to $d\sigma^-/dy_W$.

The charge asymmetry in the $p_{T,W}$ distribution reflects both the differences in the relative cross sections but also, what will be crucial for the studies presented in this Chapter, in the shape of their distributions. The nontrivial shape of $\text{Asym}^{(+,-)}(p_{T,W})$ is due to the flavour asymmetries in the distributions of quarks producing W^+ and W^- bosons. The latter are predominantly driven by the u – d quark asymmetries. Then the CKM mixing involves the other s , c and b flavours among which –as it will be shown– the non equality of the s and c quark masses add up to the main u – d charge asymmetries. This can be analysed with the flavour structure of the W bosons charge asymmetries by writing explicitly the simplified Born level formulæ of the total cross section charge asymmetries for $p\bar{p}$ and pp collisions

$$(\sigma^+ - \sigma^-)_{p\bar{p}}(S) = 0, \quad (4.1)$$

$$\begin{aligned} (\sigma^+ - \sigma^-)_{pp}(S) \propto \iint dx_q dx_{\bar{q}} \left\{ |V_{ud}|^2 \left[u^{(v)}(x_q) \bar{d}(x_{\bar{q}}) - d^{(v)}(x_q) \bar{u}(x_{\bar{q}}) \right] \right. \\ \left. + u^{(v)}(x_q) \left[|V_{us}|^2 \bar{s}(x_{\bar{q}}) + |V_{ub}|^2 \bar{b}(x_{\bar{q}}) \right] \right. \\ \left. - |V_{cd}|^2 d^{(v)}(x_q) \bar{c}(x_{\bar{q}}) \right\} \tilde{\sigma}_{q\bar{q}}(\hat{s}), \end{aligned} \quad (4.2)$$

where in these expressions d, u, s, c and b on the right hand side denote the PDFs of the corresponding quark flavours and the (v) superscript stands for valence quarks, V_{ij} is the CKM matrix element for the i and j flavours, while $\tilde{\sigma}_{q\bar{q}}(\hat{s})$ is the “CKM matrix element stripped” partonic cross section for the W boson production with $\hat{s} = x_q x_{\bar{q}} S$. Let us stress that the above expressions are over simplified for pedagogical reasons and do not reflect the physics implemented in the WINHAC event generation. We have omitted the explicit dependence of the PDFs on the factorisation scheme, on the transverse momenta k_T of annihilating partons present both in the “ k_T -non integrated” PDFs, and in the partonic cross sections (via k_T dependence of \hat{s}). All the above effects are present in WINHAC. In our analysis partons have both the primordial transverse momenta and the perturbative generated ones as modeled by the initial state parton shower of the PYTHIA generator. Their transverse momenta depend on the Bjorken x of the annihilating (anti-)quark and, for heavy quarks (here c and b), also on their masses (see Ref. [117] for more details).

As one can see in Eq. (4.1), the charge asymmetry disappears for the $p\bar{p}$ collision mode if, as assumed in the presented studies $M_{W^+} = M_{W^-}$. Let us note that this equality holds no matter the level of the corrections embraced in the calculus. Therefore, this collision scheme would be, on a theoretical level, the optimal one for measuring $M_{W^+} - M_{W^-}$. Any deviation from the equality of the masses would result in non zero asymmetries regardless of the level of understanding of the flavour and momentum structure of the beam particles. For pp collisions several effects, reflecting the present understanding of the partonic content of the beam particles –in particular, the understanding of the momentum distribution of valence quarks– contribute to the charge asymmetry of the $p_{T,W}$ distribution and may mimic $M_{W^+} \neq M_{W^-}$ effects.

The asymmetries in pp collisions can be really reduced when going to isoscalar collisions. For example in dd collisions the asymmetries in the quark flavour can be deduced easily from Eq. (4.2) by considering here $u(x) = d(x)$. We obtain then

$$(\sigma^+ - \sigma^-)_{dd}(S) \propto \iint dx_q dx_{\bar{q}} u^{(v)}(x_q) \left[|V_{us}|^2 \bar{s}(x_{\bar{q}}) - |V_{cd}|^2 \bar{c}(x_{\bar{q}}) + |V_{ub}|^2 \bar{b}(x_{\bar{q}}) \right] \tilde{\sigma}_{q\bar{q}}(\hat{s}), \quad (4.3)$$

where here the PDFs have to be understood as the parton distributions functions inside a deuteron contrary to Eqs. (4.1–4.2) where they were the one related to the proton. This was omitted on purpose not to overload the expressions. Here then, the asymmetry is driven by the Cabibbo suppressed difference of the distribution of the strange and charm quarks, weighted by the distributions of the valence quarks. The dd collision scheme is introduced at this point in order to analyse the relative importance of the valence quark and “ $s - c$ ” effects.

In what follows the numerical importance of the various terms appearing in the above equations is studied. For that purpose, to visualise the size coming from certain quarks contributions we reject

all the contributions which we are not interested in (basically weight these events by zero) and in some occasions we modify the predictions of the PDFs by hand using the framework described in Fig. 3.7 of § 3.3.1. The results are presented in Fig. 4.2 by looking each time at $\text{Asym}^{(+,-)}(p_{T,W})$.

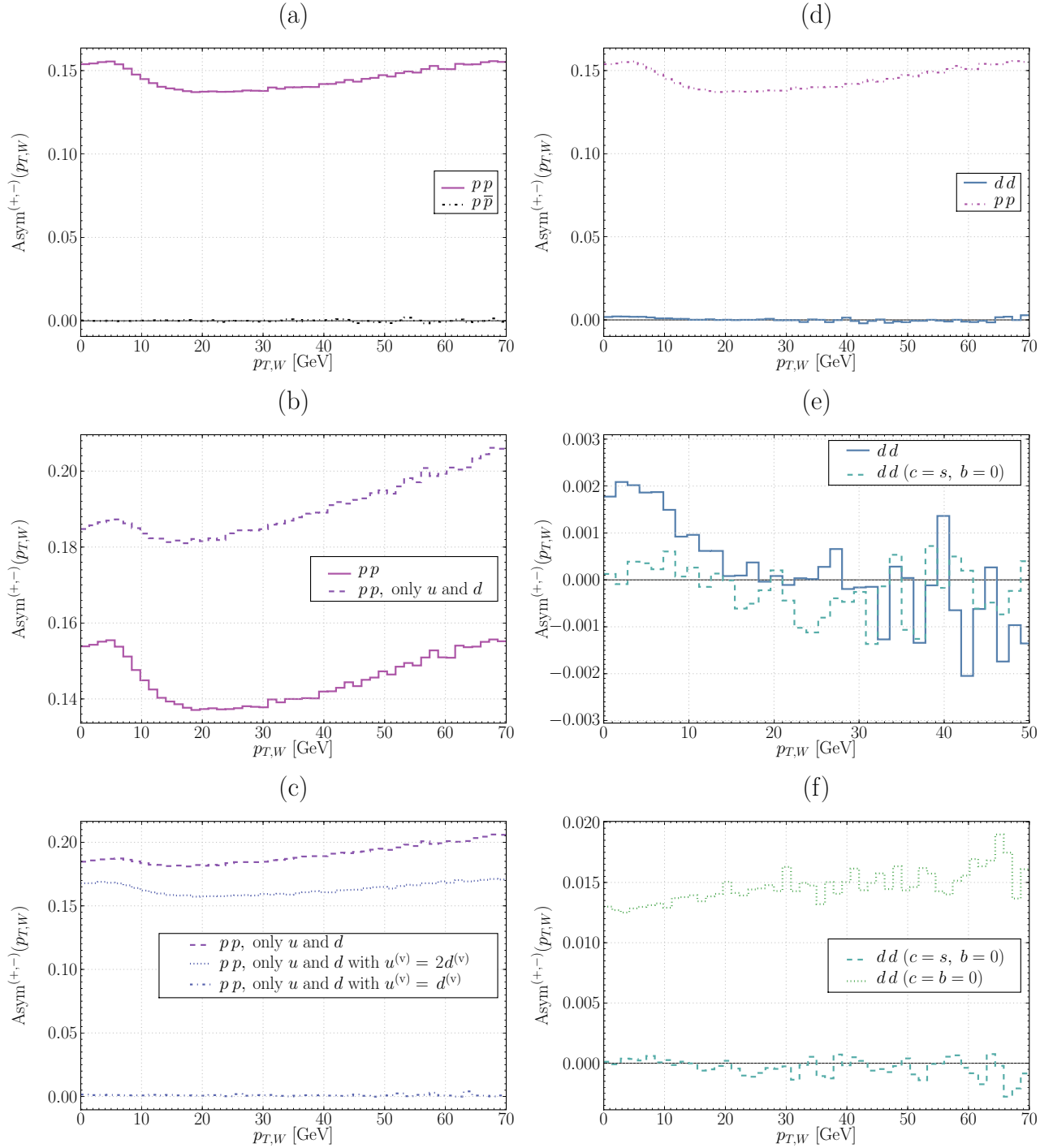


Figure 4.2: The charge asymmetries for $p_{T,W}$: pp vs. $p\bar{p}$ (a), pp vs. pp (u and d quarks only) (b), pp (u and d quarks only) vs. pp (u and d quarks only and $u^{(v)} = 2d^{(v)}$) (c), dd vs. pp (d), dd vs. dd ($c = s$ and no b contributions and with a focus on low $p_{T,W}$) (e), and finally dd ($c = s$ and no b contributions) vs. dd with no c nor b contributions) (f).

The first frame (a) compares pp collisions with the charge asymmetry free $p\bar{p}$ collisions. The charge asymmetry for pp collisions is large and is varying with $p_{T,W}$.

The next frame, (b), shows the comparison of the pp asymmetry from the previous plot with the case where only the “ $u \rightarrow d$ ” contributions ($u\bar{d}$ for W^+ production and $d\bar{u}$ for W^- production) have been kept. The small gap between the two curves, compared to the size of the latter, reflects the small overall influence of s , c and b flavours in the asymmetry compared to the contribution of the u and d quarks.

Frame (c) demonstrates this asymmetry is slightly reduced when in top of having only u and d quarks we have $u^{(v)} = 2d^{(v)}$, *i.e.* when the u and d valence quark PDFs are assumed to have the same shape and differ only by the normalisation factor corresponding to their number in the proton. In addition, let us note that the asymmetry becomes flatter as a function of $p_{T,W}$ indicating the role of the relative x -shape of the u and d quarks PDFs. Finally, the asymmetry is reduced drastically when adding to the previous constraints $u^{(v)} = d^{(v)}$, as it would be the case when colliding isoscalar beams. This shows the consequences of $\bar{u}^{(s)} < \bar{d}^{(s)}$ for $10^{-4} < x$, which was found to be of the order of $\approx 0.05\%$. In the rest of the plots the simplest isoscalar beam collision scheme, dd , is considered.

The frame (d) shows that the charge asymmetry for dd is much smaller than the one for pp with only small discrepancies mainly at low $p_{T,W}$. This results from the two following facts: (1) now all the terms contributing to the charge asymmetry include only off-diagonal CKM matrix elements and (2) contributions of the s , c and b quark PDFs are smaller than the ones coming from sea u and d quark PDFs. Hence this shows how in pp collisions the bulk of the charge asymmetries comes from the term $\propto |V_{ud}|^2$ in Eq. (4.2).

The remaining charge asymmetry is at the level of 0.002 as can be seen in the zoomed frame (e) and it can be reduced to a statistically negligible level when setting $c = s$ and rejecting b quarks contributions. The first constraint, because $|V_{us}|^2 \approx |V_{cd}|^2$, assures to cancel the two first terms in the bracket of the RHS of Eq. (4.3) while the second finalise the rise of any asymmetry.

Finally the frame (f) shows the effect of the deviation of the charge asymmetry due to the difference of the masses and of the momentum distributions of the strange and charm quarks in the extreme case where the c contributions are rejected as well with the collisions involving b . In that case, the obtained asymmetry is significantly higher, at a level of 0.01 – 0.015. It is a factor of ~ 10 bigger than the asymmetry for the dd collisions assuming the present understanding of the relative asymmetry in the distribution of the strange and charm quarks.

In the analysis presented so far the $p_{T,W}$ distribution is inclusive, in other words it has been integrated over the full range of allowed x_q and $x_{\bar{q}}$. In order to optimise the measurement strategy of the W mass charge asymmetry, we now discuss the charge asymmetry $p_{T,W}$ distributions restricted to selected kinematics regions. The most obvious method to reduce the contributions of the valence quarks is to restrict the analysis to the $y_W \sim 0$ region, where $x_q \sim x_{\bar{q}} \approx 6 \times 10^{-3}$, *i.e.* where the valence quarks are largely outnumbered by the sea quarks.

Figure 4.3 presents the asymmetries for pp and dd collisions for the narrow central bins in the W rapidity (a), and in the lepton pseudo-rapidity (b). In the frame (a) the pp charge asymmetry is reduced and flattened by more than a factor of 3 for the range of the W boson rapidity $y_W < 0.3$. Now since y_W cannot be measured directly it is natural to check if a comparable reduction can be obtained using the η_l variable which is correlated with y_W . Unfortunately, this is not the case, as shown in frame (b). The η_l variable has thus significantly lower discriminative power to reduce the valence quark contribution with respect to the y_W variable. For the dd collisions the asymmetry restricted to the narrow η_l bin increases considerably. This observation draws our attention to the fact that the asymmetry in the decay mechanism of the W^+ and W^- bosons will have an important impact on the asymmetry of leptonic observables. This will be discussed in detail in the next section.

Let us conclude by noticing there can also be a contribution to the charge asymmetry coming from the QED radiation from quarks, as upper and lower components of quark doublets have different electric charges. However, it was found with the PYTHIA parton shower model to be of the order of $\text{Asym}^{(+,-)}(p_{T,W}) \approx 2.5 \times 10^{-4}$, which is insignificant compared to the other previous contributions to the asymmetries for pp and dd .

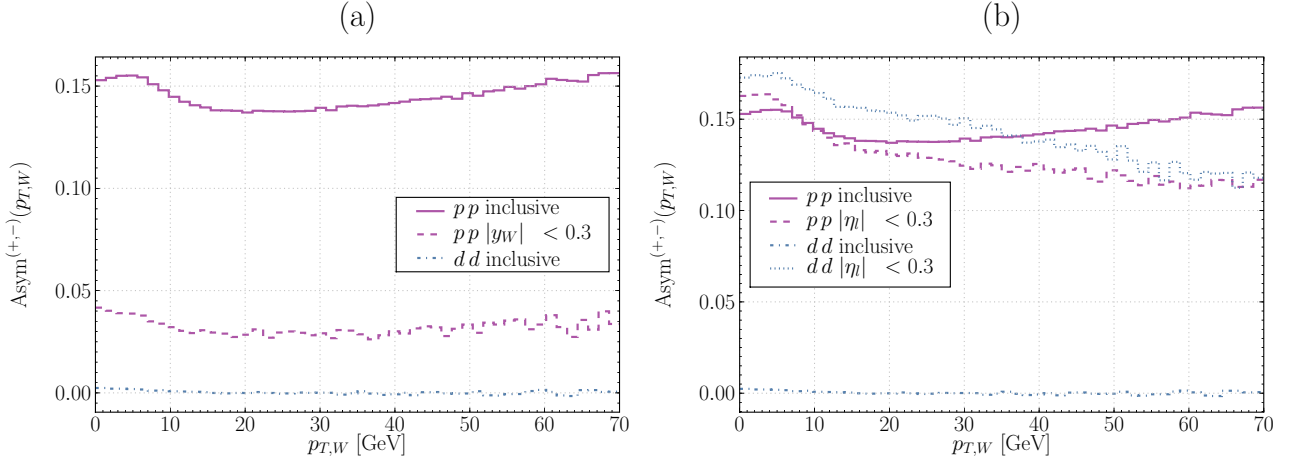


Figure 4.3: The charged asymmetries of $p_{T,W}$ for inclusive pp , dd collisions and with cuts: $|y_W| < 0.3$ for pp (a) and $|\eta| < 0.3$ for pp and dd (b).

4.3 Decays of W^+ and W^- bosons

In this section the W boson decay mechanism and its influence on the charge asymmetries are studied in both $p\bar{p}$ and pp collisions by looking at the charged lepton pseudo-rapidity and transverse momentum spectra.

First, in an overview, we see why in $p\bar{p}$ collisions we continue to observe perfectly symmetric features while in pp collisions we observe larger charge asymmetries than in the initial state due to the decay properties of the leptons. After that, to emphasise the arguments delivered in the previous overview a detailed description of the W^+ and W^- decays in specific regions of y_W -space is presented.

4.3.1 Overview in proton–anti-proton and proton–proton collisions

Figure 4.4 presents the charged lepton η and $p_{T,l}$ distributions along with their associated charge asymmetries. Let us start by noticing that when studying the pattern of the η spectra the influence of $p_{T,W}$ can be neglected in the discussion since $p_{T,W} \ll |\vec{p}_{z,W}|$. More qualitatively, the improved LO affects the LO differential η cross sections only to $\sim 4\%$ maximum, thus –just in those cases– we can consider $\vec{p}_{z,W} \sim \vec{p}_W$.

Proton–anti-proton collisions. Starting with $p\bar{p}$ collisions one can see the η distributions (Fig. 4.4.(a)) are each other mirror reflection with respect to $\eta = 0$ this being a consequence of the symmetry of the problem as discussed in the previous section. Here it simply translates into that the whole l^+ event generation is exactly the same than the one of the l^- up to the transformation $\theta_{l^-} = \pi - \theta_{l^+}$.

Once again this symmetry implies that projecting the charged leptons momenta on the $r - \phi$ plane gives identical $p_{T,l}$ distributions for positive and negative charges which is shown in Fig. 4.4.(c).

Proton–proton collisions. For pp collisions, on the other hand, at first sight the positively and negatively charged leptons display highly non symmetric behaviour between each other. The pseudo-rapidity distributions indicates that l^+ leptons decay preferentially in the opposite direction of \vec{p}_W while l^- leptons display the inverse behaviour (Fig. 4.4.(b)). The size of the charge asymmetry in $p_{T,l}$ is much larger than the one in $p_{T,W}$ and further investigations proved it is explained by the privileged decay of l^+ leptons in the direction of $\vec{p}_{T,W}$ while l^- leptons decay in most cases in the opposite direction of $\vec{p}_{T,W}$ (Fig. 4.4.(d)). The reason for these two behaviours in η and $p_{T,l}$ finds its fundamental origin in the $V - A$ coupling of the leptons to the W bosons. Indeed, as seen in Chapter 1,

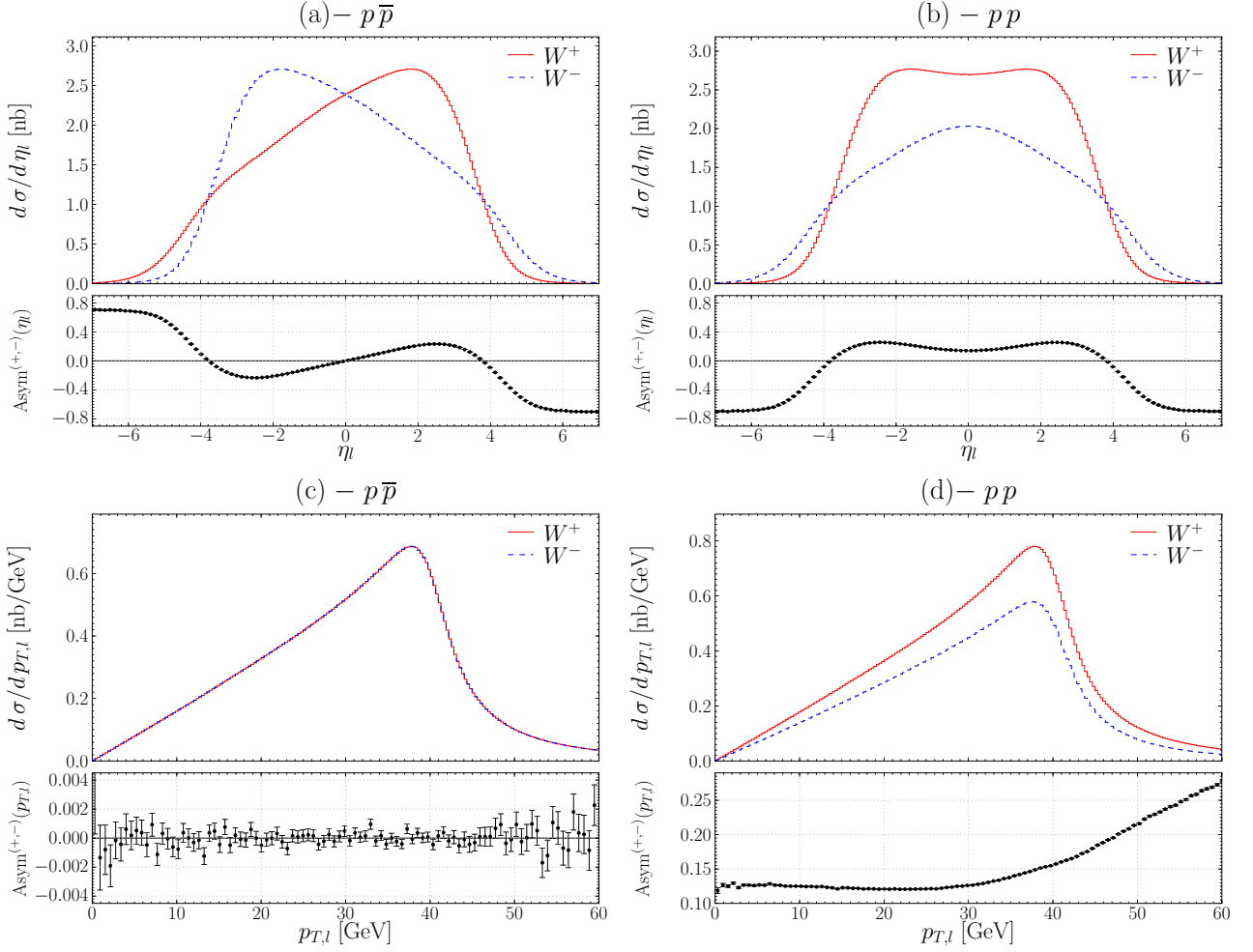


Figure 4.4: The pseudo-rapidity η_l and transverse momentum $p_{T,l}$ distributions for charged leptons produced in W boson decays for the $p\bar{p}$ (a,b) and pp (c,d) collisions.

at the level of the differential partonic cross section the angular distribution in the WRF of the final state charged lepton decaying from a W boson of a given polarisation state can be expressed

$$d\hat{\sigma}^{W_T^Q}/d\cos\theta_{W,l}^* \propto (1 + \lambda Q \cos\theta_{W,l}^*)^2, \quad (4.4)$$

$$d\hat{\sigma}^{W_L^Q}/d\cos\theta_{W,l}^* \propto \sin^2\theta_{W,l}^*, \quad (4.5)$$

where, for reminders, $\theta_{W,l}^*$ is the charged lepton polar angle with respect to the direction of the W momentum \vec{p}_W in the laboratory frame (Eq. (1.30)), Q is the W boson electric charge in units of $|e|$ and $\lambda = 0, \pm 1$ is the W boson helicity. As can be seen, the angular distributions of l^+ and l^- for longitudinally polarised W bosons (W_L for $\lambda = 0$) are the same while for the transversely polarised W bosons (W_T for $\lambda = \pm 1$), they depend upon the W boson helicity. To simplify the rest of the argumentation we will not consider the decay of longitudinally polarised W . This leaves us with transversely polarised W bosons which, due to the excess of matter from valence quarks¹ in LHC collisions, are produced in larger proportions with negative helicities, *i.e.* $W(\lambda = +1) < W(\lambda = -1)$.

The consequences of this excess of $W(\lambda = -1)$ accounts for the behaviour of the pseudo-rapidity distributions illustrated in Fig. 4.5 in both WRF and laboratory frame (LAB): l^- access larger pseudo-rapidity than the l^+ . Note this behaviour is already observed at leading order where $p_{T,W} = 0$

¹From another point of view the charge asymmetries can be seen as the consequence of a lack of anti-matter (valence anti-quarks) that cannot match this excess of matter from valence quarks.

and is only slightly affected by $p_{T,W}$ in the improved LO. The features observed in the longitudinal direction being understood we now turn our attention to the asymmetric pattern present in the transverse direction.

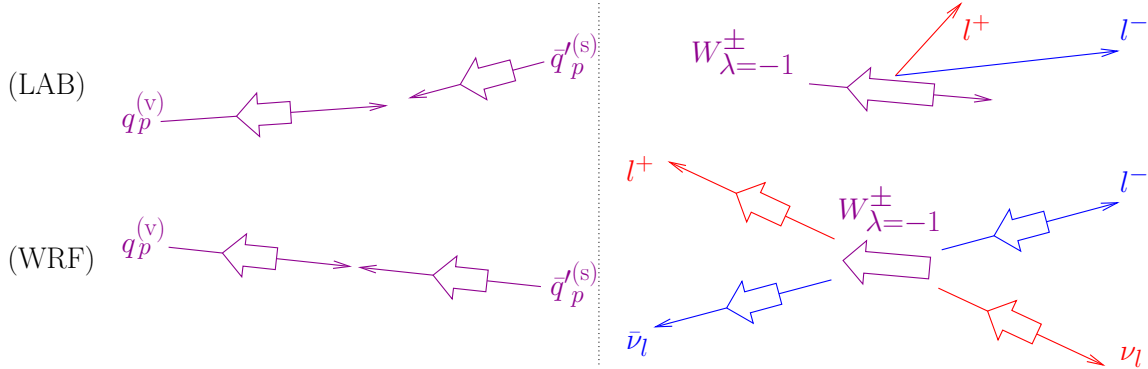


Figure 4.5: Valence quark and sea anti-quark annihilation producing a negative helicity state for the W . The collision is represented in both the laboratory frame (up) and in the W RF (down) and for both initial (left) and intermediate/final state (right).

Schematic representation of the privileged angular decay of the charged lepton within the W rest frame

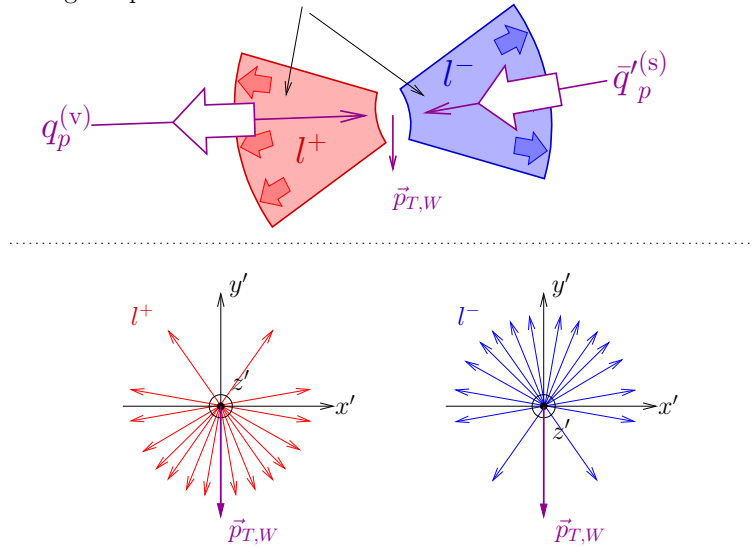


Figure 4.6: Schematic representation of a valence quark and sea anti-quark annihilation seen in the laboratory frame but, for convenience, with the charged leptons decays represented in the W RF (up). Below, in the W RF, the consequent azimuthal anisotropy with respect to the $\vec{p}_{T,W}$ direction is represented for the decay of the charged leptons (down).

As explained above a deeper investigation shows the l^+ leptons decay preferentially in the direction of $\vec{p}_{T,W}$ while the l^- lepton display the inverse behaviour. This effect is the result of the $V - A$ coupling properties folded to the transverse motion of the W or, more precisely, the relative size of the valence and sea (anti-)quarks in the collision. Indeed, in a collision involving a valence quark the sea anti-quark carries in general a higher transverse motion (cf. § 4.A.6) which, as can be understood using kinematic momentum conservation rules of thumb, constrains the charged lepton to privilege a certain azimuthal direction depending on the helicity it is holding. Figure 4.6 illustrates these effects, since the l^+ leptons have a positive helicity, aligning it on the one of the sea quarks constrains it to decay in the same direction of the $\bar{q}'^{(s)}$ anti-quark and by extension, since the latter carries most of the transverse motion, with the one of $\vec{p}_{T,W}$. On the other hand negative helicity l^- leptons, under

the same kinematics, are constrained to prefer a decay in the opposite direction of the $\bar{q}^{(s)}$ anti-quark/ $\vec{p}_{T,W}$. Eventually it turns out the l^+ leptons intrinsic transverse momentum are amplified by $p_{T,W}$ while in the case of the l^- leptons they are reduced by $p_{T,W}$. Let us emphasise that even though this effect is ignited by the $V - A$ coupling attribute its amplitude depends of the relative unbalance in the transverse motion of the colliding valence quark and sea anti-quark, which is governed by the colliding energy \sqrt{S} in the center of mass. Also worth noticing is that even at the leading order there are already charge asymmetries in the $p_{T,l}$ spectra, still, due to their smaller size with respect to the one discussed above, their study is treated in § 4.A.4.

In the rest of this section the previous distributions are reviewed for two narrow absolute rapidity regions, respectively in a central domain ($|y_W| < 0.3$) and in a forward domain ($3.5 < |y_W| < 4.5$). In the central region, the W bosons are produced from quark–anti-quark pairs having $x_q \sim x_{\bar{q}} \approx 6 \times 10^{-3}$ leading to small valence quarks contributions, and as a consequence, the assumed isospin symmetry in sea quarks flavours cannot produce charge asymmetries. On the other hand, in the forward region the production of W bosons involve most of the time a valence (anti-)quark in $p\bar{p}$ collisions and a valence quark in pp collisions.

4.3.2 Proton–anti-protons collisions

The explanations in this subsection can be followed looking at Fig. 4.7 showing the η , $p_{T,l}$ and $\text{Asym}^{(+,-)}(p_{T,l})$ distributions in $|y_W| < 0.3$ and $3.5 < |y_W| < 4.5$ rapidity regions.

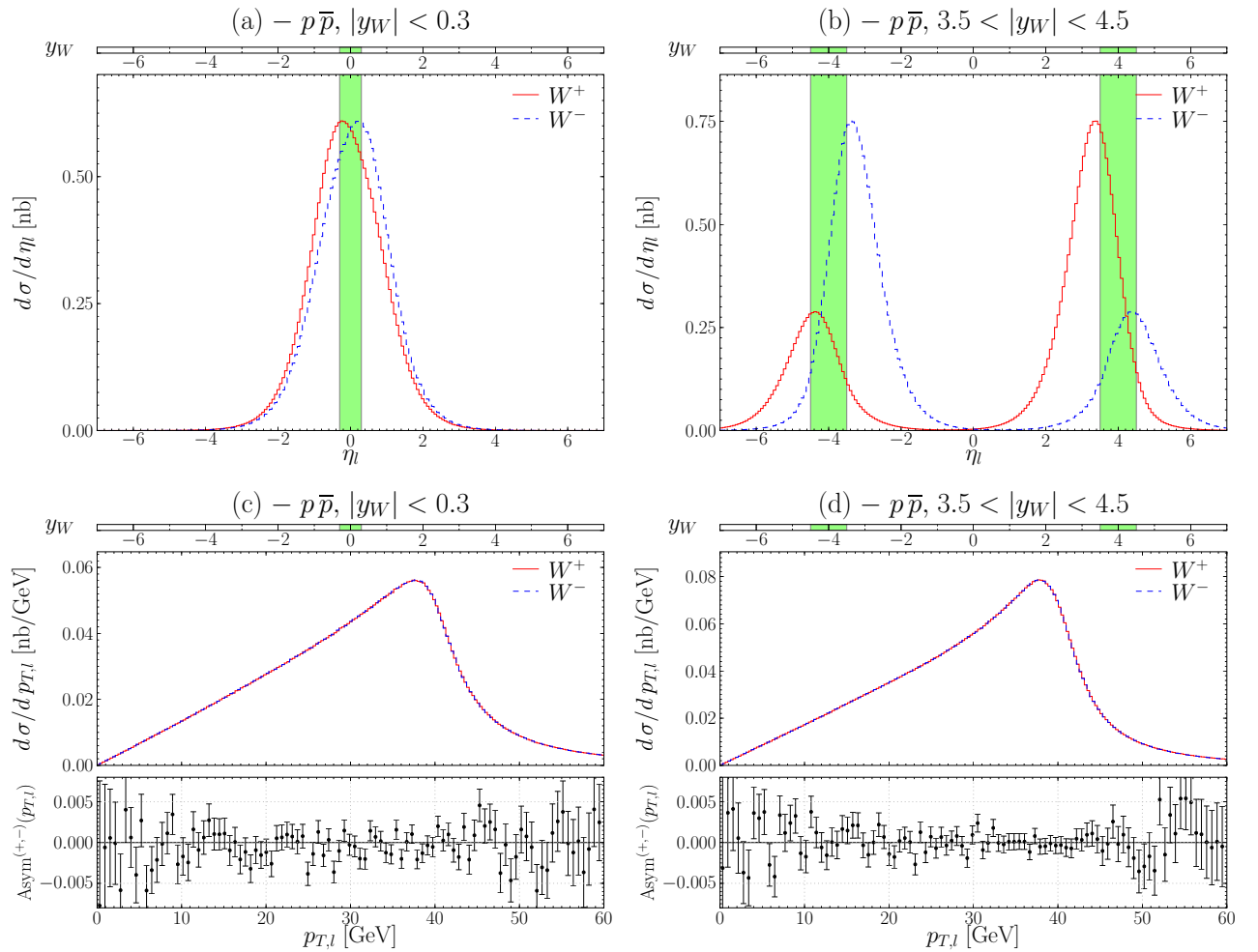


Figure 4.7: Positively and negatively charged lepton pseudo-rapidity distributions for $p\bar{p}$ collisions in two different ranges of the W rapidity: $|y_W| < 0.3$ (a,c) and $3.5 < |y_W| < 4.5$ (b,d).

W^+ and W^- pseudo-rapidity distributions. In the narrow central rapidity region as it has been established valence (anti-)quark contributions are rather small, then l^+ and l^- leptons display in a first approximation the same behaviour. The discrepancies come from the small influence of valence (anti-)quarks.

In the forward rapidity region the valence (anti-)quarks influence creates large local asymmetries in both η_{l^+} and η_{l^-} distributions. Those behaviours can be understood looking at the pseudo-rapidity. Using the LO approximation from Eq. (1.70) gives

$$\eta_{l^+} \approx y_W + y_{l^+}^*, \quad (4.6)$$

$$\eta_{l^-} \approx y_W + y_{l^-}^*, \quad (4.7)$$

where $y_{l^+}^*$ and $y_{l^-}^*$ are respectively the intrinsic rapidity of the positively and negatively charged leptons. The rapidity of the W is much larger than the intrinsic $y_{l^\pm}^*$ (cf. §1.4.2), also the pattern of the distributions in Fig. 4.7.(b) can be seen as the consequence of: (1) the high longitudinal $p_{z,W} (\Leftrightarrow y_W)$ component of the boost that fixes roughly the center of the η_l spectrum at $\eta_l \approx y_W$ and (2) the polar decay of the lepton –ruled by the $V - A$ coupling– which smears the η_l distribution from the central “ y_W -induced” value. Let us look at the case of the lepton l^+ . In the region $3.5 < y_W < 4.5$, W^+ bosons are produced mainly via $u_p^{(v)} \bar{d}_p^{(s)}$ pair collision, where for reminder (v) stands for valence and (s) for sea. In other words we have mostly $W^+(\lambda = -1)$ which, combined to the $V - A$ coupling constrain the decaying l^+ to be preferentially emitted in the opposite direction to \vec{p}_{W^+} . This can be seen as most of the η_{l^+} distribution tends to shift to lower values of η_l . On the other side, where $-4.5 < y_W < -3.5$, bosons are produced mainly via $u_p^{(s)} \bar{d}_p^{(v)}$ annihilation which gives $W^+(\lambda = +1)$. Here the decaying l^+ lepton prefers to be emitted following the \vec{p}_{W^+} direction. Let us note the difference of height between two opposite η_l bumps comes from the fact that $\bar{d}_p^{(v)} < u_p^{(v)}$. The same ideas can be applied to the case of the l^- lepton decay, this time the opposite behaviour is observed with the exact same proportions

W^+ and W^- transverse momenta distributions. The forward rapidity region is exclusively addressed as we know the issues related to the valence contributions are more important there. In the WRF, the spectrum of the relative angle between the l^+ and the W^+ in $3.5 < y_W < 4.5$ is exactly the same than the one between the l^- and the W^- in $-4.5 < y_W < -3.5$ as shown in Fig. 4.7.(b). This is true independently of the relative unbalance in the colliding quark–anti-quark p_T , thus the W boost are identical and give eventually the same kinematics –up to a vertical flip– for the l^+ and l^- from these opposite y_W -space domains. The same idea can be used to account for the equality of the p_{T,l^+} distribution in $-4.5 < y_W < -3.5$ with the p_{T,l^-} distribution in $3.5 < y_W < 4.5$. Then, as long the rapidity selection is achieved on the absolute value $|y_W|$ the positive and negative leptons transverse momenta show no asymmetries as displayed in Fig. 4.7.(d). This property is obviously conserved when integrating over the whole phase space.

4.3.3 Proton–proton collisions

Considering now the case of pp collisions we repeat the same path of reasoning followed for the $p\bar{p}$ case. The η_l and $p_{T,l}$ distributions in pp collisions for the narrow central and forward W rapidity regions are shown in Fig. 4.8.

Pseudo-rapidity distributions. Once again going to $|y_W| < 0.3$ allows to get rid of most of the valence quarks which, as it was found out in the overview is the source of the asymmetries in pp collisions (Fig. 4.8.(a)). The small discrepancies are due to non negligible contributions from valence quarks.

Now moving to the $3.5 < |y_W| < 4.5$ region (Fig. 4.8.(b)) the general pattern can be understood using Eqs. (4.6–4.7). Both η_{l^+} and η_{l^-} distributions are found in the vicinity of $|\eta_l| \approx |y_W|$ and the

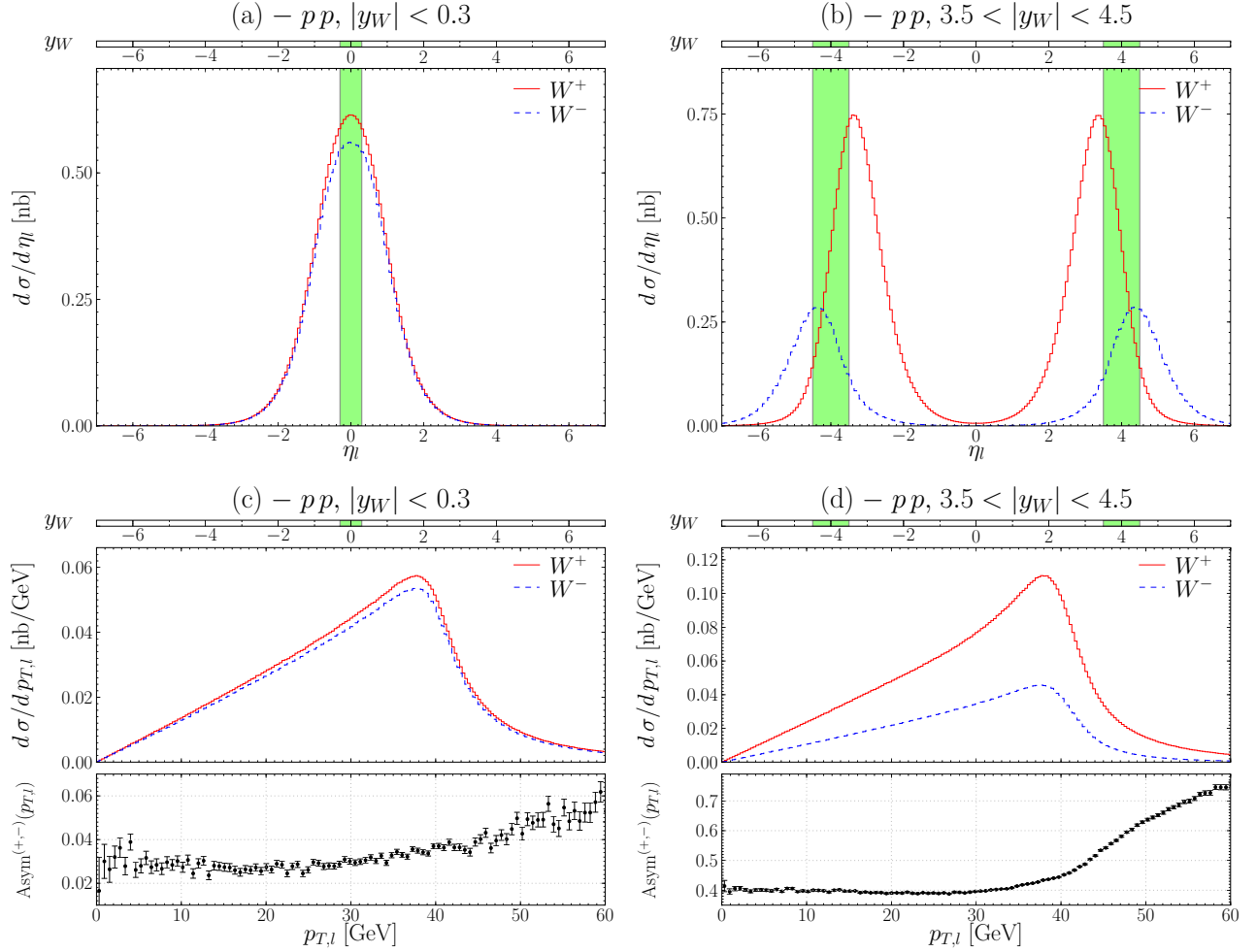


Figure 4.8: Positively and negatively charged lepton pseudo-rapidity/transverse momenta distributions for ranges of the W rapidity: $|y_W| < 0.3$ (a,c) and $3.5 < |y_W| < 4.5$ (b,d).

deviations from this central value are due to lepton decay in θ ruled by the $V - A$ coupling, *i.e.* only positive helicity l^+ and negative helicity l^- can couple to W bosons.

We start by analysing the positively charge lepton l^+ . Here, in both positive ($3.5 < y_W < 4.5$) and negative ($-4.5 < y_W < -3.5$) rapidity domains the W^+ are produced most likely from a $u_p^{(v)} \bar{d}_p^{(s)}$ annihilation providing to the boson a negative helicity. Then the l^+ preferentially decay in the opposite direction of \vec{p}_W . This explains why the η_{l^+} spectrum is slightly shifted to smaller absolute η_l values. The same idea can be applied to the other charged lepton. One finds eventually that this time the l^- decays in most cases in the same direction of \vec{p}_W which translates here that the η_{l^-} spectrum is slightly shifted to higher absolute values of η_l . This explains why we observed in Fig. 4.4.(b) a widening of the l^- pseudo-rapidity distribution from y_{W^-} while the l^+ pseudo-rapidity tends to narrow from the inner y_{W^+} spectrum. The relative size of the peaks is explained to the light that, as said previously, in a proton there are more $u^{(v)}$ than $d^{(v)}$.

Let us stress that the differences between the y_W -bands width and the associated spread η_l distributions demonstrates that η_l has a significantly weaker resolution power for the momenta of annihilating quarks than y_W , and, as a consequence, weaker resolving power of the W boson polarisation. This gives already an idea of the loss of information one has to accept when trading the knowledge of the W rapidity with the charged lepton pseudo-rapidity.

Transverse momenta distributions in forward rapidity region. The behaviour of the charged lepton transverse momenta are discussed exclusively in the forward rapidity region (Fig. 4.8.(d)). For $3.5 < y_W < 4.5$, in the WRF the relative angle between the l^+ and the W^+ is different from the one of l^- and the W^- due to the larger value of the sea quark transverse momentum with respect to the one of the valence quark. The $V - A$ coupling as shown in Fig. 4.6, by forcing the l^+ and l^- to decay in opposite direction induce the l^+ to follow the transverse motion held mostly by the sea quark while the l^- decays in the opposite direction of the latter. Taking into consideration the negative rapidity stripe concurs to roughly double the size of the asymmetry. The consequences of this effect on the pattern of the transverse momenta of the l^+ and l^- has dramatic effects.

Figure 4.9 quantifies this important aspect at the inclusive level by displaying the $\phi_{W,l}^*$ spectra which is defined as the azimuthal angle of the charged lepton in the WRF with respect to the direction of the transverse momentum of the W boson in the laboratory frame, that is

$$\phi_{W,l}^* \equiv \cos^{-1} \left(\frac{\vec{p}_{T,W} \cdot \vec{p}_{T,l}^*}{|\vec{p}_{T,W}| |\vec{p}_{T,l}^*|} \right). \quad (4.8)$$

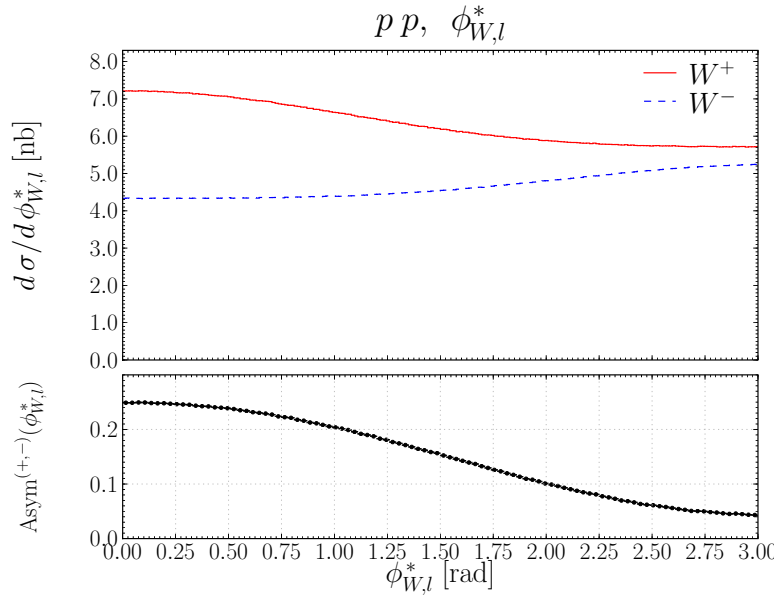


Figure 4.9: Distributions of $\phi_{W,l}^*$ in pp collisions showing the azimuthal anisotropy in the charged leptons decays.

In conclusion the absence of valence anti-quarks makes the production of W^+ and W^- at the LHC irretrievably different. The increase of the transverse momenta of the W bosons produced at high absolute rapidity amplifies the impact of the W boson polarisation asymmetry on the charge asymmetry of its decay products. These effects will give rise to important measurement biases which were not present in the $p\bar{p}$ collision mode but will show up in the measurement of the W boson properties in the LHC pp collision mode.

In order to illustrate a little bit more the charge asymmetry in $p_{T,l}$ Figure 4.10.(a) shows the imperfect match between the $d\sigma^+/d p_{T,l}$ and $d\sigma^-/d p_{T,l}$ histograms when normalised to unit. This demonstrates that the difference of scale being removed the discrepancies are important enough to be noticed by the eye. Especially frame (b) shows a zoom on the jacobian peak which shape is of crucial importance for the extraction of the W boson mass. In particular we can distinguish a particular feature, that is at the LHC energies we are to expect :

$$\langle p_{T,l^-} \rangle < \langle p_{T,l^+} \rangle, \quad (4.9)$$

where $\langle p_{T,l} \rangle$ is the average p_T of the charged lepton l . To be more precise, using the WINHAC Monte Carlo event generator for a statistic of 100,000 inclusive events we find

$$\langle p_{T,l^+} \rangle \approx 40.17 \text{ GeV}, \quad (4.10)$$

$$\langle p_{T,l^-} \rangle \approx 39.98 \text{ GeV}. \quad (4.11)$$

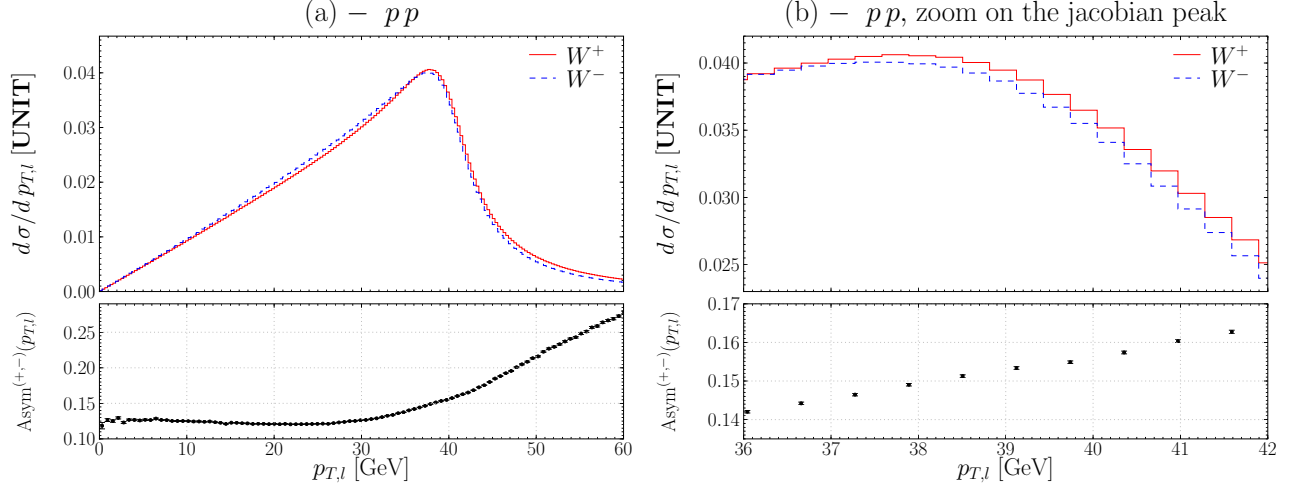


Figure 4.10: Positive and negatively charged leptons transverse momenta distributions normalised to unit, for the whole range in (a) and for a zoom on the jacobian peak (b). Note the charge asymmetries are obtained from histograms normalised to nb.

4.3.4 More details on the leptons transverse momenta charge asymmetry in pp collisions

To analyse a little bit more the relative position of the jacobian peaks between the two channels, $p_{T,l}$ distributions were studied for narrow central and forward y_W and η_l , respectively $|y_W|, |\eta_l| < 0.3$ and $3.5 < |y_W|, |\eta_l| < 4.5$ selections as shown in Fig. 4.11. The selection in η_l being justified to show how the ambiguity becomes large when making a selection with the latter. This gives complements on the low x -selection resolution one have to deal when relying on η_l rather than y_W . To quantify the impact on the jacobian peak position we applied an empirical procedure consisting into fitting p_{T,l^+} and p_{T,l^-} spectra by a polynomial of second order in the vicinity of the peak. This range was taken to be $37 \text{ GeV} < p_{T,l} < 40 \text{ GeV}$. The $p_{T,l}$ value corresponding to the two parabolas are noted ϖ_+ for p_{T,l^+} and ϖ_- for the one of p_{T,l^-} . The difference between these two position $\varpi_+ - \varpi_-$ is considered to quantify the variation of the peaks position. The results are gathered in the table below

phase space domain	$\varpi_+ - \varpi_-$ [MeV]
Inclusive	170
$ y_W < 0.3$	-100
$ \eta_l < 0.3$	-240
$3.5 < y_W < 4.5$	300
$3.5 < \eta_l < 4.5$	2000

As can be seen the difference are varying a lot depending on the cut compared to the “reference” from the inclusive case. Nonetheless let us remind those results correspond only to purely empirical attempt to quantify the $p_{T,l}$ shapes relative variations observed in Fig. 4.11.

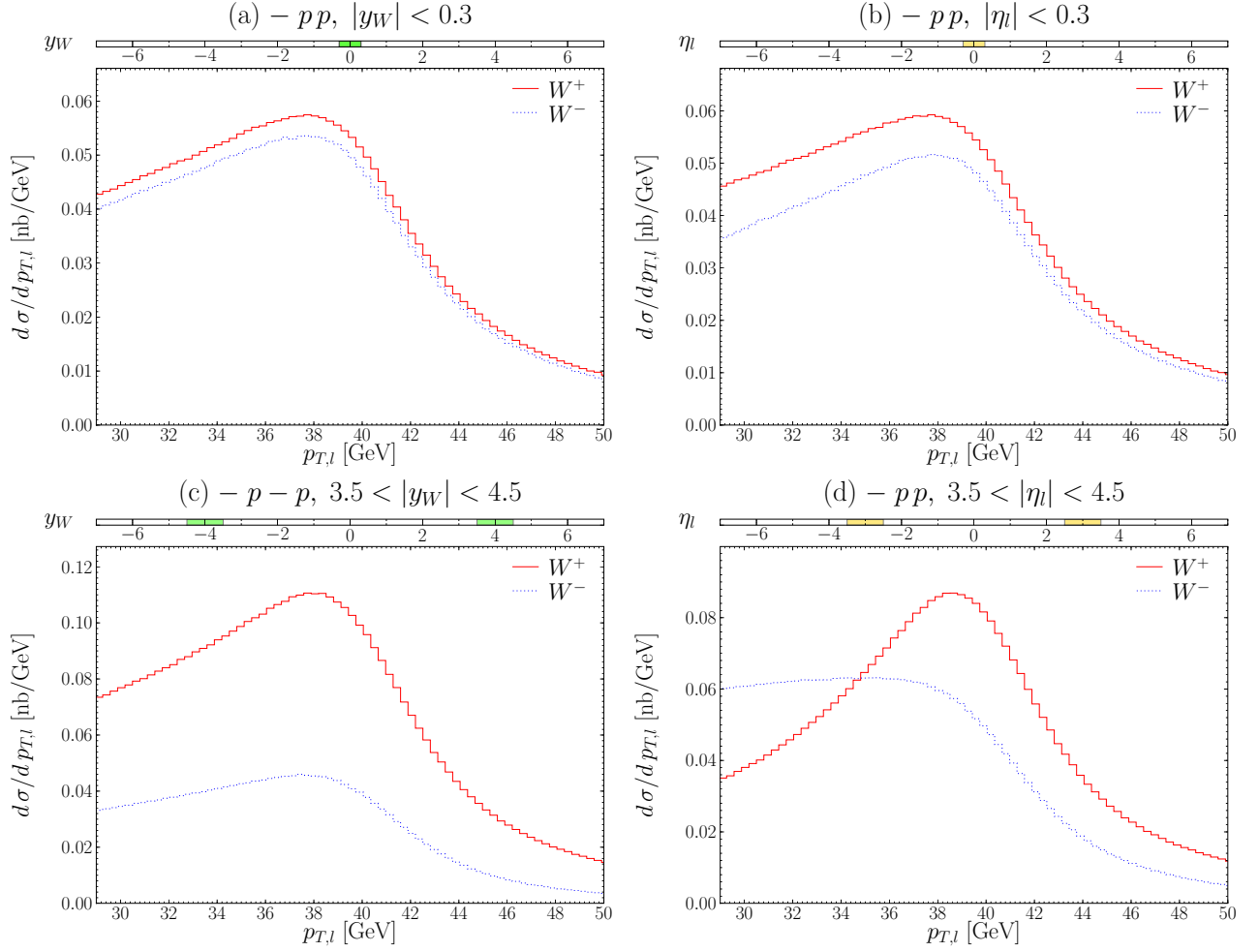


Figure 4.11: Charged lepton transverse momenta for central (a) and forward (b) region of y_W selection.

4.3.5 Summary on the sources of charge asymmetries in proton–proton collisions

To summarise, at the LHC, the difference between the positive and negative kinematics of the charged leptons result from the interplay of the three following effects :

- (1) the $V - A$ coupling of the W boson to fermions in electroweak interactions, *i.e.* only positive helicity l^+ and negative helicity l^- couples to the W bosons,
- (2) the absence of valence anti-quarks to perfectly match via CP the charge asymmetries induced by the valence quarks,
- (3) the non-zero transverse momentum of the W boson or, more precisely, the fact that in a $q^{(v)} \bar{q}^{(s)}$ collision the sea quarks carries most of the time the higher transverse motion with respect to the valence quark.

These asymmetries will depend strongly on the choice of the kinematic region used in the analysis. If expressed in terms of leptonic variables, the differences are amplified due to induced biases in the effective x -regions of partons producing positively and negatively charged W bosons. As these differences could mimic the asymmetry in the masses of positively and negatively charged W boson, all these effects must be controlled to a high precision and/or, as advocated in our work, eliminated by using LHC dedicated measurement strategy.

Finally let us remind the reader the above presentation is addressing only the essential points to understand the original LHC features. The Appendix that follows takes back from the beginning this presentation in a more pedestrian manner and provide much more details to understand thoroughly all effects participating to this charge asymmetries.

4.A Detailed description of W in Drell–Yan for $p\bar{p}$, pp and dd collisions

Mister Fantastic: “This device apparently caused sub-atomic particle dissociation, reducing us, as we entered, to proto-matter, which it stored until it teleported us here, to pre-set coordinates in space where it reassembled us inside a self generated life-support environment !”

The Hulk: “That’s obvious Richards !”

Iron Man: “Obvious ? What’d he say ?”

The Torch: “Just hang out Iron man ! Reed will get tired of talking in five dollar words in a minute, and then he’ll explain in English ! Then he’ll explain it again to the Thing in one-syllable words !”

The Thing: “Hey Torch– why don’tcha just shut up and look awestruck like the rest of us ?”

Marvel Superheroes Secret Wars #1 - The War begins (May 1984)

This Appendix presents with more details the studies carried out to understand thoroughly the asymmetries between the W^+ and W^- production in Drell–Yan for $p\bar{p}$, pp and dd collisions. To reach this goal a few observables related to the W boson and the charged leptons were considered, each allowing to comprehend both dynamic and kinematic issues from different point of views. Although some histograms below were not addressed in the core of the Chapter it has to be realised that the material presented here is the bulk of the work achieved which allowed to present previously the gist of W physics features in Drell–Yan at the LHC.

4.A.1 Observables and context of the discussion

The study the W boson properties is made looking at its invariant mass m_W defined like

$$m_W \equiv \sqrt{E_W^2 - \vec{p}_W^2}, \quad (4.12)$$

its rapidity y_W and its transverse momentum $p_{T,W}$.

The study of the charged lepton properties are made by analysing its pseudo-rapidity η_l and its transverse momentum $p_{T,l}$. The study of the charged lepton angular decay in the WRF relatively to the W motion is quantified with the angle $\theta_{W,l}^*$ defined as the opening angle between the charged lepton in the WRF and the direction of the W boson in the laboratory frame, which analytically reads

$$\cos \theta_{W,l}^* \equiv \frac{\vec{p}_W \cdot \vec{p}_l^*}{|\vec{p}_W| |\vec{p}_l^*|}. \quad (4.13)$$

Due to the importance of the transverse direction for the extraction of the W properties we consider as well the angle $\phi_{W,l}^*$ corresponding to the opening angle of the charged lepton transverse momentum in the WRF with the direction of the W transverse momentum in the laboratory frame, which analytically translates to

$$\phi_{W,l}^* \equiv \cos^{-1} \left(\frac{\vec{p}_{T,W} \cdot \vec{p}_{T,l}^*}{|\vec{p}_{T,W}| |\vec{p}_{T,l}^*|} \right). \quad (4.14)$$

Some of the previous variables are studied in bins of y_W and η_l to emphasise the variation of the charge asymmetries in function of the phase space region considered. Not to overload the discussion all those observables will not be discussed for each case but rather the most important one to draw relevant conclusions.

These variables being reminded we state a few conventions adopted throughout the rest of the Appendix. First, let us remind the notation W indifferently stands for W^+ or W^- and that respectively l stands for l^+ or l^- .

Now, for convenience, the production of W bosons is considered to be the addition of two type of contributions: (1) the contributions involving at least one valence (anti-)quark and (2) the contributions involving only sea quarks. Due to the isospin symmetry $q^{(s)} = \bar{q}^{(s)}$ assumed in our model (CTEQ6.1M) the observed charged asymmetries are, as we will see, to be charged to the contributions of type (1). In top of that, for argumentation, we will always consider regions of the phase space where these valence (anti-)quarks asymmetries contribute the most, *i.e.* we will always implicitly assume in our examples the most probable cases where the valence (anti-)quark has a more larger longitudinal momentum than the one of the sea (anti-)quark it enters in collisions with: $x_{q,\bar{q}}^{(v)} > x_{q,\bar{q}}^{(s)}$. In the case of protons–anti-protons collisions valence quark and valence anti-quarks collisions happen too but they can be neglected in the discussion. Indeed, at $\sqrt{S} = 14$ TeV, if one of the valence (anti-)quark possesses a high fraction of the longitudinal momentum of the hadron (\bar{p}) it belongs to, say $10^{-1} \lesssim x_1$, then the other valence (anti-)quark in the collision must carry, due to the rough constrain $x_1 x_2 S \sim M_W^2$, a fraction of momentum verifying $x_2 \lesssim 4 \times 10^{-4}$. As Figure 1.11 shows it, finding a valence (anti-)quark at such low x is negligible. Hence, in $p\bar{p}$ or LHC collisions, when addressing issues centered on valence (anti-)quark, we will always discuss valence–sea collisions that hereafter will be mentioned as “valence” collisions/contributions.

Another important aspect in the upcoming discussion consists to address the decaying angle of the charged leptons with respect to the W motion. For that matter the emphasis will be given to the transverse polarisation states of the W which gives different decaying angle between the positively and negatively charged lepton as seen in Eq. (4.4). For the longitudinal W bosons (Eq. (4.5)) the decays of the leptons are charge independent, hence the charge discrepancies that can be observed are only due to the difference between the kinematics of the W^+ and the W^- specific to the collision mode under consideration. These charge asymmetries are of lesser importance compared to the one consequent to the decay of transversely polarised W bosons and will maybe studied in future works.

Also let us stress that some of the plots and explanations below are already present in the core of the Chapter but, for convenience, they were reviewed to make this Appendix fully understandable and complete by itself.

In what follows the description of hadron–hadron collisions are considered for the cases of:

- Hadron–hadron collisions with no valence quark inside the hadrons with $\sqrt{S} = 14$ TeV.
- $p\bar{p}$ collisions with $\sqrt{S} = 14$ TeV.
- pp collisions with $\sqrt{S} = 14$ TeV.
- dd collisions with $\sqrt{S} = 7$ TeV.

where each time \sqrt{S} refers to the energy in the nucleon–nucleon center of mass inertia frame. After those points a discussion on the relative transverse motion of the quarks and anti-quark is provided.

4.A.2 A study of the purely sea contributions

We start this discussion by looking at the fictitious case where there is no valence (anti-)quarks in the hadrons entering in collision. This illustrates that in the assumed isospin symmetry there are absolutely no charge asymmetries. For that matter we remove manually the valence terms from the CTEQ6.1M previsions and run pp collisions which, in the present context, is equivalent to the $p\bar{p}$ mode, explaining the $p\bar{p}^{(-)}$ notation afterward. We obtain for the observables y_W , $p_{T,W}$, η_l and $p_{T,l}$ the histograms shown in Fig. 4.12.

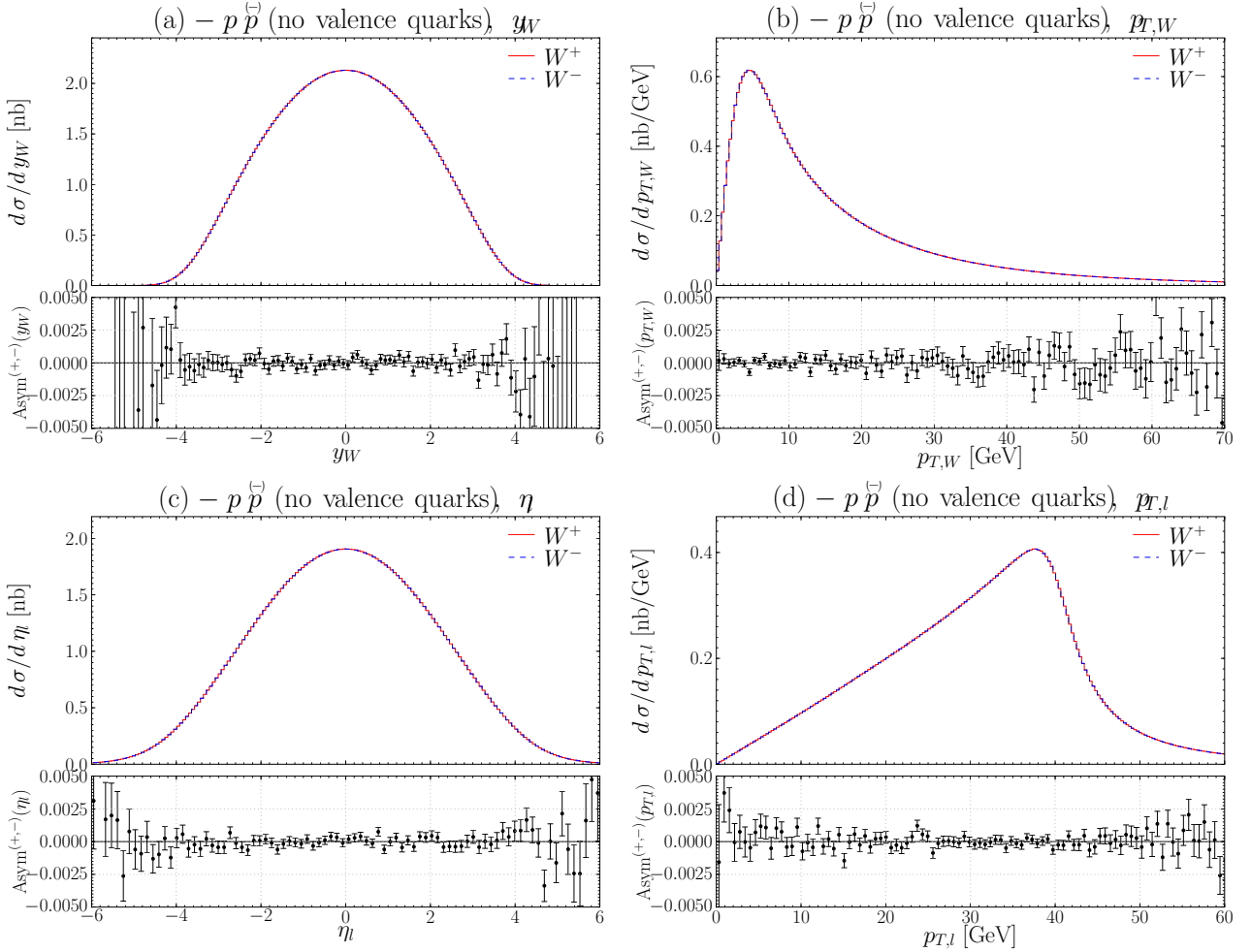


Figure 4.12: Distributions of the W boson rapidity (a) and transverse momentum (b) along with the one of the charged lepton pseudo-rapidity (c) and transverse momentum (d) in $pp(p\bar{p})$ collisions when all valence contributions are removed.

Here let us emphasise the charge symmetry is perfect, by that we mean that in a given point $d\Phi$ of the phase space the associated infinitesimal cross sections $d\sigma^+/d\Phi$ and $d\sigma^-/d\Phi$ are exactly equal. This allows us to get rid in the rest of the discussion.

Nonetheless, let us mention that the difference in the PDFs distributions induce an asymmetry between the left and right polarisation states of the W. Indeed, as can be seen in Fig. 4.13 the leptons preferentially decay in the direction of the momentum of the W which means –using helicity conversation rule of thumb– that $W^+(\lambda = -1) < W^+(\lambda = +1)$ and $W^-(\lambda = -1) > W^-(\lambda = +1)$. This can be understood by considering the four main contributions to the W^+ production. If we ignore the negligible contributions involving the \bar{b} flavour we are left with: \textcircled{a} : $u^{(s)}\bar{d}^{(s)}|V_{ud}|^2$, \textcircled{b} : $u^{(s)}\bar{s}|V_{us}|^2$, \textcircled{c} : $c\bar{d}^{(s)}|V_{cd}|^2$, \textcircled{d} : $c\bar{s}|V_{cs}|^2$. In the case \textcircled{b} the quark $u^{(s)}$ possesses in general a higher longitudinal momentum than the quark \bar{s} it enters in collision with which means

$x_{u^{(s)}} > x_{\bar{s}} \Rightarrow W^+(\lambda = -1) > W^+(\lambda = +1)$. On the other hand in the cases \textcircled{a} , \textcircled{c} and \textcircled{d} , it is the other way around², *i.e.* $x_{\bar{q}} > x_q$ which means now $W^+(\lambda = -1) < W^+(\lambda = +1)$. This hypothesis is proved when looking at the individual behaviour of these four contributions in Fig. 4.13.(b), where, to fit the present range in coordinate, the \textcircled{b} and \textcircled{c} contributions are respectively multiplied by factors 10 and 8. Actually this shows the predominance of right W^+ is essentially the consequence of the dominating \textcircled{a} -terms that overrule the other ones.

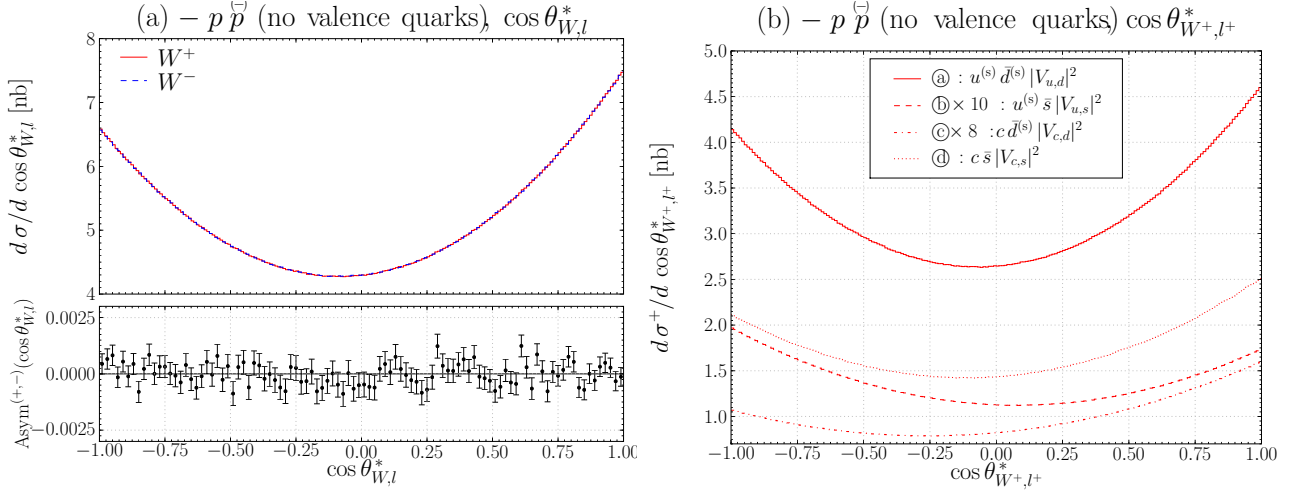


Figure 4.13: Distributions of $\cos \theta_{W,l}^*$ in $pp(p\bar{p})$ collisions with no valence quarks in the hadrons, first with all the sea quarks contributions (a) and then with the four main contributions from a CKM point of view (b).

Also worth mentioning is the angle $\phi_{W,l}^*$ which is not, as displayed by Fig. 4.14, flat along the whole $[0, \pi]$ range. The reasons for that comes from the $V - A$ coupling of the leptons to the W and to the presence of non-zero and asymmetric p_T of the colliding quarks. Still the explanations to amend this pattern is reported to the study of the $p\bar{p}$ and pp collisions since in those cases the effects are much higher and then easier to explain (note the important zoom in coordinates show the distribution is actually quite flat). The important point here is that just like for $\cos \theta_{W,l}^*$ there are no charge asymmetries which means no impact for a study of $M_{W^+} - M_{W^-}$.

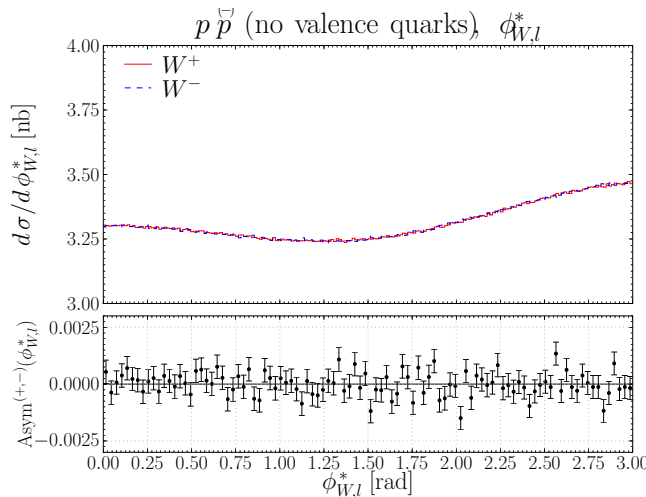


Figure 4.14: Distributions of $\phi_{W,l}^*$ in $pp(p\bar{p})$ collisions with no valence quarks in the hadrons

²To a good approximation for \textcircled{a} we have $x_{u^{(s)}} \sim x_{\bar{d}^{(s)}}$ except for $10^{-4} < x$ where $x_{u^{(s)}} \lesssim x_{\bar{d}^{(s)}}$.

4.A.3 Proton–anti-proton collisions

Now we review the $p\bar{p}$ collisions mode reminding the features that makes it perfectly symmetric between the production of W^+ and W^- . Let us remind that in our conventions the proton impinges in the $+z$ direction while the anti-proton does from the $-z$ direction.

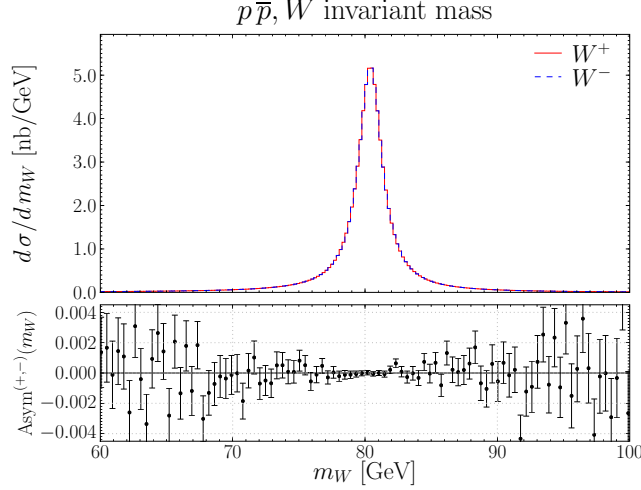


Figure 4.15: Invariant mass of the W boson in $p\bar{p}$ collisions.

First we turn our attention to the invariant mass m_W of the positively and negatively charged W as shown in Fig. 4.15. Note these invariant masses are to be understood as the result of the production of W bosons as Breit–Wigner resonances weighted by the PDFs, which adds up to the former behaviour the probability of occurrence of a given mass m_W . Hence, even if here $m_{W^+} = m_{W^-}$ such an equality is non trivial and has to be seen as the consequence that W^+ and W^- are produced with the same dynamics in the very particular case of $p\bar{p}$ collisions.

The observables y_W , $p_{T,W}$, η_l and $p_{T,l}$ are shown in Fig. 4.16. In $p\bar{p}$ collisions the production of the W^+ and of the W^- are produced with the same dynamics since to every element of the phase-space of, say the W^+ , exists the perfect CP match in an other phase-space point of W^- . This symmetry translates in coordinate space into that the $W^+(l^+)$ and $W^-(l^-)$ kinematics are the same up to a vertical flip with respect to the interaction point. This behaviour can be seen in the y_W and η_l distributions but is no longer decipherable when projecting the W or the charged lepton transverse momenta on the transverse plane. Note in the y_W and η_l distributions the labels \textcircled{c} and \textcircled{d} attached to the W^+ data. Focusing on the main “valence” term $u\bar{d}|V_{ud}|^2$, in each of these regions the W^+ are produced respectively via $\textcircled{c} : u_p^{(s)} \rightarrow \leftarrow \bar{d}_p^{(v)}$ and $\textcircled{d} : u_p^{(s)} \rightarrow \leftarrow \bar{d}_p^{(s)}$ for which the inequality $\textcircled{c} < \textcircled{d}$ materialises the fact that since $\bar{d}_p^{(v)} \equiv d_p^{(v)}$ we have

$$d_p^{(v)} < u_p^{(v)}. \quad (4.15)$$

This last inequality explains the presence of the exact same asymmetry for the case of the W^- production.

The angular distributions of $\cos\theta_{W,l}^*$ and $\phi_{W,l}^*$ are shown in Fig. 4.17. We start by looking at $\cos\theta_{W,l}^*$. Both W^+ and W^- distributions are superimposed and display a small asymmetry with respect to the origin. This pattern can be explained by focusing on the W^+ and the two labels \textcircled{g} and \textcircled{h} attached to it in Fig. 4.17.(b). The configurations where the W^+ are produced via $\textcircled{g} : u_p^{(v)} \bar{d}_p^{(s)} \rightarrow W^+(\lambda = -1)$ are such that the l^+ will decay preferentially in the opposite direction of the W^+ momentum. In the cases where the boson is produced like $\textcircled{h} : u_p^{(s)} \bar{d}_p^{(v)} \rightarrow W^+(\lambda = +1)$ the l^+ will decay preferentially in the same direction of the W^+ momentum. Then, the $\textcircled{g} > \textcircled{h}$

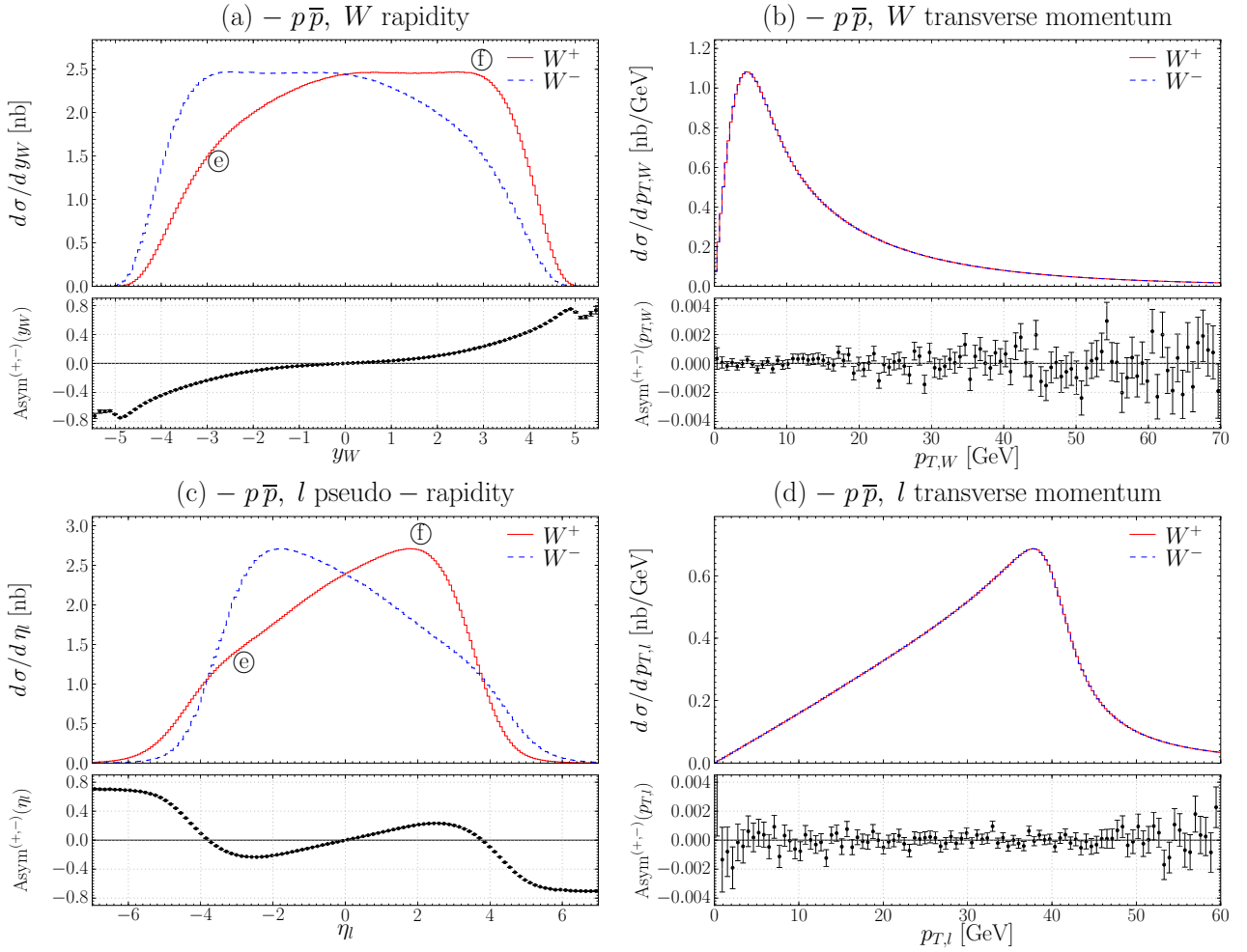


Figure 4.16: Distributions of the W boson rapidity (a) and transverse momentum (b) along with the one of the charged lepton pseudo-rapidity (c) and transverse momentum (d) in $p\bar{p}$ collisions.

pattern shares the same origin than the asymmetries seen in the y_W and η_l distributions and written in Eq. (4.15). Previously, while studying the pure sea contributions, the inverse unbalance was observed, but now the main “valence” term $u\bar{d}|V_{ud}|^2$ overrules the latter.

Now even more interesting is the fact that Fig. 4.17 shows l^+ and l^- preferentially decays in the same direction of $p_{T,W}$ which, as we know, must have dramatic consequences on the smearing of the $p_{T,l}$ distributions. Before explaining what happens we take a step back to the LO order and understand how the lack of transverse motion in this approximation induce no asymmetry in the azimuthal decay of the leptons. Figure 4.18 shows the collinear quark–anti-quark collisions of $q^{(v)}\bar{q}^{(s)}$ (left) and $q^{(s)}\bar{q}^{(v)}$ (right). In both cases the valence quarks hold most of the longitudinal momentum and the privileged direction of decays of the positively and negatively charged leptons (symbolised in the WRF) which, even if opposite with each other, do not induce any anisotropic behaviour in ϕ . Moving to the improved leading order picture, now quarks and anti-quarks possess a transverse initial motion and radiate gluons and photons on their way to the collision. We end up this time with “valence” cases with the valence (anti-)quark that bears most of the longitudinal momentum and on the other side the sea (anti-)quark which bears most of the transverse motion. In this context the higher transverse momentum of the sea (anti-)quark constrain the leptons to modify their privileged decaying angle to satisfy the kinematic momentum conservation as shown in Fig. 4.18 Hence for $q^{(v)}\bar{q}^{(s)}$ events the l^+ decays preferentially along the direction of $p_{T,W}$ while the l^- decays preferentially in the opposite direction of $p_{T,W}$. In the case of $q^{(s)}\bar{q}^{(v)}$ it is the exact

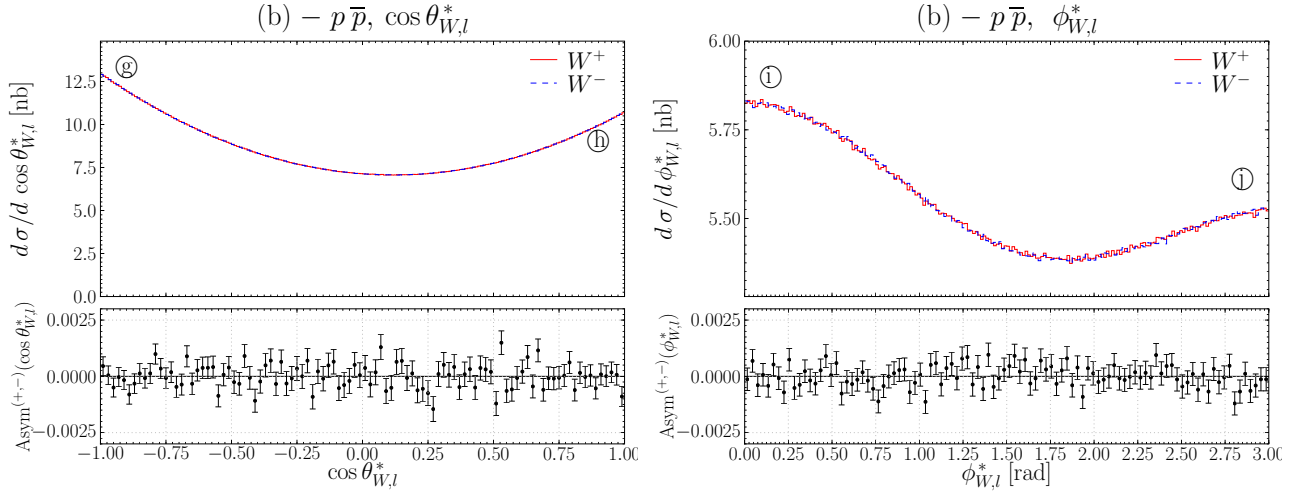
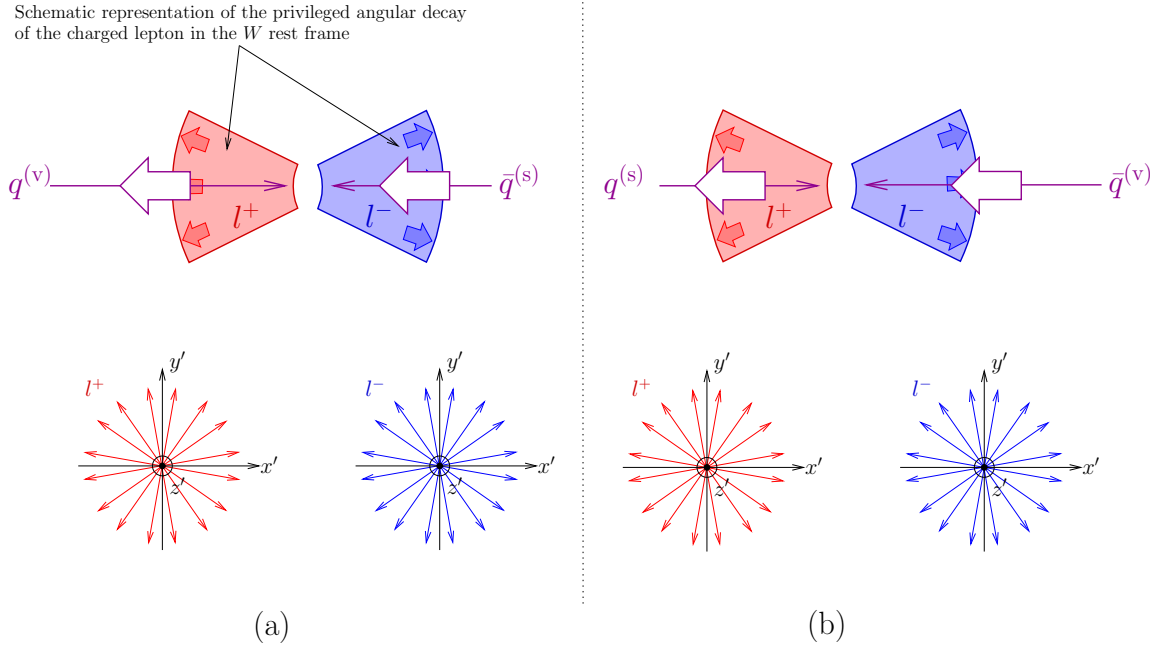
Figure 4.17: Distributions of $\cos\theta_{W,l}^*$ (a) and $\phi_{W,l}^*$ (b) in $p\bar{p}$ collisions.

Figure 4.18: Schematic representations of the decay of the charged leptons at the leading order. For convenience, even though the quarks are represented in the laboratory frame the decay of the charged leptons are symbolised in the WRF. Frame (a) represents the case of “valence” contribution involving a quark of valence while frame (b) displays the case of “valence” contribution involving an anti-quark of valence.

opposite. Now, in the context of the W^+ production, focusing again on the main “valence” term $u\bar{d}|V_{ud}|^2$ Figure 4.19.(a) translates to $u_p^{(v)} \rightarrow \leftarrow \bar{d}_p^{(s)}$ while (b) translates to $u_p^{(s)} \rightarrow \leftarrow \bar{d}_p^{(v)}$. Because of the $d < u$ inequality (Eq. (4.15)) (a)-cases overrule (b)-cases and the l^+ prefers, in general, to decay in the direction of $p_{T,W}$. The same argument can explain the asymmetry observed in the negative channel. So far, while the fact the valence (anti-)quark hold most of the longitudinal momentum is well known, we did not justified the fact that the sea (anti-)quark hold most of the transverse motion. The very last section of this Appendix address this issue. For now we can justify it heuristically by stating that the sea (anti-)quark having a small fraction x is the result of the loss of energy on the way to the collision by gluon/photon emission which confers to the (anti-)quark more transverse

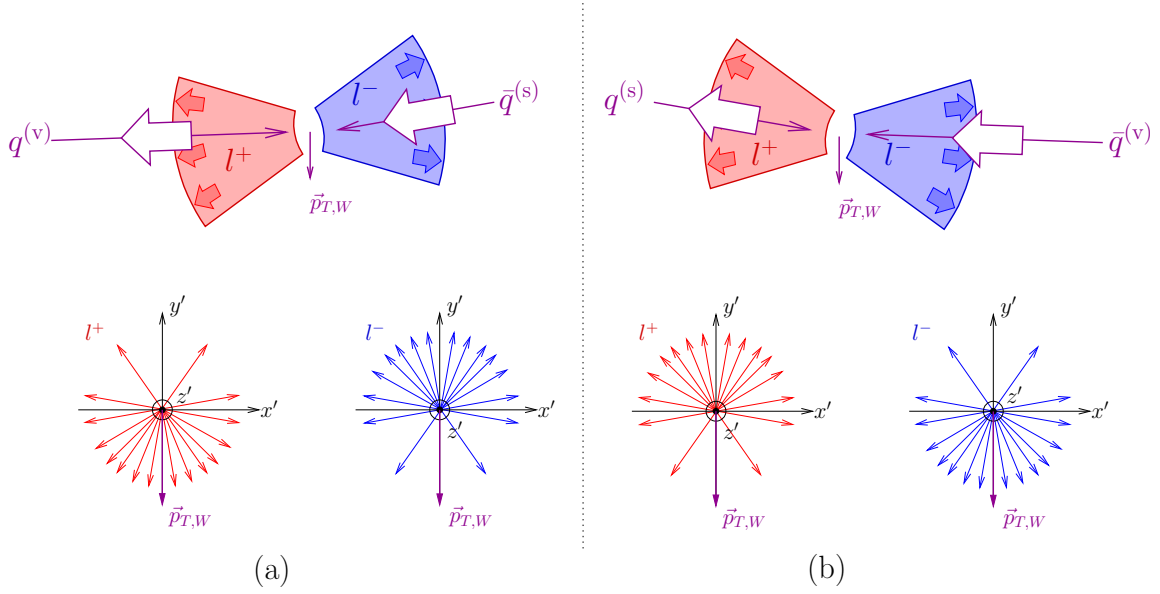


Figure 4.19: Schematic representations of the decay of the charged leptons at the improved leading order. For convenience, even though the quarks are represented in the laboratory frame the decay of the charged leptons are symbolised in the WRF. Frame (a) represents the case of “valence” contribution involving a quark of valence while frame (b) displays the case of “valence” contribution involving an anti-quark of valence.

motion than the valence (anti-)quark.

Figure 4.20 by showing the η_l distribution in bins of y_W and *vice versa* illustrates the importance of the “valence” contributions in function of the fraction of momentum $x_{q,\bar{q}}$. Starting with η_l in bins of y_W (left) we see the pseudo-rapidity distribution is the addition of two quantities : (1) the rapidity y_W inherited from the W boost and that confers to the charged lepton most of its longitudinal motion and (2) the decay of the charged lepton governed by the $V - A$ coupling of leptons to W which eventually gives this bump representing the angular coverage of the charged leptons $\theta_l \in [0, \pi]$. Let us remind $p_{T,W}$ participates in the shape of (2) but can be neglected in this discussion since $p_{T,W} \ll |\vec{p}_{z,W}|$. In the narrow central bin region where all events verify $|y_W| < 0.5$ the small charge asymmetry is due to non-negligible “valence” quark contributions. As the selection in rapidity increases, the “valence” contributions rise displaying in consequence large charge asymmetries in the lepton decay for a local value of η . Turning to $3.5 < |y_W| < 4.5$, for the negative values of η the “valence” contributions $\textcircled{K} : u_p^{(s)} \rightarrow \leftarrow \bar{d}_p^{(v)}$ give $W^+(\lambda = +1)$ bosons while $\textcircled{L} : d_p^{(s)} \rightarrow \leftarrow \bar{u}_p^{(v)}$ give $W^-(\lambda = +1)$ bosons. The “valence” terms contribute then in both cases to produce right W bosons, which imply the $l^+(l^-)$ decays preferentially in the same(opposite) direction of the W momentum. Going to the positive value of η_l is achieved by taking the CP transformation of the previous example, this time we have $\textcircled{M} : u_p^{(v)} \rightarrow \leftarrow \bar{d}_p^{(s)}$ giving $W^+(\lambda = -1)$ bosons and $\textcircled{N} : d_p^{(v)} \rightarrow \leftarrow \bar{u}_p^{(s)}$ $W^-(\lambda = -1)$ bosons. Note that considering at the same time those two opposite y_W -phase space regions completely reestablish the equivalence in the dynamic production of the W^+ and the W^- bosons which, using the label notation, would write $\textcircled{K} + \textcircled{M} \equiv \textcircled{L} + \textcircled{N}$.

On the right of Fig. 4.20 the y_W distributions in bins of η_l hold more or less the same information than the previous plots. Here though, looking at the y_W variable allows to look at the smearing of the distributions from the W boost point of view while earlier the smearing was essentially the one arising from the $V - A$ coupling of the charged leptons to the W . Also now we can see that a given slice of η_l receives contributions from an important range of different y_W rapidity. Although it is not important here as no $p\bar{p}$ collisions can be made at the LHC it will give insight for LHC collisions at which level the narrow η_l selection in our analysis are contaminated by high rapidity region and hence from “valence” contributions.

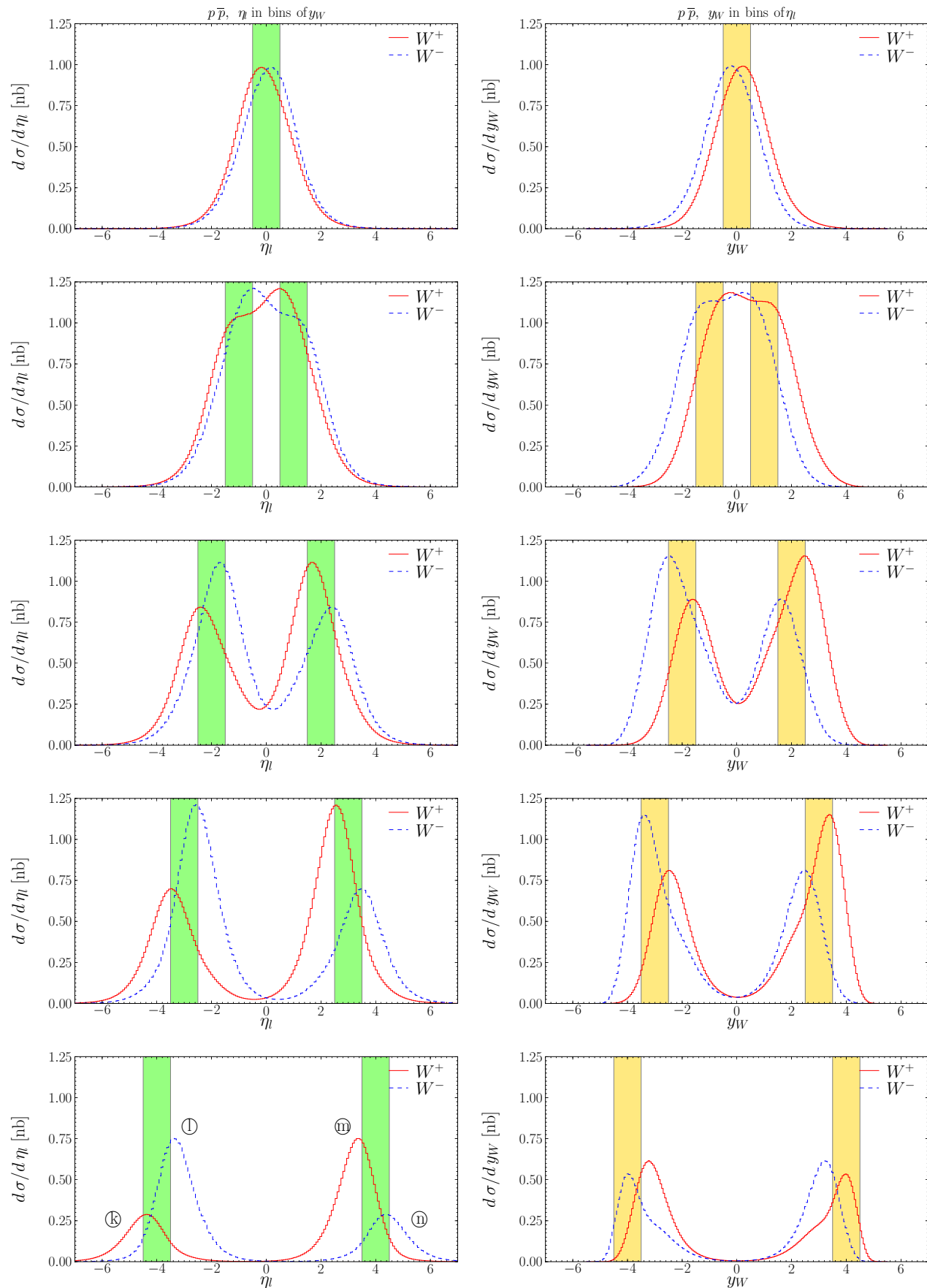


Figure 4.20: W boson rapidity distributions in bins of the charged lepton pseudo-rapidity (left) and *vice versa* (right) in the case of $p\bar{p}$ collisions. In each plot the corresponding y_W or η selection is materialised by the colored stripe(s).

Finally we show the behaviour of the “valence” contribution in bins of y_W from the point of view of $\cos\theta_{W,l}^*$ and $\phi_{W,l}^*$ in Fig. 4.21 where both charged channels show the same behaviour with almost no asymmetries in $|y_W| < 0.5$ because of the negligible “valence” contributions. As the “valence” contributions increases with the selection in rapidity we see that the supremacy of left(right) $W^+(W^-)$ which was observed inclusively with $\textcircled{g} > \textcircled{h}$ is back in Fig. 4.17.

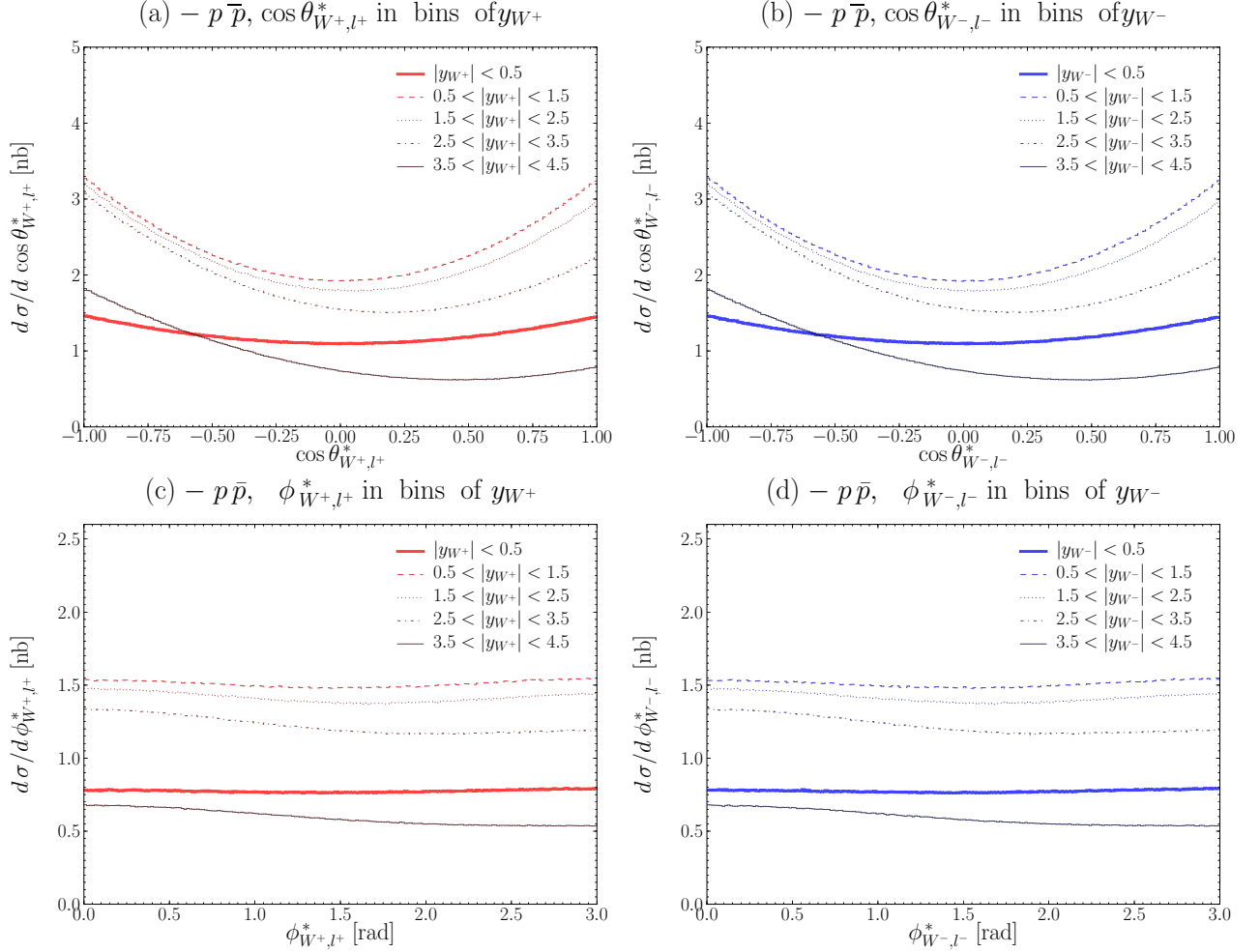


Figure 4.21: Distributions of $\cos\theta_{W,l}^*$ and $\phi_{W,l}^*$ in bins of y_W for the positively (a,c) and negatively (b,d) charged channel in $p\bar{p}$ collisions.

4.A.4 Proton–proton collisions

As we have seen previously even in the case of the $p\bar{p}$ collisions there are different asymmetries appearing in the decay of the lepton but eventually no charge asymmetries are observed. Here in pp collisions, the absence of anti-quarks of valence will open the door to the previous asymmetries to fully express themselves and create important asymmetries between the positive and negative kinematics, especially in the final state.

First of all, before looking at the W boson and charged leptons kinematics in specific domain of the phase-space we quantify the global charge asymmetry at the inclusive level due to the fact that in overall we produce more W^+ than W^- . Taking the numerical values of the inclusive cross sections for pp collision (Table 4.1) and writing A_{pp} the global charge asymmetry we evaluate it like

$$A_{pp} \equiv \frac{\sigma_{\text{incl.}}^+ - \sigma_{\text{incl.}}^-}{\sigma_{\text{incl.}}^+ + \sigma_{\text{incl.}}^-}, \quad (4.16)$$

$$\approx 0.1478. \quad (4.17)$$

Then, when looking further one at the discrepancies between the two charged channels in the observable a via $\text{Asym}^{(+,-)}(a)$, all deviations from the horizontal axis A_{pp} have to be understood as the result –in the considered point of phase space– of dynamic issues creating noticeable differences between the positive and negative kinematics in top of the global larger production of W^+ with respect to W^- .

This remark can be applied to the very first example in Fig. 4.22 where we can see the peak of the invariant mass of the W^+ is slightly centered to a higher mass than the one of the W^- . We observe $m_{W^+} - m_{W^-} \sim \mathcal{O}(10 \text{ MeV})$. Let us emphasise this behaviour is already present at LO. We explain this effect heuristically with the following idea. In the quark–anti-quark collision the more energy is brought, the more the mass of the W can take its share for its mass m_W . The cases which fall under this category are the one involving a valence u quark, for a W^+ , and a valence d quark for a W^- . Since in general u quarks carry more longitudinal momentum than the d quarks it turns out they have more opportunities to participate to the production of a high mass W . Hence, eventually, at the hadronic level W^+ are produced with higher masses with respect to the W^- .

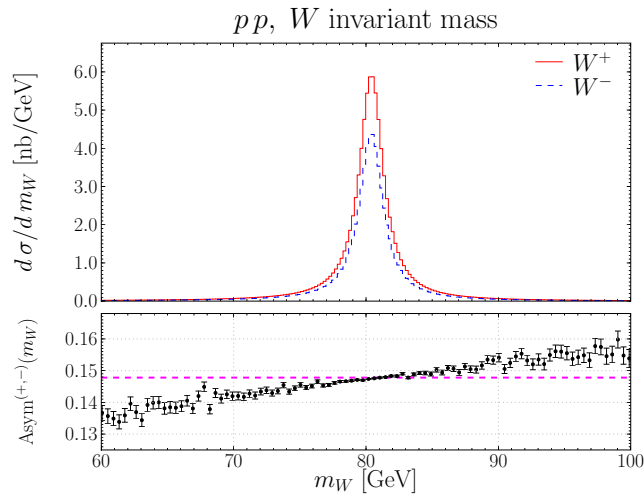


Figure 4.22: Invariant mass of the W boson in pp collisions.

Figure 4.23 shows now the kinematics of the W bosons and of the charged leptons. The rapidity displays two striking features, the first and most trivial, is a difference in the scale which simply relates that we have roughly twice many u than d in pp collisions. The second feature shows the W^+ rapidity extends to a wider range than the W^- which means the W^+ can gain a more important

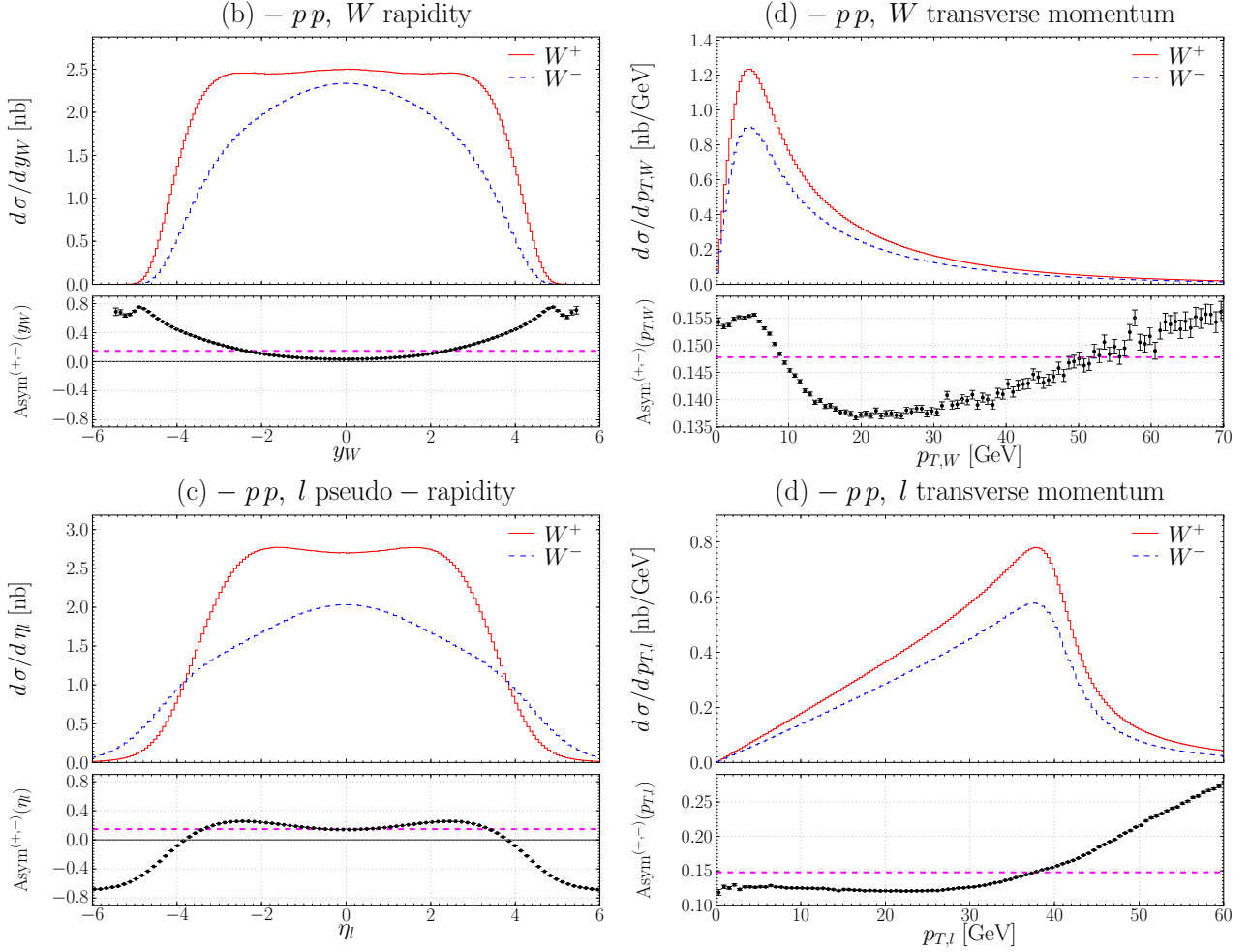


Figure 4.23: Distributions of the W boson rapidity (a) and transverse momentum (b) along with the one of the charged lepton pseudo-rapidity (c) and transverse momentum (d) in pp collisions.

longitudinal motion than the W^- which is the consequence that the u quarks carry most of the proton momentum. The charge asymmetries in $p_{T,W}$ comes from the difference in the production of the W^+ and W^- . Because of the important implications in terms of systematic errors in the study of $M_{W^+} - M_{W^-}$ this specific topic was discussed in the core of the Chapter (cf. § 4.2). Turning now to the charged lepton kinematics we observe that the pseudo-rapidity distribution follows roughly the pattern of the rapidity with the particular feature that the l^- tends to decay in the direction of the W momentum direction while it is the inverse behaviour for the l^+ . This pattern will be detailed further while looking at the η_l distributions in y_W bins, at this stage we can already understand that the excess of matter in pp collisions implies

$$\bar{q} < q \quad \Rightarrow \quad W(\lambda = +1) < W(\lambda = -1). \quad (4.18)$$

To the light of the known behaviour of the charged lepton in their decay under the constrain of the $V - A$ coupling in EW interactions, this explains respectively the narrowing and flattening of the η_{l^+} and η_{l^-} distributions. This can be seen more directly in Fig. 4.25.(a) looking at the $\cos\theta_{W,l}^*$ distributions. To the purely sea pattern seen in Fig. 4.13.(a), we add up the “valence” terms but consider for simplicity in the discussion only the main term $u_p^{(v)} \bar{d}_p^{(s)} |V_{ud}|^2$ for the W^+ and $d_p^{(v)} \bar{u}_p^{(s)} |V_{ud}|^2$ for the W^- . Events such as $u_p^{(v)} \rightarrow \leftarrow \bar{d}_p^{(s)}$ give $W^+(\lambda = -1)$ bosons from which the l^+ leptons decay preferentially in the opposite direction of \vec{p}_{W^+} materialising eventually as \odot in the Figure. For W^- bosons, this time $d_p^{(v)} \rightarrow \leftarrow u_p^{(s)}$ create $W^-(\lambda = -1)$ bosons from which the l^- leptons decay most

of the time in the direction of \vec{p}_{W^-} . Eventually the inequality in the gaps “ $\textcircled{O} - \textcircled{R}$ ” $>$ “ $\textcircled{Q} - \textcircled{P}$ ” is explained once again by $d < u$, *i.e.* from the common pattern of the purely sea contribution the predominance of u quarks in the collision adds up a larger asymmetry in W^+ relatively to the one for W^- .

Coming back to the charged lepton kinematics the transverse momentum of the charged lepton shows very important charge asymmetries. The sources for those are: (1) $m_{W^+} > m_{W^-}$, (2) $p_{T,W^+} \neq p_{T,W^-}$ and (3) the non isotropic azimuthal decay of the charged leptons with respect to the direction of $p_{T,W}$ feature which has been already discussed in the case of $p\bar{p}$ collisions. The first source cannot be the one responsible for the size of these effects. Figure 4.24 proves it by showing $\text{Asym}^{(+,-)}(p_{T,l})$ at LO where $m_{W^+} > m_{W^-}$ is already present while (2) and (3) are not, and at the improved LO where all three effects are present.

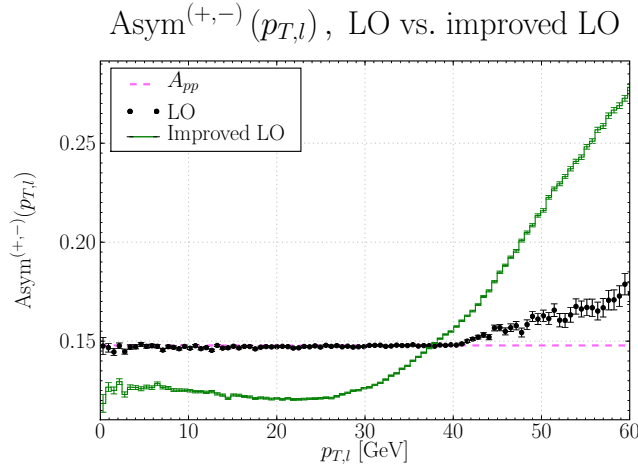


Figure 4.24: Final state charge asymmetry at the leading order and improved leading order.

The reason for these large asymmetries in the $p_{T,l}$ distributions is explained by the predisposition of the l^+ leptons to decay preferentially in the direction of $p_{T,W}$ while it is the over way around for the l^- leptons. This can be seen directly in Fig. 4.25.(b) showing the $\phi_{W,l}^*$ distribution. The explanations of this effect can be followed looking at Fig. 4.19, where this time the total absence of the (b) contribution involving valence anti-quarks open the door to effects (a) to fully express their charge dependent discrepancies. We start by addressing the case of the W^+ through the main “valence” term $u_p^{(v)} \rightarrow \leftarrow \bar{d}_p^{(s)}$ where, the higher transverse motion held by the \bar{d} forces the l^+ to decay most of the time so that $\phi_{W^+,l^+}^* \approx 0$. The case of the W^- is identical but this time the opposite helicity of the l^- makes it so it decays preferentially in the opposite direction of $\vec{p}_{T,W}$, *i.e.* $\phi_{W^-,l^-}^* \approx \pi$. Once again the relative size of the “ $\textcircled{S} - \textcircled{U}$ ” and “ $\textcircled{T} - \textcircled{V}$ ” gaps is justified by $d < u$.

Figure 4.26.(left) allows now to see the difference in the behaviour of the decaying leptons in bins of y_W through their pseudo-rapidity. Just like in $p\bar{p}$ collisions the asymmetry due to the “valence” contributions is almost negligible in the central narrow y_W selection and then rise with the rapidity except that this time the asymmetries are not matched between W^+ and W^- when summing the two opposite y_W slices contributions but rather magnified. In the case of $3.5 < |y_W| < 4.5$, the excess of $W^+(\lambda = -1)$ is such that in average most of the l^+ leptons decay in the opposite direction of \vec{p}_W as shown by the bumps in \textcircled{X} and \textcircled{Y} . On the other hand the l^- , due to the excess of $W^-(\lambda = -1)$, follow the W bosons momentum direction as displayed by the \textcircled{W} and \textcircled{Z} bumps.

This large influence of the valence quarks in the high rapidity region suggests that for a measurement of $M_{W^+} - M_{W^-}$, selecting charged leptons emitted from low W rapidity would at least allow to reduce the systematics uncertainties related to the valence or sea quarks. By going to the narrow region $|\eta| < |0.5$ one can see the size of the “valence” contamination in this region is non negligible.

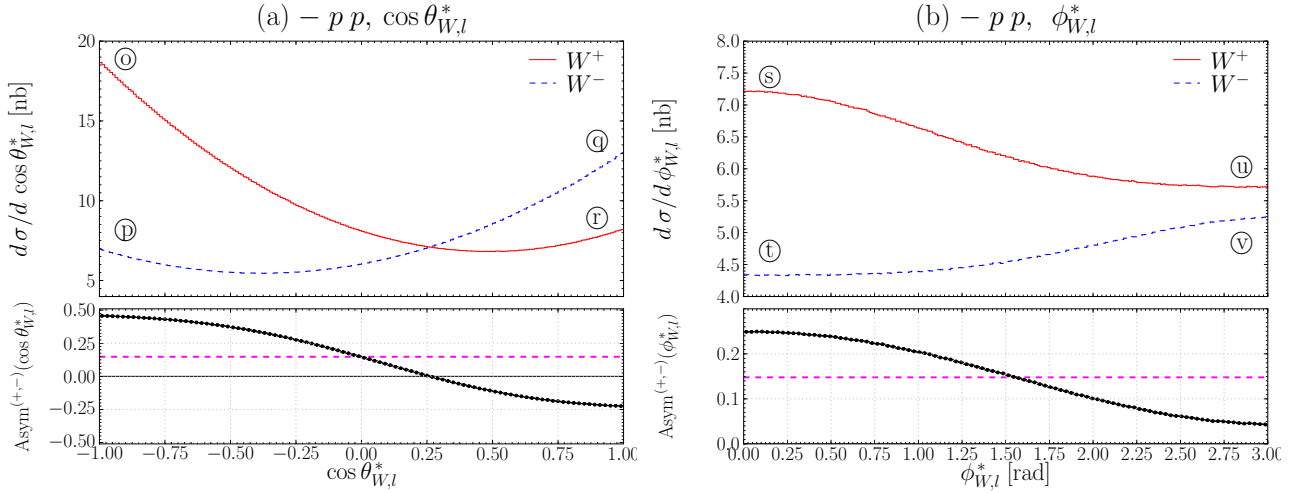


Figure 4.25: Distributions of $\cos\theta_{W,l}^*$ (a) and $\phi_{W,l}^*$ (b) in pp collisions.

This is the reason why in the core of the Chapter the narrow selection was made rather to $|\eta_l| < 0.3$ since it was found to be the best compromise for a realistic measurement prospect in Chapter 5.

Figure 4.27 shows the size of the initial state charge asymmetries by looking at the transverse momentum of the W boson. Figure 4.28 shows the increase of the final state charge asymmetry in bins of y_W and η_l . Another vision of the growth of the “valence” contributions in function of y_W can be made looking at the $\cos\theta_{W,l}^*$ and $\phi_{W,l}^*$ distributions in bins of y_W (Fig. 4.29). In the central region the asymmetry between left and right W is hardly decipherable (contrary to the same phenomenon seen in η_l -space).

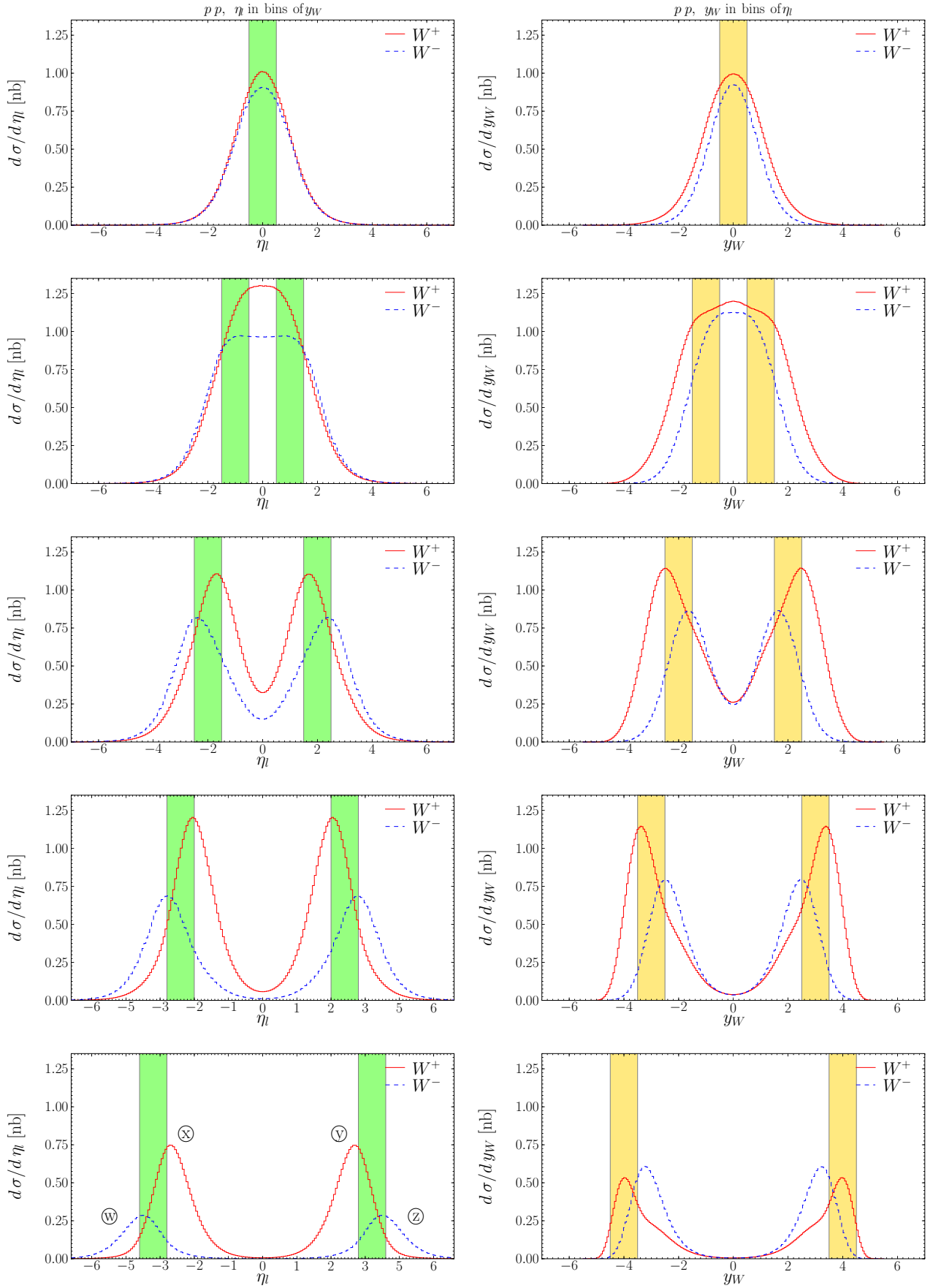
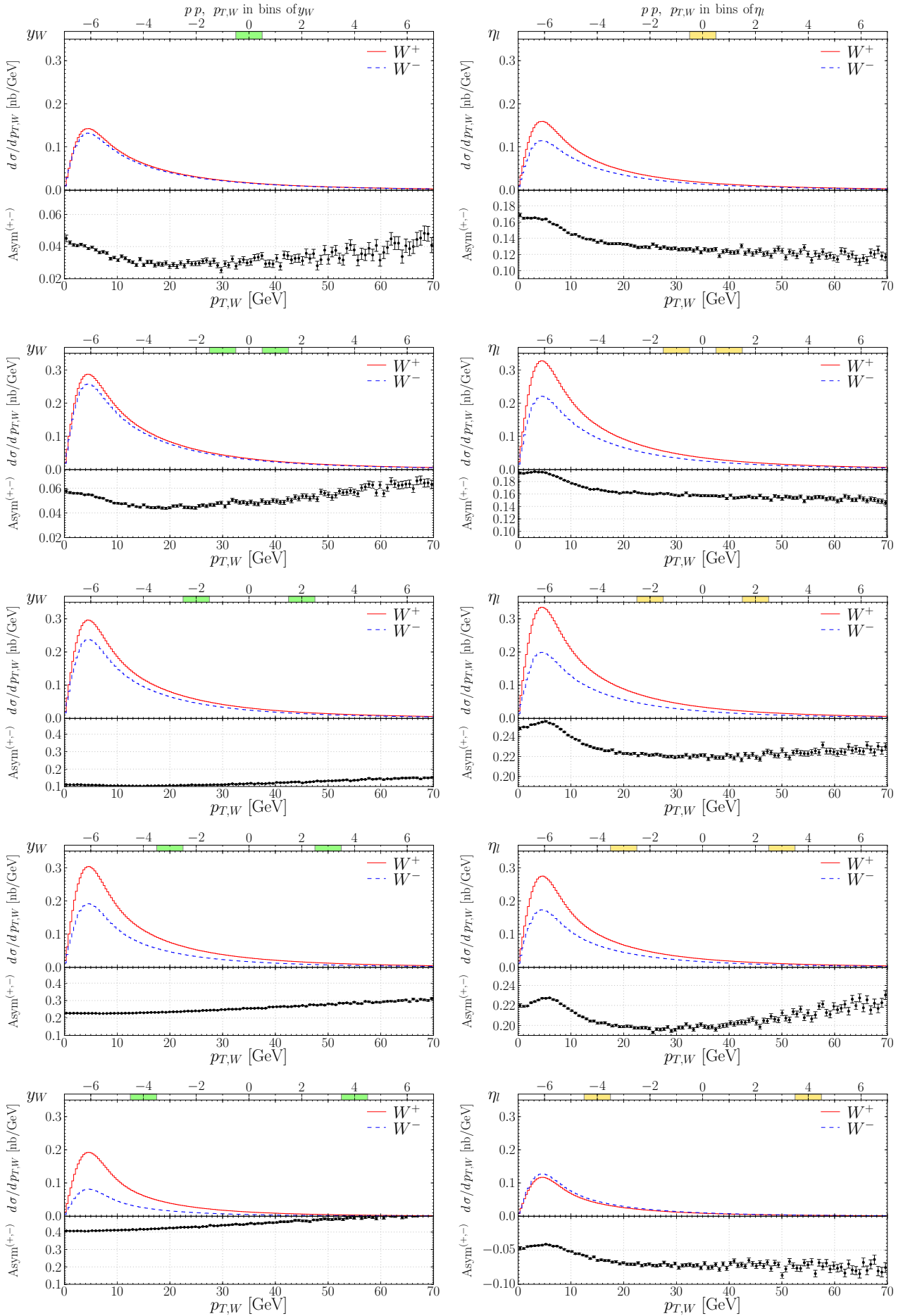
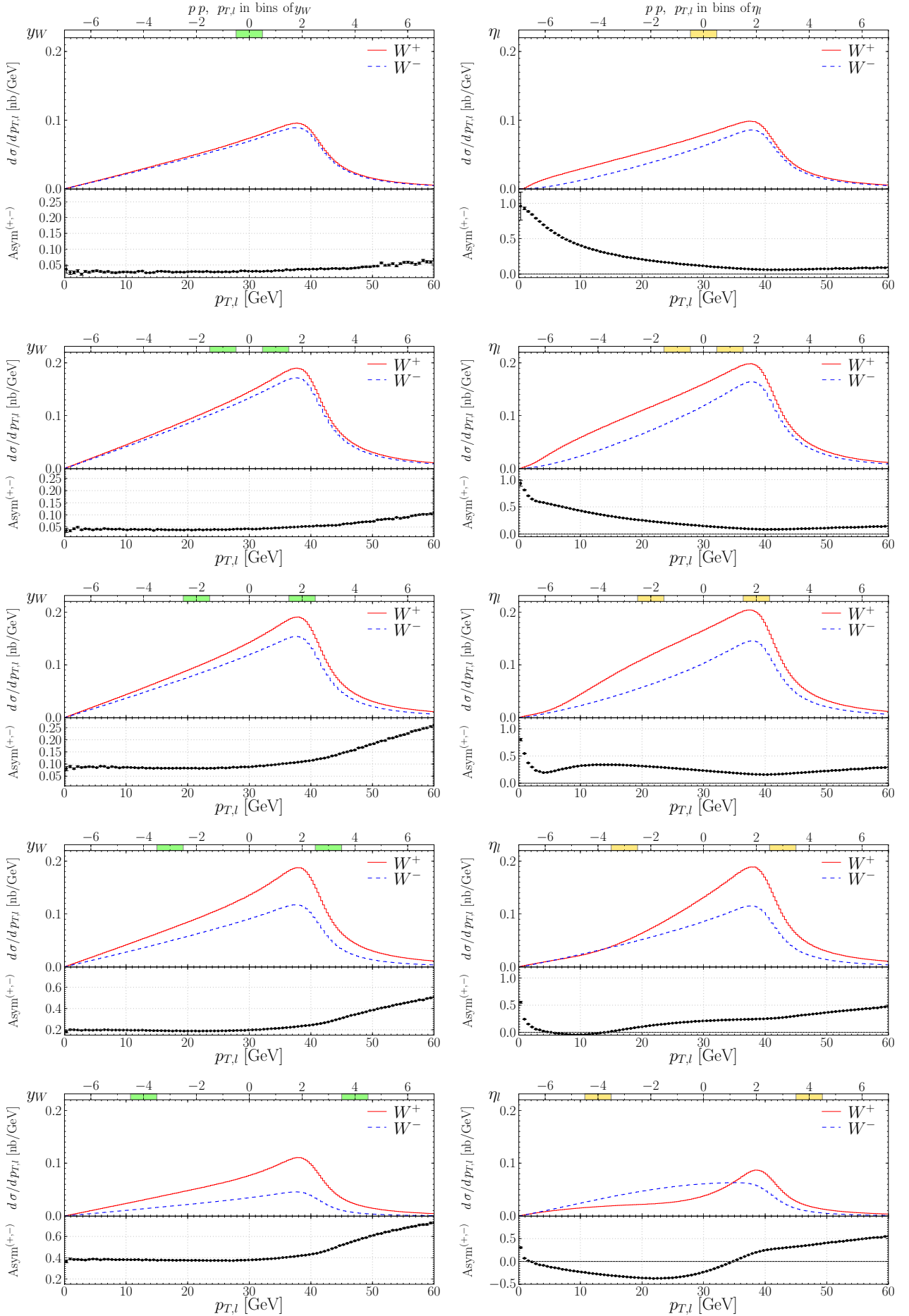


Figure 4.26: W boson rapidity distributions in bins of the charged lepton pseudo-rapidity (left) and *vice versa* (right) in the case of pp collisions. In each plot the corresponding y_W or η selection is materialised by the colored stripe(s).

Figure 4.27: W boson transverse momentum in bins of y_W (left) and in bins of η (right) in pp collisions.

Figure 4.28: Charged lepton transverse momentum in bins of y_W (left) and in bins of η_l (right) in pp collisions.

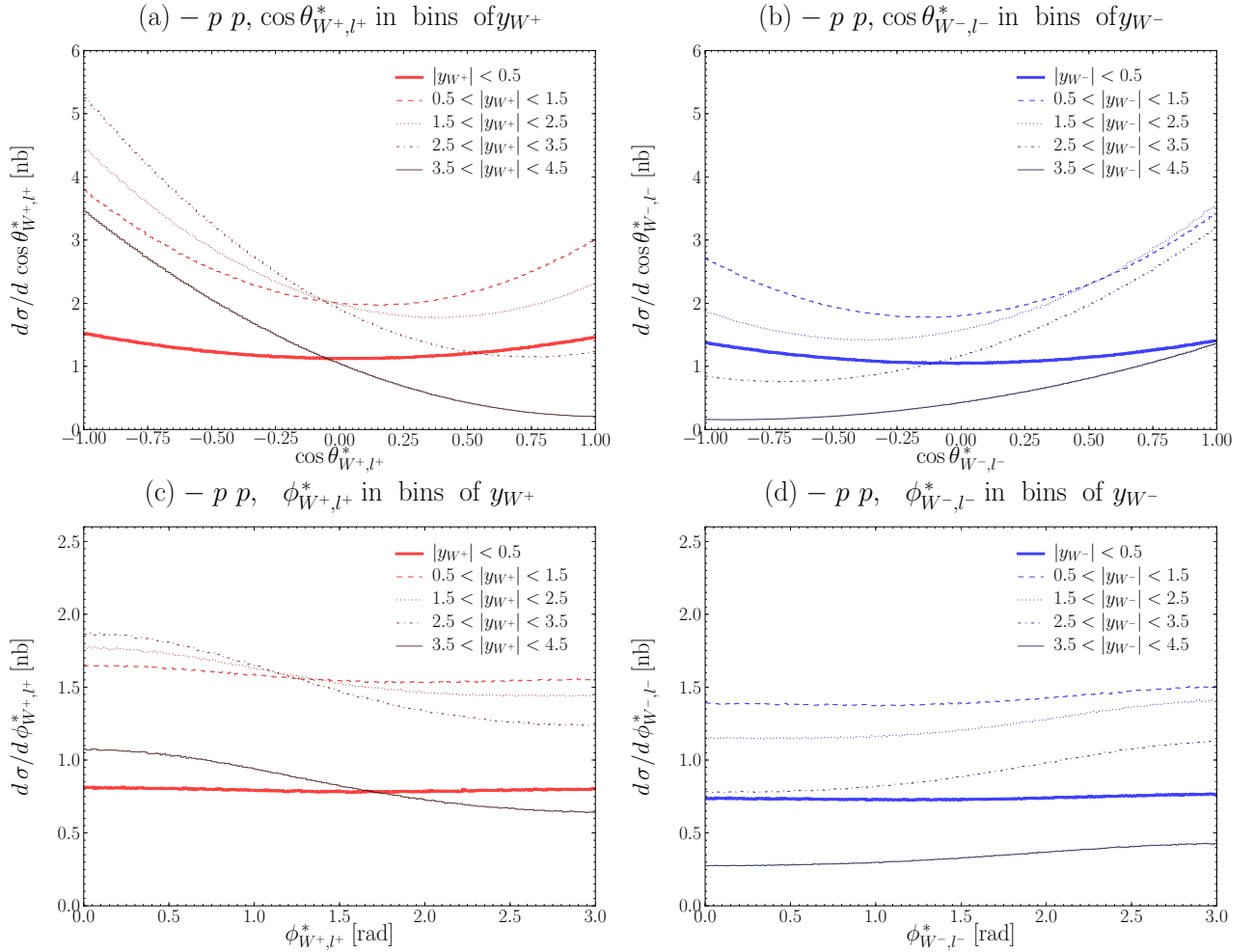


Figure 4.29: Distributions of $\cos \theta_{W,l}^*$ and $\phi_{W,l}^*$ in bins of y_W for the positively (a,c) and negatively (b,d) charged channel in pp collisions.

4.A.5 Deuteron–deuteron collisions

Here, the overall charge asymmetry based on the inclusive cross sections from Table 4.1 gives

$$A_{dd} \approx 0.0015. \quad (4.19)$$

The predictions for dd collisions can be understood from the previous study of pp collisions. Indeed, here the novelty is that reaching the equality $u^{(v)} = d^{(v)}$ allows to cancel out the most important differences between the W^+ and W^- at the level of the production.

The invariant masses of the W^+ and W^- in Fig. 4.30 are now superimposed up to the very small A_{dd} offset. Hence here the W^+ and W^- masses occur with almost the same probabilities, we find $m_{W^+} - m_{W^-} \sim \mathcal{O}(0.1 \text{ MeV})$.

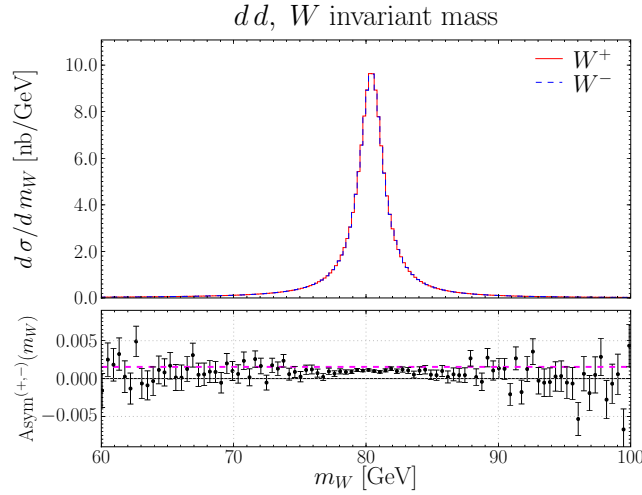


Figure 4.30: Invariant mass of the W boson in dd collisions with $\sqrt{S_{n_1 n_2}} = 7 \text{ TeV}$.

Concerning the main kinematics y_W , $p_{T,W}$, η_l and $p_{T,l}$ shown in Fig. 4.31 the most striking feature is the gain of charge symmetry in the initial state with respect to pp collisions. Because now the production of the W^+ and W^- is almost the same in proportions the rapidity and transverse momentum distributions almost perfectly match each other. On the other hand in the final state the $V - A$ effect folded to the issues related to the transverse motion of the W gives unchanged features such as: (1) the flattening of the η_- and narrowing of the η_+ distributions with respect to y_W and (2) the privileged decay of the $l^+(l^-)$ in the same(opposite) direction of $\vec{p}_{T,W}$. These two effects can be seen respectively more directly from the angular point of view with $\cos \theta_{W,l}^*$ and $\phi_{W,l}^*$ in Fig. 4.25. Let us note as well the size of $\text{Asym}^{(+,-)}(p_{T,l})$ which is different from pp collisions. This is due to the energy in the collision which, being lower here, gives more importance to the valence quarks while at $\sqrt{S} = 14 \text{ TeV}$ the latter are drowned in the large purely sea contributions. This variation of $\text{Asym}^{(+,-)}(p_{T,l})$ as a function of \sqrt{S} is treated in the next sub-section.

Figure 4.33 shows the η_l distributions in bins of y_W and *vice versa*. Note the charged leptons behaviour are the same than in pp collisions but now the proportions of W^+ and W^- are the same, which is particularly noticeable in the last two lines where the positive and negative η_l -pieces of the plots do not interpenetrate each other. Figure 4.34 shows the transverse momentum of the W in bins of y_W and η_l . As can be seen, even if here the discrepancies are induced by the s , c and b flavours since they are weighted by the valence quarks (Eq. (4.3)) it is in the forward rapidity region they are the most important. Figure 4.35 displays the charge asymmetry of the charged leptons transverse momenta in bins of y_W (left) and η_l (right). Again we observe the growth of the charge asymmetry as y_W increases and in general using a crude η_l selection we witness a rather poor correlation with respect to the reference y_W selection results. The $\cos \theta_{W,l}^*$ and $\phi_{W,l}^*$ distributions in bins of y_W are presented in Fig. 4.36.

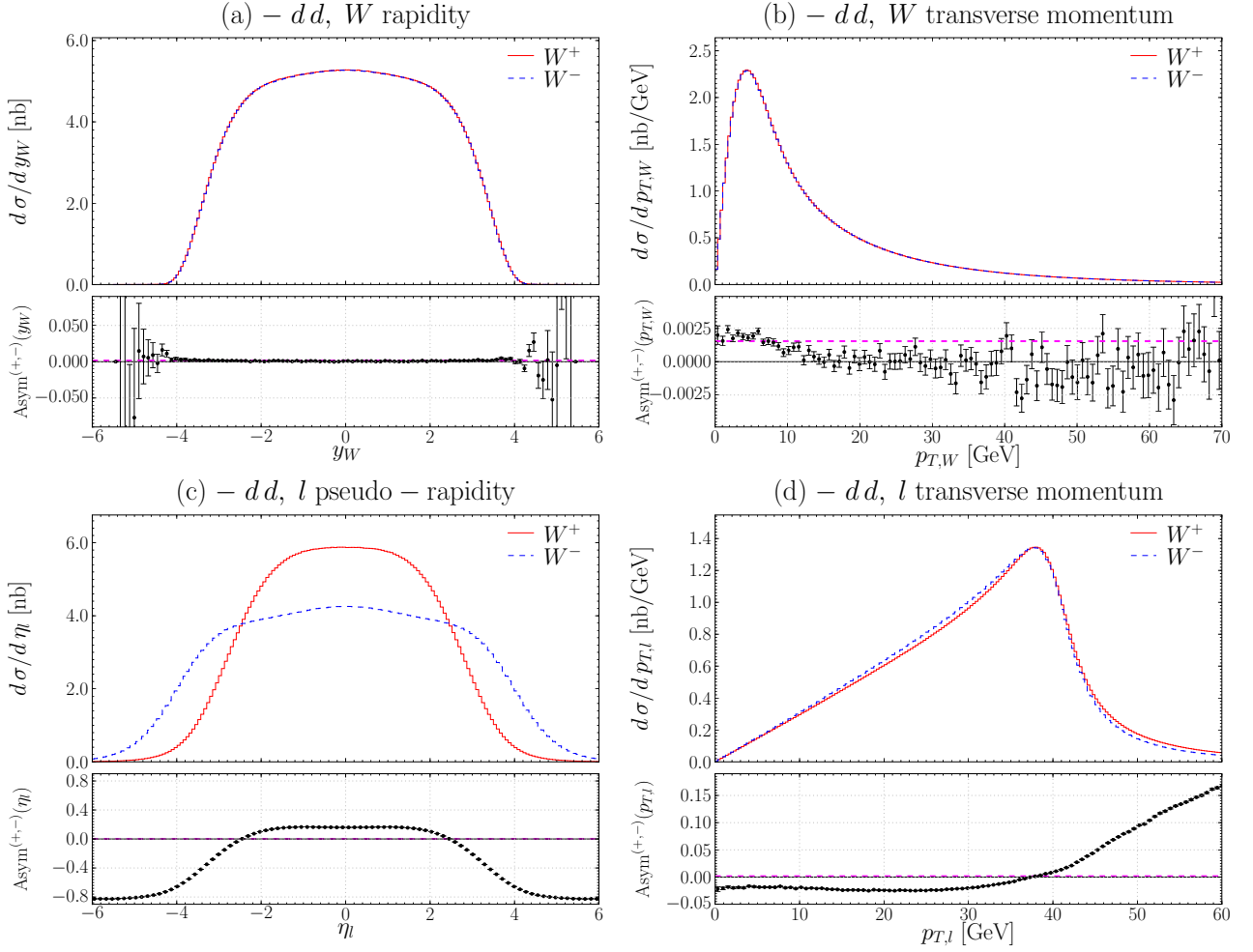


Figure 4.31: Distributions of the W boson rapidity (a) and transverse momentum (b) along with the one of the charged lepton pseudo-rapidity (c) and transverse momentum (d) in dd collisions with $\sqrt{S_{n_1 n_2}} = 7$ TeV.

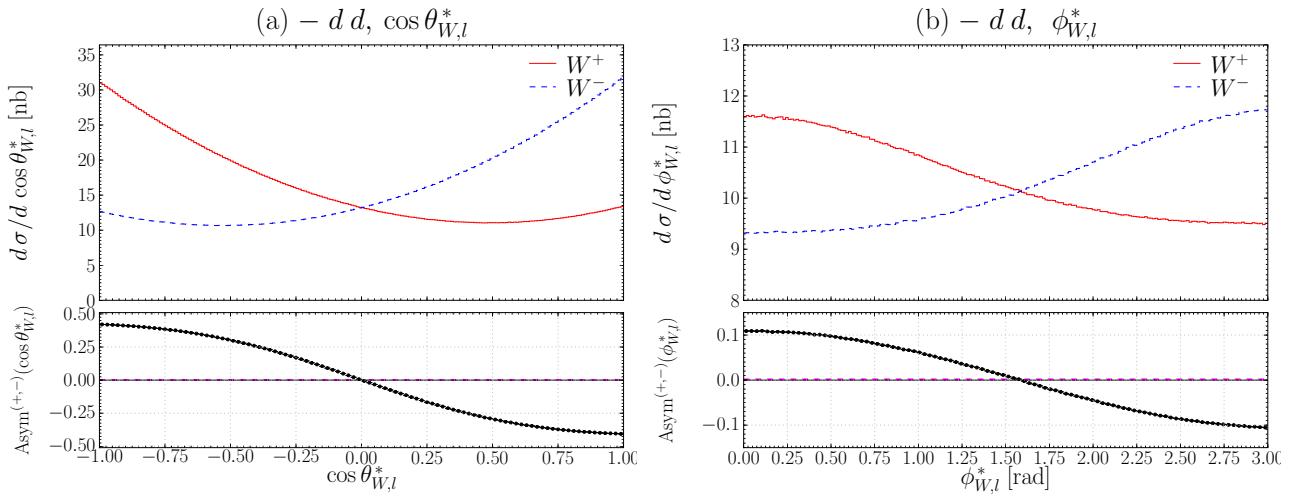


Figure 4.32: Distributions of $\cos \theta_{W,l}^*$ (a) and $\phi_{W,l}^*$ (b) in dd collisions with $\sqrt{S_{n_1 n_2}} = 7$ TeV.

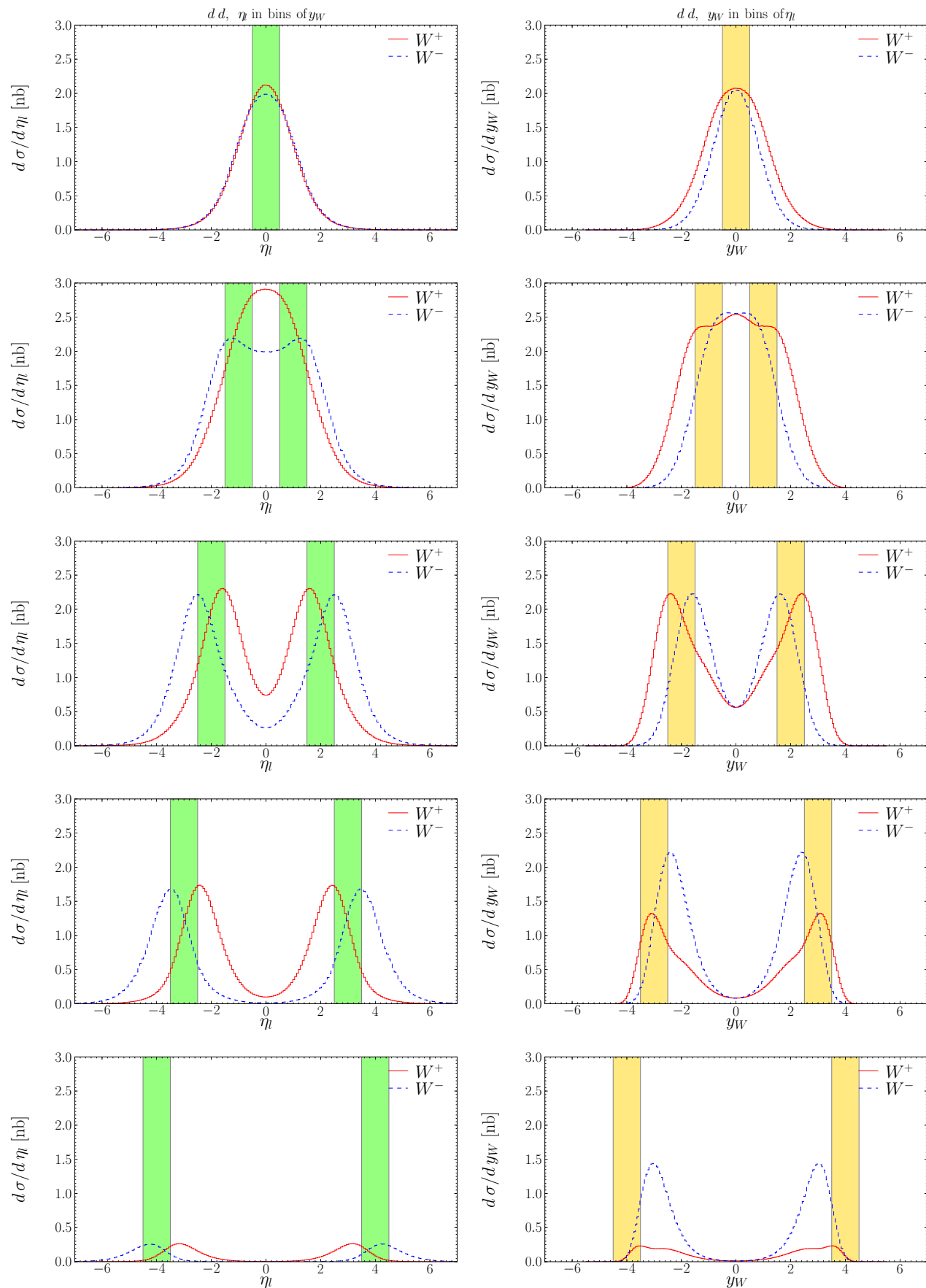


Figure 4.33: W boson rapidity distributions in bins of the charged lepton pseudo-rapidity (left) and *vice versa* (right) in the case of dd collisions with $\sqrt{S_{n_1 n_2}} = 7$ TeV. In each plot the corresponding y_W or η_l selection is materialised by the colored stripe(s).

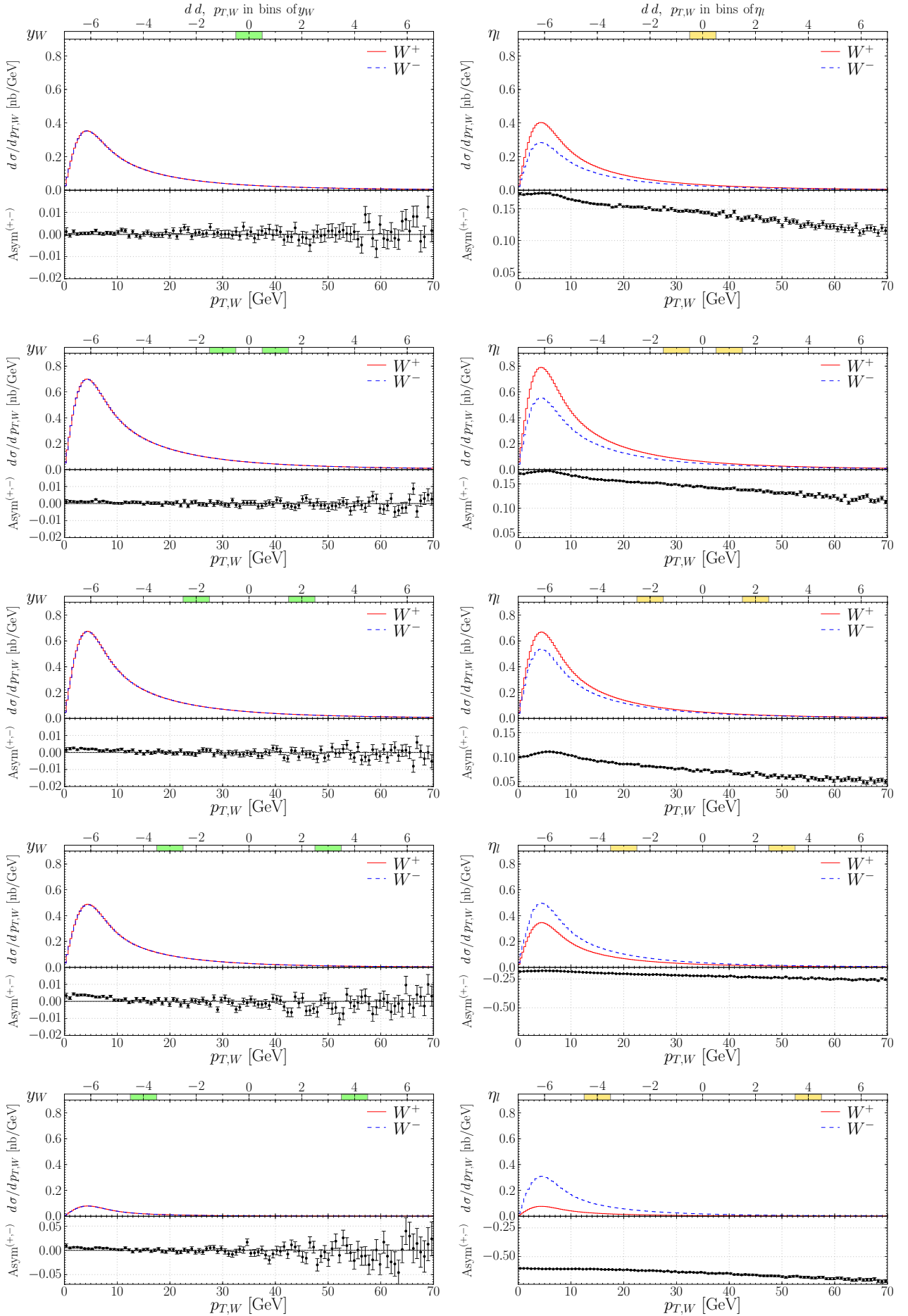


Figure 4.34: W boson transverse momentum in bins of y_W (left) and in bins of η (right) in dd collisions with $\sqrt{S_{n_1 n_2}} = 7$ TeV.

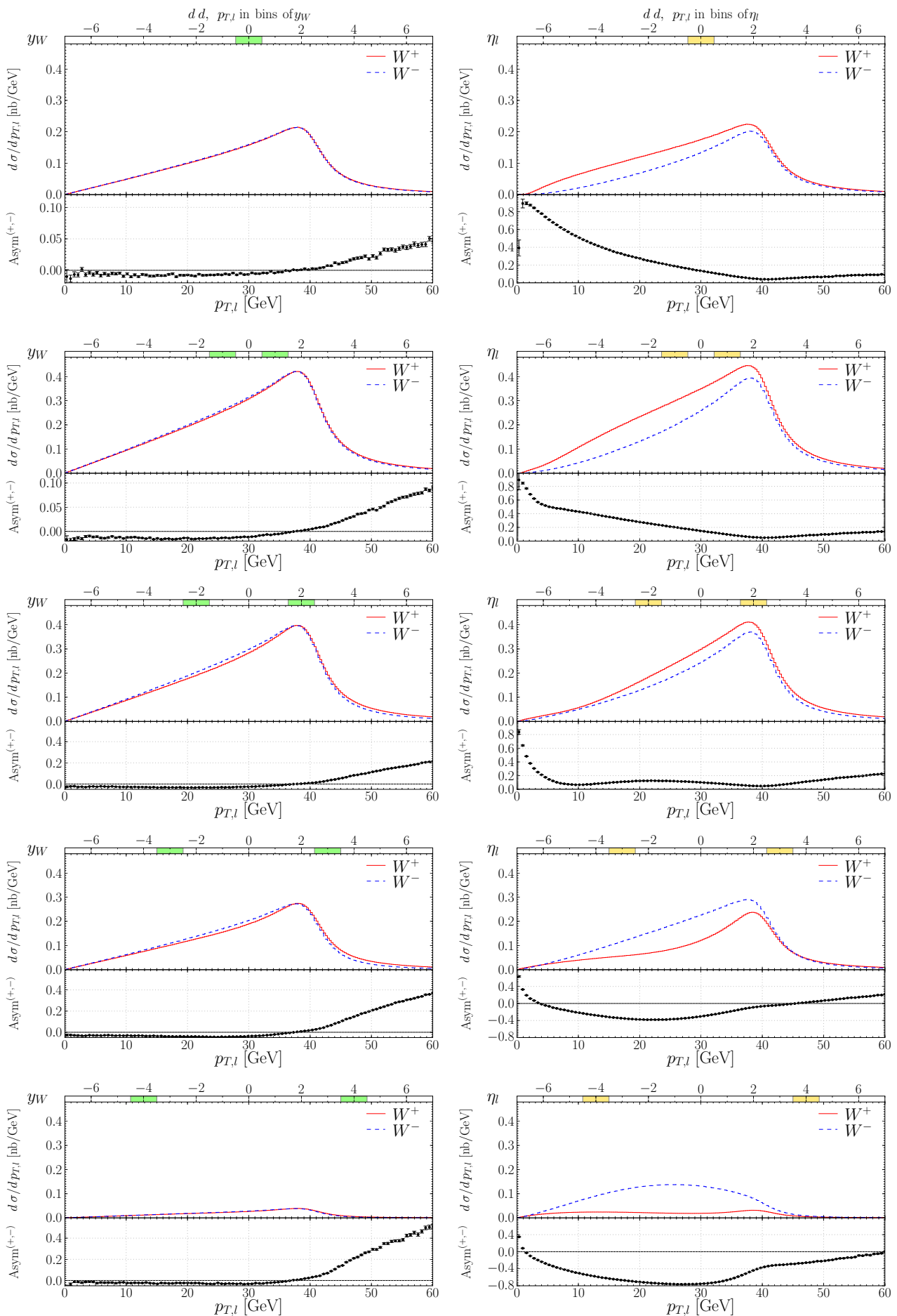


Figure 4.35: Charged lepton transverse momentum in bins of y_W (left) and in bins of η_l (right) in dd collisions with $\sqrt{S_{n_1 n_2}} = 7$ TeV.

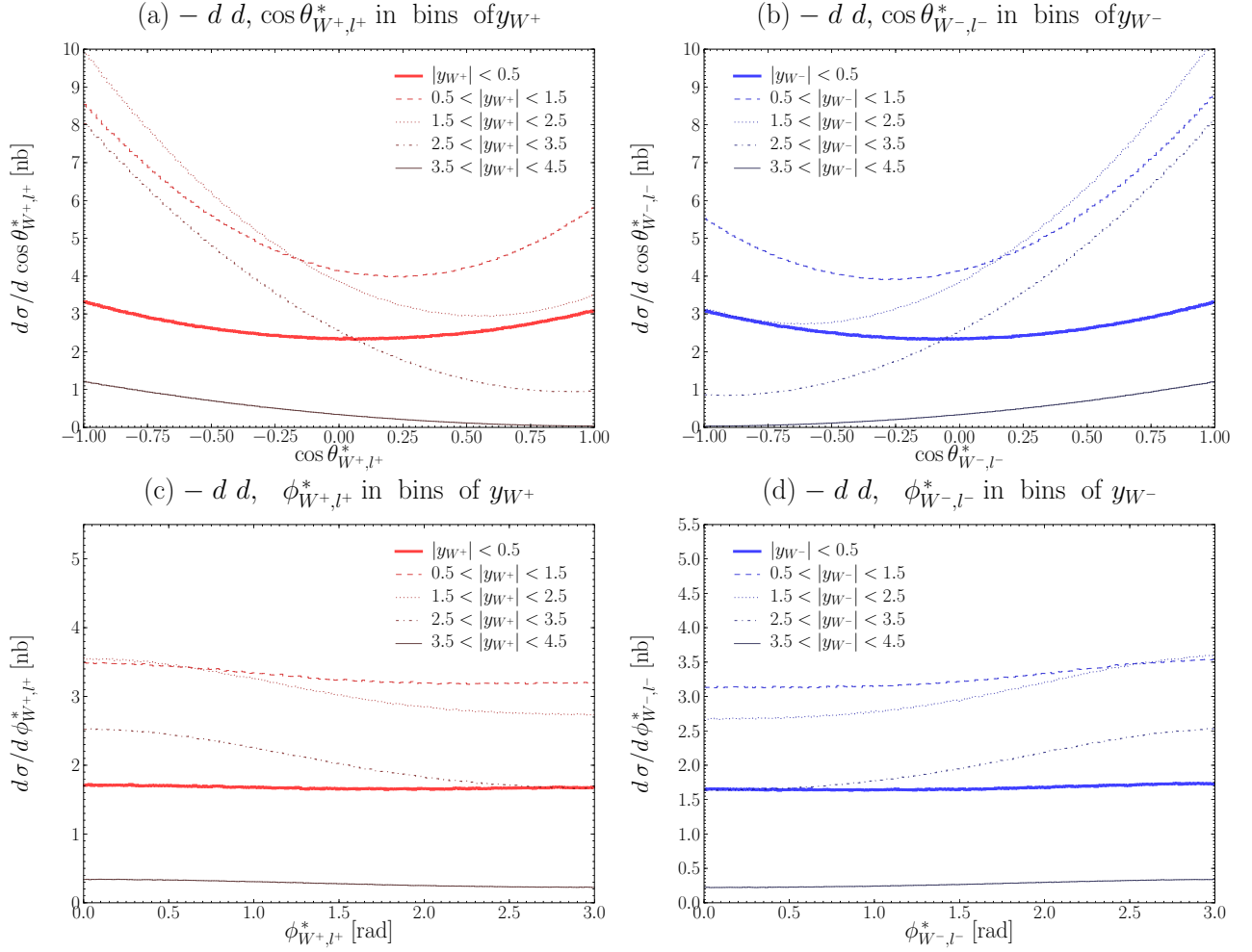


Figure 4.36: Distributions of $\cos \theta_{W,l}^*$ and $\phi_{W,l}^*$ in bins of y_W for the positively (a,c) and negatively (b,d) charged channel in dd collisions with $\sqrt{S_{n_1 n_2}} = 7$ TeV.

4.A.6 Transverse momentum of the (anti-)quarks for W in Drell–Yan

This sub-section presents more explanations on the transverse momenta unbalance between the valence quark and the sea anti-quark.

In most cases the valence quarks bring most of the energy in the collision. These $q^{(v)}\bar{q}'^{(s)}$ configurations with high x_q for the valence quark and low $x_{\bar{q}'}$ for the sea anti-quark are already well known. Now the thing is that a parton with a small x will have in general a higher transverse motion gained on its way to the collision by radiating gluons and photons (note also the low x (anti-)quark can be as well the product of the radiation of a gluon via $g \rightarrow q'\bar{q}'$).

Finally because of the CKM missing angles the other flavours such as \bar{s} , \bar{c} and \bar{b} have their transverse motion influenced as well. To emphasise this aspect let us note that in the case of the production of Z bosons since the previous flavours create Z bosons only via $s\bar{s}$, $c\bar{c}$, $b\bar{b}$ annihilation we observe $p_{T,q} = p_{T,\bar{q}}$ in those specific cases (we used for that the generator WINHAC which as said earlier can produce Z bosons, cf. § 3.1.2).

The previous ideas are illustrated in Fig. 4.37 with the histograms of the inclusive transverse momenta of the u and \bar{d} flavours in the W^+ production (a) and the one of the d and \bar{u} flavours in the W^- production (b). In both cases the sea quark shows larger probability to hold a high p_T while the valence quark holds a low p_T . These histograms were obtained, like the others, for a statistic of 200 millions of weighted events.

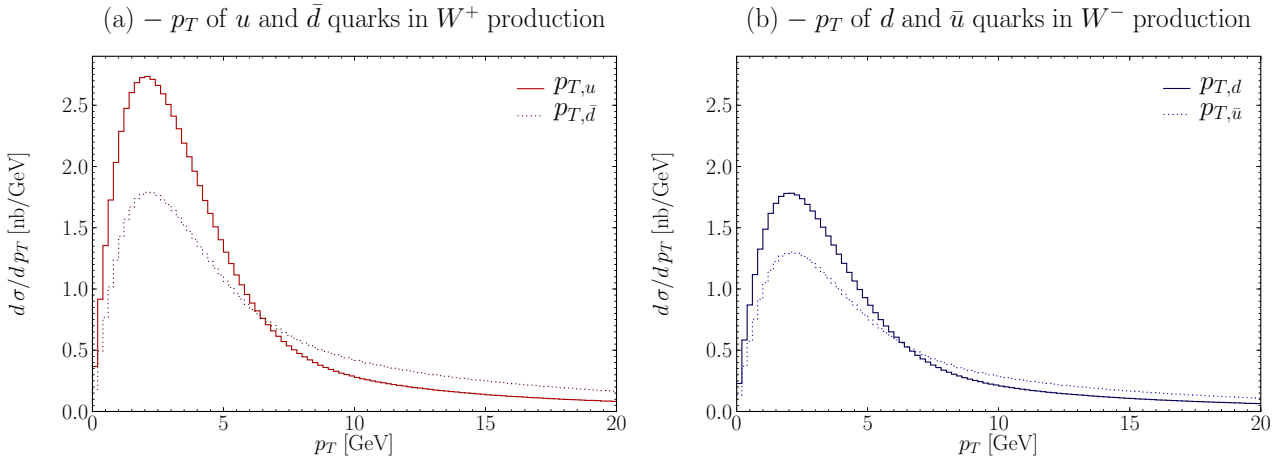


Figure 4.37: Transverse momenta of the u and \bar{d} quarks in W^+ production (a) along with the one of the d and \bar{u} quarks in W^- production (b).

The corresponding estimation of the average p_T of the u , \bar{u} and d , \bar{d} quarks are

$$\langle p_{T,u} \rangle \approx 7.05 \text{ GeV}, \quad \langle p_{T,\bar{d}} \rangle \approx 12.58 \text{ GeV} \quad \text{in } W^+ \text{ production} \quad (4.20)$$

$$\langle p_{T,d} \rangle \approx 7.65 \text{ GeV}, \quad \langle p_{T,\bar{u}} \rangle \approx 11.77 \text{ GeV} \quad \text{in } W^- \text{ production} \quad (4.21)$$

Anyhow in the previous values $u^{(s)}$ and $d^{(s)}$ values intervene, to factorise in a better way the asymmetries induced by the cases where there is a valence quark involved in the collisions we repeat the previous study putting to zero the sea contributions $u^{(s)}$ and $d^{(s)}$, in that context, the average p_T of the quarks in $q^{(v)}\bar{q}'^{(s)}$ “valence” contributions for W^+ production of

$$\langle p_{T,u^{(v)}} \rangle \approx 4.99 \text{ GeV} \longleftrightarrow \begin{cases} \langle p_{T,\bar{d}} \rangle \approx 14.91 \text{ GeV} \\ \langle p_{T,\bar{s}} \rangle \approx 15.77 \text{ GeV} \\ \langle p_{T,\bar{b}} \rangle \approx 21.97 \text{ GeV} \end{cases}, \quad (4.22)$$

and for $d^{(v)} \bar{q}'^{(s)}$ “valence” contributions in W^- production of

$$\langle p_{T,d^{(v)}} \rangle \approx 5.03 \text{ GeV} \longleftrightarrow \begin{cases} \langle p_{T,\bar{u}} \rangle \approx 14.64 \text{ GeV} \\ \langle p_{T,\bar{c}} \rangle \approx 16.88 \text{ GeV} \end{cases} \quad (4.23)$$

In both cases we observe that the valence quark holds a very low transverse motion with respect to the anti-quark. Note also that the transverse motion of the sea anti-quark increases with the mass of the quark.

Now these average p_T of the quarks for purely sea contribution are :

$$\langle p_{T,u^{(s)}} \rangle \approx 9.87 \text{ GeV} \longleftrightarrow \begin{cases} \langle p_{T,\bar{d}} \rangle \approx 9.04 \text{ GeV} \\ \langle p_{T,\bar{s}} \rangle \approx 10.71 \text{ GeV} \\ \langle p_{T,\bar{b}} \rangle \approx 16.19 \text{ GeV} \end{cases} \quad (4.24)$$

for the W^+ production. Because $u^{(s)} < d^{(s)}$ for $10^{-4} < x$ we observe $\langle p_{T,u^{(s)}} \rangle > \langle p_{T,\bar{d}} \rangle$ while it was the other way around for “valence” contributions. Also let us remark again that the higher the mass of a quark is the higher its transverse motion is. In the case of the W^- production we have

$$\langle p_{T,d^{(s)}} \rangle \approx 9.29 \text{ GeV} \longleftrightarrow \begin{cases} \langle p_{T,\bar{u}} \rangle \approx 9.97 \text{ GeV} \\ \langle p_{T,\bar{c}} \rangle \approx 12.69 \text{ GeV} \end{cases} \quad (4.25)$$

Let us remark that averaging the “valence” and purely sea contributions does not give exactly the values estimated when taking all contributions. This can be explained by the fact the proton’s integrity cannot be exactly factorised into “valence” and purely sea contributions.

4.A.7 Amplitude of the final state charge asymmetries in function of the energy in the collision

As observed in the study of deuteron–deuteron collisions the final state charge asymmetries in the observable $p_{T,l}$ is larger than for the case of proton–proton collisions. The energy in the collision is the parameter responsible for those effects. To see how this works we study $\text{Asym}^{(+,-)}(p_{T,l})$ as a function of the energy \sqrt{S} in the center of mass frame (Fig. 4.38.(a)). As \sqrt{S} increases we witness the decrease of the charge asymmetry. Knowing the charge asymmetry comes from “valence” contributions as the energy rise the charge symmetric purely sea contributions increases and we end up with a lower and lower proportion of asymmetry due to “valence” terms. Nonetheless, the asymmetry in the quarks p_T for “valence” contributions $q^{(v)} \bar{q}'^{(s)}$ increases with \sqrt{S} . We find for example in the two extreme cases and the nominal $\sqrt{S} = 14 \text{ TeV}$ collision mode :

$$\text{for } \sqrt{S} = 2 \text{ TeV} \quad : \quad \langle p_{T,u^{(v)}} \rangle \approx 4.73 \text{ GeV} \longleftrightarrow \langle p_{T,\bar{d}} \rangle \approx 8.43 \text{ GeV} \quad (4.26)$$

$$\text{for } \sqrt{S} = 14 \text{ TeV} \quad : \quad \langle p_{T,u^{(v)}} \rangle \approx 4.99 \text{ GeV} \longleftrightarrow \langle p_{T,\bar{d}} \rangle \approx 15.77 \text{ GeV} \quad (4.27)$$

$$\text{for } \sqrt{S} = 20 \text{ TeV} \quad : \quad \langle p_{T,u^{(v)}} \rangle \approx 4.99 \text{ GeV} \longleftrightarrow \langle p_{T,\bar{d}} \rangle \approx 15.90 \text{ GeV} \quad (4.28)$$

To emphasise the increase of the asymmetry in absolute as \sqrt{S} grows we look at the bare difference of the positively and negatively charged histograms. This is shown in Fig. 4.38.(b), the purely sea contributions giving exactly the same contributions we are left with the difference between the “valence” terms only.

Anyhow, the important idea here is to understand that the energy in the collision which is lower in the hypothetical case of dd collisions runs at the LHC forces us to deal with larger charge asymmetries with respect to the seen in pp collisions runs. This will explain the different behaviour of the systematic analysis prospect between dd and pp collisions in the next and final Chapter.

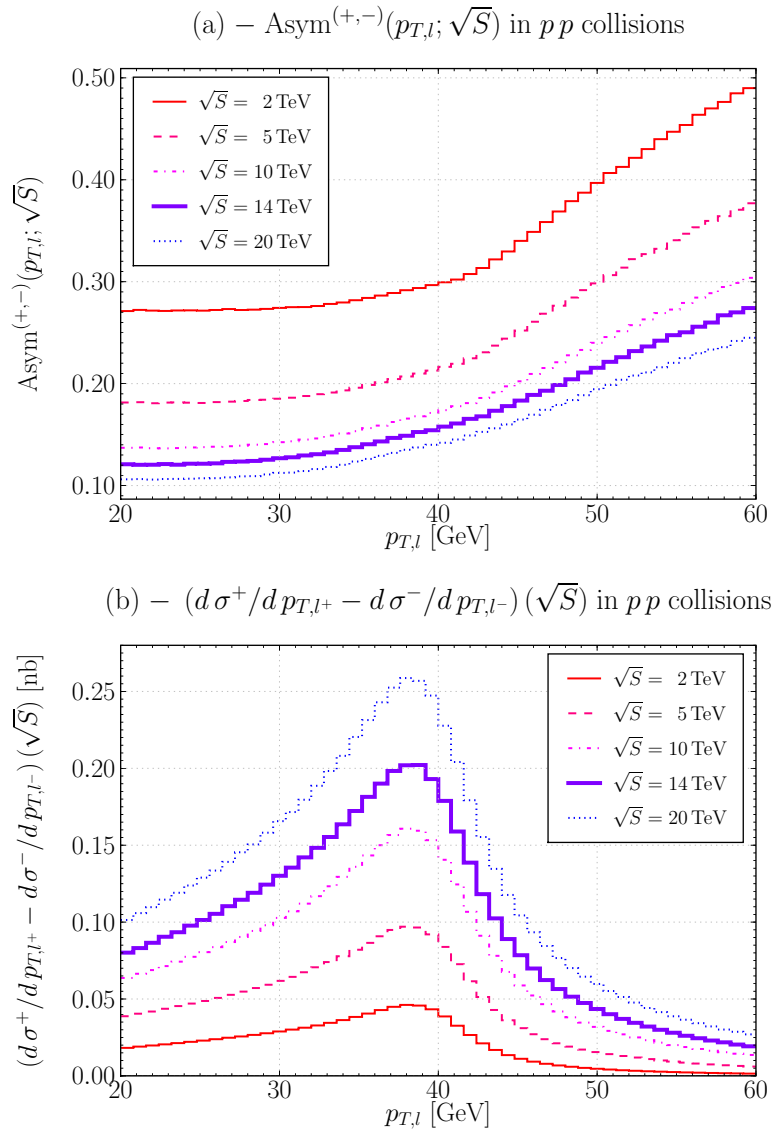


Figure 4.38: Charge asymmetry (a) and bare difference (b) of the transverse momenta distributions of the charged leptons for several values of \sqrt{S} .

Chapter 5

Strategy for a reduction of the systematic errors on $M_{W^+} - M_{W^-}$

“But then . . .” I venture to remark, “you are still far from the solution. . . .”
“I am very close to one,” William said, “but I don’t know which.”
“Therefore you don’t have a single answer to your questions ?”
“Adso, if I did I would teach theology in Paris.”
“In Paris do they always have the true answer ?”
“Never,” William said, “but they are very sure of their errors.”

The Name of the Rose
UMBERTO ECCO

Here we finally present the dedicated strategies that were devised –based on the knowledge built throughout Chapter 4– to prepare a measurement of $M_{W^+} - M_{W^-}$ at the LHC. As already mentioned in the first Chapter while at the Tevatron the statistical and systematic errors where of the same order at the LHC the first one will drop to ≈ 5 MeV for just one year of harvesting data at low luminosity. On the other hand the systematic error will be still important and we show how using the LHC and ATLAS detector capabilities we could eventually decrease those systematic errors and thus enhance by a factor 20 the actual precision on $M_{W^+} - M_{W^-}$. The most important results below were presented in Ref. [146].

The Chapter is divided as follow. The first Section presents the strategies and observables developed in our collaboration which, according to us, should be more robust to address this particular measurement at the LHC. Following that a presentation of the general context for studying W in Drell–Yan is briefly reminded. The second Section describes the principle of the analysis to extract the mass parameter for both the classic and the new suggested methods. The third Section addresses the sources of theoretical and experimental systematic errors that should be taken into account in the estimation of the error on this measurement. Finally in the last Section our strategies robustness with respect to both theoretical and apparatus unknowns addressed in our analysis are improved on the example of the simulation of one year of data taking at low luminosity.

5.1 Measurement strategies

5.1.1 Event selection

As mentioned earlier the extraction of the W and Z bosons properties is achieved by studying their electronic and muonic decays, that is respectively $W \rightarrow l \nu_l$ and $Z \rightarrow l^+ l^-$. The choice for leptonic decays is motivated by the fact the di-jet background is of several orders of magnitude more important than the $W \rightarrow q \bar{q}'$ and $Z \rightarrow q \bar{q}$ signals we would be interested in while the leptonic decays provide clean processes (*i.e.* absence of QCD in the final state) with large cross sections. The decays to the

tau channel is not considered though because the mass of the charged τ is such that it decays within $\approx 300 \times 10^{-15}$ s, which leads to at least two neutrinos to deal with for the detection of the final state.

The particular study of the W^+ and W^- bosons is made by splitting the data collected for the W bosons into positively and negatively charged leptons in the final state to get the corresponding W^+ and W^- data. The main criteria used in hadronic collider to study W bosons are to have a high energy charged lepton in the high precision detector volume of the detector associated with high transverse missing energy \cancel{E}_T that betrays the presence of the neutrino. Also, to reduce the background, rejection are made using constraints on the recoil \vec{u} defined as the sum of all momenta recoiling against the W system

$$\vec{u} \equiv -\vec{p}_W, \quad (5.1)$$

$$= -\vec{p}_l - \vec{p}_{\nu_l}, \quad (5.2)$$

but again, due to the non possibility to measure the longitudinal component of the particles escaping the beam-pipe, its transverse component u_T is considered instead.

From the total number of events produced inclusively (Eq. (2.5)) now must be taken into account the effects of the acceptance selection, the reconstruction efficiency and the background processes whose kinematics can lure the trigger to recognise them as lepton pair decaying from single W . Taking that into account, eventually the number of W candidates $N_W^{(\text{candidates})}$ from Drell–Yan are

$$N_W^{(\text{candidates})} \equiv N_W^{(\text{acc.})} + N_W^{(\text{bckg.})}, \quad (5.3)$$

where $N_W^{(\text{acc.})}$ is the number of accepted W events by the cuts and $N_W^{(\text{bckg.})}$ is the number of background events. The expression of $N_W^{(\text{acc.})}$ reads

$$N_W^{(\text{acc.})} = L \sigma_W^{(\text{cut})} \varepsilon, \quad (5.4)$$

where L the integrated luminosity, $\sigma_W^{(\text{cut})}$ the cross section that the $W \rightarrow l\nu_l$ events fulfill the selection requirements and ε is the efficiency reconstruction for the signal in the given fiducial region. The number of background events can be expressed like

$$N_W^{(\text{bckg.})} = L \sigma_{W \text{ bckg.}}^{(\text{cut})} \varepsilon + B, \quad (5.5)$$

where $\sigma_{W \text{ bckg.}}^{(\text{cut})}$ is the cut cross section of all the processes that displays kinematics in their final state that mimic the features of the final state leptons from Drell–Yan W and B is the contribution term due to the electronic noise, the cavern background, *etc.* Below, more details on these criteria are given for the case of CDF, ATLAS and finally for our stand-alone analysis prospect.

Event selection in CDF. In CDF II [51] a Drell–Yan W is recognised by having at least one lepton candidate in the central region ($|\eta_l| \lesssim 1$) and by applying the following narrowing selection on the kinematics :

- The charged lepton p_T must verify : $30 \text{ GeV} < p_{T,l} < 55 \text{ GeV}$.
- The neutrino p_T , deduced from the measurement of \cancel{E}_T , must verify : $30 \text{ GeV} < \cancel{p}_{T,\nu_l} < 55 \text{ GeV}$.
- The leptons transverse mass must verify : $60 \text{ GeV} < m_{T,l\nu_l} < 100 \text{ GeV}$
- The transverse recoil must verify : $u_T < 15 \text{ GeV}$.

Additional cuts are made to reject background from Z leptonic decays. Eventually the measurement of the W properties in Ref. [51] based on these selection criteria provided $\approx 50,000$ candidates events for $W \rightarrow \mu\nu_\mu$ ($L \approx 191 \text{ pb}^{-1}$) and $\approx 64,000$ candidates events for $W \rightarrow e\nu_e$ ($L \approx 220 \text{ pb}^{-1}$).

Expected event selection in ATLAS. In ATLAS, although no data is there yet to confirm which criteria would fit the best the LHC context the adopted requirements taken from Ref. [71] are:

- Have a charged muon or isolated electron with $p_{T,l} > 20$ GeV in the precision physics acceptance volume ($|\eta_l| < 2.5$).
- Have a missing transverse energy of $\cancel{E}_T > 20$ GeV.
- No jets in the event with $p_T > 30$ GeV to reject backgrounds from jets and $t\bar{t}$ events.
- A recoil $u_T < 50$ GeV to avoid too much the influence of the $p_{T,W}$ smearing on the leptons observables

In ATLAS, these constraints should be such that from the ≈ 350 millions of W bosons produced for an integrated luminosity of $L = 10 \text{ fb}^{-1}$ only 60 millions should be accepted (no matter the charge or the decay channel).

Event selection for the present study. The W boson production events used in our studies are selected by requiring that the simulated decaying charged electron or muon satisfy the following requirements:

$$p_{T,l} > 20 \text{ GeV} \quad \text{and} \quad |\eta_l| < 2.5. \quad (5.6)$$

We assume that by using a suitable \cancel{E}_T cut the impact of the uncertainty in the background contribution on the measurement of the charge asymmetry of the W boson mass at the LHC can be made negligible. This allows us to skip the generation and simulation of the background event samples for our studies. It has to be stressed that the above assumption is weaker for the measurement of the charge asymmetry than for the measurement of the average W boson mass [57, 58] because, to a good approximation, only the difference of the background for the positive and negative lepton samples will bias the measurement. The presentation of the results of our studies is largely simplified by noticing that they are insensitive to the presence of the \cancel{E}_T cut in the signal samples. Therefore, the results are based on selection of events purely on the basis of the reconstructed charged lepton kinematics variables as shown in Eq. (5.6). Studies have shown that these results will remain valid whatever \cancel{E}_T cut will be used at the LHC to diminish the impact of the background contamination at the required level of precision. To be more precise, in our simple model this \cancel{E}_T cut was emulated by a direct \cancel{p}_{T,ν_l} cut. Nonetheless, in the specific purpose of a cut, this approximation is believed to be fully justified.

The detector response is based on the ATLAS tracker which, for reminder, was emulated using Gaussian resolutions for p_T and $\cotan \theta$ of the charged electron and muons according to Eqs. (2.15–2.16).

Concerning the statistic, in absence of background and imperfect reconstruction efficiencies, we simply have

$$N_W^{(\text{acc.})} = L \sigma_W^{(\text{cut})}. \quad (5.7)$$

The cut cross section corresponding to the requirements of Eq. (5.6) and for the expected LHC energies for pp (Eq. (2.11)) and dd (Eq. (2.12)) collisions are compiled in Table 5.1. Table 5.2 gives the correspondence in terms of number of events obtained by using the respective integrated luminosities for pp and dd collisions (Eqs. (2.11–2.12)) in Eq. (5.7).

5.1.2 Observables

The values of the W^+ and W^- boson masses can be unfolded from the measured lepton charge distributions $p_{T,l}$, \cancel{p}_{T,ν_l} and from the transverse mass $m_{T,l\nu_l}$. We discuss only the methods based on the measurement of $p_{T,l}$. These methods are almost insensitive to the detector and modeling biases in the reconstructed values of the neutrino transverse momentum p_{T,ν_l} . We are aware that,

Collisions	$\sigma_{W^+}^{(\text{incl.})}$ [nb]	$\sigma_{W^-}^{(\text{incl.})}$ [nb]	$\sigma_W^{(\text{incl.})}$ [nb]	$\sigma_{W^+}^{(\text{cut})}$ [nb]	$\sigma_{W^-}^{(\text{cut})}$ [nb]	$\sigma_W^{(\text{cut})}$ [nb]
pp	19.81	14.72	34.53	10.95	7.92	18.87
dd	32.52	32.44	64.96	22.14	17.75	39.89

Table 5.1: Inclusive ($\sigma^{(\text{incl.})}$) and cut ($\sigma^{(\text{cut})}$) cross sections σ_{W^+} , σ_{W^-} and σ_W for pp ($\sqrt{S} = 14 \text{ TeV}$) and for dd ($\sqrt{S}_{n_1 n_2} = 7 \text{ TeV}$ in the $n_1 n_2$ nucleon–nucleon center of mass energy).

Collisions	$N_{W^+}^{(\text{incl.})}$	$N_{W^-}^{(\text{incl.})}$	$N_W^{(\text{incl.})}$	$N_{W^+}^{(\text{acc.})}$	$N_{W^-}^{(\text{acc.})}$	$N_W^{(\text{acc.})}$
pp	198.1	147.2	345.3	109.5	79.2	188.7
dd	81.3	81.1	162.4	55.3	44.4	99.7

Table 5.2: Produced inclusive and accepted millions ($\times 10^6$) of events (for $p_{T,l} > 20 \text{ GeV}$ and $|\eta_l|, 2.5$) for W^+ , W^- and W for one year of data collection at low luminosity ($L = 10 \text{ fb}^{-1}$ for pp and $L = 2.5 \text{ fb}^{-1}$ for dd).

for the measurement of the average mass of the W boson, this merit is outbalanced by the drawback of their large sensitivity to the precise understanding of the distribution of the W boson transverse momentum $p_{T,W}$ (Fig. 1.15). However, for the measurement of the charge asymmetry of the masses this is no longer the case because QCD radiation –which drives the shape of the $p_{T,W}$ distribution– is independent of the charge of the produced W boson. In our view the $p_{T,l}$ based methods will be superior with respect to the $m_{T,l\nu_l}$ based ones, in particular for the first measurements of the W mass charge asymmetries at the LHC.

(a) Commonly used observables

In the context of a $p_{T,l}$ based method for the extraction of $M_{W^+} - M_{W^-}$, the most natural method is to analyse separately the l^+ and l^- event samples and determine independently the masses of the W^+ and W^- bosons. This method, that will be investigated, is based on independent measurements of the $d\sigma/dp_{T,l^+}$ and $d\sigma/dp_{T,l^-}$ distributions. It will be called hereafter the classic method and actually corresponds to what physicists did at with the CDF detector to provide measurements of $M_{W^+} - M_{W^-}$.

(b) The charge asymmetry

A new method proposed and evaluated in our collaboration is based on the measurement of the charge asymmetry (Eq. (1.7)) of the $p_{T,l}$ distribution. This method will be called hereafter the charge asymmetry method. The distribution of $\text{Asym}^{(+,-)}(p_{T,l})$ is, by definition, robust with respect to those of systematic measurement effects and those of model dependent effects that are independent of the lepton charge. The acceptance, and the lepton selection efficiency corrections for this observable will, in the leading order approximation, reflect only their lepton charge dependent asymmetries. In addition, the $\text{Asym}^{(+,-)}(p_{T,l})$ observable is expected to be robust with respect to the modeling uncertainty of the QCD and QED radiation processes.

If extrapolated from the experience gained at the Tevatron (cf. Appendix 2.A), the precision of the charge asymmetry method will be limited by the understanding of relative biases in the reconstructed transverse momenta for positively and negatively charged particles (cf. § 2.4). These biases, contrary to the lepton charge averaged biases, cannot be controlled using the J/ψ , Υ and Z “standard candles” that helps only to correct for the absolute energy scale. This problem leads us to the third and final observable for our study : the double charge asymmetry.

(c) The double charge asymmetry

The double charge asymmetry is defined like

$$\text{DAsym}^{(+,-)}(\rho_{T,l}) \equiv \frac{1}{2} \left[\text{Asym}_{\vec{B}=B\vec{e}_z}^{(+,-)}(\rho_{T,l}) + \text{Asym}_{\vec{B}=-B\vec{e}_z}^{(+,-)}(\rho_{T,l}) \right], \quad (5.8)$$

where the variable $\rho_{T,l}$ defined like $\rho_{T,l} \equiv 1/p_{T,l}$ (cf. § 1.3), represents the radius of the track curvature at the W boson production vertex in the plane $r - \phi$ perpendicular to the beam collision axis and B is the strength of the solenoidal magnetic field bathing the inner tracker. The choice on $\rho_{T,l}$ was cast to follow the notation adopted in our former work [145]. The measurement method using the $\text{DAsym}^{(+,-)}(\rho_{T,l})$ distribution will be called hereafter the double charge asymmetry method.

The $\text{DAsym}^{(+,-)}(\rho_{T,l})$ distribution is expected to be robust with respect to the charge dependent track measurement biases if the following two conditions are fulfilled: (1) the inversion of the z -component of the magnetic field in the tracker volume can be controlled to a requisite precision and (2) the $\vec{E} \times \vec{B}$ Lorentz drift relative corrections to the reconstructed hit positions for the two magnetic field configurations, in the silicon tracker could be determined to a requisite precision. Discussing these two conditions in details is beyond the scope of this work. Nonetheless the second point, in view of the ATLAS detector design was considered qualitatively in our work [111] with regard to the specificity of the pixel, SCT and TRT barrel modules.

First, the inversion of the magnetic field should *a priori* have no influence on the TRT intrinsic capabilities since the measurement of the hit is based solely on the time it takes for electrons to drift to the center wire as shown in Fig. 2.18.(b). Then, reverting the magnetic field should reverse the drift paths of the electron but not affect the drift time. Concerning the SCT barrel modules the tilt angle for the invert magnetic field configuration is now worsening the nominal hit resolution as depicted in Fig. 5.1. In the best case scenario the Lorentz drift angle made by the drifting electrons is well under control and the resolution of the SCT for the inverted magnetic field should be well accounted. If that would not be the case then the resolution of the SCT modules will change. Nonetheless the double layer feature of silicon wafers, by providing an average offline hit position, should help to tackle such problems. This is no longer the case for the pixel detector whose modules possess only one layer. As

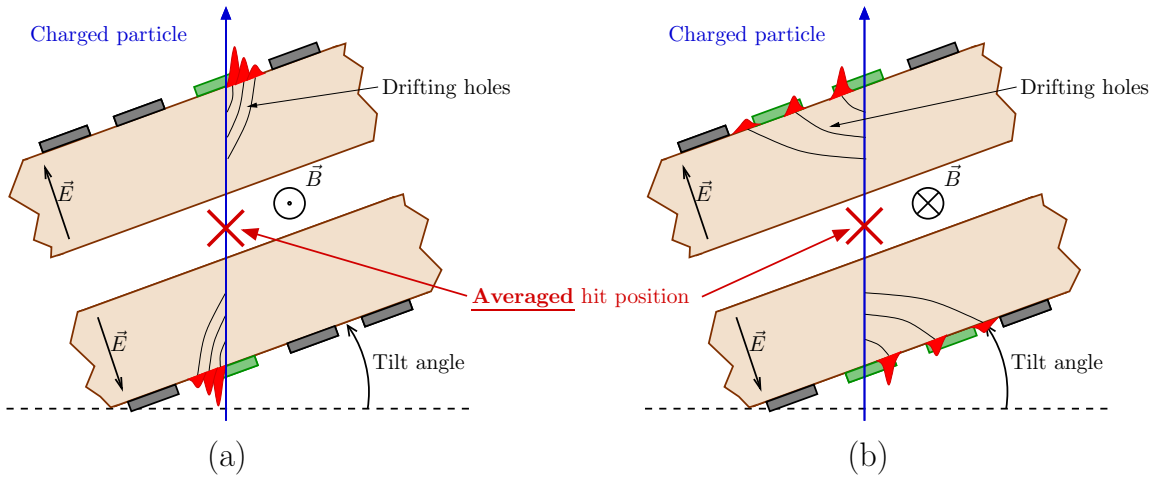


Figure 5.1: Schematic representation of the reconstructed hit in a barrel module of the SCT detector for the nominal (a) and inverted (b) configurations of the solenoidal magnetic field.

seen previously the pixel hits are important as they provide data on the particles before they start to lose energy to the apparatus and also because of the important lever arm they have for the track fitting reconstruction procedure. Here, to each event, looking at the origins of the other particles tracks should help for a possible correction of the production vertex of the W leptonic decay.

To conclude, in Fig. 5.2 we show the distributions of $d\sigma/dp_{T,l}$ and $\text{Asym}^{(+,-)}(p_{T,l})$ for: (1) the generated and unselected sample of events, (2) the generated and selected sample of events and (3) the unbiased simulated detector response and selected sample of events. The corresponding histograms in $p_{T,l}$ -space can be seen in Figs. 5.7.(a), (b) and (c) of Appendix 5.A. The analysis of the systematic biases affecting these distributions allows to evaluate the precision of the measurement methods discussed in this section.

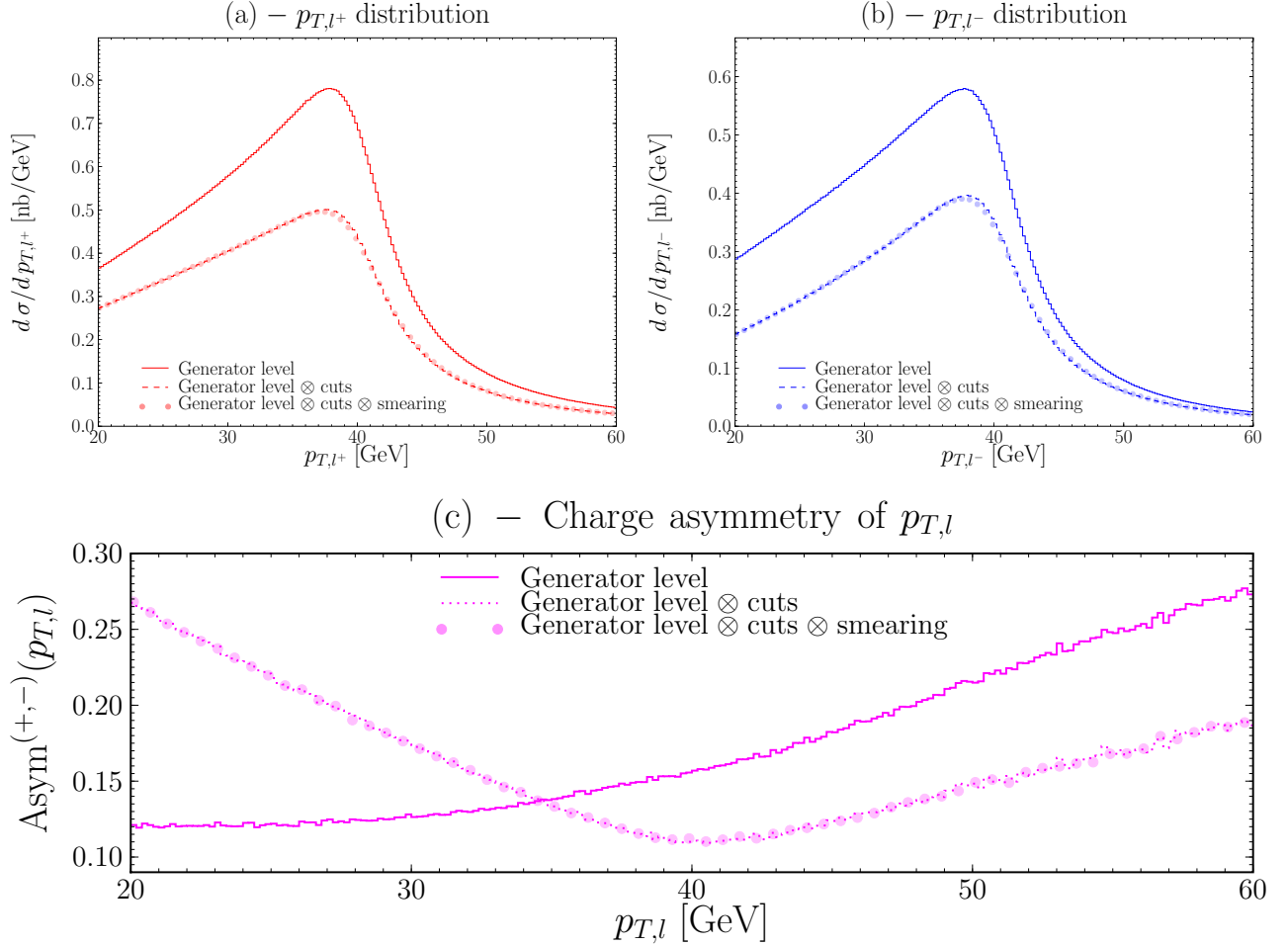


Figure 5.2: The $p_{T,l}$ distributions for the positive (a) and negative (b) leptons and $\text{Asym}^{(+,-)}(p_{T,l})$ at the generator level, after the cuts ($p_{T,l} > 20$ GeV and $|\eta_l| < 2.5$), and finally, by adding the inner detector smearing.

5.1.3 The machine and the detector settings

The primary goal of the ATLAS and other LHC experiments is to search for new phenomena at the highest possible collision energy and machine luminosity. It is obvious that, initially, the machine and the detector operation modes will be optimised for the above research program. The main target presented here is to evaluate the precision of the measurement of the W mass charge asymmetry which is achievable in such a phase of the detector and machine operation.

A natural extension of this work is to go further and investigate if, and to which extent, the precision of measurement of the Standard Model parameters could be improved in dedicated machine and detector setting runs. In our first work [145] we discussed the role of: (1) dedicated runs with reduced beam collision energies, (2) dedicated runs with isoscalar beams and (3) runs with dedicated detector magnetic field settings; in optimising the use of the Z boson production processes as a

“standard candle” for the W boson processes. Here some of these dedicated settings were found to be of interest but the most important ones were devised in the particular context of this measurement of $M_{W^+} - M_{W^-}$. More precisely, we discuss the possible improvement in the measurement precision of the charge asymmetry of the W boson mass which can be achieved (1) by replacing the proton beams with light isoscalar-ion beams and (2) by running the detector for a fraction of time with the inverse direction of the solenoidal magnetic field. These and other dedicated operation modes could be tried in the advanced “dedicated measurement phase” of the LHC experimental program. Such a phase, if ever happens, could start following the running period when the collected luminosity will become a linear function of the running time and the gains/cost ratio of its further increase will be counterbalanced by the gains/cost ratio of running dedicated machine and detector operation modes.

5.2 The analysis method

In this section we present the technical aspects of the analysis method used in the evaluation of the achievable precision of the measurement of the charge asymmetry of the W boson masses, $M_{W^+} - M_{W^-}$, denoted sometimes for a matter of convenience $\Delta_{(+,-)}$.

The shapes of the experimental distribution (generator level \otimes cuts \otimes smearing) shown in Fig. 5.2 are sensitive to: (1) the assumed values of M_{W^+} and M_{W^-} , (2) the values of the other parameters of the Standard Model, (3) the modeling parameters of the W boson production processes and (4) the systematic measurement biases. Our task is to evaluate the impact of the uncertainties of (2), (3) and (4) on the extracted values of M_{W^+} and M_{W^-} for each of the proposed measurement methods. It is done using a likelihood analysis of the distributions for the pseudo-data (\mathcal{PD}) event samples and those for the mass template (\mathcal{MT}) event samples. Each \mathcal{PD} sample represents a specific measurement or modeling bias, implemented respectively in the event simulation or event generation process. Each \mathcal{MT} sample was generated by assuming a specific M_{W^+} (M_{W^-}) value or a value of their charge asymmetry $\Delta_{(+,-)}$. The \mathcal{MT} samples are simulated using the unbiased detector response and fixed values of all the parameters used in the modeling of the W boson production and decays except for the mass parameters. The likelihood analysis, explained below in more detail, allows us: (1) to find out which of the systematic measurement and modeling errors, could be falsely absorbed into the measured value of the W boson masses and (2) to evaluate quantitatively the corresponding measurement biases.

5.2.1 Likelihood analysis

Let us consider, as an example, the impact of a systematic effect ξ on the bias in the measured value of the W^+ mass determined from the likelihood analysis of the $d\sigma/dp_{T,l^+}$ distributions. Since some of the upcoming results were carried based on $\rho_{T,l}$ observable as well we mention already the correspondence in terms of resolution and range.

The simulation of the pseudo-data event sample, \mathcal{PD} , representing a given systematic bias ξ , is carried out for a fixed value of the mass $M_W^{(\text{ref.})}$. Subsequently, a set of the $2\mathcal{N} + 1$ unbiased (*i.e.* $\xi = 0$) template data samples \mathcal{MT} is simulated. Each sample n of the \mathcal{MT} set corresponds to a given value of

$$M_{W^+}^{(n)} = M_W^{(\text{ref.})} + \delta M_{W^+}^{(n)}, \quad (5.9)$$

with $n = \{-\mathcal{N}, \dots, \mathcal{N}\}$ and where for the rest of the document $M_W^{(\text{ref.})} = 80.403$ GeV. The likelihood between the binned $d\sigma/dp_{T,l^+}$ distributions for the n^{th} \mathcal{MT} sample and the ξ -dependent \mathcal{PD} sample is quantified in terms of the χ^2 value:

$$\chi^2(p_{T,l^+}; \xi, n) = \sum_i^{N_{\text{bins}}^{\text{tot.}}} \frac{(d\sigma_{i;\xi} - d\sigma_{i;\xi=0,n})^2}{(\Delta d\sigma_{i;\xi})^2 + (\Delta d\sigma_{i;\xi=0,n})^2}, \quad (5.10)$$

where $d\sigma_i \equiv d\sigma_i/dp_{T,l+}$ is the content of the i^{th} bin of the histogram entering in the analysis and $\Delta d\sigma_i$ is the corresponding statistical error. In total, $N_{\text{bins}}^{\text{tot}}$ bins enters in the analysis, it represents the degrees of freedom (dof), $\text{dof} \equiv N_{\text{bins}}^{\text{tot}}$. The bulk of the results presented has been obtained using a bin size corresponding to $\delta p_{T,l} = 200 \text{ MeV}$ (respectively $\delta \rho_{T,l} = 0.2 \text{ MeV}^{-1}$) which is approximately the anticipated measurement resolution of the track curvature [96] and the summation range satisfying the following condition for $p_{T,l}$ ($\rho_{T,l}$)

$$30 \text{ GeV} < p_{T,l} < 50 \text{ GeV} \quad (0.02 \text{ GeV}^{-1} < \rho_{T,l} < 0.03 \text{ GeV}^{-1}), \quad (5.11)$$

which corresponds to degrees of freedom of $\text{dof}_{p_{T,l}} = 100$ ($\text{dof}_{\rho_{T,l}} = 49$). This choice is justified as the CDF II measurements were realised for the $p_{T,l}$ observable in the range $32 \text{ GeV} < p_{T,l} < 48 \text{ GeV}$ to get rid as much of the background by focusing on the jacobian peak region.

The $\chi^2(p_{T,l+}; \xi, n)$ dependence upon $\delta M_{W^+}^{(n)}$ is fitted by a polynomial of second order. The position of the minimum, $M_{W^+}(\xi)_{\text{min}}$, of the fitted function determines the systematic mass shift $\Delta M_{W^+}(\xi) = M_{W^+}(\xi)_{\text{min}} - M_{W^+}^{(\text{ref.})}$ due to the systematic effect ξ . If the systematic effect under study can be fully absorbed by a shifted value of W^+ , then the expectation value of $\chi_{\text{min}}^2/\text{dof}$ is ≈ 1 and the error on the estimated value of the mass shift, $\delta(\Delta M_{W^+}(\xi))$, can be determined from the condition $\chi^2(M_{W^+}(\xi)_{\text{min}} + \delta(\Delta M_{W^+}(\xi))) \equiv \chi_{\text{min}}^2 + 1$ (see Ref. [1] for further details on this topic).

Of course, not all the systematic and modeling effects can be absorbed into the variation of a single parameter, even if the likelihood is estimated in a narrow bin-range, purposely chosen to have the highest sensitivity to the mass parameters. In such cases the value of $\chi_{\text{min}}^2/\text{dof}$ can be substantially larger than 1, and $\delta(\Delta M_{W^+}(\xi))$ loses its statistical meaning. This can partially be recovered by introducing additional degrees of freedom (the renormalisation of the \mathcal{PD} samples, discussed later on in § 5.2.3, is an example of such a procedure). However, even in such a case the estimated value of $\delta(\Delta M_{W^+}(\xi))$ will remain slightly dependent upon the number of the $2\mathcal{N} + 1$ \mathcal{MT} samples, more precisely their M_{W^+} spacing in the vicinity of the minimum and the functional form of the fit. Varying these parameters in our analysis procedure in a ξ -dependent manner would explode the PC farm CPU time and was abandoned. Instead, we calibrated the propagation of statistical bin-by-bin errors into the $\delta(\Delta M_{W^+}(\xi))$ error, and checked the biases of all the aspects of the above method using the statistically independent “ \mathcal{PD} -calibration samples” in which, instead of varying the ξ effects, we varied the values of M_{W^+} .

5.2.2 The \mathcal{MT} and \mathcal{PD} event samples

(a) Classic method

In the classic method the bias of $\Delta_{(+,-)}(\xi)$ resulting from the systematic effects ξ is determined in the following three steps:

1. Determine $\Delta M_{W^+}(\xi) \pm \delta[\Delta M_{W^+}(\xi)]$ using $\chi^2(d\sigma/dp_{T,l+}; \xi)$.
2. Determine $\Delta M_{W^-}(\xi) \pm \delta[\Delta M_{W^-}(\xi)]$ using $\chi^2(d\sigma/dp_{T,l-}; \xi)$.
3. Combine these results and derive respectively the central error for $\Delta_{(+,-)}(\xi)$ and the associated error $\delta[\Delta_{(+,-)}(\xi)]$ by adding up quadratically the errors on each charged channel

$$\Delta_{(+,-)}(\xi) \equiv \Delta M_{W^+}(\xi) - \Delta M_{W^-}(\xi), \quad (5.12)$$

$$\delta[\Delta_{(+,-)}(\xi)] \equiv \sqrt{(\delta[\Delta M_{W^+}(\xi)])^2 + (\delta[\Delta M_{W^-}(\xi)])^2} \quad (5.13)$$

In the generation of the \mathcal{PD} samples we assumed $M_{W^+}^{\mathcal{PD}} = M_{W^-}^{\mathcal{PD}} = M_W^{(\text{ref.})}$. The \mathcal{MT} samples have been generated for $\delta M_{W^+}^{(n)} = \delta M_{W^-}^{(n)} = n \times 5 \text{ MeV}$ with $n = \pm 1, \dots, \pm 6$ and for $\delta M_{W^+}^{(n)} = \delta M_{W^-}^{(n)} = \pm 40, \pm 50, \pm 75, \pm 100, \pm 200 \text{ MeV}$ with $n = \pm 7, \dots, \pm 11$. In total 46 \mathcal{MT} samples, corresponding

to $\mathcal{N} = 11$, have been generated. Table 5.3 recaptures in the left column the shifted values from the $M_W^{(\text{ref.})}$ used to generate both positive and negatively W bosons \mathcal{MT} .

This procedure is illustrated in Fig. 5.3 where, for convenience, and just for this specific figure, the extreme mass templates were generated with ± 500 MeV to make it possible to see the difference between the three distributions. As expected since there is no bias the parabola fit is centered on $M_{W^+}^{\mathcal{PD}} - M_W^{(\text{ref.})} = 0$, more precisely $M_{W^+}^{\mathcal{PD}} - M_W^{(\text{ref.})} = (-1.4 \pm 2.7)$ MeV with $\chi_{\text{min}}^2/\text{dof} = 0.86$. The same procedure applied for the negatively charged channel gives the result $M_{W^-}^{\mathcal{PD}} - M_W^{(\text{ref.})} = (-2.2 \pm 3.1)$ MeV with $\chi_{\text{min}}^2/\text{dof} = 0.98$. These two results, once combined, give

$$M_{W^+}^{\mathcal{PD}} - M_W^{(\text{ref.})} = (0.8 \pm 5.8) \text{ MeV} \quad (5.14)$$

It shows that no systematic biases are introduced by the proposed analysis method and give an idea on the size of the statistical errors.

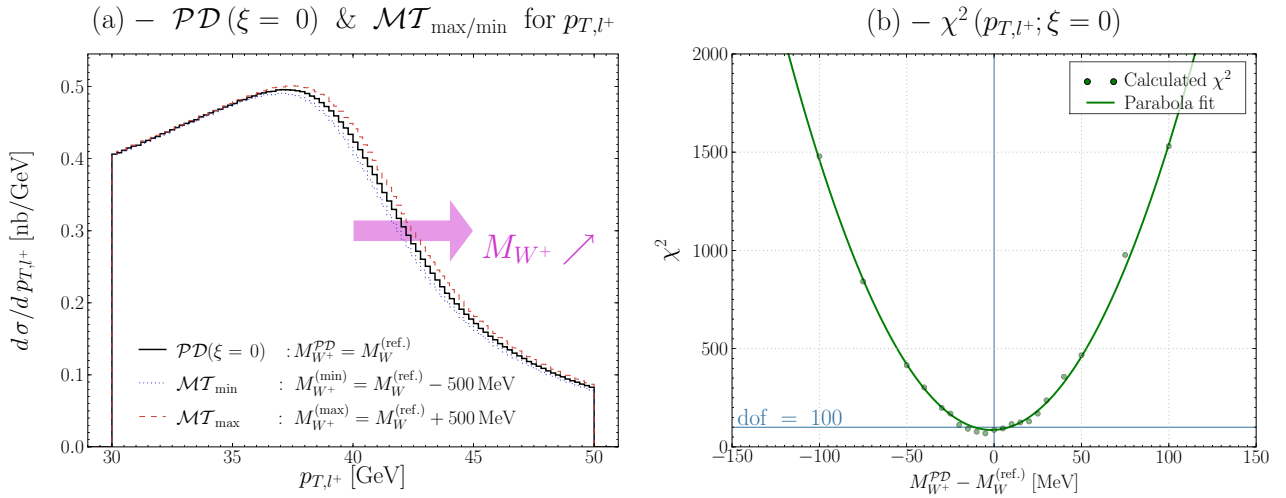


Figure 5.3: Distribution of the transverse momentum of the positively charged lepton for the three values of $\delta M = -500, 0, +500$ MeV with respect to 80.403 GeV (a) and the χ^2 dependence for each $\{\mathcal{PD}, \mathcal{MT}\}$ couple (points) and their associated polynomial fit (line) in function of $\Delta_{(+,-)}$ (b).

(b) Charge asymmetry method

In this method the biases $\Delta_{(+,-)}(\xi)$ resulting from the systematic effects are determined by a direct analysis of the $\text{Asym}^{(+,-)}(p_{T,l})$ distributions for the \mathcal{MT} and \mathcal{PD} event samples. For the \mathcal{MT} samples, combining the event sample $-\mathcal{N}$ and \mathcal{N} produced shifts for the $\Delta_{(+,-)}$ parameter as shown in the second column of Table 5.3. Even though the basics \mathcal{MT} allowed us to spread the range of the analysis to ± 400 MeV, most of the values for the systematic errors are such that it proved to be reasonable to stay in the ± 200 MeV range.

In preliminary studies the charge asymmetry method was first verified using two charge symmetric procedures. In the first one the variation of $\Delta_{(+,-)}$ was made by fixing $M_{W^+} = M_W^{(\text{ref.})}$ and by changing M_{W^-} . In the second one we inverted the role of M_{W^+} and M_{W^-} . The results obtained with these two charge symmetric methods were found to agree within the statistical errors.

The first measurement of the charge asymmetry of the W boson masses at the LHC will have to use, as the first iteration step, the best existing constraints on the W boson masses. The best available constraint is the average mass of the W^+ and W^- bosons: $M_W = M_W^{(\text{ref.})}$. To mimic the way how the measurement will be done at the LHC, we thus fixed $M_{W^+}^{\mathcal{PD}} + M_{W^-}^{\mathcal{PD}} = M_W^{(\text{ref.})}$ value and varied, in a correlated way, both the M_{W^+} and M_{W^-} values when constructing the $\Delta_{(+,-)}$ dependent \mathcal{MT} samples. For that matter the templates generated previously for the classic method prospect

$\delta M_W^{(n)}$ [MeV]		$\Delta_{(+,-)}^{(n)}$ [MeV]
0	→	0
± 5	→	± 10
± 10	→	± 20
± 15	→	± 30
± 20	→	± 40
± 25	→	± 50
± 30	→	± 60
± 40	→	± 80
± 50	→	± 100
± 75	→	± 150
± 100	→	± 200
± 200	→	± 400

Table 5.3: Basic mass templates \mathcal{MT} generated for W^+ and W^- used with the classic method (left column) and the corresponding $\Delta_{(+,-)}^{(n)}$ \mathcal{MT} samples (right column) constructed for the study of the charge asymmetry method. Note though $\Delta_{(+,-)} = \pm 400$ MeV was not used so in both classic and charge asymmetry methods the \mathcal{MT} span the range ± 200 MeV.

where used in the creation of these new templates for the charge asymmetry. In top of saving CPU time it allows as well to share the same data and then improve the safety in our analysis. For that reason the pseudo-data were also shared among all methods.

This procedure is illustrated in Fig. 5.4 for the case of the charge asymmetry method. The $\text{Asym}^{(+,-)}(p_{T,l})$ distribution is plotted in Fig. 5.4.(a) as a function of $p_{T,l}$ for three values $\Delta_{(+,-)}$. This plot illustrates the sensitivity of the $\text{Asym}^{(+,-)}(p_{T,l})$ distribution to the $\Delta_{(+,-)}$ value. In Fig. 5.4.(b) the χ^2 variable is plotted for the \mathcal{PD} -calibration sample corresponding to $\Delta_{(+,-)}^{\text{(ref.)}} = 0$ and to an unbiased detector response, as a function of $\Delta_{(+,-)}$. The position of the minimum is

$$\Delta_{(+,-)}(\xi = 0) = (1.2 \pm 4.1) \text{ MeV}, \quad (5.15)$$

with a convergence of $\chi_{\text{min}}^2/\text{dof} = 0.82$. This plot illustrates the calibration procedure. It calibrates the statistical precision of the measurement for the integrated luminosity of 10 fb^{-1} , and based on the error obtained for the classic method in the rest of the Chapter we round all results to the MeV. Our goal will be to reduce the systematic biases in the measurement of $\Delta_{(+,-)}$ with a comparable precision than the statistical error.

(c) Double charge asymmetry method

The \mathcal{MT} event samples for this methods are exactly the same as for the charge asymmetry method. The \mathcal{PD} event samples have been simulated in two steps corresponding to the two half-a-year periods of data taking corresponding to the two magnetic field configurations.

5.2.3 Scaling distributions for quarks flavors systematics

Most of systematic measurement and modeling biases discussed in this work lead to a distortion of the distributions and do not change their overall normalisation. The notable exception, discussed in more detail in the next section, are the biases driven by the PDFs uncertainties. These biases cannot be “absorbed” by the corresponding $\Delta_{(+,-)}(\xi)$ shifts and require an adjustment of the event/nb normalisation of the corresponding \mathcal{MT} samples to obtain acceptable χ^2 values.

The most natural method would be to extend the one-dimensional analysis presented in this section into two-dimensional analysis of both the mass and the normalisation parameters. Such an analysis

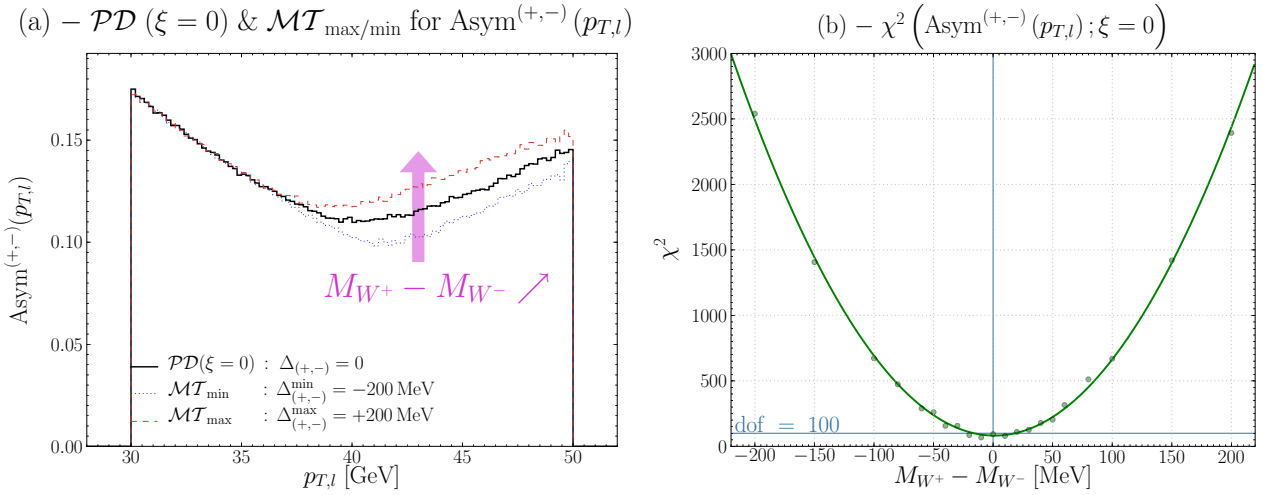


Figure 5.4: The charge asymmetry of $p_{T,l}$ for the three values of $\Delta_{(+,-)}$: -200 , 0 , $+200$ MeV (a) and the χ^2 dependence for each $\{\mathcal{PD}, \mathcal{MT}\}$ couple (points) and their associated polynomial fit (line) in function of $\Delta_{(+,-)}$ (b).

would have, however, “squared” the necessary computing time of the \mathcal{MT} samples and, therefore, was not feasible in our time-scale. Instead, we have tried to un-correlate the adjustment of the normalisation parameter and the mass parameters. As can be seen in Fig. 5.4.(a) the $\text{Asym}^{(+,-)}(p_{T,l})$ distribution is, in the region of small $p_{T,l}$ ($p_{T,l} \lesssim 35$ GeV), independent of the variations of $\Delta_{(+,-)}$ over the range discussed here. We use this observation and modify correspondingly the likelihood analysis method. Before calculating χ^2 , the \mathcal{PD} and \mathcal{MT} distributions are integrated in the range:

$$\int_{20 \text{ GeV}}^{35 \text{ GeV}} d p_{T,l} \left(\frac{d \text{Asym}^{(+,-)}}{d p_{T,l}} \right), \quad (5.16)$$

giving respectively two scalars: α and $\beta^{(n)}$. Then we re-normalise the n^{th} \mathcal{MT} distribution by the factor $\alpha/\beta^{(n)}$ and calculate the χ^2 values for the rescaled distributions. We have checked that the above procedure improves significantly the resulting χ^2 values for each of the three analysis methods. By changing the integration region we have verified that the above procedure does not introduce significant biases in the estimated $\Delta_{(+,-)}(\xi)$ values.

The effect of this trick can be visualised on a concrete example where we consider the incriminated bias to reflect an overestimation of the PDF. The consequences of the different cross section between the \mathcal{PD} with respect to the one of the central $\mathcal{MT}^{(0)}$ ($\Delta_{(+,-)} = 0$) histogram can be seen directly in Fig. 5.5.(a) and more finely in frame (c) where the normalised difference between the two histograms have been drawn. In (c) then, we observe an overall scaling factor –constant below the jacobian peak– between the two plots that will ultimately wreck any chance for the χ^2 test to converge and then give a relevant result. Computing the scalars α and $\beta^{(0)}$ allows to scale $\mathcal{MT}^{(0)}$ by multiplying it with $\alpha/\beta^{(0)}$ as shown in Figs. 5.5.(b) and (d).

5.3 Systematic error sources

In this section we identify and model the systematic error sources that will limit the precision of the $M_{W^+} - M_{W^-}$ measurement at the LHC. Each of these error source will be modeled and reflected in the corresponding \mathcal{PD} sample of events.

These error sources are of two kinds: (1) those reflecting uncertainties in modeling of the W boson production and decay processes, (2) those reflecting the event selection and event reconstruction biases. A large fraction of the error sources have been identified [51] and reevaluated in the context of the measurement of the average mass of the W boson at the LHC [57, 58]. We focus our discussion

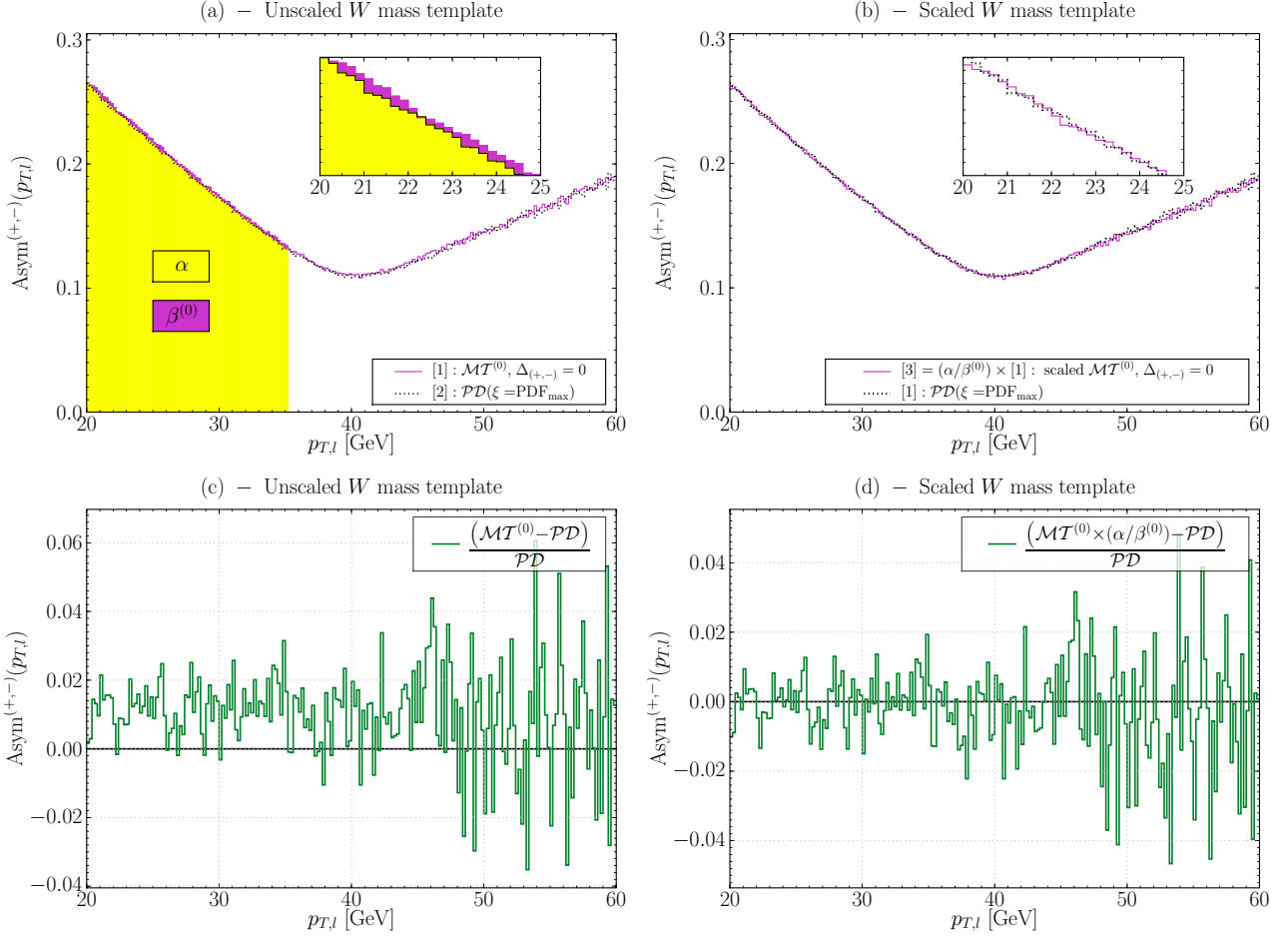


Figure 5.5: Central mass template $\mathcal{MT}^{(0)}$ ($\Delta_{(+,-)} = 0$) distribution with a biased pseudo-data histogram \mathcal{PD}_{\max} (overestimation of the PDFs weights) before scaling (a) and after scaling (b) and refined visualisation of the latter in (c) and (d) by looking at the normalised difference $(\mathcal{MT} - \mathcal{PD}) / \mathcal{PD}$.

on the dominant errors for the measurement of the W mass charge asymmetry, in particular on those that are specific to the LHC environment and have not been identified in the earlier studies. We shall not discuss here: (1) the measurement errors reflecting the uncertainties in the background estimation and in the efficiency of the events selection, (2) other measurement uncertainties which can be studied to the required level of precision only once the real data are collected. As demonstrated in the analysis of the Tevatron data [51], they are of secondary importance.

5.3.1 Phenomenological modeling uncertainties

The uncertainties in the modeling of the production and decay of the W bosons include: (1) the uncertainties in modeling of non-perturbative effects, (2) the approximations present in theoretical modeling of the perturbative EW and QCD effects, (3) the uncertainties in the parameters of the Standard Model and (4) a possible presence of the Beyond Standard Model (BSM) effects, affecting both the production and decay mechanisms of the W bosons. The two first items of them limit our present understanding of the Wide-Band-partonic-Beam (WBpB) at the LHC.

(a) WBpB at LHC

The measurement precision of the W mass charge asymmetry will depend upon the level of understanding of the flavour structure, the momentum spectrum and the emittance of the WBpB at the

LHC collision energy. The hard scale dependent emittance of the WBpB is defined here, in analogy to the emittance of the parent hadron beam, in terms of its transverse momentum distribution and in terms of its transverse and longitudinal beam-spot sizes. The above dynamic properties of the WBpB are highly correlated. Only their scale dependence can be controlled by the Standard Model perturbative methods. In addition, several aspects of such a control, in particular the precise modeling of the correlations between the flavour, the longitudinal and the transverse momentum degrees of freedom of the WBpB have not so far been implemented in the Monte Carlo generators available for the initial phase of the LHC experimental program.

The *statu quo* of understanding of the WBpB at the LHC is driven by the presently available Monte Carlo generator tools. Within this *statu quo*, the flavour dependent longitudinal momentum distribution of the WBpB, specified by ‘collinear’ PDFs, is fed to one of the available parton shower MC generators. The transverse momentum distribution of the WBpB is then derived from the assumed longitudinal one. This procedure depends upon a particular evolution scheme dependent form of the parton shower and upon the order of the perturbative expansion. It depends as well upon the modeling method of the quark flavour (quark mass) effects in the parton shower generation. The effects of the flavour dependence of the beam size in the transverse plane are partially controlled using auxiliary, impact parameter dependent re-summation procedures. Finally, the scale dependent evolution of the longitudinal beam spot size is presently assumed to be driven by the DGLAP evolution equations [30, 31, 32].

It is obvious that the precision of the present understanding of the WBpB at the LHC is difficult to assess within the above modeling environment. Since its impact on the precision measurements of electroweak processes will be significantly higher for the LHC WBpB with respect to the Tevatron one, some novel measurement and/or modeling schemes must be developed. They must assure either better theoretical control of the WBpB parameters or, as proposed, reduce their impact on the measured observables to such an extent that their detailed modeling becomes irrelevant. For the latter strategy it is sufficient to rely on crude modeling methods of the WBpB at the LHC which are available within the WINHAC generator.

(b) Uncertainty of PDFs

The uncertainties in PDFs are, most often, propagated to the measurement errors of the physics observables by varying the PDF sets chosen in the event generation process. Alternatively, the uncertainties of the QCD fit parameters of a given PDF set are propagated by re-weighting the generated events with “min” and “max” weights, $\text{PDF}_{\text{max/min}} = \text{PDF}_{\text{cen}} \pm \delta\text{PDF}$, where PDF_{cen} are the central value distributions of a given PDF set and δPDF is computed according to the method described in Ref. [66]. We followed the latter method, mostly because of computing time constraints. We have used the CTEQ6.1M PDF set [192] in modeling of the standard PDFs uncertainties. The above methods, in our view, largely underestimate the influence of the PDFs uncertainty on the measurement precision of the W boson mass.

As discussed in the last Chapter, the charge asymmetry of the W boson production and decay processes is sensitive: (1) the presence of valence quarks in the WBpB, (2) the flavour asymmetry of their longitudinal momentum distribution (called hereafter the $u^{(v)} - d^{(v)}$ asymmetry) and (3) the asymmetry in the relative momentum distribution of the strange and charm quarks (the $s - c$ asymmetry). The corresponding uncertainties must be modeled directly using the existing (future) experimental constraints rather than be derived from the uncertainty of the PDF set parameters. This is because they are driven almost entirely by the non perturbative effects, and because the QCD evolution effects are, except for the quark mass dependency, flavour independent.

(c) Uncertainty of $u^{(v)} - d^{(v)}$ asymmetry.

We assume the following two ways of modeling the uncertainty in the $u^{(v)} - d^{(v)}$ asymmetry:

$$u_{\text{max/min}}^{(v)} = u^{(v)} \pm 0.05 u^{(v)}, \quad d_{\text{min/max}}^{(v)} = d^{(v)} \mp 0.05 u^{(v)}, \quad (5.17)$$

and

$$u_{\text{max/min}}^{(v)} = u^{(v)} \pm 0.02 u^{(v)}, \quad d_{\text{min/max}}^{(v)} = d^{(v)} \mp 0.08 d^{(v)}. \quad (5.18)$$

The first one preserves the sum of the distribution of the u and d quarks and is constrained, to a good precision, by the measured singlet structure function in neutrino and anti-neutrino Deep Inelastic Scattering (DIS) of isoscalar nuclei. At the LHC the sum of the distributions will be constrained by the rapidity distribution of the Z bosons (d quarks and u quarks contribute with similar weights). The second one assures the correct propagation of the measurement errors of the sum of the charge square weighted distributions of the u and d quarks, constrained by the high precision charged lepton beam DIS data, to the uncertainty of the individual distributions.

While the sums of the distributions are well controlled by the existing and future data, their mutually compensating shifts are not. The only experimental constraints on such shifts come from: (1) the measurements of the ratio of the cross sections for deep inelastic scattering of charged leptons on proton and deuteron targets and (2) the measurements of the ratio of the neutrino–proton to anti-neutrino–proton DIS cross sections. They determine the present uncertainty range of the $u^{(v)} - d^{(v)}$ asymmetry. Improving this uncertainty range in the standard pp LHC colliding mode will be difficult and ambiguous. It will require simultaneous unfolding of the momentum distribution and the charge asymmetry of the sea quarks.

(d) Uncertainty of $s - c$ asymmetry

The cs annihilation represent $\approx 7\%$ of the total contribution to the W boson production cross section at the Tevatron collision energy. At the LHC collision energy it rises to $\approx 25\%$ and becomes charge asymmetric: $\approx 21\%$ for the W^+ boson and $\approx 28\%$ for the W^- boson. The uncertainty in the relative distribution of the strange and charm quarks becomes an important source of systematic measurement errors of both the average W boson mass and its charge asymmetry.

We assume the two following ways of modeling the uncertainty in the $s - c$ asymmetry:

$$s_{\text{max/min}} = s \pm \gamma c, \quad c_{\text{min/max}} = c \mp \gamma c \quad (5.19)$$

with $\gamma = \{0.2, 0.1\}$ representing respectively the present and future uncertainty range for the relative shifts in the s and c quark distributions. As in the case of the $u^{(v)} - d^{(v)}$ asymmetry, we have assumed that the sum of the distribution of the s and c quarks will be controlled to a very good precision by the Z boson rapidity distribution. Therefore we have introduced only unconstrained, mutually compensating modifications of the s and c quark distributions¹. As seen previously in Eqs. (4.2) and (4.3), the valence quarks excess magnifies the contribution of the $s - c$ uncertainty to the measurement precision of W boson mass.

(e) WBpB emittance

The $u^{(v)} - d^{(v)}$ and $s - c$ longitudinal momentum asymmetries would have no effect on the measured W boson mass asymmetry in the case of the collinear partonic beams. The angular divergence (transverse momentum smearing) of the WBpB at the LHC is driven by the gluon radiation. Its parton shower Monte Carlo model determines the relationship between the longitudinal and the transverse degrees of freedom of the WBpB. It gives rise to the parton shower model dependent asymmetries of the W^+ and W^- boson transverse momenta.

Instead of trying to estimate the uncertainties related to the precision of the parton shower modeling of the the quark flavour dependent effects, we allow for exceedingly large uncertainty in the size of the flavour independent primordial transverse momentum Gaussian smearing of the WBpB: $\langle k_T \rangle = 4_{-2}^{+3}$ GeV (the \mathcal{PD} samples have been simulated for the following values of the sigma parameter of the Gaussian smearing: $\langle k_T \rangle = 2, 3, 4, 5, 6, 7$ GeV). Such a large uncertainty range,

¹In reality, the s and c quarks couple to the Z boson with slightly different strength but the resulting effect will play no important role in the presented analysis.

easily controllable using the Z boson transverse momentum distribution, represents the effect of amplifying (small values of $\langle k_T \rangle$) or smearing out (large values of $\langle k_T \rangle$) the flavour dependent asymmetries of the WBpB transverse momentum. The range has been chosen to be large enough to cover the uncertainties due to: (1) non perturbative effects, *e.g.* those discussed in [193], (2) the quark mass effects and (3) re-summation effects.

(f) EW radiative corrections

Out of the full set of the EW radiative corrections implemented in the WINHAC generator, those representing the emission of real photons could contribute to the measured W mass charge asymmetry. Two effects need to be evaluated: the charge asymmetric interference terms between the photon emission in the initial and final states, and the radiation of the photons in the W boson decays in the presence of the $V - A$ couplings. The above corrections are described to a high precision by WINHAC, as has been shown in Refs. [140, 142]. Therefore, their influence on the W mass charge asymmetry measurement can be modeled very accurately. We did not consider these effects, leaving a detailed study for our future works.

5.3.2 Experimental uncertainties

(a) Energy scale (ES) of the charged lepton

The uncertainty in the lepton energy scale is the most important source of the M_W measurement error for the Tevatron experiments. At the LHC, the production of unequal numbers of W^+ and W^- bosons, its impact on the overall measurement precision will be amplified. For the measurement methods discussed the lepton energy scale error will be determined: (1) by the curvature radius measurement errors, (2) by the uncertainties in the magnetic field maps within the tracker volume and (3) by the modeling precision of the physics processes which drive the link between the measurements of the particle hits in the tracker and the reconstructed particle momentum. While the first two sources of the measurement error are independent of the lepton flavour, the third one affects the electron and muon samples differently. In the following we shall assume, on the basis of the Tevatron experience, that modeling of physics processes of particle tracking will be understood at the LHC to the required level of precision, on the basis of dedicated auxiliary measurements². This simplification allows us to discuss the muon and electron track measurement simultaneously. We assume as well that the solenoid magnetic field strength in the volume of the tracker will be understood to better than 0.1% of its nominal value. We base this assumption on the precision of 0.01% achieved *e.g.* by the H1 experiment at HERA [194] and by the ALEPH experiment at LEP [195]. If this condition is fulfilled, the energy scale error ε_l is driven by the curvature radius measurement error

$$\rho_{T,l}^{(\text{rec.})} = \rho_{T,l}^{(\text{smr.})} (1 + \varepsilon_l), \quad (5.20)$$

where $\rho_{T,l}^{(\text{rec.})}$ and $\rho_{T,l}^{(\text{smr.})}$ are, respectively, the reconstructed and the true curvature smeared by the unbiased detector response function.

Based on the initial geometrical surveys, the initial scale of $\rho_{T,l}$ will be known to the precision of 0.5%. This precision will have to be improved at least by a factor of 10 to match the precision of the Tevatron experiments, if the same measurement strategy is applied. To achieve such a precision, the local alignment of the tracker elements and/or average biases of the reconstruction of the trackers space-points must be known to the $\approx 3 \mu\text{m}$ precision. In addition, the global deformation of the tracker elements assembly must be controlled to a precision which is beyond the reach of the survey methods.

Several modes of the global deformations can be considered in a first approximation as discussed in Ref. [107]. Below we make a sum up of the conclusions drew from § 2.4 and Appendix 2.A. The

²For example, the energy loss of the electrons in the dead material within the tracker volume will be understood using a conjugate process of the photon conversion.

main difference between the measurements of the W boson properties at the Tevatron and the LHC boils down to their sensitivity to the different types of the global deformation modes. Both for the Tevatron and LHC measurements the Δz translations are of no consequences since they do not affect the shape of the transverse projection of the particle helix. The Δr deformations (the radial expansion $r \Delta r$, the elliptical flattening $\phi \Delta r$ and the bowing $z \Delta r$) give rise to common biases for positive and negative particle tracks. On the other hand, the $\Delta \phi$ curl and twist deformations give rise to biases which are opposite for negative and positive particles. In the case of the Tevatron $p\bar{p}$ collisions, producing equal numbers of the W^+ and W^- bosons, the dominant effect of $\pm z$ -coherent curling of the outer tracker layers with respect to the inner tracker layers has residual influence on the uncertainty of the average W boson mass, leaving the residual effect of relative twist of the $+z$ and $-z$ sides of the tracker volume as the principal source of the measurement error. For the LHC pp collisions, producing unequal numbers of the W^+ and W^- bosons, both deformation modes influence the measurement biases of the average W boson mass. In the case of the LHC there is no escape from the necessity of precise understanding of the lepton charge dependent biases on top of the lepton charge independent biases.

In the presence of the above two sources of biases the energy scale bias ε_l can be expressed in the limit of small deformations (cf. Eqs. (2.22–2.23)) as follow

$$\varepsilon_{l+} = \varepsilon_{\Delta\phi} + \varepsilon_{\Delta r}, \quad (5.21)$$

$$\varepsilon_{l-} = -\varepsilon_{\Delta\phi} + \varepsilon_{\Delta r}, \quad (5.22)$$

where $\varepsilon_{\Delta\phi}$ represents the particle charge dependent $\Delta\phi$ -type bias and $\varepsilon_{\Delta r}$ represents the charge independent Δr -type bias.

While the $\varepsilon_{\Delta r}$ -type biases can be controlled with the help of the Z boson, Υ and J/Ψ “standard candles”, *e.g.* using the CDF procedures, the global charge dependent and symmetric $\varepsilon_{\text{curl}}$ biases cannot. At the Tevatron these biases were investigated using the electron samples by studying the charge dependent E/p distribution, where E is the energy of the electron (positron) measured in the calorimeter and p is its reconstructed momentum. The relative scale error of positive and negative electrons was re-calibrated using the mean values of the E/p distributions. The achieved precision was the principal limiting factor of the measurement of $\Delta_{(+,-)}$. Even if the statistical precision of such a procedure can be improved significantly at the LHC, this method is no longer unbiased. This is related to the initial asymmetry of the transverse momentum distribution for positive and negative leptons in the selected W boson decay samples. As a consequence, both the positive and negative lepton events, chosen for the calibration on the basis of the energy deposited in the calorimeter, will no longer represent charge unbiased samples of tracks. The biases will be driven both by the influence of distribution shape and by the migration in and out of the chosen energy range. A partial remedy consists of using a statistically less precise sample of positive and negative lepton tracks in a selected sample of Z boson decays. However, due to the different weights of the $V - A$ and $V + A$ couplings of the Z boson to leptons, even these track samples are biased. In both cases these biases can be corrected for, but the correction factor will be sensitive to the uncertainty in the momentum spectra of the valence quarks.

Given the above sources of the uncertainties, we assume the following two values for the size of the biases, both for the charge independent and charge dependent scale shifts

$$\varepsilon_{l+} = +\varepsilon_{l-} = \pm 0.5\%, \pm 0.05\%, \quad (5.23)$$

$$\varepsilon_{l+} = -\varepsilon_{l-} = \pm 0.5\%, \pm 0.05\%. \quad (5.24)$$

The first value corresponds to the precision which can be achieved on the basis of the initial geometrical survey and the initial measurement of the field maps. The second one corresponds to what, in our view, can be achieved using the above data based on the calibration methods –given all the LHC specific effects– which make this procedure more difficult at the LHC than at the Tevatron.

(b) Resolution (RF) of the charged lepton track parameters

The finite resolution of measuring the lepton track parameters may lead to biases in the measured value of $M_{W^+} - M_{W^-}$. We model the possible biases introduced by the ambiguity in the assumed size of the σ_{1/p_T} (Eq. (2.15)) and $\sigma_{\cotan\theta}$ (Eq. (2.16)) smearing by decreasing or increasing the widths of their Gaussian distributions by the factor $\text{RF} = 0.7, 1.3$.

5.4 In search for the optimal measurement strategy

5.4.1 Validation of the framework and behaviour of the likelihood analysis

Before presenting the results, now that we have a global idea of the challenge we present a few more details on the validation of the analysis framework from both technical and physical point of views and look also at the influence on the results of some input parameters to the analysis process. The following tests were performed for trivial ($\xi = 0$) as well as non trivial results ($\xi \neq 0$) when necessary, *i.e.* when $\Delta_{(+,-)}(\xi)_{\min} \gg 0$ and/or $\chi^2_{\min}/\text{dof} \gg 1$. Since most of these tests are quite redundant they were not included in the core of the Chapter in the aim not to break the flow of the expose. Rather than that, the gist of it was compiled at the end of the present Chapter. Hence, in what follows the corresponding sections in the Appendix are indicated so that the reader wishing to have quantitative results on a particular topic knows where to find them.

The first test consisted to cross check the framework using for all three methods the observable $p_{T,l}$ (§ 5.A.1.(a)). All results ($\xi = 0$ and $\xi \neq 0$) confirmed the calculus using $p_{T,l}$ -based methods.

Since trivial validation tests ($\xi = 0$) displays $M_{W^+} - M_{W^-} = 0$ the relevancy of the sign of the result cannot be checked, also we generated \mathcal{PD} with a shift of +100 MeV with respect to the mass of reference of the W bosons and saw that indeed the signs were coherent (§ 5.A.1.(b)).

Using these shifted masses in the \mathcal{PD} allow on a technical level to see at which level the convergence of a result depends of the number and localisation of \mathcal{MT} from the minimum of the parabola. Thus, by playing with the number of the \mathcal{MT} samples participating to the analysis and choosing them such that all \mathcal{MT} masses are far and on one side only from the minimum we can show that the convergence, and in consequence $\Delta_{(+,-)}$, suffers in such extreme configurations (§ 5.A.2.(a)). Nonetheless the order of the size of the error is respected. Also, despite our reduced number of \mathcal{MT} samples, in what follows results displaying large values of $\Delta_{(+,-)}(\xi)_{\min}$ can be trusted.

The influence of the detector resolution on the results was investigated by increasing the size of the bin widths of the \mathcal{PD} and \mathcal{MT} histograms before performing the analysis. It proved that the χ^2 test is quite robust so that values are very close to the one obtained with the nominal resolution, excepted for the convergence accuracy which suffers much more from lower resolution when $\Delta_{(+,-)}(\xi)_{\min} \gg 0$ (§ 5.A.2.(b)).

The charge asymmetry method being new we considered a spread in the analysis range to perform the χ^2 analysis which is not possible in the classic method without a very good knowledge of the background at low p_T and of the influence of Γ_W at high p_T . Tests based on $\text{Asym}^{(+,-)}(p_{T,l})$ performed in the range $20 \text{ GeV} < p_{T,l} < 50 \text{ GeV}$ and then in $20 \text{ GeV} < p_{T,l} < 60 \text{ GeV}$ displayed no real enhancements on the results apart from slightly increasing the precision of the convergence χ^2_{\min}/dof (§ 5.A.2.(c)). This can be understood as the mass of the W has a real impact on the region where the jacobian peak arise. Nonetheless with real data this could provide a good test to see a dependence of the results from the background and W width influence on the extraction of the mass with this method.

Last but not least the test of the influence of a \cancel{E}_T cut on the result was performed by doing at the stage of the generation directly a cut on p_{T,ν_l} . The consequences on the results are absolutely not visible and it is believed that a realistic cut based on \cancel{E}_T would display the same feature (§ 5.A.2.(d)). This test justify then the non treatment of realistic \cancel{E}_T cuts and recoil modeling in our analysis.

To conclude, from all these tests the one having the most striking effect on the calculus was found to be the lack of \mathcal{MT} samples thinly separated and covering a large range of masses. As

stated previously the CPU was prohibitive to refine the analysis and would not have brought much enhancement as most of the systematic error $\Delta_{(+,-)}(\xi)$ absolute values, as it will be shown, are such that $|\Delta_{(+,-)}(\xi)| < 200 \text{ MeV}$. Also, to preserve a better clarity of the discussion –as independent as possible from the choice of the input parameters– we have chosen that all the χ^2 presented in the core of the Chapter were made for mass templates \mathcal{MT} covering the range $\pm 200 \text{ MeV}$.

Finally, just out of curiosity and to insist on the difference between the kinematics of the charged lepton decaying from a W^+ or a W^- at the LHC we considered the case where –not aware of the $V - A$ coupling of fermions in electroweak interactions– the χ^2 test is made between pseudo-data related to the W^+ information and the mass templates related to the W^- information. Performing such a naive test assuming similar kinematics for the positive and negative charged leptons gives absolutely non relevant results, such that $M_{W^+} - M_{W^-}(\xi = 0) \sim 1 \text{ GeV}$ and $\chi^2_{\text{min}}/\text{dof} \sim 10,000$ (cf. Appendix 5.B).

5.4.2 Reducing impact of systematic measurement errors

In Section 5.1 three measurement methods of $\Delta_{(+,-)}$ have been presented: the classic, charge asymmetry and double charge asymmetry methods. The basic merits of the two latter methods is that they use the dedicated observables which are meant to be largely insensitive to the precise understanding of the event selection and reconstruction efficiency, the background contamination level, understanding to the absolute calibration and the biases of the reconstruction of the neutrino transverse momentum, the internal and external (dead-material) radiation. It will remain to be proved, using the data collected at the LHC, that all these error sources have negligible impact on the precision of the $\Delta_{(+,-)}$ measurement. At present, such a statement must rely on the extrapolation of the Tevatron experience. In what follows, links to detailed comments and/or graphics for each addressed systematic error are made to the Appendix 5.C since for clarity we kept only the essential information in the core of the Chapter.

The impact of the remaining measurement errors specified in the previous Section and quantified using the analysis methods discussed in Section 5.2 is presented in Table 5.4.

The precision of estimating the systematic shifts of $\Delta_{(+,-)}(\xi)$ for each of the systematic effect ξ and each measurement method is assessed using the validation procedures described in Section 5.2. The resulting $\delta [\Delta_{(+,-)}(\xi)]$ of $\approx 5 \text{ MeV}$ corresponds the collected luminosity of 10 fb^{-1} . The first observation is that the precise understanding of the measurement smearing RF of the track parameters does not introduce any bias in the measured values of $\Delta_{(+,-)}$. The impact of the energy scale errors on the $\Delta_{(+,-)}$ biases differs for each of the discussed methods.

For the lepton charge independent shift even the “initial” (0.5%) scale error has no statistically significant impact on the measurement precision for the charge asymmetry method. For the classic method the scale error has to be reduced to the “ultimate” value of (0.05%) to achieve a comparable measurement precision of $\Delta_{(+,-)}$.

For the lepton charge dependent shifts the classic and asymmetry methods provide similar measurement precision. The measurement error remains to be of the order of $\approx 60 \text{ MeV}$ even if the ultimate precision of controlling the energy scale biases to 0.05% is reached. The double charge asymmetry method reduces the measurement error to the extend that the resulting bias is statistically insignificant, even for the initial scale uncertainty. This is illustrated in Figures 5.6.(a) and 5.6.(b). These plots show the comparison of the χ^2 fits for the charge asymmetry method and the double charge asymmetry method for the lepton charge dependent scale error of $\varepsilon_l = \pm 0.05\%$ (a), and the χ^2 fit corresponding to $\varepsilon_l = \pm 0.5\%$ for the double charge asymmetry method (b). The results for the double charge asymmetry correspond to $\varepsilon_{l^+} = -\varepsilon_{l^-} > 0$ for the first running period with the standard magnetic field configuration and $\varepsilon_{l^+} = -\varepsilon_{l^-} < 0$ for the running period with the inverted direction of the z -component of the magnetic field.

The above reduction of the measurement sensitivity to the energy scale error can be achieved for the initial survey precision of the tracker alignment. Such a survey will have to be made at the beginning of each of the two running periods. A special care will have to be taken to understand

		$M_{W^+} - M_{W^-}$ [MeV]			
		Systematic ξ	“Classic” Method	Asym ^(+,-) ($p_{T,l}$)	DAsym ^(+,-) ($\rho_{T,l}$)
MC truth	$\xi = 0$		-2 ± 3	-1 ± 3	0 ± 3
Cent. Exp.	$\xi = 0$		1 ± 4	1 ± 4	0 ± 4
ES [%]	$\varepsilon_{l^+} = +\varepsilon_{l^-} = +0.05\%$		3	2	×
	$\varepsilon_{l^+} = +\varepsilon_{l^-} = -0.05\%$		-2	0	
	$\varepsilon_{l^+} = +\varepsilon_{l^-} = +0.50\%$		16	8	
	$\varepsilon_{l^+} = +\varepsilon_{l^-} = -0.50\%$		-36	-6	1
	$\varepsilon_{l^+} = -\varepsilon_{l^-} = +0.05\%$		-56	-57	
	$\varepsilon_{l^+} = -\varepsilon_{l^-} = -0.05\%$		57	57	
	$\varepsilon_{l^+} = -\varepsilon_{l^-} = +0.50\%$		-567	-611	
$\varepsilon_{l^+} = -\varepsilon_{l^-} = -0.50\%$		547	515	-1	
RF	0.7		1	-2	×
	1.3		-3	3	

Table 5.4: Experimental systematic errors for the classic method, the charge asymmetry and the double charge asymmetry. In Appendix 5.C.1, Table 5.9 reproduces the present results with more details.

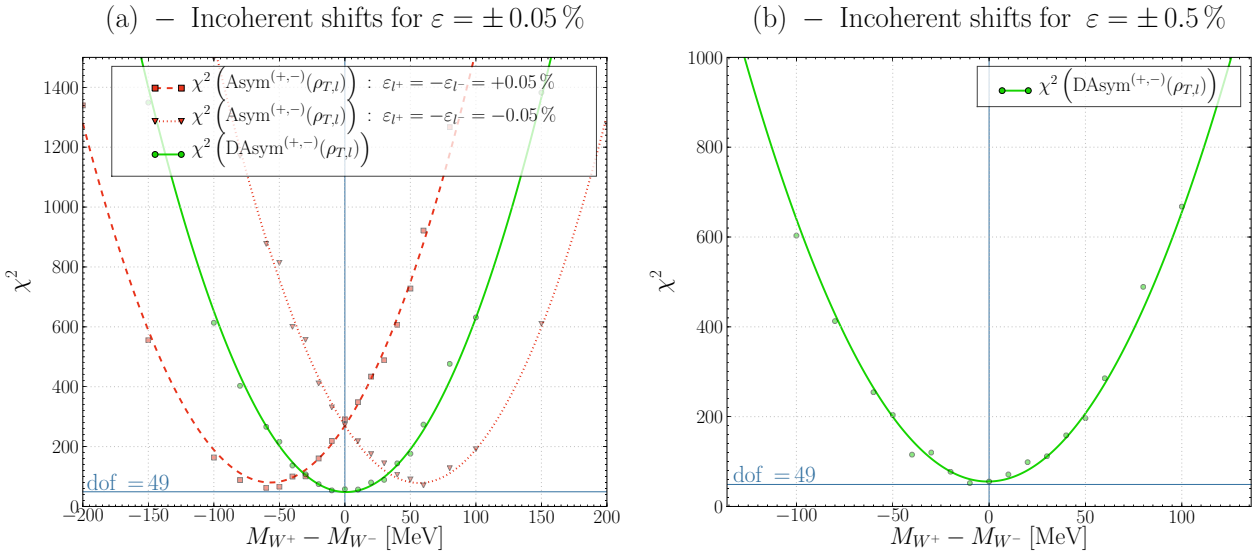


Figure 5.6: The χ^2 results for the incoherent shifts of the energy scale for both the asymmetry and the double charge asymmetry using $\varepsilon = \pm 0.05\%$ in (a), and only for the double charge asymmetry with $\varepsilon = \pm 0.5\%$ ($\varepsilon_{l^+} = -\varepsilon_{l^-} > 0$ for the first half year and $\varepsilon_{l^+} = -\varepsilon_{l^-} < 0$ during the over half) in (b).

the relative curl and twist deformations induced by reversing the current in the solenoid. It has to be stressed that the precision of the double charge asymmetry method is insensitive to the relative $\vec{E} \times \vec{B}$ biases of the reconstructed hit positions for the two data taking periods, provided that they are not larger than 10 times the average hit reconstruction precision achieved in the standard field configuration running period. Worsening of the hit position resolution for the inverted field configu-

ration, driven by the geometrical layout of the silicon tracker modules, have no significant effect on the measurement precision. Similarly, the required level of precision of understanding the hysteresis effects, leading to inequality of the absolute field strength in the two running periods, corresponding to reverse solenoid current directions can be achieved with the standard field mapping methods. Note that the precision required for the asymmetry measurement may be up to 10 times worse with respect to the one needed for the measurement of the average W boson mass. The reduced sensitivity to all the above effects is due to the fact that the impact of each of these effects is, to a large extent, canceled in each of the running periods. This is done in the same way as canceling the time-dependent effects of the detector response, calibration and alignment procedures. Note, that the residual impact of all the above effects can be reduced further (if necessary) using the \vec{B} -field configuration dependent analyses of straight track residua and/or the position of the reconstructed Z boson mass peak.

Detailed comments and graphics on the impact of the energy scale ES of the charged lepton and of the resolution smearing RF of its track parameters are presented respectively in § 5.C.(a) and § 5.C.(b) of Appendix 5.C.

5.4.3 Reducing impact of systematic modeling errors

As discussed in the previous section, by using the charge asymmetry (double charge asymmetry) methods the systematic measurement precision of $\Delta_{(+,-)}$ could be reduced to the level of $\mathcal{O}(10)$ MeV. In this section we discuss the impact of the modeling uncertainties described in Subsection 5.3.1 on the measurement precision of $\Delta_{(+,-)}$ for the charge asymmetry method³. The detailed discussion and graphics related to the systematic errors due to the uncertainties on the intrinsic k_T , global PDF, the valence $u - d$ and sea $s - c$ asymmetry are present from § (c) through § (e) of Appendix 5.C.

In Table 5.5 we show, in the first column, the expected measurement biases of $\Delta_{(+,-)}$ due to the dominant modeling uncertainties, discussed in the previous section, for pp collisions at the LHC energy. We do not see a significant impact of the coherent shifts of the partonic distributions, defined in the previous section and denoted as the PDFs uncertainty. It would be, however, misleading to conclude prematurely that the $\Delta_{(+,-)}$ biases are insensitive to the uncertainties in the partonic distributions.

Indeed, the present uncertainty of the relative distribution of the the u and d valence quarks (the $u^{(v)} - d^{(v)}$ asymmetry) leads to large shifts in the $\Delta_{(+,-)}$ values. These shifts are specific to the LHC pp collider and are largely irrelevant for the Tevatron $p\bar{p}$ collisions. This might explain why they were neglected in the previous studies [57, 58], in spite that they concern the average W boson mass measurement. There are three origins for these shifts. The effects due to each of them add up and result in the amplification of the biases. The discussion and the numbers provided in § 4.A.6 of Chapter 4 might be helpful to understand the following ideas. Firstly, increasing the $u^{(v)}$ content of the proton shifts downwards the average momentum of the \bar{d} anti-quarks. This leads to an increase of the average transverse momentum $\langle p_{T,\bar{d}} \rangle$ of the \bar{d} anti-quarks producing W^+ , mimicking the increase of the W^+ boson mass. Simultaneous decreasing of the $d^{(v)}$ acts in the opposite direction for W^- , *i.e.* this time the average p_T of the colliding sea quark decreases which lead to large and positive values of $\Delta_{(+,-)}$. Secondly, at the LHC, contrary to the Tevatron, the presence of the $d^{(v)}$ quarks leads to an asymmetry in the production rate of the W boson from the c quarks and \bar{c} anti-quarks. Since the average transverse momentum of the charm quarks is higher with respect to the light quarks, this asymmetry shows up in the relative shifts in the $p_{T,l}$ distributions for positive and negative leptons. Increasing the density of the $d^{(v)}$ quarks mimics thus the effect of increasing the mass of the W^- with respect to the W^+ boson. The above two effects are amplified by the bias in the degree of the transverse polarisation of W^- with respect to W^+ , induced by the event selection procedure based on the lepton kinematics. The relative movements of the $d^{(v)}$ and $u^{(v)}$ amplify (attenuate) the initial event selection procedure bias. What must be stressed is that if the $d^{(v)}$ shifts are compensated by

³From the point of view of the modeling uncertainties, the charge asymmetry and the double charge asymmetry methods are equivalent and the discussed results are the same for both methods.

		$M_{W^+} - M_{W^-}$ [MeV] results using the Charge Asymmetry of $p_{T,l}$			
Systematic ξ		$pp - \eta < 2.5$	$pp - \eta < 0.3$	$pp - y_W < 0.3$	$dd - \eta < 2.5$
MC truth	$\xi = 0$	-1 ± 3	0 ± 1	0 ± 1	0 ± 5
Cent. Exp.	$\xi = 0$	1 ± 4	0 ± 4	1 ± 4	4 ± 5
$\langle k_T \rangle$ [GeV]	2	8	0	2	28
	3	7	3	-2	20
	5	-4	-3	-6	-15
	6	-8	2	-5	-35
	7	-16	2	-8	-49
PDF ^(*)	Min.	-4	6	0	-3
	Max.	4	-8	5	8
$u^{(v)}, d^{(v)*}$	$u_{\max}^{(v)} = 1.05 u^{(v)}$ $d_{\min}^{(v)} = d^{(v)} - 0.05 u^{(v)}$	115	69	-38	3
	$u_{\min}^{(v)} = 0.95 u^{(v)}$ $d_{\max}^{(v)} = d^{(v)} + 0.05 u^{(v)}$	-139	-87	60	5
	$u_{\max}^{(v)} = 1.02 u^{(v)}$ $d_{\min}^{(v)} = 0.92 d^{(v)}$	84	53	-31	1
	$u_{\min}^{(v)} = 0.98 u^{(v)}$ $d_{\max}^{(v)} = 1.08 d^{(v)}$	-89	-57	44	6
	$c_{\min} = 0.9 c,$ $s_{\max} = s + 0.1 c$	17	10	7	20
$s, c^{(*)}$	$c_{\max} = 1.1 c,$ $s_{\min} = s - 0.1 c$	-11	-10	0	-16
	$c_{\min} = 0.8 c,$ $s_{\max} = s + 0.2 c$	39	25	6	38
	$c_{\max} = 1.2 c,$ $s_{\min} = s - 0.2 c$	-29	-24	1	-34

Table 5.5: The shifts of the W -mass charge asymmetry corresponding to various modeling effects. The systematic labeled * are obtained using the scaling trick mentioned in § 5.2.3. In Appendix 5.C § 5.C.1 Table 5.10 presents a detailed reproduction of these results.

the corresponding shifts of the $u^{(v)}$ distributions, they cannot be constrained to a better precision by the present data, and they will not affect the rapidity distributions of the Z boson. Thus, it will be difficult to pin them down using the standard measurement procedures.

The uncertainties of the relative density of the strange and charm quarks, the $s - c$ asymmetry, gives rise to smaller but significant biases in the $\Delta_{(+,-)}$ values, as shown in the first column of Table 5.5. Since the transverse momentum of the c quarks is significantly higher than the corresponding momentum for the s quarks, this effect, even if Cabibbo suppressed, cannot be neglected. What must be stressed again is that if the c shifts are compensated by the corresponding shifts of the s distributions, they will not affect the rapidity distributions of the Z bosons. Thus, it will be difficult to pin them down using the standard measurement procedures. This asymmetry can be constrained unambiguously only by using dedicated measurements, *e.g.* by measuring the associated production of the W bosons and charmed hadrons.

Compared to the above, the biases corresponding to the uncertainties in the flavour independent smearing of the intrinsic transverse momentum distribution of partons are smaller in magnitude and can be neglected, if the intrinsic transverse momentum of partons is controlled to the precision of 2 GeV.

It is obvious from the above discussion that using the standard measurement procedures, the modeling uncertainties will be the dominant source of the measurement errors of the W boson mass asymmetry, already for the collected luminosity 100 times smaller than the one considered here. In order to diminish the impact of the modeling errors on the measurement of $\Delta_{(+,-)}$ to a level comparable to statistical and experimental measurement errors, some dedicated measurement methods must be applied. Two such procedures are proposed and evaluated below: (1) the narrow bin method and (2) the isoscalar beams method.

(a) Narrow bin method

As discussed previously, the dominant source of large uncertainties in $\Delta_{(+,-)}$ comes from the presence of the valence quarks in the WBpB and from the uncertainties in their flavour dependent momentum distributions. In order to reduce this effect we propose to profit from the large centre of mass energy of the LHC and measure $\Delta_{(+,-)}$ using a selected fraction of the W bosons which are produced predominantly by the sea rather than by the valence quarks. These W bosons are produced with small longitudinal momentum in the laboratory frame.

Two methods of selecting such a sample are discussed below. The first is based on restricting the measurement region to $|\eta| < 0.3$. The merit of the η -cut based selection is that it uses a directly measurable kinematic variable. Its drawback is that rather broad spectrum of the longitudinal momenta of annihilating partons is accepted due to the large mass of the W boson. The second is based on restricting the measurement region to $|y_W| < 0.3$. Here, only a narrow bin of the longitudinal momenta of annihilating partons is accepted in the region where the sea quarks outnumber the valence quarks. However, y_W cannot be measured directly. It has to be unfolded from the measured transverse momentum of the charged lepton and the reconstructed transverse momentum of the neutrino. The unfolding procedure [67] neglects the width of the W boson and depends upon the initial assumption of the relative momentum spectra of the valence and sea quarks. However, in the selected kinematic region the above approximation are expected to lead to a negligible measurement bias. It has to be stressed that the narrow bin measurements will require a 10 times higher luminosity to keep the statistical error of $\Delta_{(+,-)}$ at the level of 5 MeV. Therefore, the results presented below for the narrow bin method correspond to an integrated luminosity of 100 fb^{-1} and are based on the dedicated set of the simulated mass template and pseudo-data samples. Each sample contains $N_{W^+} = 1.74 \times 10^9$ and $N_{W^-} = 1.14 \times 10^9$ simulated (weighted) events, respectively.

The systematic biases of $\Delta_{(+,-)}$ due to modeling uncertainties discussed in the previous sections are presented in columns 2 and 3 of Table 5.5 respectively for the $|\eta| < 0.3$ and $|y_W| < 0.3$ selections. The η -cut based method reduces slightly the biases related to the uncertainties in the $u^{(v)} - d^{(v)}$

and $s - c$ asymmetries. The gain in the measurement precision is clearly seen for the y_W -cut based method which reduces to a negligible level the $s - c$ biases. It is interesting to note that the $u^{(v)} - d^{(v)}$ shifts in $\Delta_{(+,-)}$ change their signs for the above two methods, reflecting the importance of the W boson polarisation effects discussed earlier.

The narrow bin method allows, thus to reduce the impact of the W boson modeling uncertainties on the $\Delta_{(+,-)}$ biases to the level comparable to the statistical precision for all the effects, except for the $u^{(v)} - d^{(v)}$ asymmetry effect. Here another remedy has to be found.

(b) Isoscalar beams

Isoscalar targets have been successfully used in most of the previous fix-target deep inelastic scattering experiments at SLAC, FNAL and CERN, but this aspect has been rarely discussed in the context of the electroweak physics at the LHC. The merits of the ion beams for the generic searches of the electroweak symmetry breaking mechanism at the LHC have been discussed in [144]. Their use as carriers of the parasitic electron beam, to measure the emittance of the WBpB at the LHC, has been proposed in [196]. In our work we strongly advocate the merits of the isoscalar beams in improving the measurement precision of the parameters of the Standard Model. In this section we discuss their role in increasing the precision of the measurement of $\Delta_{(+,-)}$. We shall consider light ions: deuterium or helium. As far as the studies of the W boson asymmetries are concerned, they are equivalent because shadowing corrections are quark-flavour independent. The energies of the LHC ion beams satisfy the equal magnetic rigidity condition. For the isoscalar beams the nucleon energy is thus two times lower than the energy of the proton beam. In the presented studies we assume that the ion-ion luminosity is reduced by the factor A^2 with respect to the pp luminosity (cf. § 2.1.1).

In column 4 of Table 5.5 we present the impact of the modeling uncertainties on the $\Delta_{(+,-)}$ biases. The isoscalar beams allow to reduce the measurement biases due to the $u^{(v)} - d^{(v)}$ asymmetry effect to a negligible level. This colliding beam configuration allows to profit from the isospin symmetry of the strong interactions which cancels the relative biases in the momentum distribution of the u and d quarks. It is interesting to note that, as expected, the $s - c$ biases are similar for the proton and for the light isoscalar beams. On the contrary, the biases related to the flavour independent intrinsic momentum of the quarks and anti-quarks are amplified due to the reduced centre of mass collision energy⁴. Indeed, as seen already in § 4.A.7 we came up to the conclusion that at lower energies in the center of mass the charge asymmetry in the final state is much more visible since the charge symmetric sea contributions are not large enough.

5.4.4 Two complementary strategies

Two complementary strategies to achieve the ultimate measurement precision of $\Delta_{(+,-)}$ will certainly be tried. The first one will be based on an attempt to reduce the size of the systematic measurement and modeling uncertainties, discussed in the previous section. In our view, such a strategy will quickly reach the precision brick wall – mostly due to the a lack of data-driven constraints on modeling the flavour dependent W boson production at the LHC energy. The second one, instead of reducing the size of the uncertainties, attempts to reduce their impact on the systematic error of the measured quantity by applying the dedicated methods. Such a strategy requires running the dedicated machine and detector configurations. It is thus time and luminosity consuming. However, in our view, only such a strategy allows to measure the W mass charge asymmetries at the precision comparable to the one achieved in the muon decay experiments.

Let us recollect the main elements of the proposed dedicated measurement strategy that allow to reduce the systematic errors to the level shown in the shaded areas of Table 5.5:

⁴In order to amplify this effect, we have kept the same central value of the intrinsic transverse momentum smearing in the reduced collision energy as for the nominal collision energy.

- The charge asymmetry method allows to reduce the impact of most of the systematic measurement errors, except for the relative momentum scale errors for the positive and negative leptons. If they cannot be experimentally controlled to the level of $\mathcal{O}(10^{-4})$, their impact can be drastically reduced in the dedicated LHC running periods using the double charge asymmetry method.
- The impact of the uncertainty in modeling of the intrinsic transverse momentum of the WBpB can be reduced to a negligible level using the narrow bin measurement method.
- The impact of the $s - c$ uncertainty can be attenuated using the y_W selection based method in narrow bin.
- Finally, the impact of the $u^{(v)} - d^{(v)}$ uncertainty can be annihilated in the dedicated LHC runs with light isoscalar beams.

5.A Validation tests and miscellanea technical variations of the analysis

Buster: “Actually, I’m studying cartography now, the mapping of uncharted territories.”

Michael: “Sure. Hasn’t everything already sort of been discovered, though, by, like Magellan and Cortés? NASA, . . . you know ?”

Buster: “Oh, yeah, yeah. . . Those guys did a pretty great job.”

Lucile: (appearing between her sons) “Never hurts to double-check.”

Arrested Development - Extended Pilot

This Appendix presents in details the validations tests that were achieved to improve the analysis framework. The points addressed are the following.

The first part presents trivial results carried using the observable $\rho_{T,l}$ to crosscheck the one made with $p_{T,l}$. Other trivial tests were made as well with $p_{T,l}$ -based distributions using shifted W masses in the pseudo-data. The second part treats of the steadiness of the results with respect to certain input parameters for the analysis, such as the influence of the number of templates and their localisation with respect to the χ^2 minimum, the number of bins of the histograms, the window range for the analysis and the emulation of \cancel{E}_T cuts.

In the rest of this Appendix unless stated otherwise the tests are made preferentially using pp collisions selected with the requirements shown in Eq. (5.6) and in the conventional range of $30 \text{ GeV} < p_{T,l} < 50 \text{ GeV}$.

5.A.1 Details on the validation of the analysis framework

(a) Cross check of the analysis using the observable $\rho_{T,l}$

Since the observable $\rho_{T,l}$ is booked at the time of the generation it is pertinent to cross check the framework with $\rho_{T,l}$ -based methods for the case of trivial ($\xi = 0$) as well as non trivial ($\xi \neq 0$) tests. Besides, this simple studies allows as well to get accustomed to the behaviour of the variable $\rho_{T,l}$ and $\text{Asym}^{(+,-)}(\rho_{T,l})$. Starting with that last remark, Figure. 5.7 presents in frames (a), (b) the behaviour of the observable $\rho_{T,l}$ for: (1) the generated and unselected sample of events, (2) the generated and selected sample of events and (3) the unbiased simulated detector response and selected sample of events. In the each frame the range for the analysis $0.02 \text{ GeV} < \rho_{T,l} < 50 \text{ GeV}$ –equivalent to $30 \text{ GeV} < p_{T,l} < 50 \text{ GeV}$ – is highlighted. Just like for the $p_{T,l}$ distribution we can see that the cuts are responsible of a drastic change in the behaviour of the $\rho_{T,l}$ spectrum in particular in the region of the jacobian slope. In Fig. 5.7.(d) a trivial χ^2 test was performed for an unbiased pseudo-data using $\text{Asym}^{(+,-)}(\rho_{T,l})$. As expected the value $\Delta_{(+,-)} = 0$ is found. The results for $\xi \neq 0$ were found to be in a complete agreement –up to non avoidable numerical discrepancies– with the one provided by $p_{T,l}$ -methods.

(b) Validation using shifted mass for the W boson mass in the pseudo-data

Even though the previous trivial tests were found to be relevant, as long as the $\Delta_{(+,-)} = 0$ value doesn’t have a sign it is –so far– impossible to fully check the relevancy of the values. Also, the next logical step was to simulate unbiased pseudo-data but with shifted masses with respect to $M_W^{(\text{ref.})}$ for the boson and see if in the analysis we rediscover those shifts. Three tests were carried for that purpose using both classic and charge asymmetry methods. In each of these tests, the central values for the masses of the W^+ and W^- bosons were fixed for the generation of the pseudo-data to:

1. $M_{W^+}^{\text{PD}} = M_W^{(\text{ref.})} + 100 \text{ MeV}$ & $M_{W^-}^{\text{PD}} = M_W^{(\text{ref.})}$.
2. $M_{W^+}^{\text{PD}} = M_W^{(\text{ref.})}$ & $M_{W^-}^{\text{PD}} = M_W^{(\text{ref.})} + 100 \text{ MeV}$.

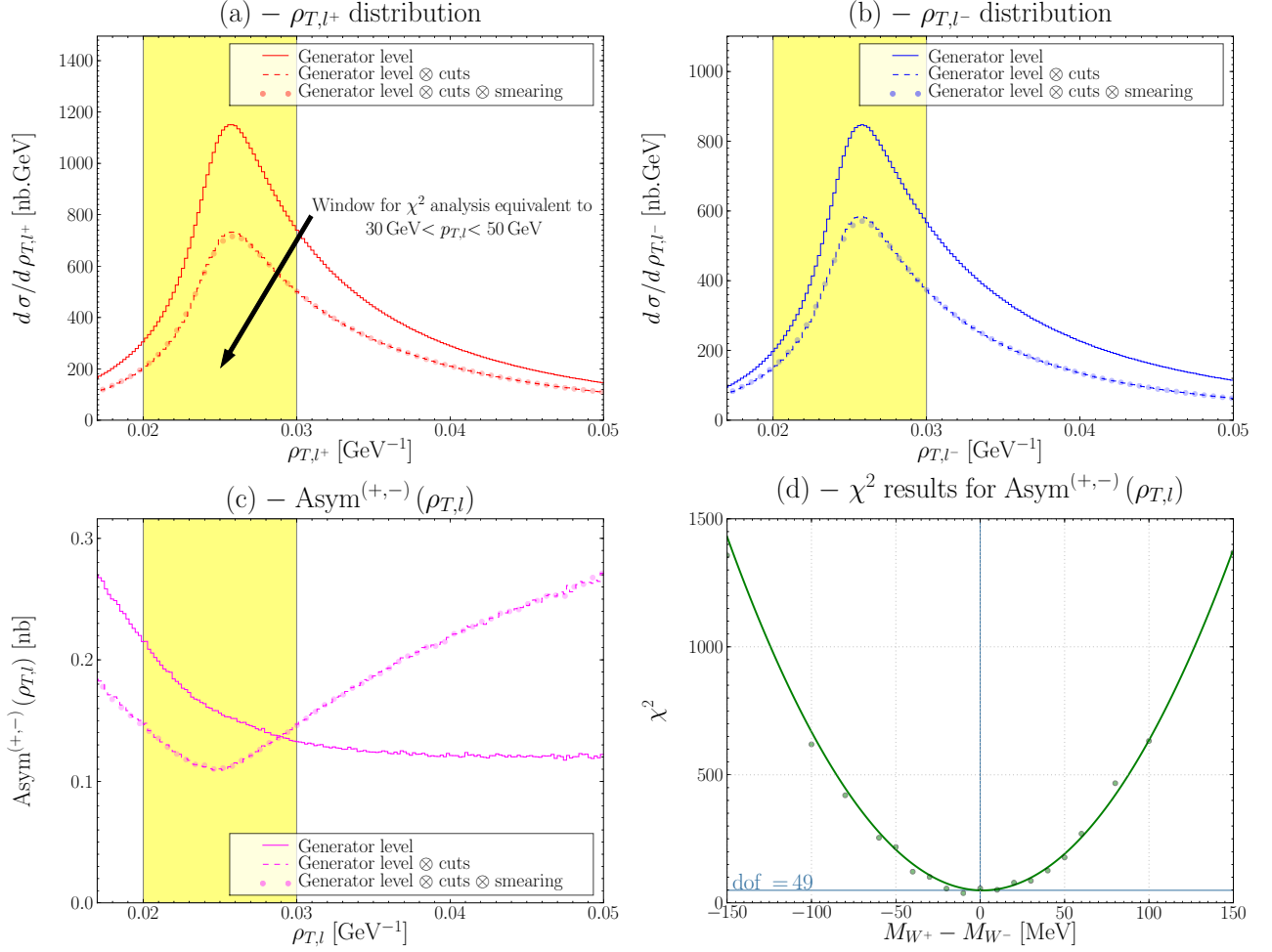


Figure 5.7: Visualisation of the inverse of the positive (a) and negative (b) charged lepton transverse momenta and associated charge asymmetry (c) at the generator level, adding up cuts and detector smearing. Frame (d) shows the trivial χ^2 results for unbiased pseudo-data ($\xi = 0$).

$$3. M_{W^+}^{\mathcal{PD}} = M_W^{(\text{ref.})} + 100 \text{ MeV} \quad \& \quad M_{W^-}^{\mathcal{PD}} = M_W^{(\text{ref.})} + 100 \text{ MeV}.$$

while the \mathcal{MT} remained the same *i.e.* generated with no biases and with $M_{W^+} = M_{W^-} = M_W^{(\text{ref.})}$ and where for reminder $M_W^{(\text{ref.})} = 80.403 \text{ GeV}$.

The Figure 5.8 presents in the first three frames ((a), (b) and (c)) the \mathcal{PD} histograms of p_{T,l^+} , p_{T,l^-} and $\text{Asym}^{(+,-)}(p_{T,l})$ for the case (1) of the previous item list where the mass of the W^+ has been fixed to 80.503 MeV while the mass of the W^- has been kept to 80.403 MeV . The two extrema \mathcal{MT} samples, \mathcal{MT}_{\min} and \mathcal{MT}_{\max} , have been drawn as well to enhance the deviation of the unbiased $\mathcal{PD}(\xi = 0)$ with respect to the half way position between them. Starting with Fig. 5.8.(a), the jacobian peak of the W^+ \mathcal{PD} is slightly shifted to higher p_T while the one for W^- in frame (b) is half-way between the two \mathcal{MT} . In frame (c), the charge asymmetry of $p_{T,l}$ is closer to the \mathcal{MT} for which $\Delta_{(+,-)} = +200 \text{ MeV}$. This is understandable as in general beyond the jacobian peak (*i.e.* $p_{T,l} > 40 \text{ GeV}$ or $\rho_{T,l} < 0.025 \text{ GeV}^{-1}$ in $\rho_{T,l}$ -space) the following equation holds

$$\left. \frac{d\sigma}{da} \right|_{M_W^{(2)}} > \left. \frac{d\sigma}{da} \right|_{M_W^{(1)} < M_W^{(2)}}, \quad (5.25)$$

where a is to be replaced by $p_{T,l}$ or $\rho_{T,l}$. Then, because of the form of the charge asymmetry (Eq. (1.7)), in this first test, increasing the mass M_{W^+} increases the p_{T,l^+} spectrum for each fixed p_T

value beyond the jacobian peak with respect to its former value eventually leading to an increase of both numerator and denominator. In the end, we observe that the kinematics at the LHC are such that the charge asymmetry of $p_{T,l}$ or $\rho_{T,l}$ are growing functions in the parameter $\Delta_{(+,-)}$ as already hinted by the behaviour of the \mathcal{MT} .

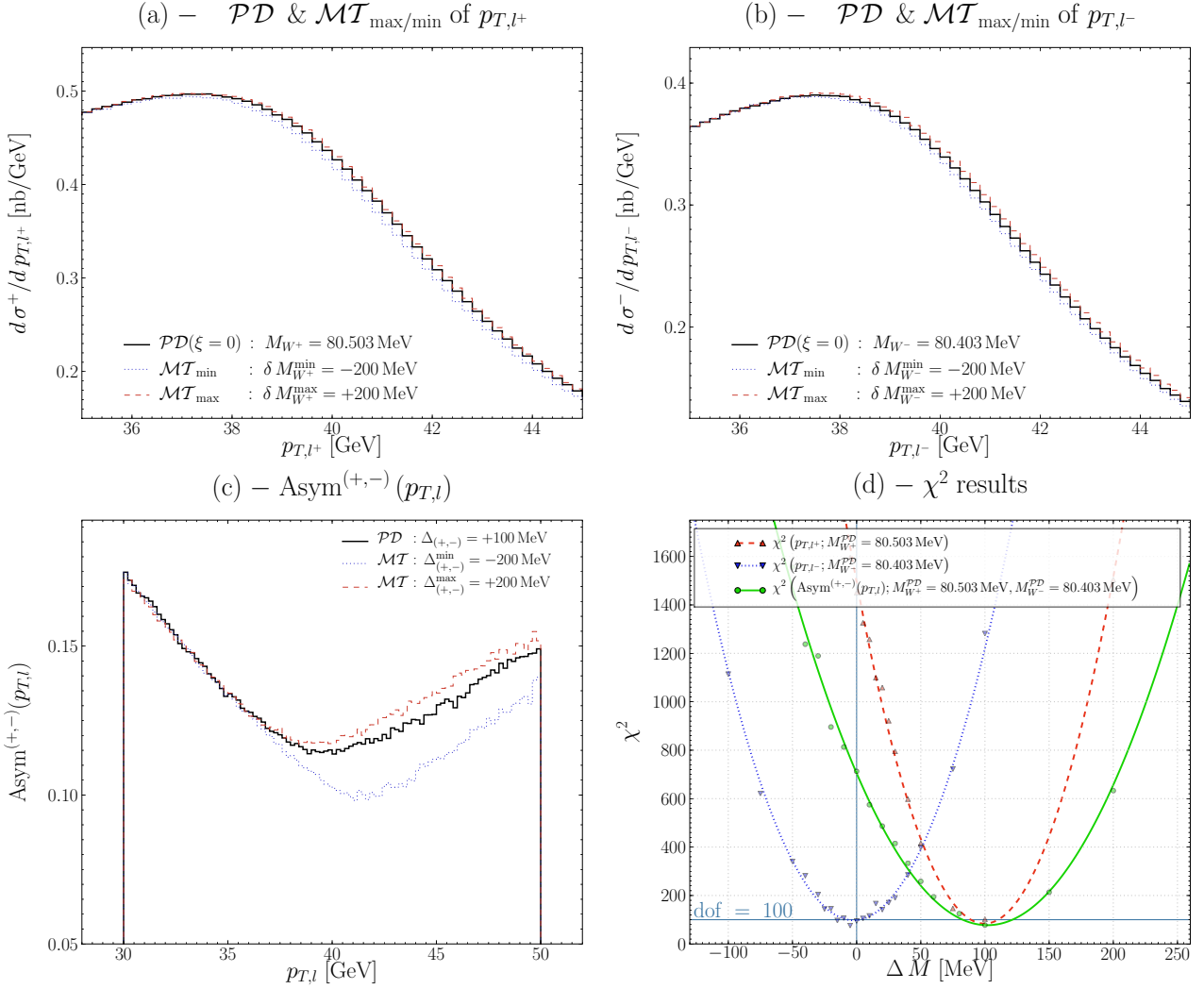


Figure 5.8: Histograms of the two extrema mass templates and for the particular case of unbiased pseudo-data \mathcal{PD} having $M_{W^+} = 80.503$ GeV and $M_{W^-} = 80.403$ GeV for the bare positive (a) and negative (b) $p_{T,l}$ spectra and charge asymmetry of $p_{T,l}$ (c) along with the corresponding χ^2 results (d) where ΔM are defined according to Eqs. (5.26).

Finally the χ^2 tests for the p_{T,l^+} , p_{T,l^-} and $\text{Asym}^{(+,-)}(p_{T,l})$ spectra are represented in Fig. 5.8.(d). The meaning of ΔM depends on the parabola we look at, we have:

$$\begin{aligned}
 \Delta M &\equiv M_{W^+}^{\mathcal{PD}} - M_W^{(\text{ref.})} && \text{if looking at } \chi^2(p_{T,l^+}), \\
 \Delta M &\equiv M_{W^-}^{\mathcal{PD}} - M_W^{(\text{ref.})} && \text{if looking at } \chi^2(p_{T,l^-}), \\
 \Delta M &\equiv M_{W^+}^{\mathcal{PD}} - M_{W^-}^{\mathcal{PD}} && \text{if looking at } \chi^2(\text{Asym}^{(+,-)}(p_{T,l})).
 \end{aligned} \tag{5.26}$$

Starting with the χ^2 associated to p_{T,l^+} we find a shift of 100 MeV present in the pseudo-data with respect to the reference mass confirming that $M_{W^+}^{\mathcal{PD}} = 80.503$ GeV while looking at the negatively charged p_{T,l^-} analysis we find $M_{W^-}^{\mathcal{PD}} = 80.403$ GeV. Finally the case of the analysis based on the charge asymmetry gives direct access to the charge difference between the masses of the pseudo-data

\mathcal{MT} range [MeV]	χ^2_{\min}/dof	$\Delta_{(+,-)}(\xi = 0)$ [MeV] ($M_{W^+}^{\mathcal{PD}} - M_{W^-}^{\mathcal{PD}} = 100 \text{ MeV}$)
± 200	0.77	102.0
± 150	0.84	103.7
± 80	1.20	95.4
± 60	1.69	89.3
± 20	2.34	73.9

Table 5.6: Influence of the lack of mass templates in the vicinity of the χ^2 parabola fit minimum looking at the trivial case where $\xi = 0$ with $M_{W^+}^{\mathcal{PD}} = M_{W^-}^{\mathcal{PD}} + 100 \text{ MeV}$ and using the $\text{Asym}^{(+,-)}(p_{T,l})$ method.

W bosons, that is $M_{W^+}^{\mathcal{PD}} - M_{W^-}^{\mathcal{PD}} = 100 \text{ MeV}$. For the cases (2) and (3) of the previous item list the results were found to be relevant as well.

Let us note that in the case of the $p_{T,l+}$ and $\text{Asym}^{(+,-)}(p_{T,l})$ parabola the fact there are less points in the vicinity of the parabola minimum does not decrease the degree of convergence of the calculus. For non trivial analysis where $\xi \neq 0$ we often observe shifts of such amplitude that most of the points are localised on one side only of the fitted parabola. Hence a question we can ask is at which point the small number of considered mass templates is sufficient to provide a relevant value. In the next Subsection we investigate this issue by using the present pseudo-data for unbiased χ^2 tests.

5.A.2 Influence on the results of some input parameters to the analysis

(a) Influence of the localisation and number of templates

In this part we consider the problem where the systematic error is such that there are no simulated mass templates having masses of the order of the systematic error. In other words we want to address the problem where we have to perform of parabola fit with the points being far from the parabola minimum and localised in one side only of the minimum. For that purpose we consider the same pseudo-data with $\xi = 0$ than in the case (1) of the item list of the previous section, that is with $M_{W^+}^{\mathcal{PD}} = M_W^{(\text{ref.})} + 100 \text{ MeV}$, $M_{W^-}^{\mathcal{PD}} = M_W^{(\text{ref.})}$, $M_W^{(\text{ref.})} = 80.403 \text{ MeV}$ and use the charge asymmetry method. This emulates in a good way the cases where $\Delta_{(+,-)}(\xi) \gg 0$ for $\xi \neq 0$.

To see at which point the localisation of the templates matters we reduce the range covered by the templates to see at which level the convergence and $\Delta_{(+,-)}$ value changes. The results are shown in Table. 5.6. Then we come to the conclusion that as long as the systematic errors $\Delta_{(+,-)}$ are such that $|\Delta_{(+,-)}(\xi)| < 200 \text{ MeV}$ if the convergence is poor ($\chi^2_{\min}/\text{dof} \gg 1$) it has to be blamed purely on the distortion on the \mathcal{PD} affected by the bias ξ . On the other hand, for the cases where $|\Delta_{(+,-)}(\xi)| > 200 \text{ MeV}$ a bad convergence will always be observed because of the lack of mass templates which eventually will provide values of $\Delta_{(+,-)}$ which will differ from the one to be observed if having generated much more templates.

Nonetheless, with the chosen biases ξ values and the analysis techniques developed most of the errors $\Delta_{(+,-)}$ are within the $\pm 200 \text{ MeV}$ range which justify why the extension of the range was not considered a vital problem to extract the essential physics from our analysis.

(b) Influence of the resolution of the histograms

In this part we considered changes to larger bins for the analysis with respect to the one used for the generation to see at which level the bin width of the histograms is important. Let us remind the former binning corresponded to a resolution of 200 MeV, which in the range of $20 \text{ GeV} < p_{T,l} < 60 \text{ GeV}$ corresponded to 200 bins.

Number of bins	δp_T [GeV]	Classic $\Delta_{(+,-)}^{(\chi_{+,-}^2/\text{dof})}$	Charge Asymmetry $\Delta_{(+,-)}^{(\chi_{\text{min}}^2/\text{dof})}$
200	0.2	0.8 ± 5.8 $\begin{matrix} (0.86) \\ (0.98) \end{matrix}$	1.2 ± 4.1 (0.82)
100	0.4	0.9 ± 5.7 $\begin{matrix} (0.94) \\ (1.10) \end{matrix}$	1.3 ± 4.1 (0.95)
50	0.8	1.0 ± 5.8 $\begin{matrix} (0.97) \\ (1.06) \end{matrix}$	1.5 ± 4.1 (0.90)
25	1.6	1.2 ± 5.7 $\begin{matrix} (1.02) \\ (1.23) \end{matrix}$	1.9 ± 4.1 (0.96)

Table 5.7: Influence of the binning of the histograms for the likelihood analysis. These results corresponds to unbiased ($\xi = 0$), the number of bins corresponds to the one for the range $20 \text{ GeV} < p_{T,l} < 60 \text{ GeV}$.

We present here the results for the classic and charge asymmetry methods in the case of pp collisions for the standard cuts of $p_{T,l} > 20 \text{ GeV}$ and $|\eta_l| < 2.5$. The likelihood test was carried for the case of unbiased pseudo-data ($\xi = 0$). The procedure for the likelihood test between the pseudo-data $\mathcal{PD}(\xi = 0)$ and the n^{th} -mass template $\mathcal{MT}^{(n)}$ was done in two steps: (1) \mathcal{PD} and $\mathcal{MT}^{(n)}$ histograms were re-binned to a lower resolution, (2) the likelihood analysis was carried out, *i.e.* the two histograms are cut to the standard analysis window of $30 \text{ GeV} < p_{T,l} < 50 \text{ GeV}$ and then the χ^2 test was done.

Table 5.7 shows the influence of different δp_T resolutions for the charged lepton on the χ^2 results while Figure 5.9 present p_{T,l^+} and $\text{Asym}^{(+,-)}(p_{T,l})$ spectra with a resolution of $\delta p_T \approx 0.8 \text{ GeV}$.

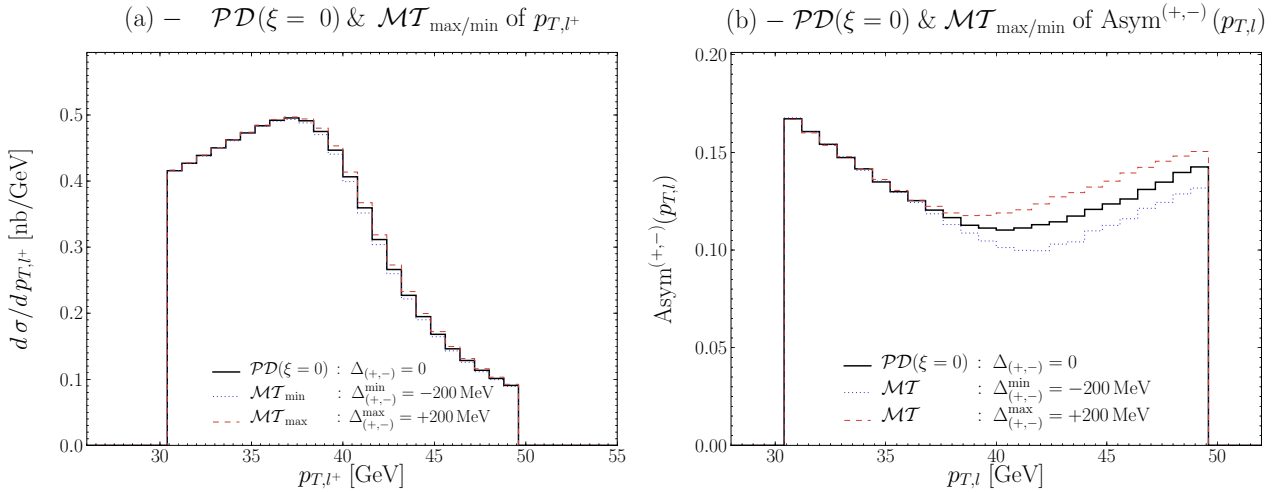


Figure 5.9: Pseudo-data and extrema mass templates p_{T,l^+} (a) and $\text{Asym}^{(+,-)}(p_{T,l})$ (b) histograms for a resolution of $\delta p_T = 0.8 \text{ GeV}$.

(c) Influence of the window in $p_{T,l}$

We look now at the influence of the window for the χ^2 analysis. Enlarging the range at low and high p_T would imply in reality to test the sensibility of the charge asymmetry observable as a mean to extract the W mass respectively toward the modeling of the low p_T background differences between the W^+ and the W^- production and the influence of the Γ_W and/or $\Gamma_{W^+} \neq \Gamma_{W^-}$ in the high p_T region.

In the first step the high $p_{T,l}$ is maintained at 50 GeV. Then, taking the minimum value of 20 GeV

for the low cut we found for trivial results using the charge asymmetry of $p_{T,l}$:

$$20 \text{ GeV} < p_{T,l} < 50 \text{ GeV} \quad \Rightarrow \quad \Delta_{(+,-)}(\xi = 0) = 1.3 \pm 4.1 \quad (\text{with } \chi_{\min}^2/\text{dof} = 0.84), \quad (5.27)$$

which does not enhance the former result seen in Eq. (5.15). Now, considering the whole range used for the p_{T,l^+} and p_{T,l^-} histograms, still using the charge asymmetry $\text{Asym}^{(+,-)}(p_{T,l})$ we find:

$$20 \text{ GeV} < p_{T,l} < 60 \text{ GeV} \quad \Rightarrow \quad \Delta_{(+,-)}(\xi = 0) = 1.1 \pm 3.9 \quad (\text{with } \chi_{\min}^2/\text{dof} = 0.87), \quad (5.28)$$

that is here we have a slightly better result.

Since the results do not change a lot this would eventually allow by first reducing the lower cut on p_T to see the influence of the different background contributions in the positive and negative channels. Note that the lower cut should not be too close from the trigger cut to avoid the possible charge dependency from the selection process. On the other hand, maintaining the lower cut fixed and exploring higher p_T cuts would allow now to study the influence of the W boson width on the results.

(d) Influence of p_{T,ν_l} cuts

The influence of the \cancel{E}_T cut was investigated with the best emulation achievable in our framework, that is during the generation process in top of the requirements from Eq. (5.6), the simulated events were selected if and only if the decaying neutrino displays $p_{T,\nu_l} > 20 \text{ GeV}$. All χ^2 ($\xi = 0$ and $\xi \neq 0$), up to non avoidable numerical discrepancies, were of the same values than the data gathered without doing any cut on the neutrino.

Just to cite two numbers, the Monte Carlo truth test gave:

$$\Delta_{(+,-)}(\xi = 0) = -1.0 \pm 3.3 \text{ MeV} \quad \text{with } \chi_{\min}^2/\text{dof} = 0.98, \quad (5.29)$$

while the unbiased experimental test gave:

$$\Delta_{(+,-)}(\xi = 0) = 1.0 \pm 4 \text{ MeV} \quad \text{with } \chi_{\min}^2/\text{dof} = 0.81. \quad (5.30)$$

Both of these values are very close to the one present in Table 5.4. This justified for the rest of the study the non necessity to take care of such cuts.

5.B Measurement of the W mass charge asymmetry: the How Not To

“That’s not right. It’s not even wrong.”

WOLFGANG PAULI’s words of wisdom
(Kept alive nowadays by M.W.K.)

We consider a particular context to extract $M_{W^+} - M_{W^-}$ that stresses the charge asymmetry between the p_{T,l^+} and p_{T,l^-} distributions at the LHC. For that matter we propose to assume just for a moment that we are not aware of the $V - A$ coupling of W bosons to fermions in the Standard Model and that the W^+ and W^- , which are particle and antiparticle of each other provide positively and negatively decaying charged leptons with the same kinematics. Putting aside the fact that the detector measurement are different between positively and negatively charged leptons we consider the extraction of $M_{W^+} - M_{W^-}$ could be obtained directly by confronting the data from one charge to mass templates generated for the opposite charge.

To be more precise, the data is here represented by Monte Carlo pseudo-data simulations of the W^+ confronted via χ^2 likelihood tests with Monte Carlo simulations of the W^- bosons. Unaware of the $V - A$ coupling and of all its consequences seen in Chapter 4 one would expect that in this configuration a trivial χ^2 test with unbiased W^+ pseudo-data should give $M_{W^+} - M_{W^-} = 0$ with a good convergence ($\chi^2_{\min}/\text{dof} \approx 1$).

Figure 5.10 shows the χ^2 test using the unbiased pseudo-data of the p_{T,l^+} distribution and using p_{T,l^-} for the mass templates (covering here the range ± 500 MeV). The result obtained is $\chi^2_{\min}/\text{dof} \approx 14,000$ and $M_{W^+} - M_{W^-} \approx 2.3$ GeV. The poor quality of this result can be understood using the arguments from the previous Appendix: the number of \mathcal{MT} is too small and far from the expected parabola minimum. Nonetheless as we saw the order is still more or less correct and gives an idea of the size of the error, hence here we can say that going to such a naive test imply an error of the order of the GeV which is completely ruled out by the actual measurements as seen in Table 1.2.

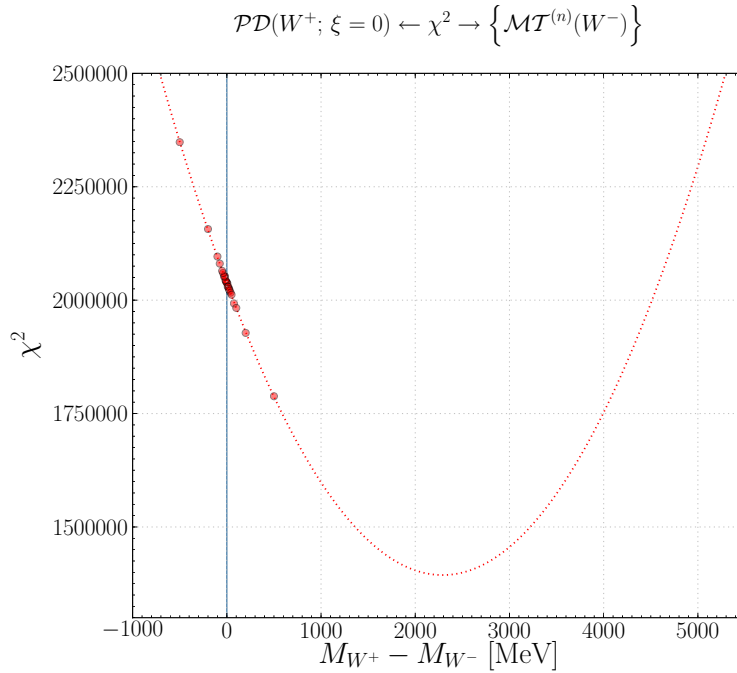


Figure 5.10: χ^2 results when considering the unbiased ($\xi = 0$) pseudo-data built from the positive charged lepton data and the mass templates built from the negatively charged lepton data

5.C Step-by-step interpretations of systematic errors results

Reggie: “Trucks come in and out of here all day long. Truck comes in, you unload it. Truck goes out, you load it. Next truck comes in, you unload it. Next truck. . .”

Randy (very confused): “Wait a second. Go back to that first truck.”

My Name is Earl - Get a real job

In this Appendix more details are given on the results presented in the core of the Chapter. For that purpose step-by-step comments of the tables are provided with the help of visual support.

The first Subsection introduces the notation implemented in the more detailed versions of the tables shown in the core of the Chapter. Then in a second part the comments of these detailed tables are made based each time on the relevant \mathcal{PD} and \mathcal{MT} histograms and χ^2 . The influence of the following effects are addressed in that chronological order

- (a) Energy scale of the charged lepton
 - Coherent biases between the positively and negatively charged lepton tracks (noted some-time for convenience “coherent biases”)
 - Incoherent biases between the positively and negatively charged lepton tracks (noted some-time for convenience “incoherent biases”)
- (b) Resolution of the charged lepton track parameters
- (c) Intrinsic k_T of the partons
- (d) $u^{(v)} - d^{(v)}$ asymmetry
- (e) $s - c$ asymmetry

5.C.1 Detailed tables

The Tables 5.9 and 5.10 in the following pages are just reproduction of Tables 5.4 and 5.5 from the core of the Chapter with some additive information. More precisely, each systematic error is now given with a precision of 0.1 MeV along with the associated χ^2_{\min}/dof value providing then further details on the degree of convergence of the calculus.

Besides, as explained previously, different random numbers sets were used for each event generation to emulate as better as possible uncorrelated events. For that purpose 100 independent seeds set were produced and tagged from set number 00 to set number 99. Practically the generation of $\approx 10^8$ events needed to be achieved by splitting each generation into several sub-generations. Each sub-generation were produced so that all the $100 \times n_s$ seeds were different to ensure the best possible un-correlation between different event batches. For the standard generation of one year of low luminosity, each W generation were split in average to 10 sub-generations, hence we used here $n_s = 20$. Concerning the generation in the narrow lepton pseudo-rapidity or W boson rapidity region this time each W generation were split in average into 50 hence here $n_s = 100$.

The seeds tags used for producing each pseudo-data \mathcal{PD} will be as well displayed in the tables, the one for the W^+ being labeled “(+)” each time written in top of the one used for W^- labeled “(-)”. Concerning the mass templates \mathcal{MT} , each $\mathcal{MT}^{(n)}$ template seed tag are indicated on the next page in Table 5.8.

$\delta M_W^{(n)}$ [MeV] for $\mathcal{MT}^{(n)}$	W^+ seed tag	W^- seed tag
0	10	50
-5	11	51
5	12	52
-10	13	53
10	14	54
-15	15	55
15	16	56
-20	17	57
20	18	58
-25	19	59
25	20	60
-30	21	61
30	22	62
-40	23	63
40	24	64
-50	25	65
50	26	66
-75	27	67
75	28	68
-100	29	69
100	30	70
-200	31	71
200	32	72

Table 5.8: Seed set associated to each mass templates generation.

		$M_{W^+} - M_{W^-}$ (χ^2_{\min}/dof) [MeV]			
Systematic ξ		Seed tag	Classic Method	Asym ^(+,-) ($\rho_{T,l}$)	DAsym ^(+,-) ($\rho_{T,l}$)
MC truth	$\xi = 0$	01 04	-1.6 ± 3.2 ^(1.05) _(0.95)	-1.0 ± 3.3 ^(0.98)	0.2 ± 3.3 ^(0.85)
Cent. Exp.	$\xi = 0$	01 04	0.8 ± 4.1 ^(0.86) _(0.98)	1.2 ± 4.1 ^(0.82)	0.4 ± 4.1 ^(0.90)
ES [%]	$\varepsilon_{l^+} = +\varepsilon_{l^-} = +0.05\%$	01 04	3.4 ^(1.35) _(1.39)	1.6 ^(0.99)	×
	$\varepsilon_{l^+} = +\varepsilon_{l^-} = -0.05\%$	01 04	-2.4 ^(1.19) _(1.24)	-0.3 ^(1.06)	
	$\varepsilon_{l^+} = +\varepsilon_{l^-} = +0.50\%$	01 04	15.9 ⁽³⁰⁾ ₍₂₄₎	7.9 ^(1.53)	
	$\varepsilon_{l^+} = +\varepsilon_{l^-} = -0.50\%$	01 04	-35.8 ⁽²⁷⁾ ₍₂₁₎	-6.2 ^(1.59)	0.9 ^(0.98)
	$\varepsilon_{l^+} = -\varepsilon_{l^-} = +0.05\%$	01 04	-56.1 ^(1.35) _(1.24)	-56.8 ^(1.48)	
	$\varepsilon_{l^+} = -\varepsilon_{l^-} = -0.05\%$	01 04	57.1 ^(1.19) _(1.39)	56.9 ^(1.48)	
	$\varepsilon_{l^+} = -\varepsilon_{l^-} = +0.50\%$	01 04	-567.2 ⁽³⁰⁾ ₍₂₁₎	-611.2 ⁽³⁰⁾	-0.6 ^(1.13)
$\varepsilon_{l^+} = -\varepsilon_{l^-} = -0.50\%$	01 04	547.2 ⁽²⁷⁾ ₍₂₄₎	514.8 ⁽⁵⁹⁾		
ERF	0.7	01 04	1.1 ⁽¹⁶⁾ ₍₁₃₎	-2.3 ^(0.95)	×
	1.3	01 04	-2.6 ⁽²³⁾ ₍₂₂₎	2.5 ^(1.08)	

Table 5.9: Experimental systematics errors for the classic method, the charge asymmetry and the double charge asymmetry. The results in the case of the double charge asymmetry are the one for $\varepsilon_{l^+} = -\varepsilon_{l^-} > 0$ for the first six months and $\varepsilon_{l^+} = -\varepsilon_{l^-} < 0$ for the last six months.

	Systematic ξ	Seed (+) (-)	$M_{W^+} - M_{W^-}$ (χ^2_{\min}/dof) [MeV] using Asym ^(+,-) ($p_{T,l}$)			
			$pp - \eta < 2.5$	$pp - \eta < 0.3$	$pp - y_W < 0.3$	$dd - \eta < 2.5$
MC truth	$\xi = 0$	01 04	-1.0 ± 3.3 (0.98)	-0.2 ± 1.2 (0.82)	-0.1 ± 1.2 (0.83)	-0.2 ± 4.5 (1.01)
Cent. Exp.	$\xi = 0$	01 04	1.2 ± 4.1 (0.82)	-0.2 ± 4.1 (1.19)	-1.1 ± 4.1 (1.06)	4.2 ± 5.2 (0.94)
$\langle k_T \rangle$ [GeV]	2	90 93	7.7 (1.02)	0.0 (1.26)	1.8 (0.98)	27.9 (1.28)
	3	00 03	7.0 (1.04)	2.8 (1.10)	-1.7 (1.01)	19.9 (1.10)
	5	02 05	-3.8 (0.89)	-3.4 (1.12)	-6.4 (1.15)	-14.7 (1.07)
	6	91 94	-7.6 (1.14)	2.3 (0.98)	-5.1 (1.11)	-34.5 (1.65)
	7	92 95	-15.8 (1.36)	1.8 (1.24)	-8.1 (1.00)	-48.5 (2.53)
PDF(*)	Min.	01 04	-4.1 (0.85)	5.6 (1.23)	-0.4 (1.13)	-2.5 (0.94)
	Max.	01 04	4.2 (0.81)	-8.4 (1.20)	4.6 (1.11)	7.5 (0.92)
$u^{(v)}, d^{(v)*}$	$u_{\max}^{(v)} = 1.05 u^{(v)}$ $d_{\min}^{(v)} = d^{(v)} - 0.05 u^{(v)}$	76 77	114.5 (7.52)	68.7 (3.21)	-38.1 (1.44)	2.9 (0.95)
	$u_{\min}^{(v)} = 0.95 u^{(v)}$ $d_{\max}^{(v)} = d^{(v)} + 0.05 u^{(v)}$	78 79	-138.5 (7.93)	-87.2 (3.41)	59.8 (1.44)	4.5 (0.94)
	$u_{\max}^{(v)} = 1.02 u^{(v)}$ $d_{\min}^{(v)} = 0.92 d^{(v)}$	86 87	83.7 (3.92)	52.6 (2.09)	-30.5 (1.27)	1.0 (0.99)
	$u_{\min}^{(v)} = 0.98 u^{(v)}$ $d_{\max}^{(v)} = 1.08 d^{(v)}$	88 89	-88.5 (4.30)	-56.7 (2.26)	44.4 (1.36)	5.7 (1.13)
$s, c^{(*)}$	$c_{\min} = 0.9 c$, $s_{\max} = s + 0.1 c$	78 79	17.1 (0.99)	9.9 (1.12)	7.3 (1.01)	19.7 (0.99)
	$c_{\max} = 1.1 c$, $s_{\min} = s - 0.1 c$	80 81	-10.8 (1.22)	-10.3 (1.24)	-0.3 (1.16)	-15.7 (1.17)
	$c_{\min} = 0.8 c$, $s_{\max} = s + 0.2 c$	76 77	38.8 (1.38)	24.7 (1.31)	6.1 (1.10)	38.0 (1.71)
	$c_{\max} = 1.2 c$, $s_{\min} = s - 0.2 c$	82 83	-29.0 (1.42)	-23.7 (1.29)	1.0 (1.27)	-33.8 (2.00)

Table 5.10: The shifts of the W -mass charge asymmetry corresponding to various modeling effects. The systematic labeled * are obtained using the scaling trick mentioned in § 5.2.3.

5.C.2 Detailed comments and graphics

(a) Energy scale of the charged lepton

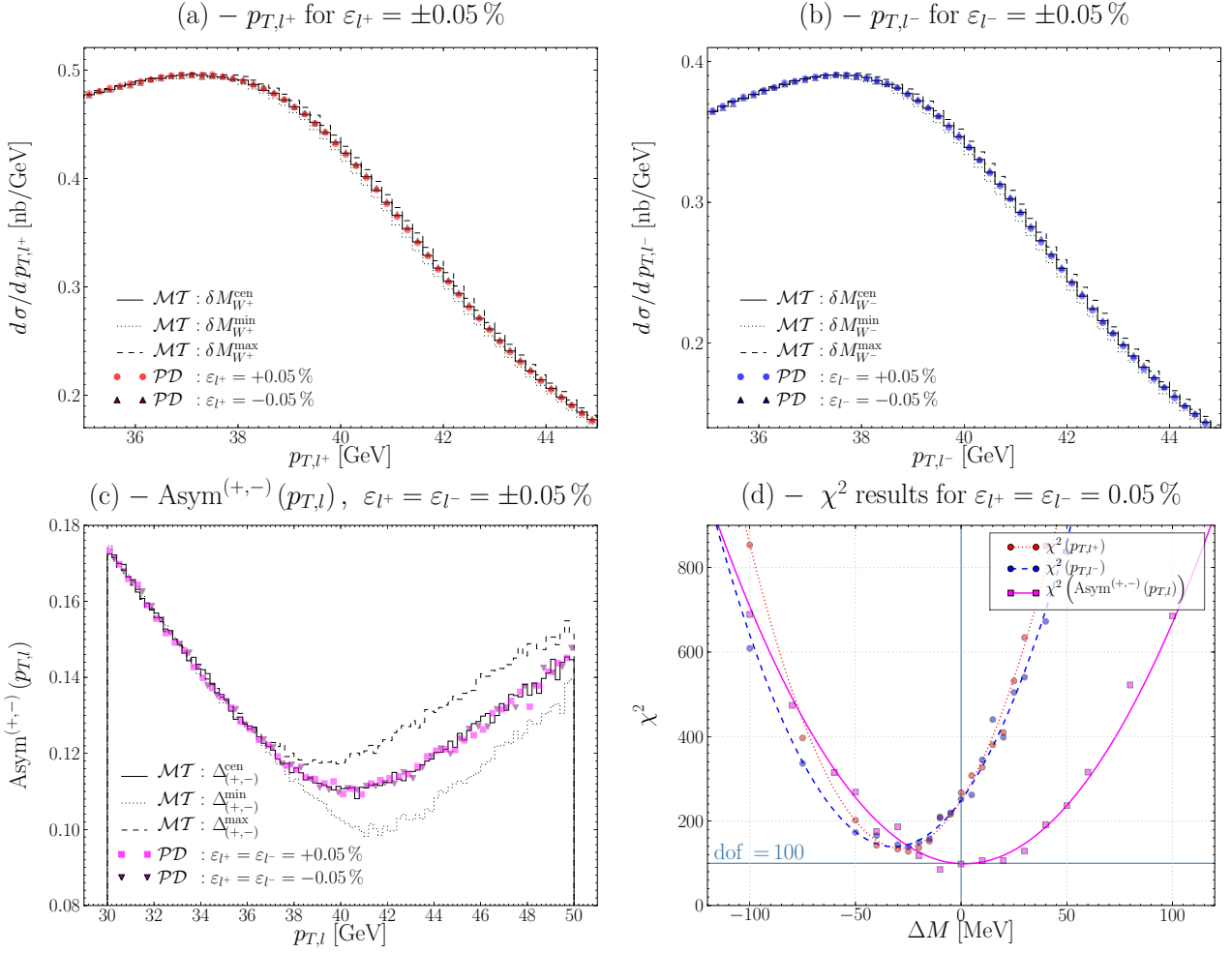


Figure 5.11: Systematic error on $M_{W^+} - M_{W^-}$ due to coherent energy scale biases ($\varepsilon_l = 0.05\%$) between the positively and negatively charged lepton reconstructed transverse momenta and for both classic and charge asymmetry methods. Frames (a) and (b) display respectively the jacobian peaks of the p_{T,l^+} and p_{T,l^-} spectra for the minimum, central and maximum \mathcal{MT} and for the two biased \mathcal{PD} distributions corresponding to $\varepsilon_l = \pm 0.05\%$ while frame (c) displays the same data but for $\text{Asym}^{(+,-)}(p_{T,l})$. Frame (d) presents the χ^2 results for the classic and charge asymmetry methods for the case of $\varepsilon_{l^+} = \varepsilon_{l^-} = 0.05\%$, $\Delta M \equiv M_{W^\pm}^{\mathcal{PD}} - M_W^{\text{(ref.)}}$ for the classic method results and $\Delta M \equiv M_{W^+} - M_{W^-}$ for the charge asymmetry result.

We start our detailed review on the energy scale systematics looking at the coherent biases. The plots above in Fig. 5.11 illustrate the consequences of coherent biases between the positively and negatively charged lepton reconstructed tracks. Fig. 5.11.(a) represents several distributions of the transverse momentum of the l^+ lepton. For the sake of clarity, only three mass templates \mathcal{MT} from the entire collection have been drawn, the minimum template ($\delta M_{W^+} = -200$ MeV), the central one ($\delta M_{W^+} = 0$ MeV) and the maximum one ($\delta M_{W^+} = +200$ MeV). Although the histograms are considered for the analysis in the range of $30 \text{ GeV} < p_{T,l} < 50 \text{ GeV}$, a zoom was made on the jacobian peaks to make it possible to resolve by the eye the differences between the three \mathcal{MT} . In top of these histograms the \mathcal{PD} histograms corresponding to $\varepsilon_{l^+} = -0.05\%$ and $\varepsilon_{l^+} = +0.05\%$ are shown. For such values the deviation from $\Delta_{(+,-)}^{\text{cen}}$ is hardly decipherable. Fig. 5.11.(b) shows the exact same thing than in (a) but this time for the negative lepton. Fig. 5.11.(c) represents the charge asymmetry of $p_{T,l}$ for its central \mathcal{MT} ($\delta M_{W^+}^{\text{cen}} \equiv 0$ MeV), minimum \mathcal{MT} ($\Delta_{(+,-)}^{\text{min}} \equiv -200$ MeV) and maximum

\mathcal{MT} ($\Delta_{(+,-)}^{\max} \equiv +200 \text{ MeV}$). Are also present the two \mathcal{PD} for which $\varepsilon_{l^+} = \varepsilon_{l^-} = \pm 0.05\%$. Note here that the difference between the \mathcal{MT} is much more magnified which is directly associated with the fact that the charge asymmetry, by its form, get rid of the common features from both p_{T,l^+} and p_{T,l^-} histograms and as a consequence emphasise the discrepancies among them. Note also that to decipher between the points of the two different \mathcal{PD} , in each distribution a point is being skipped. Fig. 5.11.(d) presents the χ^2 results for both classic and charge asymmetry methods for the case of $\varepsilon_{l^+} = \varepsilon_{l^-} = 0.05\%$. As seen in Table 5.9 both errors are quite steady with respect to the considered value of $|\varepsilon_l| = 0.05\%$, nonetheless the convergence for the charge asymmetry method is slightly better than for the classic method.

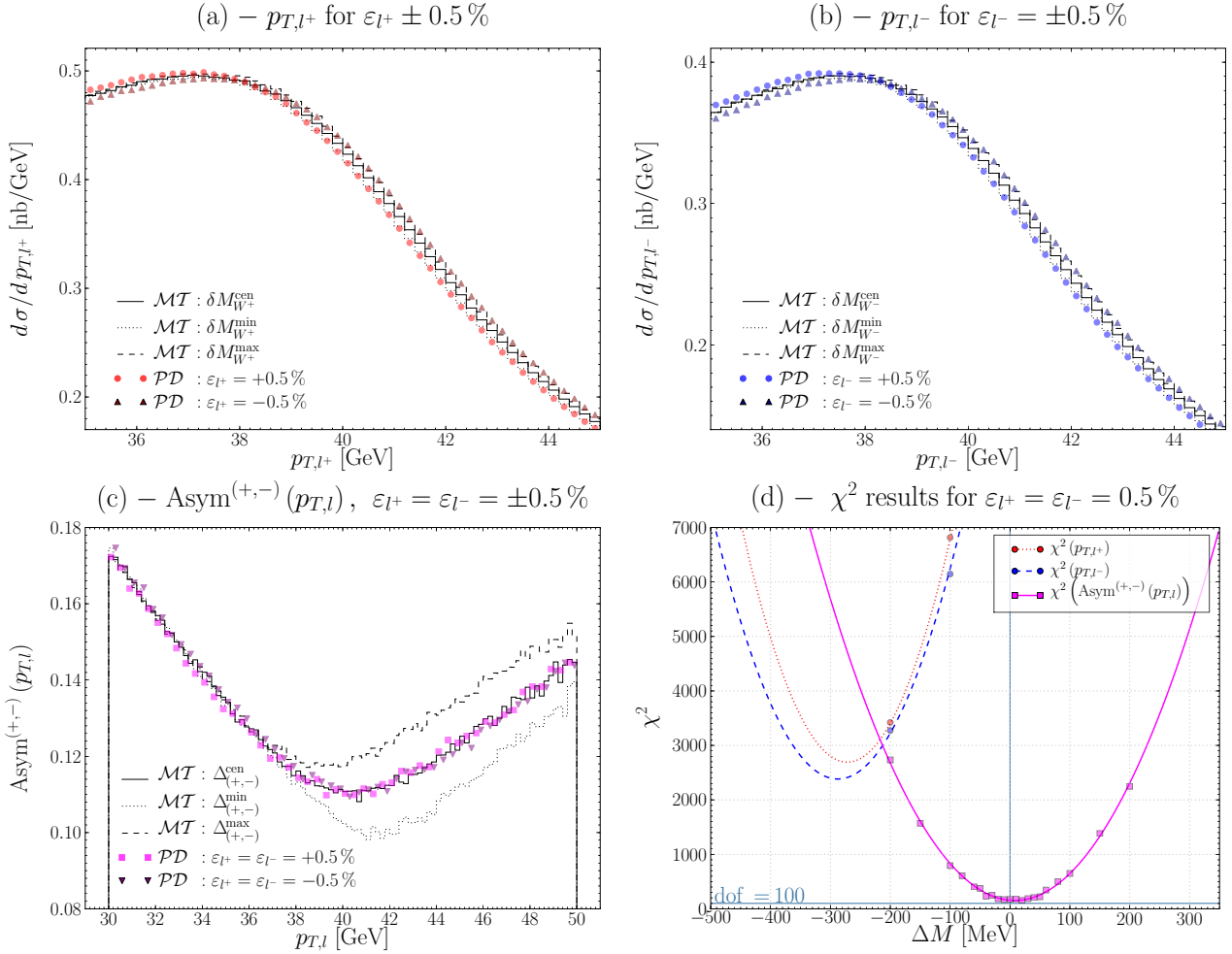


Figure 5.12: Systematic error on $M_{W^+} - M_{W^-}$ due to coherent energy scale biases ($\varepsilon_l = \pm 0.5\%$) between the positively and negatively charged lepton reconstructed transverse momenta and for both classic and charge asymmetry methods. Frames (a) and (b) display respectively the jacobian peaks of the p_{T,l^+} and p_{T,l^-} spectra for the minimum, central and maximum \mathcal{MT} and for the two biased \mathcal{PD} distributions corresponding to $\varepsilon_l = \pm 0.5\%$ while frame (c) displays the latter distributions for $\text{Asym}^{(+,-)}(p_{T,l})$. Frame (d) presents the χ^2 results for the classic and charge asymmetry methods for the case of $\varepsilon_{l^+} = \varepsilon_{l^-} = 0.5\%$, $\Delta M \equiv M_{W^\pm}^{\mathcal{PD}} - M_W^{\text{(ref.)}}$ for the classic method results and $\Delta M \equiv M_{W^+} - M_{W^-}$ for the charge asymmetry result.

Now Fig. 5.12 represents the same histograms than in Fig. 5.11 but this time with $\varepsilon_l = \pm 0.5\%$. Now the bias is large enough so we can see some differences. Indeed, starting with Fig. 5.12.(a) the jacobian peaks of the \mathcal{PD} are slightly shifted to higher p_T for $\varepsilon_l = -0.5\%$ and to lower p_T for $\varepsilon_l = 0.5\%$. This can seem quite non intuitive but let us remind the biases are applied to $\rho_{T,l}$, the inverse of $p_{T,l}$, hence as long as $\varepsilon_l \ll 1$, the bias on $p_{T,l}^{\text{(rec.)}}$ can be deduced at first order from the

expression of $\rho_{T,l}^{(\text{rec.})}$:

$$\rho_{T,l}^{(\text{rec.})} = \rho_{T,l}^{(\text{true})} (1 + \varepsilon_l) \quad \Rightarrow \quad p_{T,l}^{(\text{rec.})} = p_{T,l}^{(\text{true})} (1 - \varepsilon_l), \quad (5.31)$$

justifying the inverse behaviour between $\rho_{T,l}$ and $p_{T,l}$ biases. Then, considering for example the case of $\varepsilon_l = -0.5\%$, in both Figs. 5.12.(a) and (b) the jacobian peaks of the \mathcal{PD} being shifted to lower p_T both $M_{W^+}^{\mathcal{PD}}$ and $M_{W^-}^{\mathcal{PD}}$ are underestimated by ≈ 300 MeV as seen in frame (c). Nonetheless, since these biases are coherent the impact on $M_{W^+} - M_{W^-}$ is of the order of 16 MeV only. The low convergences $\chi_{\text{min}}^2/\text{dof} \approx 30$ is due to the lack of enough mass templates. In Fig. 5.12.(c) the charge asymmetry of $p_{T,l}$ the two \mathcal{PD} show more steadiness than the bare $p_{T,l}$ spectra. Again for the sake of clarity in each \mathcal{PD} distribution one point is being skipped each time. As expected the stability of the charge asymmetry with respect to biases of $|\varepsilon_l| = 0.05\%$ is such that the χ^2 shows good convergence and no particular deviation from the central $M_{W^+} - M_{W^-} = 0$.

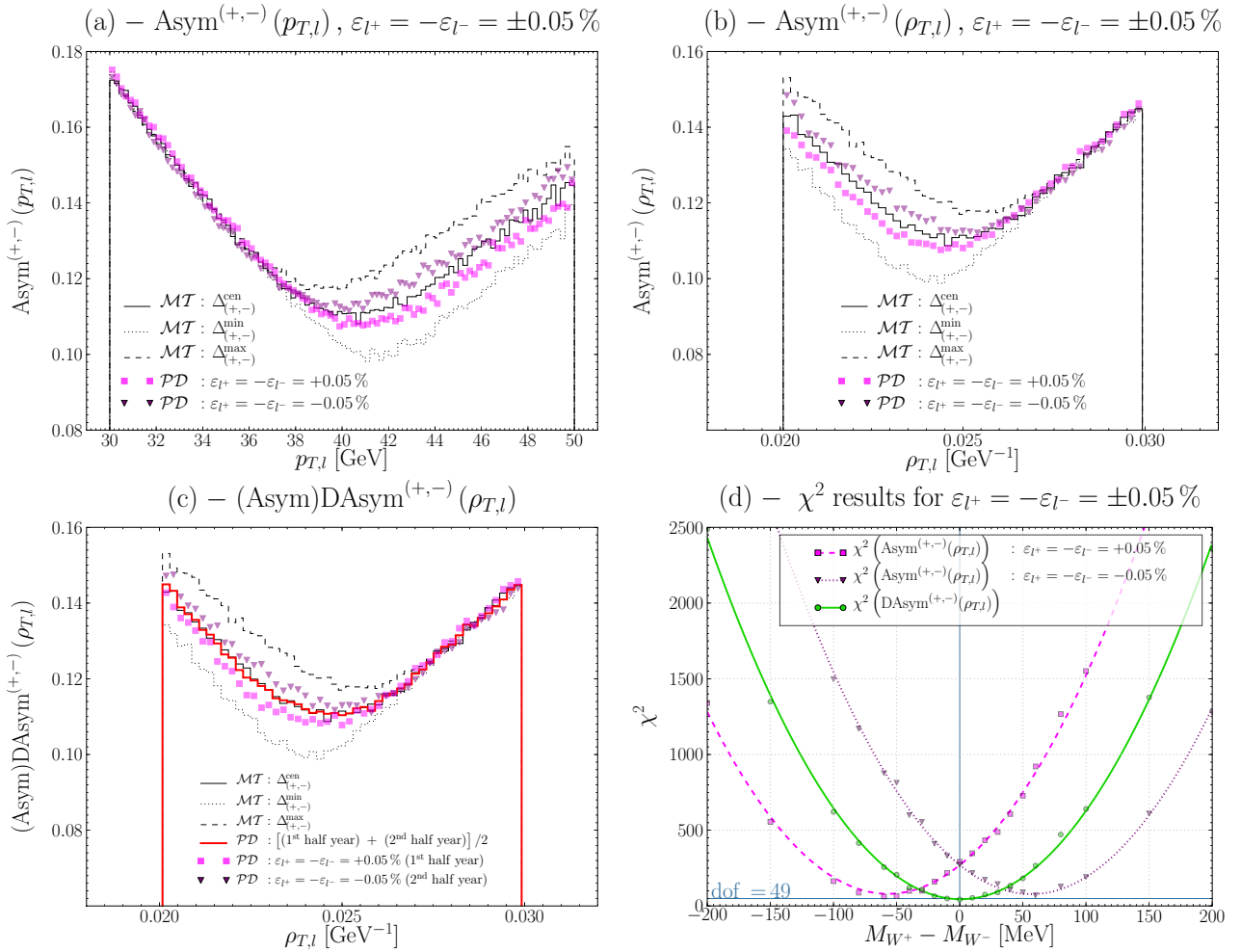


Figure 5.13: Systematic error on $M_{W^+} - M_{W^-}$ due to incoherent energy scale biases ($\varepsilon_l = \pm 0.05\%$) for both charge and double charge asymmetry methods. Frames (a) and (b) display respectively the charge asymmetry of $p_{T,l}$ and $\rho_{T,l}$ for the minimum, central and maximum \mathcal{MT} along with the \mathcal{PD} corresponding to incoherent biases of size $\varepsilon_l = \pm 0.05\%$. Frame (c) displays the latter distributions for $\text{DAsym}^{(+,-)}(\rho_{T,l})$. Frame (d) presents the χ^2 results for both charge and double charge asymmetry methods for the case of $\varepsilon_{l^+} = \varepsilon_{l^-} = 0.05\%$.

The incoherent biases for the energy scale between the positive and negative charged lepton is now addressed starting with Fig. 5.13 that considers the case of $\varepsilon_{l^+} = -\varepsilon_{l^-} = \pm 0.05\%$. This time the classic method is no longer treated since the χ^2 are too much out of charts. Instead the charge and double charge asymmetry are confronted. First, Fig. 5.13.(a) shows the charge asymmetry of $p_{T,l}$ for

the usual central and extrema \mathcal{MT} and the two \mathcal{PD} biased by energy scales of $\varepsilon_{l+} = -\varepsilon_{l-} = \pm 0.05\%$. In Fig. 5.13.(b) the same data is drawn in function of $\rho_{T,l}$ since it is in that space the χ^2 is performed. Unlike the “coherent biases” here the \mathcal{PD} deviation from the central \mathcal{MT} are such that in (d) the systematic error are quite important, more precisely of the order of ± 50 MeV. Now in Fig. 5.13.(c) the case of the double charge asymmetry is considered in the $\rho_{T,l}$ space. The \mathcal{MT} are exactly the same than the one used in (b), and the pseudo-data shows the cases where $\varepsilon_{l+} = -\varepsilon_{l-} = 0.05\%$ during the first year of the data collection and $\varepsilon_{l+} = -\varepsilon_{l-} = -0.05\%$ for the second half of the year due to the reversing of the solenoidal magnetic field of the tracker. Averaging the two data batches from the two six months period gives eventually a data collection which is localised near the central \mathcal{MT} . The consequence can be seen in Fig. 5.13.(d), the double charge asymmetry is robust against such incoherent biases.

Finally, the “incoherent biases” are considered for $\varepsilon_{l+} = -\varepsilon_{l-} = \pm 0.5\%$ as shown in Fig. 5.14. Here we can see the biased data are completely different from the templates. Nonetheless, for the double charge asymmetry the average of the two “six-months-data” gives again a total pseudo-data batch centered on the central \mathcal{MT} distribution. Then, once again, the systematic error is still negligible for the double charge asymmetry while the charge asymmetry is not sufficient to draw any conclusion.

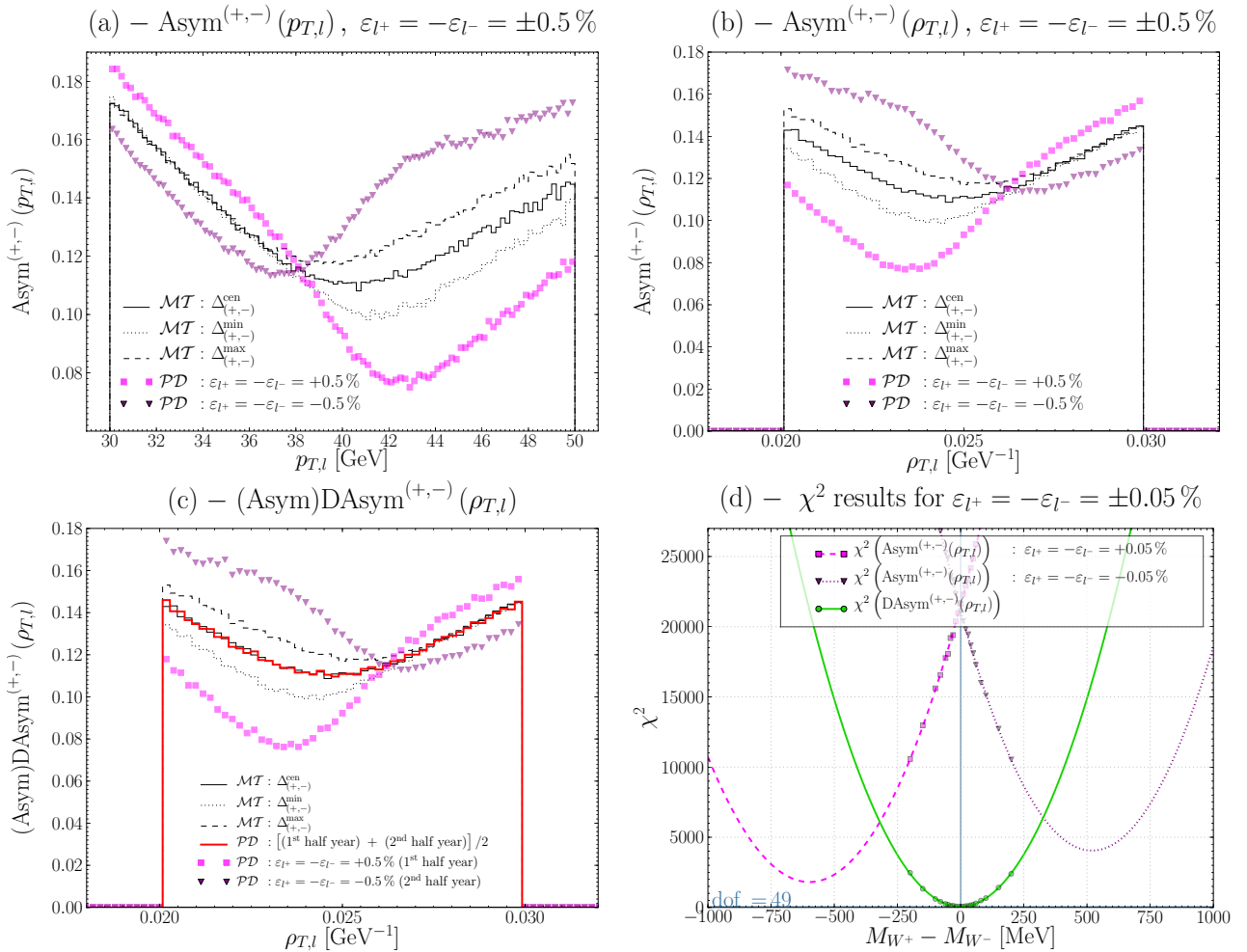


Figure 5.14: Systematic error on $M_{W^+} - M_{W^-}$ due to incoherent energy scale biases ($\varepsilon_l = \pm 0.5\%$) for both charge and double charge asymmetry methods. Frames (a) and (b) display respectively the charge asymmetry of $p_{T,l}$ and $\rho_{T,l}$ for the minimum, central and maximum \mathcal{MT} along with the \mathcal{PD} corresponding to incoherent biases of size $\varepsilon_l = \pm 0.5\%$. Frame (c) displays the latter distributions for $\text{DAsym}^{(+,-)}(\rho_{T,l})$. Frame (d) presents the χ^2 results for both charge and double charge asymmetry methods for the case of $\varepsilon_{l+} = \varepsilon_{l-} = 0.5\%$.

(b) Resolution of the charged lepton track parameters

The influence of the resolution of the charged lepton track are displayed in Fig. 5.15 for both p_{T,l^+} (a,b) and charge asymmetry of $p_{T,l}$ (c). The value $\text{ERF} = 0.7$ tends to narrow the bare $p_{T,l}$ distribution while having $\text{ERF} = 1.3$, by widening this time the width of the Gaussian response, tends to smear the sharpness of the distributions. Starting with the classic method we see that no matter which value is used here the bias on the intrinsic determination of M_{W^+} and M_{W^-} , and as a consequence on $M_{W^+} - M_{W^-}$, is not very strong. We can note though that here in top of shifting the unbiased bare spectra to different p_T the widening/narrowing change locally the normalisation. The consequence is that without any other technical refinement the \mathcal{PD} can hardly apparent itself to any of the histogram. Also, even though the impact is negligible on the mass determination the convergence is very low, *i.e.* $\chi^2_{\min}/\text{dof} \approx 20$. In the frame (c) the charge asymmetry shows, no matter the used ERF values good steadiness and stays again in the vicinity of the central \mathcal{MT} . Then, the result for the likelihood are good from both physics and convergence point of view.

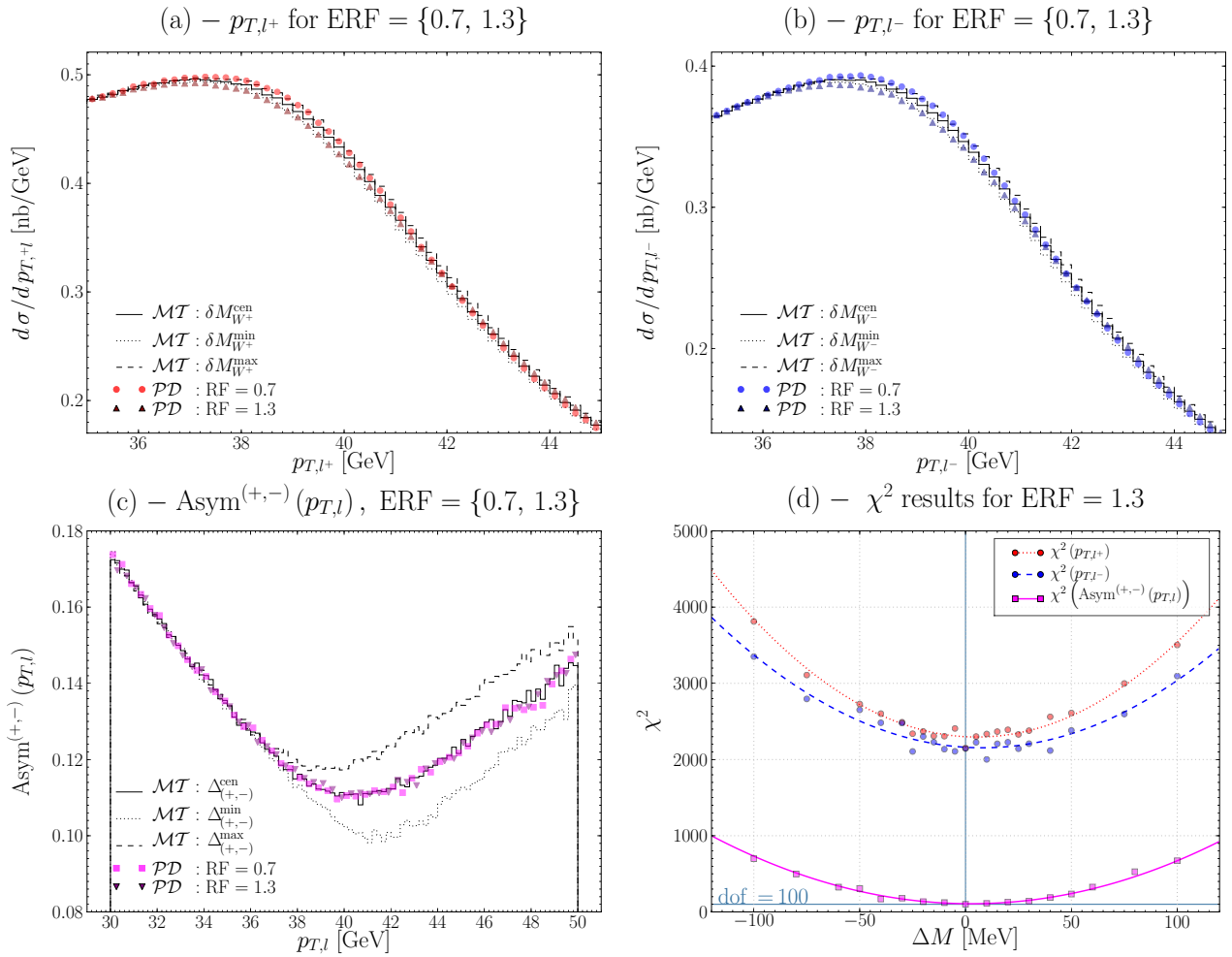


Figure 5.15: Systematic error on $M_{W^+} - M_{W^-}$ due to the resolution on the charged lepton track for p_{T,l^+} (a) and p_{T,l^-} (b) and charge asymmetry (c) spectra. In each frame the central and extrema \mathcal{MT} are drawn along with the two $\text{ERF} = \{0.7, 1.3\}$ \mathcal{PD} . In frame (d) the corresponding χ^2 for $\text{ERF} = 1.3$.

(c) Systematic due to the intrinsic k_T of the partons

The impact of the intrinsic k_T of partons is studied with the charge asymmetry method. First, Fig. 5.16 shows the impact of the change of $\langle k_T \rangle$ on the jacobian peaks of the p_{T,l^+} and p_{T,l^-} spectra. As expected when the more important is the average intrinsic k_T the more the jacobian peaks are shifted to higher $p_{T,l}$ values.

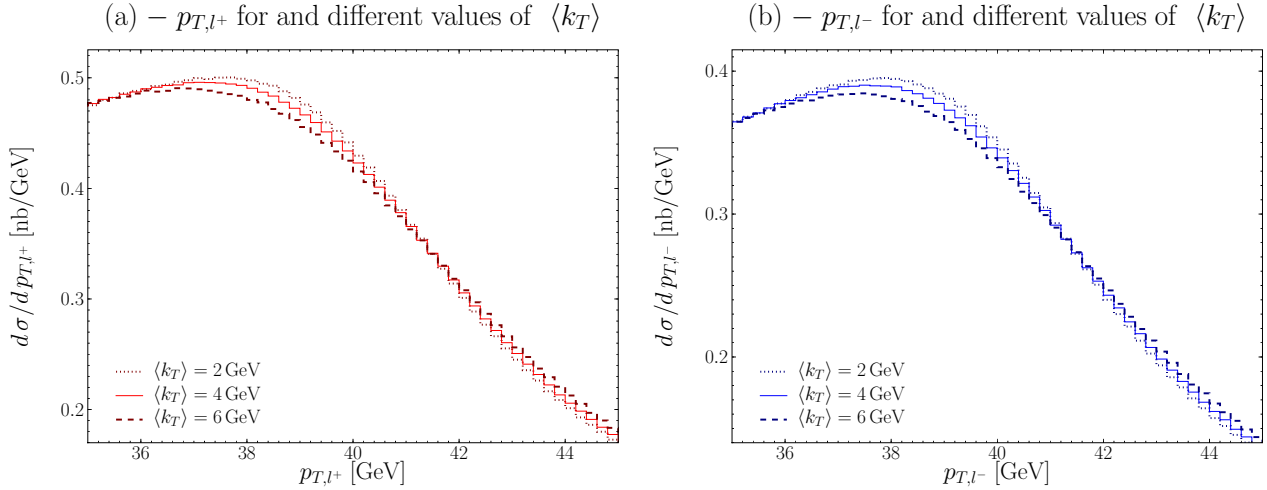


Figure 5.16: Transverse momentum distribution for several values of the intrinsic $\langle k_T \rangle = \{2, 4, 6\}$ GeV of the partons for positively charge lepton (a) and the negatively charged lepton (b),

Fig. 5.17 on the next page presents in each frame the χ^2 results for pp collisions with $p_{T,l} > 20$ GeV and respectively for the three following acceptance cuts :

$$|\eta_l| < 2.5,$$

$$|\eta_l| < 0.3 \text{ and}$$

$$|y_W| < 0.3.$$

The frames in Fig. 5.17 represent respectively the χ^2 results obtained for these three cases and for the values of $\langle k_T \rangle$ of 2, 3, 4, 5, 6 and 7 GeV. The value $\langle k_T \rangle = 4$ GeV is the central one but it was repeated to ensure the continuity in the pattern the χ^2 follow as $\langle k_T \rangle$ increases. The cuts made using $|\eta_l| < 0.3$, up to a lower convergence accuracy, displays a good steadiness with respect to the uncertainty on $\langle k_T \rangle$.

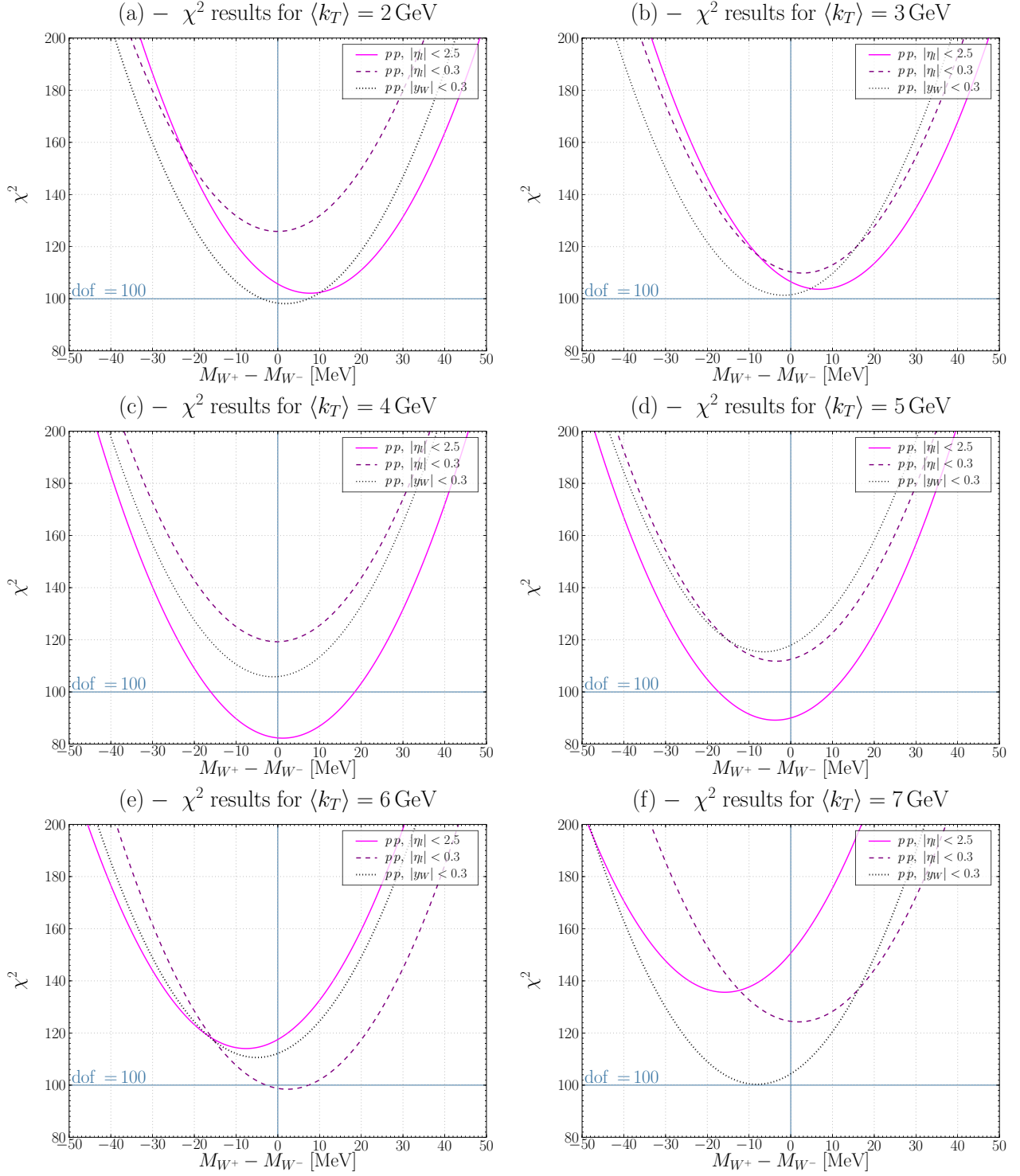


Figure 5.17: χ^2 results for the asymmetry method depending on the intrinsic $\langle k_T \rangle$ and for the cuts $p_{T,i} > 20$ GeV and respectively $|\eta| < 2.5$, $|\eta| < 0.3$ and $|y_W| < 0.3$.

(d) $u^{(v)} - d^{(v)}$ asymmetry

Figure 5.18 presents the χ^2 results obtained for the study of the $u^{(v)} - d^{(v)}$ asymmetry in the cases where $u_{\max}^{(v)} = 1.05 u^{(v)}$ and $d_{\min}^{(v)} = d^{(v)} - 0.05 u^{(v)}$ in (a) and where $u_{\max}^{(v)} = 0.95 u^{(v)}$ and $d_{\min}^{(v)} = d^{(v)} + 0.05 u^{(v)}$ in (b). The narrow selection on η shows only a slight enhancement while the use of dd collisions, even with an acceptance of $|\eta| < 2.5$, remove the ambiguities on the valence PDF errors.

This can be understood quite easily looking at the impact of the modeled systematic error on the production of a W^+ and a W^- for both pp and dd collisions. In the first case, for pp collision we consider the W^+ and W^- are respectively produced via $u^{(v)} \bar{d} \rightarrow W^+$ and $d^{(v)} \bar{u} \rightarrow W^-$. Making explicit the expressions of the biased valence distributions in functions of the LHAPDF (LHA) predictions gives

$$W^+ : u_{\text{biased}}^{p,(v)} \bar{d} = \left(u_{\text{L}}^{p,(v)} + \delta \right) \bar{d}, \quad (5.32)$$

$$W^- : d_{\text{biased}}^{p,(v)} \bar{u} = \left(d_{\text{L}}^{p,(v)} - \delta \right) \bar{u}, \quad (5.33)$$

where δ is the error on the PDF we've been introducing by hand. In this configuration we observe incoherent shift between the production of W^+ and W^- . Now, for dd collisions we explicit this time the biased valence $u^{d,(v)}$ and $d^{d,(v)}$ expressions having in mind that in a neutron n we have $u^n = d^p$ and $d^n = u^p$. This leads to cancel incoherent biases between the $u^{(v)}$ and $d^{(v)}$:

$$W^+ : u_{\text{biased}}^{d,(v)} \bar{d} = \left(u_{\text{LHA}}^{p,(v)} + \delta + d_{\text{LHA}}^{p,(v)} - \delta \right) \bar{d}, \quad (5.34)$$

$$= \left(u_{\text{LHA}}^{p,(v)} + d_{\text{LHA}}^{p,(v)} \right) \bar{d}, \quad (5.35)$$

$$= u_{\text{LHA}}^{d,(v)} \bar{d}, \quad (5.36)$$

$$W^- : d_{\text{biased}}^{d,(v)} \bar{d} = \left(d_{\text{LHA}}^{p,(v)} - \delta + u_{\text{LHA}}^{p,(v)} + \delta \right) \bar{u}, \quad (5.37)$$

$$= \left(d_{\text{LHA}}^{p,(v)} + u_{\text{LHA}}^{p,(v)} \right) \bar{u}, \quad (5.38)$$

$$= d_{\text{LHA}}^{d,(v)} \bar{u}, \quad (5.39)$$

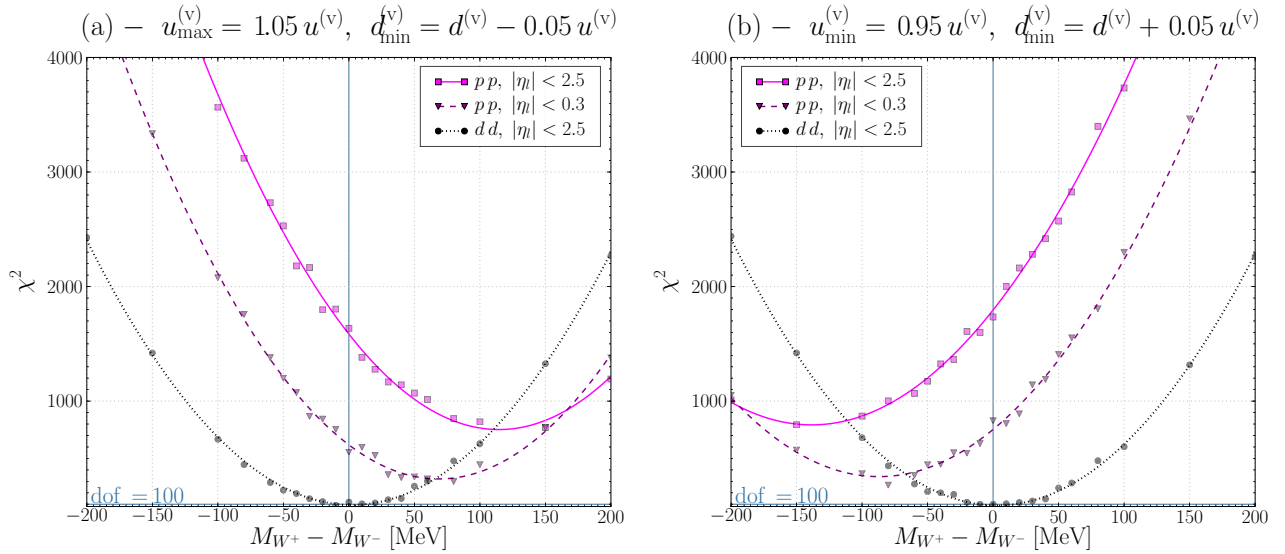


Figure 5.18: χ^2 results for $u_{\max}^{(v)} = 1.05 u^{(v)}$ and $d_{\min}^{(v)} = d^{(v)} - 0.05 u^{(v)}$ (a) and $u_{\max}^{(v)} = 0.95 u^{(v)}$ and $d_{\min}^{(v)} = d^{(v)} + 0.05 u^{(v)}$ (b) for pp and dd collisions.

(e) $s - c$ asymmetry

Figure 5.19 shows the χ^2 results for the study of $c_{\max} = 1.2c$ and $s_{\min} = s - 0.2c$ in (a) and $c_{\min} = 0.8c$ and $s_{\max} = s + 0.2c$ in (b). In that case we see that having access to a narrow cut in the rapidity would improve a lot the independence from these quark flavours asymmetry in our measure.

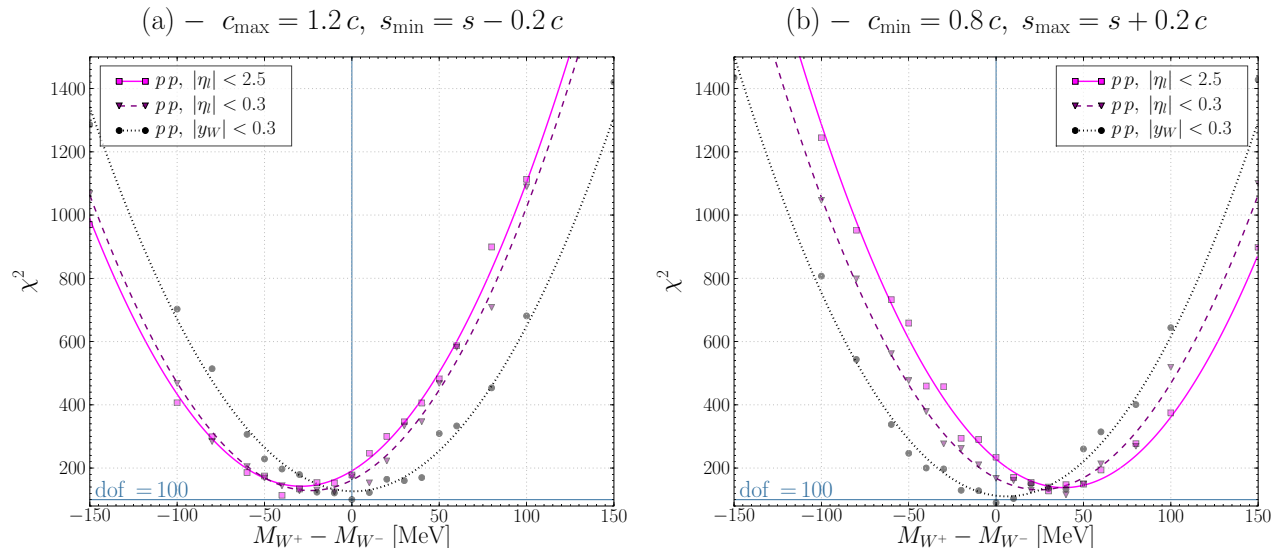


Figure 5.19: χ^2 results for $c_{\max} = 1.2c$ and $s_{\min} = s - 0.2c$ (a) and $c_{\min} = 0.8c$ and $s_{\max} = s + 0.2c$ (b) for different acceptance criteria for the decaying charged lepton.

Conclusion

Dobranoc, idę spać,

...

Piosenka dla Edka
MARIA PESZEK

The work that has been presented in this document corresponds to the second stage in the optimisation of measurement strategies of the Standard Model parameters at the LHC. It presented a brand new dedicated strategy for the precision measurement of the charge asymmetry of the W boson mass specific to the LHC collider physics.

This measurement must, in our view, precede the measurement of the charge averaged mass of the W boson and the measurement of $\sin\theta_W$, in order to diminish the risk of false absorption of variety of unknown Beyond Standard Model effects within the Standard Model parameter space. This measurement is of particular importance for the following two reasons. Firstly, at the LHC – contrary to the Tevatron $p\bar{p}$ collider – we have seen the measurement of the averaged mass of the W boson cannot be dissociated from the measurement of the masses of its charge states. Secondly, the precision of verification of the charge universality of the Fermi coupling constant G_F , measured via the charge asymmetry of the muon life time, must be matched by the precision of verification of the charge universality of the $SU(2)$ coupling strength g_W . This can be achieved only if the mass difference $M_{W^+} - M_{W^-}$ can be determined with the precision of a few MeV, *i.e.* a factor of ~ 20 better than the best present measurement.

The Tevatron $p\bar{p}$ collision scheme, as far as the systematic and modeling errors are concerned, is better suited for the precision measurement of the W boson charge asymmetry. However, even if dedicated strategies, as *e.g.* those proposed in this document are used, the measurement will be limited by the statistical precision, affecting both the W boson samples and, more importantly, the Z boson calibration sample.

At the LHC the requisite statistical precision can be achieved already for the integrated luminosity of 10 fb^{-1} , *i.e.* in the first year of the LHC operation at the “low”, $\mathcal{O}(10^{33}\text{ cm}^{-2}\text{ s}^{-1})$, luminosity. However, in order to achieve a comparable systematic precision in an analysis based on the calibration and measurement strategies developed at the Tevatron, the charge dependent biases in the energy (momentum) scale of positive (negative) leptons must be controlled to the precision of 0.005%. As it was argued, it will be extremely hard, if not impossible, to achieve such a precision using the calibration methods developed at the Tevatron. Moreover, we have identified the LHC-specific sources of errors, related to the uncertainties in the present knowledge of the flavour composition of the WBpB which limit, at present, the measurement precision to $\mathcal{O}(100\text{ MeV})$. Certainly, this uncertainty will be reduced once the high statistic W boson and Z boson samples are collected. Nevertheless, it will be hard, if not impossible, to improve by a factor of 10 or more the precision of the $u^{(v)}-d^{(v)}$ and $s-c$ quark-momentum distribution asymmetries, as they are hardly detectable in the Z -boson production processes. Whether or not the requisite precision target will be reached using the standard measurement strategies remains to be seen. In our view, it will be indispensable to use the dedicated LHC-specific measurement strategies.

The strategy proposed and discussed here makes a full use of the flexibility of the machine and

detector configurations which, we hope, will be exploited in the mature phase of the LHC experimental program. It requires: (1) running for a fraction of time the inverted polarity current in the detector solenoid, (2) the dedicated trigger and data-acquisition configuration in the “high”, $\mathcal{O}(10^{34} \text{ cm}^{-2} \text{ s}^{-1})$, luminosity LHC operation mode, and (3) replacing the LHC proton beams by light isoscalar ion beams.

The underlying principle of the proposed dedicated strategy is that, instead of diminishing the systematic measurement and modeling uncertainties, it minimizes their influence on the measured value of $M_{W^+} - M_{W^-}$. We have demonstrated that already for the modest (easy to fulfill) measurement and modeling precision requirements, the resulting uncertainty of $M_{W^+} - M_{W^-}$ can be kept at the level comparable to the statistical measurement uncertainty, *i.e.* at the level of $\mathcal{O}(5 \text{ MeV})$.

It remains to be demonstrated that the remaining systematic measurement errors, of secondary importance at the Tevatron and not discussed here, could be neglected at this level of the measurement precision. This can, however, be proved only when the real data are collected and analysed, both for the standard and for the dedicated measurement strategies.

List of Figures

1.1	Feynman diagram of the leptonic decay of a W boson at the Born level	24
1.2	Representation in the WRF of the leptonic decay of a positive helicity $W(\lambda = +1)$ for both negative and positive	27
1.3	Representation of the process hadron hadron $\rightarrow W \rightarrow l \nu_l$	29
1.4	Feynman diagram for the production of a W in $q \bar{q}' \rightarrow W^- \rightarrow l^- \bar{\nu}_l$ at the Born level	30
1.5	Breit-Wigner behaviour of the off-shell W mass	31
1.6	The leading- and next-to-leading-order Feynman diagrams for W in Drell–Yan like	32
1.7	Opening angle between the quark and the charged lepton in the W rest frame	33
1.8	The two angular configurations contributing to the same value of $p_{T,l}^*$	33
1.9	Transverse momentum of the charged lepton in the W rest frame	34
1.10	Transverse momentum of the charged lepton distribution : intuition	34
1.11	CTEQ6.1M parton distributions functions	35
1.12	Radiation of real gluons and photons from the partons in the initial state	36
1.13	General features of a the W kinematics in Drell–Yan	38
1.14	General features of the charged lepton kinematics decaying from W in Drell–Yan	39
1.15	Transverse momentum of the electron and transverse mass of the electron-neutrino pair at the particle level for $p_{T,W} = 0$, $p_{T,W} \neq 0$ and for the ATLAS resolution.	41
2.1	The LHC superconducting magnet	44
2.2	The CERN accelerator complex	45
2.3	Overview of the ATLAS detector	47
2.4	Overview of particles passage through the ATLAS sub-detectors	49
2.5	ATLAS calorimetry overview	50
2.6	ATLAS electromagnetic calorimeter structure	51
2.7	Simulation on ATLAS electron trigger efficiency for $p_{T,e} = 20$ GeV	51
2.8	ATLAS hadronic tile calorimeter and end-cap	52
2.9	ATLAS muon spectrometer overview	53
2.10	Muon spectrometer MDT and CSC functioning principle	54
2.11	Muon trigger efficiency for different p_T thresholds for the Level 1 and Event Filter	54
2.12	Longitudinal cross section of the ATLAS tracker	55
2.13	Radial cross section of the ATLAS tracker precision region	55
2.14	Magnetic field lines of the ATLAS central solenoid	56
2.15	Pixel module structure from the ATLAS tracker and principle of operation	57
2.16	Alignment of the effective charge drift direction with the particle trajectory in a silicon pixel module	58
2.17	SCT module structure and principle of operation	58
2.18	TRT tubes assembly and principle of operation	59
2.19	Weak modes affecting at the tracker at first order	60
2.20	Radial expansion and curling modes consequences on positively and negatively charged particles reconstructed tracks	61
2.21	CDF central outer tracker structure	64

2.22	CDF II central outer tracker distortions between positive and negative tracks	66
2.23	CDF II $(E/p)_{e^+} - (E/p)_{e^-}$ as a function of $\cotan \theta$ before and after corrections	66
3.1	Schematic representation of the simulated/real data and reconstruction processing chains	74
3.2	Schematic representation of the steps of the data reconstruction	76
3.3	Tuned comparison between PYTHIA and WINHAC within the ATLAS software	78
3.4	Tuned comparison between PYTHIA+PHOTOS and WINHAC	79
3.5	Tuned comparison within the ATLAS software between PYTHIA/PYTHIA+PHOTOS and WINHAC for the lepton transverse mass	79
3.6	WINHAC muon kinematics at the generator and reconstructed level	80
3.7	Generation framework schematic representation	82
3.8	Analysis framework schematic representation	83
4.1	Rapidity and transverse momentum distributions of the W bosons with their charge asymmetries for $p\bar{p}$ and pp collisions	89
4.2	Charge asymmetries for $p_{T,W}$ for several modification in the proton PDFs to study the size of the flavour asymmetries for the W production in pp and dd collisions	91
4.3	Charged asymmetries of $p_{T,W}$ for inclusive pp , dd collisions and with $ y_W < 0.3$ for pp and with $ \eta_l < 0.3$ for pp and dd	93
4.4	Pseudo-rapidity η_l and transverse momentum $p_{T,l}$ distributions for charged leptons produced in W boson decays for both $p\bar{p}$ and pp collisions	94
4.5	Valence quark and sea anti-quark annihilation producing a negative helicity W boson	95
4.6	Schematic representation of a valence quark and sea anti-quark annihilation explaining the azimuthal anisotropy in the charged lepton decays with respect to the $\vec{p}_{T,W}$ direction	95
4.7	Positively and negatively charged lepton distributions of η_l and $p_{T,l}$ in $p\bar{p}$ for two different ranges of the W rapidity ($ y_W < 0.5$ and $3.5 < y_W < 4.5$	96
4.8	Positively and negatively charged lepton distributions of η_l ($p\bar{p}$, pp) and $p_{T,l}$ (pp only) for two different ranges of the W rapidity ($ y_W < 0.5$ and $3.5 < y_W < 4.5$	98
4.9	Distributions of $\phi_{W,l}^*$ in pp collisions	99
4.10	Positive and negatively charged leptons transverse momenta distributions normalised to unit	100
4.11	Charged lepton transverse momenta for central and forward region of y_W and a η_l binning	101
4.12	Distributions of the W boson rapidity and transverse momentum along with the one of the charged lepton pseudo-rapidity and transverse momentum in $pp(p\bar{p})$ collisions when all valence contributions are removed	105
4.13	Distributions of $\cos \theta_{W,l}^*$ in $pp(p\bar{p})$ collisions with no valence quarks in the hadrons, first with all the sea quarks contributions and then with all the contributions from the CKM point of view	106
4.14	Distributions of $\phi_{W,l}^*$ in $pp(p\bar{p})$ collisions with no valence quarks in the hadrons	106
4.15	Invariant mass of the W boson in $p\bar{p}$ collisions	107
4.16	Distributions of the W boson rapidity and transverse momentum along with the one of the charged lepton pseudo-rapidity and transverse momentum in $p\bar{p}$ collisions	108
4.17	Distributions of $\cos \theta_{W,l}^*$ and $\phi_{W,l}^*$ in $p\bar{p}$ collisions	109
4.18	Schematic representations of the decay of the charged leptons at the leading order	109
4.19	Schematic representations of the decay of the charged leptons at the improved leading order	110
4.20	W boson rapidity distributions in bins of the charged lepton pseudo-rapidity and <i>vice versa</i> in the case of $p\bar{p}$ collisions	111
4.21	Distributions of $\cos \theta_{W,l}^*$ and $\phi_{W,l}^*$ in bins of y_W for the positively and negatively charged channel in $p\bar{p}$ collisions	112
4.22	Invariant mass of the W boson in pp collisions	113

4.23	Distributions of the W boson rapidity and transverse momentum along with the one of the charged lepton pseudo-rapidity and transverse momentum in pp collisions	114
4.24	Final state charge asymmetry at the leading order and improved leading order	115
4.25	Distributions of $\cos\theta_{W,l}^*$ and $\phi_{W,l}^*$ in pp collisions	116
4.26	W boson rapidity distributions in bins of the charged lepton pseudo-rapidity and <i>vice versa</i> in the case of pp collisions	117
4.27	W boson transverse momentum in bins of y_W and in bins of η_l in pp collisions	118
4.28	Charged lepton transverse momentum in bins of y_W and in bins of η_l in pp collisions .	119
4.29	Distributions of $\cos\theta_{W,l}^*$ and $\phi_{W,l}^*$ in bins of y_W for the positively and negatively charged channel in pp collisions	120
4.30	Invariant mass of the W boson in dd collisions with $\sqrt{S_{n_1 n_2}} = 7$ TeV	121
4.31	Distributions of the W boson rapidity and transverse momentum along with the one of the charged lepton pseudo-rapidity and transverse momentum in dd collisions with $\sqrt{S_{n_1 n_2}} = 7$ TeV	122
4.32	Distributions of $\cos\theta_{W,l}^*$ and $\phi_{W,l}^*$ in dd collisions with $\sqrt{S_{n_1 n_2}} = 7$ TeV	122
4.33	W boson rapidity distributions in bins of the charged lepton pseudo-rapidity and <i>vice versa</i> in the case of dd collisions with $\sqrt{S_{n_1 n_2}} = 7$ TeV	123
4.34	W boson transverse momentum in bins of y_W and in bins of η_l in dd collisions with $\sqrt{S_{n_1 n_2}} = 7$ TeV	124
4.35	Charged lepton transverse momentum in bins of y_W and in bins of η_l in dd collisions with $\sqrt{S_{n_1 n_2}} = 7$ TeV	125
4.36	Distributions of $\cos\theta_{W,l}^*$ and $\phi_{W,l}^*$ in bins of y_W for the positively and negatively charged channel in dd collisions with $\sqrt{S_{n_1 n_2}} = 7$ TeV	126
4.37	Transverse momenta of the u and \bar{d} quarks in W^+ production along with the one of the d and \bar{u} quarks in W^- production	127
4.38	Charge asymmetry and bare difference of the transverse momenta distributions of the charged leptons for several values of \sqrt{S}	129
5.1	Schematic representation of the reconstructed hit in a barrel module of the SCT detector with two opposite magnetic field configurations	135
5.2	The $p_{T,l+}$, $p_{T,l-}$ and $\text{Asym}^{(+,-)}(p_{T,l})$ distributions at the generator level, after the cuts ($p_{T,l} > 20$ GeV and $ \eta_l < 2.5$) and finally, by adding the inner detector smearing	136
5.3	Distribution of the transverse momentum of the positively charged lepton for the three values of W mass and the χ^2 dependence in $\Delta_{(+,-)}$	139
5.4	Charge asymmetry of $p_{T,l}$ for the three values of $\Delta_{(+,-)}$ and the χ^2 dependence in $\Delta_{(+,-)}$	141
5.5	Scaling of a mass template distribution with a biased pseudo-data histogram	142
5.6	χ^2 results for the incoherent shifts of the energy scale for both the asymmetry and the double charge asymmetry $\varepsilon = \pm 0.05\%$ and double charge asymmetry only for $\varepsilon = \pm 0.5\%$	149
5.7	Visualisation of the inverse of the positive and negative charged lepton transverse momenta and associated charge asymmetry at the generator level, adding up cuts and detector smearing & validation χ^2 analysis for the trivial unbiased pseudo-data	156
5.8	Histograms of the two extrema mass templates and particular unbiased pseudo-data \mathcal{PD} having $M_{W^+} = 80.503$ GeV and $M_{W^+} = 80.403$ GeV for the bare positive and negative $p_{T,l}$ spectra and charge asymmetry of $p_{T,l}$ along with the corresponding χ^2 results	157
5.9	Pseudo-data and extrema mass templates for $p_{T,l+}$ and $\text{Asym}^{(+,-)}(p_{T,l})$ histograms for a resolution of $\delta p_T = 0.8$ GeV	159
5.10	χ^2 results when considering the unbiased pseudo-data built from the positive charged lepton data and the mass templates built from the negatively charged lepton data . . .	161

5.11	Systematic error on $M_{W^+} - M_{W^-}$ due to coherent energy scale biases ($\varepsilon_l = 0.05\%$) between the positively and negatively charged lepton reconstructed transverse momenta and for both classic and charge asymmetry methods	168
5.12	Systematic error on $M_{W^+} - M_{W^-}$ due to coherent energy scale biases ($ \varepsilon_l = 0.5\%$) between the positively and negatively charged lepton reconstructed transverse momenta and for both classic and charge asymmetry methods	169
5.13	Systematic error on $M_{W^+} - M_{W^-}$ due to incoherent energy scale biases ($\varepsilon_l = \pm 0.05\%$) for both charge and double charge asymmetry methods	170
5.14	Systematic error on $M_{W^+} - M_{W^-}$ due to incoherent energy scale biases ($\varepsilon_l = \pm 0.5\%$) for both charge and double charge asymmetry methods	171
5.15	Systematic error on $M_{W^+} - M_{W^-}$ due to the resolution on the charged lepton track for both classic and charge asymmetry method	172
5.16	Transverse momentum distribution for several values of the intrinsic $\langle k_T \rangle$ of the partons	173
5.17	χ^2 results for the asymmetry method depending on the intrinsic $\langle k_T \rangle$ and for the cuts $p_{T,l} > 20$ GeV and respectively $ \eta < 2.5$, $ \eta < 0.3$ and $ y_W < 0.3$	174
5.18	χ^2 results for $u_{\max}^{(v)} = 1.05 u^{(v)}$ and $d_{\min}^{(v)} = d^{(v)} - 0.05 u^{(v)}$ and $u_{\max}^{(v)} = 0.95 u^{(v)}$ and $d_{\min}^{(v)} = d^{(v)} + 0.05 u^{(v)}$ cases using pp and dd collisions	175
5.19	χ^2 results for $c_{\max} = 1.2 c$ and $s_{\min} = s - 0.2 c$ and $c_{\min} = 0.8 c$ and $s_{\max} = s + 0.2 c$ for different acceptance criteria for the decaying charged lepton	176

List of Tables

1.1	The three generations of quarks and leptons	14
1.2	Sum up of the measured values of M_W and $M_{W^+} - M_{W^-}$ with the CDF detector for the last decades (1990 \rightarrow 2007)	20
1.3	CDF II results for the mass of the W	42
3.1	Overview of some Monte Carlo capable of simulating single W or Z production in hadronic colliders	72
3.2	Radiated photons from WINHAC and PYTHIA+PHOTOS simulation	80
4.1	Inclusive hadronic cross sections $\sigma_{(\text{incl.})}^+$, $\sigma_{(\text{incl.})}^-$ and $\sigma_{(\text{incl.})}^\pm$ respectively for the W^+ , W^- and W in Drell–Yan with $\sqrt{S} = 14$ TeV for $p\bar{p}$ and pp collisions and $\sqrt{S}_{n_1 n_2} = 7$ TeV in the $n_1 n_2$ nucleon–nucleon center of mass energy for dd collisions (computed by WINHAC).	88
5.1	Total and cut hadronic cross section σ_{W^+} and σ_{W^-} for $p\bar{p}$ and pp with $\sqrt{S} = 14$ TeV and for dd with $\sqrt{S} = 7$ TeV in the nucleon–nucleon center of mass energy	134
5.2	Produced inclusive and accepted millions of events (for $p_{T,l} > 20$ GeV and $ \eta_l , 2.5$) for W^+ , W^- and W for an integrated luminosity of $L = 10 \text{ fb}^{-1}$	134
5.3	Mass templates generated for W^+ and W^- and the corresponding available $M_{W^+} - M_{W^-}$ mass templates	140
5.4	Experimental systematic errors for the classic method, the charge asymmetry and the double charge asymmetry	149
5.5	The shifts of the W -mass charge asymmetry corresponding to various modeling effects using the charge asymmetry of $p_{T,l}$ for the analysis	151
5.6	Influence of the lack of mass templates in the vicinity of the χ^2 parabola fit minimum looking at the trivial case where $\xi = 0$ with $M_{W^+}^{PD} = M_{W^-}^{PD} + 100$ MeV and using the charge asymmetry of $p_{T,l}$	158
5.7	Influence of the binning of the histograms for the likelihood analysis	159
5.8	Seed set associated to each mass templates generation	164
5.9	Experimental systematic errors for the classic method, the charge asymmetry and the double charge asymmetry (Detailed)	165
5.10	The shifts of the W -mass charge asymmetry corresponding to various modeling effects using the charge asymmetry of $p_{T,l}$ for the analysis (Detailed)	167

Bibliography

- [1] **Particle Data Group** Collaboration, C. Amsler *et. al.*, *Review of particle physics*, *Phys. Lett.* **B667** (2008) 1. [14](#), [20](#), [23](#), [27](#), [41](#), [81](#), [85](#), [138](#)
- [2] J. Thomson, *Cathode Rays*, *Phil. Mag.* **44** (1897) 292. [14](#)
- [3] W. Kaufmann *Ann. Phys.* **61** (1897) 544. [14](#)
- [4] W. Kaufmann *Ann. Phys.* **62** (1897) 588. [14](#)
- [5] S. H. Neddermeyer and C. D. Anderson, *Note on the nature of cosmic-ray particles*, *Phys. Rev.* **51** (May, 1937) 884–886. [14](#)
- [6] M. L. Perl, G. S. Abrams, A. M. Boyarski, M. Breidenbach, D. D. Briggs, F. Bulos, W. Chinowsky, J. T. Dakin, G. J. Feldman, C. E. Friedberg, D. Fryberger, G. Goldhaber, G. Hanson, F. B. Heile, B. Jean-Marie, J. A. Kadyk, R. R. Larsen, A. M. Litke, D. Lüke, B. A. Lulu, V. Lüth, D. Lyon, C. C. Morehouse, J. M. Paterson, F. M. Pierre, T. P. Pun, and P. A. Rapidis, *Evidence for anomalous lepton production in $e + -e-$ annihilation*, *Phys. Rev. Lett.* **35** (Dec, 1975) 1489–1492. [14](#)
- [7] F. Reines and C. L. Cowan, *Detection of the free neutrino*, *Phys. Rev.* **92** (1953) 830–831. [14](#)
- [8] G. Danby *et. al.*, *Observation of High-Energy Neutrino Reactions and the Existence of Two Kinds of Neutrinos*, *Phys. Rev. Lett.* **9** (1962) 36–44. [14](#)
- [9] K. Kodama *et. al.*, *Detection and analysis of tau neutrino interactions in DONUT emulsion target*, *Nucl. Instrum. Meth.* **A493** (2002) 45–66. [14](#)
- [10] H. W. Kendall, *Deep inelastic scattering: Experiments on the proton and the observation of scaling*, *Rev. Mod. Phys.* **63** (Jul, 1991) 597–614. [14](#)
- [11] T. Eichten *et. al.*, *Measurement of the neutrino - nucleon anti-neutrino - nucleon total cross-sections*, *Phys. Lett.* **B46** (1973) 274–280. [14](#)
- [12] J. J. Aubert, U. Becker, P. J. Biggs, J. Burger, M. Chen, G. Everhart, P. Goldhagen, J. Leong, T. McCarriston, T. G. Rhoades, M. Rohde, S. C. C. Ting, S. L. Wu, and Y. Y. Lee, *Experimental observation of a heavy particle j* , *Phys. Rev. Lett.* **33** (Dec, 1974) 1404–1406. [14](#)
- [13] **SLAC-SP-017** Collaboration, J. E. Augustin *et. al.*, *Discovery of a Narrow Resonance in $e+e-$ Annihilation*, *Phys. Rev. Lett.* **33** (1974) 1406–1408. [14](#)
- [14] S. W. Herb *et. al.*, *Observation of a dimuon resonance at 9.5-GeV in 400-GeV proton - nucleus collisions*, *Phys. Rev. Lett.* **39** (1977) 252–255. [14](#)
- [15] **CDF** Collaboration, F. Abe *et. al.*, *Observation of top quark production in $\bar{p}p$ collisions*, *Phys. Rev. Lett.* **74** (1995) 2626–2631, [[hep-ex/9503002](#)]. [14](#)

- [16] **D0** Collaboration, S. Abachi *et. al.*, *Observation of the top quark*, *Phys. Rev. Lett.* **74** (1995) 2632–2637, [[hep-ex/9503003](#)]. [14](#)
- [17] A. Einstein, *Concerning an heuristic point of view toward the emission and transformation of light*, *Annalen Phys.* **17** (1905) 132–148. [14](#)
- [18] **UA1** Collaboration, G. Arnison *et. al.*, *Experimental observation of isolated large transverse energy electrons with associated missing energy at $s^{**}(1/2) = 540\text{-GeV}$* , *Phys. Lett.* **B122** (1983) 103–116. [14](#)
- [19] **UA2** Collaboration, M. Banner *et. al.*, *Observation of single isolated electrons of high transverse momentum in events with missing transverse energy at the CERN anti-p p collider*, *Phys. Lett.* **B122** (1983) 476–485. [14](#)
- [20] **UA1** Collaboration, G. Arnison *et. al.*, *Experimental observation of lepton pairs of invariant mass around $95\text{-GeV}/c^{**2}$ at the CERN SPS collider*, *Phys. Lett.* **B126** (1983) 398–410. [14](#)
- [21] **UA2** Collaboration, P. Bagnaia *et. al.*, *Evidence for $Z^0 \rightarrow e^+ e^-$ at the CERN anti-p p collider*, *Phys. Lett.* **B129** (1983) 130–140. [14](#)
- [22] **TASSO** Collaboration, R. Brandelik *et. al.*, *Evidence for Planar Events in $e^+ e^-$ Annihilation at High-Energies*, *Phys. Lett.* **B86** (1979) 243. [14](#)
- [23] D. P. Barber *et. al.*, *Discovery of Three Jet Events and a Test of Quantum Chromodynamics at PETRA Energies*, *Phys. Rev. Lett.* **43** (1979) 830. [14](#)
- [24] **PLUTO** Collaboration, C. Berger *et. al.*, *Evidence for Gluon Bremsstrahlung in $e^+ e^-$ Annihilations at High-Energies*, *Phys. Lett.* **B86** (1979) 418. [14](#)
- [25] M. Gell-Mann, *A Schematic Model of Baryons and Mesons*, *Phys. Lett.* **8** (1964) 214–215. [16](#)
- [26] G. Zweig, *An $SU(3)$ model for strong interaction symmetry and its breaking*, . Reprinted in Lichtenberg, D. B. (Ed.), Rosen, S. P. (Ed.): *Developments In The Quark Theory Of Hadrons*, Vol. I, 22-101 and CERN Geneva - TH. 401 (REC.JAN. 64) 24p. [16](#)
- [27] D. J. Gross and F. Wilczek, *Asymptotically Free Gauge Theories. 1*, *Phys. Rev.* **D8** (1973) 3633–3652. [16](#)
- [28] D. J. Gross and F. Wilczek, *Asymptotically free gauge theories. 2*, *Phys. Rev.* **D9** (1974) 980–993. [16](#)
- [29] H. D. Politzer, *Reliable perturbative results for strong interactions?*, *Phys. Rev. Lett.* **30** (1973) 1346–1349. [16](#)
- [30] V. N. Gribov and L. N. Lipatov, *Deep inelastic e p scattering in perturbation theory*, *Sov. J. Nucl. Phys.* **15** (1972) 438–450. [17](#), [29](#), [143](#)
- [31] G. Altarelli and G. Parisi, *Asymptotic Freedom in Parton Language*, *Nucl. Phys.* **B126** (1977) 298. [17](#), [29](#), [143](#)
- [32] Y. L. Dokshitzer, *Calculation of the Structure Functions for Deep Inelastic Scattering and e^+e^- Annihilation by Perturbation Theory in Quantum Chromodynamics. (In Russian)*, *Sov. Phys. JETP* **46** (1977) 641–653. [17](#), [29](#), [143](#)
- [33] S. L. Glashow, *Partial Symmetries of Weak Interactions*, *Nucl. Phys.* **22** (1961) 579–588. [17](#)
- [34] A. Salam and J. C. Ward, *Electromagnetic and weak interactions*, *Phys. Lett.* **13** (1964) 168–171. [17](#)

- [35] S. Weinberg, *A Model of Leptons*, *Phys. Rev. Lett.* **19** (1967) 1264–1266. [17](#)
- [36] F. Englert and R. Brout, *Broken symmetry and the mass of gauge vector mesons*, *Phys. Rev. Lett.* **13** (1964) 321–322. [18](#)
- [37] P. W. Higgs, *Broken symmetries, massless particles and gauge fields*, *Phys. Lett.* **12** (1964) 132–133. [18](#)
- [38] G. S. Guralnik, C. R. Hagen, and T. W. B. Kibble, *Global conservation laws and massless particles*, *Phys. Rev. Lett.* **13** (1964) 585–587. [18](#)
- [39] N. Cabibbo, *Unitary Symmetry and Leptonic Decays*, *Phys. Rev. Lett.* **10** (1963) 531–533. [18](#)
- [40] M. Kobayashi and T. Maskawa, *CP Violation in the Renormalizable Theory of Weak Interaction*, *Prog. Theor. Phys.* **49** (1973) 652–657. [18](#)
- [41] G. Cohen-Tannoudji, “Une brève introduction au modèle standard.” In “Congrès de la Société Française de Physique - Strasbourg 9–13 juillet 2001”. [19](#)
- [42] I. J. R. Aitchison and A. J. G. Hey, *Gauge Theories in Particle Physics a practical introduction. Volume 1: from relativistic quantum mechanics to QED, (3rd Ed.)*. Institute of Physics Publishing, 2002. Erratum and addendum : <http://www.slac.stanford.edu/~aitchiso/>. [19](#)
- [43] I. J. R. Aitchison and A. J. G. Hey, *Gauge Theories in Particle Physics a practical introduction. Volume 2: QCD and the Electroweak Theory, (3rd Ed.)*. Institute of Physics Publishing, 2004. Erratum and addendum : <http://www.slac.stanford.edu/~aitchiso/>. [19](#)
- [44] L. H. Ryder, *Quantum Field Theory, (2nd Ed.)*. Cambridge University Press, 1996. [19](#)
- [45] M. E. Peskin and D. V. Schroeder, *An Introduction to Quantum Field Theory*. Reading, USA : Addison-Wesley, 1995. Erratum and addendum : <http://www.slac.stanford.edu/~mpeskin/QFT.html>. [19](#), [25](#)
- [46] R. K. Ellis, W. J. Stirling, and B. R. Webber, *QCD and collider physics*. Camb. Monogr. Part. Phys. Nucl. Phys. Cosmol., 1996. [19](#), [28](#), [40](#)
- [47] H. Spiesberger, M. Spira, and P. M. Zerwas, *The Standard model: Physical basis and scattering experiments*, [hep-ph/0011255](#). [19](#)
- [48] W. Pauli, *Niels Bohr and the development of Physics*. Pergamon Press, London, 1955. [20](#)
- [49] **CERN-Mainz-Daresbury** Collaboration, J. Bailey *et. al.*, *Final Report on the CERN Muon Storage Ring Including the Anomalous Magnetic Moment and the Electric Dipole Moment of the Muon, and a Direct Test of Relativistic Time Dilation*, *Nucl. Phys.* **B150** (1979) 1. [20](#)
- [50] **Muon g-2** Collaboration, G. W. Bennett *et. al.*, *Measurement of the negative muon anomalous magnetic moment to 0.7-ppm*, *Phys. Rev. Lett.* **92** (2004) 161802, [[hep-ex/0401008](#)]. [20](#)
- [51] **CDF** Collaboration, T. Aaltonen *et. al.*, *First Run II Measurement of the W Boson Mass*, *Phys. Rev.* **D77** (2008) 112001, [[arXiv:0708.3642](#)]. [20](#), [21](#), [40](#), [42](#), [63](#), [64](#), [71](#), [80](#), [132](#), [141](#), [142](#)
- [52] **CDF** Collaboration, F. Abe *et. al.*, *A Measurement of the W Boson Mass*, *Phys. Rev. Lett.* **65** (1990) 2243–2246. [20](#), [63](#)

- [53] **CDF** Collaboration, F. Abe *et. al.*, *A Measurement of the W Boson Mass in 1.8 TeV $p\bar{p}$ Collisions*, *Phys. Rev.* **D43** (1991) 2070–2093. [20](#), [63](#)
- [54] **CDF** Collaboration, F. Abe *et. al.*, *Measurement of the W boson mass*, *Phys. Rev. Lett.* **75** (1995) 11–16, [[hep-ex/9503007](#)]. [20](#), [63](#)
- [55] **CDF** Collaboration, F. Abe *et. al.*, *Measurement of the W boson mass*, *Phys. Rev.* **D52** (1995) 4784–4827. [20](#), [63](#)
- [56] **CDF** Collaboration, T. Aaltonen *et. al.*, *First Measurement of the W Boson Mass in Run II of the Tevatron*, *Phys. Rev. Lett.* **99** (2007) 151801, [[arXiv:0707.0085](#)]. [20](#), [63](#)
- [57] V. Buge *et. al.*, *Prospects for the precision measurement of the W mass with the CMS detector at the LHC*, *J. Phys.* **G34** (2007) N193–N220. [22](#), [133](#), [141](#), [150](#)
- [58] **ATLAS** Collaboration, N. Besson, M. Boonekamp, E. Klinkby, T. Petersen, and S. Mehlhase, *Re-evaluation of the LHC potential for the measurement of M_w* , *Eur. Phys. J.* **C57** (2008) 627–651, [[arXiv:0805.2093](#)]. [22](#), [133](#), [141](#), [150](#)
- [59] F. Halzen and A. D. Martin, *Quarks And Leptons: An Introductory Course In Modern Particle Physics*. New York, USA: Wiley, 1984. [25](#)
- [60] S. D. Drell and T.-M. Yan, *Partons and their applications at high energies*, *Ann. Phys.* **66** (1971) 578. [28](#)
- [61] V. Barger and R. Phillips, *Collider physics*. Addison-Wesley, 1990. [28](#), [40](#)
- [62] P. M. Nadolsky, *Theory of W and Z boson production*, *AIP Conf. Proc.* **753** (2005) 158–170, [[hep-ph/0412146](#)]. [28](#)
- [63] U. Baur, S. Keller, and D. Wackeroth, *Electroweak radiative corrections to W boson production in hadronic collisions*, *Phys. Rev.* **D59** (1999) 013002, [[hep-ph/9807417](#)]. [32](#), [71](#), [72](#)
- [64] F. A. Berends and R. Kleiss, *Hard photon effects in W^\pm and Z^0 decay*, *Z. Phys.* **C27** (1985) 365. [32](#)
- [65] S. Dittmaier and M. Kramer, *Electroweak radiative corrections to W-boson production at hadron colliders*, *Phys. Rev.* **D65** (2002) 073007, [[hep-ph/0109062](#)]. [32](#)
- [66] J. Pumplin *et. al.*, *New generation of parton distributions with uncertainties from global QCD analysis*, *JHEP* **07** (2002) 012, [[hep-ph/0201195](#)]. [35](#), [88](#), [143](#)
- [67] A. Bodek, Y. Chung, B.-Y. Han, K. McFarland, and E. Halkiadakis, *Direct measurement of W Production Charge Asymmetry at the Tevatron*, *Phys. Rev.* **D77** (2008) 111301, [[arXiv:0711.2859](#)]. [38](#), [152](#)
- [68] K. Lohwasser, *to be published*. PhD thesis, Oxford University. [40](#)
- [69] W. L. van Neerven, J. A. M. Vermaseren, and K. J. F. Gaemers, *Lepton-jet events as a signature for W production in $p\bar{p}$ collisions*, *NIKHEF-H/82-20* (November, 1982). [40](#)
- [70] J. Smith, W. L. van Neerven, and J. A. M. Vermaseren, *The transverse mass and width of the W boson*, *Phys. Rev. Lett.* **50** (1983) 1738. [40](#)
- [71] **ATLAS** Collaboration, G. Aad *et. al.*, *Expected Performance of the ATLAS Experiment - Detector, Trigger and Physics*, [arXiv:0901.0512](#). [41](#), [60](#), [76](#), [133](#)
- [72] M. W. Krasny, F. Fayette, W. Płaczek, and A. Siódmok, *Measure of the W-boson mass in the ATLAS experiment., in prepration*. [42](#), [71](#), [82](#)

- [73] A. K. Siódmok, *Theoretical predictions for the Drell–Yan process at LHC using Monte Carlo methods*. PhD thesis, Jagelionan University, 2009. 42
- [74] K. Rejzner, M. W. Krasny, F. Fayette, W. Płaczek, and A. Siódmok, *Measure of the W-boson width in the ATLAS experiment, in prepration*. 42, 71, 82
- [75] A. Asner *et. al.*, *The Large Hadron Collider in the lep tunnel*, CERN-87-05. 43
- [76] O. S. Brüning *et. al.*, *LHC Design Report, v.1*, CERN-2004-003-V-1 (2004). 43
- [77] O. S. Brüning *et. al.*, *LHC Design Report, v.2*, CERN-2004-003-V-2 (2004). 43
- [78] “Large hadron collider homepage.” <http://lh.web.cern.ch>. 43
- [79] *LHC Machine*, JINST 3 (2008) S08001. 43
- [80] “CERN Homepage.” <http://public.web.cern.ch>. 43
- [81] ATLAS Collaboration, W. Armstrong, W. *et. al.*, *ATLAS: Technical proposal for a general-purpose pp experiment at the Large Hadron Collider at CERN*, CERN-LHCC-94-43. 43
- [82] ATLAS Collaboration, G. Aad *et. al.*, *The ATLAS Experiment at the CERN Large Hadron Collider*, JINST 3 (2008) S08003. 43, 52, 54, 55, 57, 58
- [83] The Lep Injector Study Group Collaboration, *LEP design report. vol. 1*, CERN-LEP/TH/83-29 (1983) 70. 43
- [84] A. Asner *et. al.*, *Large Hadron Collider in the LEP tunnel: a feasibility study of possible options by the cern machine group*, CERN-DIR-TECH-84-01. 43
- [85] CMS Collaboration, R. Adolphi *et. al.*, *The CMS experiment at the CERN LHC*, JINST 3 (2008) S08004. 46
- [86] ALICE Collaboration, K. Aamodt *et. al.*, *The ALICE experiment at the CERN LHC*, JINST 3 (2008) S08002. 46
- [87] LHCb Collaboration, A. A. Alves *et. al.*, *The LHCb Detector at the LHC*, JINST 3 (2008) S08005. 46, 73
- [88] LHCf Collaboration, O. Adriani *et. al.*, *The LHCf detector at the CERN Large Hadron Collider*, JINST 3 (2008) S08006. 46
- [89] TOTEM Collaboration, G. Anelli *et. al.*, *The TOTEM experiment at the CERN Large Hadron Collider*, JINST 3 (2008) S08007. 46
- [90] ATLAS Collaboration, *ATLAS liquid argon calorimeter: Technical design report*, . 50, 51, 52
- [91] ATLAS Collaboration, A. Airapetian *et. al.*, *ATLAS calorimeter performance*, CERN-LHCC-96-40. 50, 51
- [92] ATLAS Electromagnetic Barrel Calorimeter Collaboration, M. Aharrouche *et. al.*, *Energy linearity and resolution of the ATLAS electromagnetic barrel calorimeter in an electron test- beam*, Nucl. Instrum. Meth. A568 (2006) 601–623, [physics/0608012]. 51
- [93] ATLAS Collaboration, *Physics performance studies and strategy of the Electron and Photon Trigger Selection*, ATLAS-PHYS-PUB-2007-000 (2008). 51

- [94] **ATLAS** Collaboration, *ATLAS tile calorimeter: Technical design report*, CERN-LHCC-96-42. 52
- [95] K. Störig, J. Grosse-Knetter, K. Kröninger, and A. Quadt, *Alignment Studies of the ATLAS Silicon Trackers with Overlap Residuals*, com-indet-2008-012. 54
- [96] **ATLAS** Collaboration, *ATLAS inner detector: Technical design report. Vol. 1*, . CERN-LHCC-97-16. 55, 56, 59, 138
- [97] **ATLAS** Collaboration, *ATLAS inner detector: Technical design report. Vol. 2*, CERN-LHCC-97-17. 56, 57, 58
- [98] **ATLAS** Collaboration, *ATLAS CSC note: The expected performance of the ATLAS tracker*, COM-PHYS-2008-105 (2008). 56
- [99] **ATLAS** Collaboration, *ATLAS: Detector and physics performance technical design report. Volume 1*, CERN-LHCC-99-14. 56, 59, 61
- [100] A. Yamamoto *et. al.*, *The ATLAS central solenoid*, *Nucl. Instrum. Meth.* **A584** (2008) 53–74. 56
- [101] C. J. S. Damerell, *Vertex detectors: The State of the art and future prospects*, *Lectures given at 23rd Annual SLAC Summer Institute on Particle Physics: The Top Quark and the Electroweak Interaction*, Stanford, CA, 10-21 Jul 1995. 57
- [102] I. Gorelov *et. al.*, *A measurement of Lorentz angle and spatial resolution of radiation hard silicon pixel sensors*, *Nucl. Instrum. Meth.* **A481** (2002) 204–221. 57, 58
- [103] T. G. Cornelissen, *Track fitting in the ATLAS experiment*. PhD thesis, Faculteit der Natuurwetenschappen, Wiskunde en Informatica, December, 2006. CERN-THESIS-2006-072. 57
- [104] T. Cornelissen *et. al.*, *Concepts, Design and Implementation of the ATLAS New Tracking (NEWT)*, CERN-LHCC-99-14. 59
- [105] R. Fruhwirth, *Application of Kalman filtering to track and vertex fitting*, *Nucl. Instrum. Meth.* **A262** (1987) 444–450. 59
- [106] P. Brückman de Renstrom and S. Haywood, *Least squares approach to the alignment of the generic high precision tracking system*, *Prepared for PHYSTATO5: Statistical Problems in Particle Physics, Astrophysics and Cosmology*, Oxford, England, United Kingdom, 12-15 Sep 2005. 59
- [107] D. Brown, A. Gritsan, and D. Roberts, *Internal alignment of the BABAR silicon vertex tracking detector*, *Prepared for 1st LHC Detection Alignment Workshop*, Geneva, Switzerland, 4-6 Sep 2006. 60, 145
- [108] K. Störig, *Alignment Studies of the ATLAS Silicon Trackers with Overlap Residuals*. PhD thesis, Georg-August-Universität Göttingen, April, 2008. 60
- [109] **CDF IIb** Collaboration, P. T. Lukens, *The CDF IIb detector: Technical design report*, FERMILAB-TM-2198. 61, 63, 64, 66
- [110] **ATLAS** Collaboration, *ATLAS detector and physics performance. Technical design report. Vol. 2*, CERN-LHCC-99-15. 61
- [111] P. Brückman de Restrom, “About the weak modes of the atlas tracker.” private communication, 2008. 62, 135

- [112] CDF Collaboration, A. A. Affolder *et. al.*, *CDF central outer tracker*, *Nucl. Instrum. Meth.* **A526** (2004) 249–299. 64
- [113] N. Metropolis and S. Ulam, *The Monte Carlo method*, *Journal of the American Statistical Association* **44** (1949) 335–341. 67
- [114] Press, William, H. and Teukolsky, Saul, A. and Vetterling, William, T. and Flannery, Brian, P., *Numerical Recipes: The Art of Scientific Computing*. 68
- [115] T. Sjöstrand, *Academic Training Lectures*, April, 2005.
<http://home.thep.lu.se/~torbjorn/talks/cern05lecture1.pdf>. 69, 70
- [116] D. E. Knuth, *The Art of Computer Programming. Vol. 2 Semi-numerical algorithms*. Addison Wesley, 1981. 69
- [117] T. Sjöstrand, S. Mrenna, and P. Skands, *PYTHIA 6.4 physics and manual*, *JHEP* **05** (2006) 026, [[hep-ph/0603175](http://arxiv.org/abs/hep-ph/0603175)]. 69, 71, 72, 77, 85, 88, 90
- [118] T. Sjöstrand, *PYTHIA 8 Status Report*, [arXiv:0809.0303](http://arxiv.org/abs/0809.0303). 69
- [119] “Homepage of the PYTHIA Event Generator.”
<http://home.thep.lu.se/~torbjorn/Pythia.html>. 69, 72
- [120] M. Bähr *et. al.*, *Herwig++ Physics and Manual*, *Eur. Phys. J.* **C58** (2008) 639–707, [[arXiv:0803.0883](http://arxiv.org/abs/0803.0883)]. 69, 72
- [121] “Homepage of the Herwig++ Event Generator.” <http://projects.hepforge.org/herwig/>. 69, 72
- [122] T. Gleisberg *et. al.*, *SHERPA 1.alpha, a proof-of-concept version*, *JHEP* **02** (2004) 056, [[hep-ph/0311263](http://arxiv.org/abs/hep-ph/0311263)]. 69, 72
- [123] “Homepage of the Sherpa Event Generator.”
www.montecarlonet.org/index.php?p=Projects/sherpa or
<http://projects.hepforge.org/sherpa/dokuwiki/doku.php>. 69, 72
- [124] E. Barberio, B. van Eijk, and Z. Was, *PHOTOS: A Universal Monte Carlo for QED radiative corrections in decays*, *Comput. Phys. Commun.* **66** (1991) 115–128. 69, 77
- [125] E. Barberio and Z. Was, *PHOTOS: A Universal Monte Carlo for QED radiative corrections. Version 2.0*, *Comput. Phys. Commun.* **79** (1994) 291–308. 69, 77
- [126] P. Golonka and Z. Was, *Next to leading logarithms and the PHOTOS Monte Carlo*, *Eur. Phys. J.* **C50** (2007) 53–62, [[hep-ph/0604232](http://arxiv.org/abs/hep-ph/0604232)]. 69, 77
- [127] S. Jadach, J. H. Kuhn, and Z. Was, *TAUOLA: A Library of Monte Carlo programs to simulate decays of polarized tau leptons*, *Comput. Phys. Commun.* **64** (1990) 275–299. 69
- [128] M. Jezabek, Z. Was, S. Jadach, and J. H. Kuhn, *The tau decay library TAUOLA, update with exact $\mathcal{O}(\alpha)$ QED corrections in $\tau \rightarrow \mu. (e)$ neutrino anti-neutrino decay modes*, *Comput. Phys. Commun.* **70** (1992) 69–76. 69
- [129] S. Jadach, Z. Was, R. Decker, and J. H. Kuhn, *The tau decay library TAUOLA: Version 2.4*, *Comput. Phys. Commun.* **76** (1993) 361–380. 69
- [130] A. Djouadi, J. Kalinowski, and M. Spira, *HDECAY: A program for Higgs boson decays in the standard model and its supersymmetric extension*, *Comput. Phys. Commun.* **108** (1998) 56–74, [[hep-ph/9704448](http://arxiv.org/abs/hep-ph/9704448)]. 69

- [131] H. Seymour, Michael, *Prediction for Higgs and Electroweak Boson Production*. PhD thesis, University of Cambridge, October, 1992.
<http://hepwww.rl.ac.uk/theory/seymour/thesis/>. 69
- [132] T. Sjöstrand, *Monte Carlo generators*, hep-ph/0611247. 69
- [133] T. Sjöstrand, “CERN Academic training lectures.”
<http://home.thep.lu.se/~torbjorn/talks/>. 69
- [134] M. Seymour, “CERN Academic training lectures.”
<http://seymour.web.cern.ch/seymour/slides/>. 69
- [135] W. Placzek, *Monte Carlo Methods in High Energy Physics - lectures given at the INFN Pavia and the University of Pavia, Italy*, October, 2004.
<http://placzek.web.cern.ch/placzek/lectures/>. 69
- [136] CTEQ, “Links to talks given during CTEQ Summer Schools.”
<http://www.phys.psu.edu/~cteq/#Summer>. 69
- [137] Talk given by J.D. Bjorken at the 75th anniversary celebration of the Max-Planck Institute of Physics, Munich, Germany, December 10th, 1992. As quoted in: *Beam Line*, Winter 1992, Vol. 22, No. 4. 70
- [138] Dissertori, Günther and Knowles, Ian G. and Schmelling, Michael, *Quantum Chromodynamics: High Energy Experiments and Theory*. Clarendon Press, 2003. 70
- [139] W. Placzek and S. Jadach, *Multiphoton radiation in leptonic W-boson decays*, *Eur. Phys. J. C* **29** (2003) 325–339, [hep-ph/0302065]. 70, 71, 72
- [140] C. M. Carloni Calame, S. Jadach, G. Montagna, O. Nicrosini, and W. Placzek, *Comparisons of the Monte Carlo programs HORACE and WINHAC for single W-boson production at hadron colliders*, *Acta Phys. Polon.* **B35** (2004) 1643–1674, [hep-ph/0402235]. 70, 145
- [141] **TeV4LHC-Top and Electroweak Working Group** Collaboration, C. E. Gerber *et. al.*, *Tevatron-for-LHC Report: Top and Electroweak Physics*, [arXiv:0705.3251](http://arxiv.org/abs/0705.3251). 70
- [142] D. Bardin, S. Bondarenko, S. Jadach, L. Kalinovskaya, and W. Placzek, *Implementation of SANC EW corrections in WINHAC Monte Carlo generator*, [arXiv:0806.3822](http://arxiv.org/abs/0806.3822). 70, 71, 145
- [143] P. Golonka and Z. Was, *PHOTOS Monte Carlo: A precision tool for QED corrections in Z and W decays*, *Eur. Phys. J. C* **45** (2006) 97–107, [hep-ph/0506026]. 70
- [144] M. W. Krasny, S. Jadach, and W. Placzek, *The femto-experiment for the LHC: The W-boson beams and their targets*, *Eur. Phys. J. C* **44** (2005) 333–350, [hep-ph/0503215]. 71, 153
- [145] M. W. Krasny, F. Fayette, W. Placzek, and A. Siódmok, *Z-boson as ‘the standard candle’ for high precision W-boson physics at LHC*, *Eur. Phys. J. C* **51** (2007) 607–617, [hep-ph/0702251]. 71, 135, 136
- [146] F. Fayette, M. W. Krasny, W. Placzek, and A. Siódmok, *Measurement of $M_{W^+} - M_{W^-}$ at the LHC*, [arXiv:0812.2571](http://arxiv.org/abs/0812.2571). 71, 131
- [147] W. Placzek and S. Jadach, “WINHAC version 1.30: The Monte Carlo event generator for single W-boson production with leptonic decays in hadron collisions.” available from <http://cern.ch/placzek/winhac>. 71, 72
- [148] D. R. Yennie, S. Frautschi, and H. Suura *Ann. Phys. (NY)* **13** (1961) 379. 71

- [149] M. R. Whalley, D. Bourilkov, and R. C. Group, *The Les Houches Accord PDFs (LHAPDF) and Lhaglu*, [hep-ph/0508110](#). 71, 75
- [150] H. Plathow-Besch, *PDFLIB: A Library of all available parton density functions of the nucleon, the pion and the photon and the corresponding alpha-s calculations*, *Comput. Phys. Commun.* **75** (1993) 396–416. 71
- [151] K. J. Eskola, V. J. Kolhinen, and C. A. Salgado, *The scale dependent nuclear effects in parton distributions for practical applications*, *Eur. Phys. J.* **C9** (1999) 61–68, [[hep-ph/9807297](#)]. 71
- [152] K. J. Eskola, V. J. Kolhinen, and P. V. Ruuskanen, *Scale evolution of nuclear parton distributions*, *Nucl. Phys.* **B535** (1998) 351–371, [[hep-ph/9802350](#)]. 71
- [153] A. Siódmok and W. Płaczek, “ZINHAC: The Monte Carlo event generator for single Z-boson production with leptonic decays in hadron collisions.” in preparation. 71
- [154] F. James, *A Review of Pseudorandom Number Generators*, *Comput. Phys. Commun.* **60** (1990) 329–344. 71, 75
- [155] G. Marsaglia, A. Zaman, and W.-W. Tsang, *A Review of Pseudorandom Number Generators*, *Stat.Prob. Lett.* **9** (1990) 35. 71
- [156] C. M. Carloni Calame, G. Montagna, O. Nicrosini, and M. Treccani, *Higher-order QED corrections to W-boson mass determination at hadron colliders*, *Phys. Rev.* **D69** (2004) 037301, [[hep-ph/0303102](#)]. 72
- [157] “Homepage of the HORACE Event Generator.”
<http://www.pv.infn.it/~hepcomplex/horace.html>. 72
- [158] G. Corcella *et. al.*, *HERWIG 6.5: an event generator for Hadron Emission Reactions With Interfering Gluons (including supersymmetric processes)*, *JHEP* **01** (2001) 010, [[hep-ph/0011363](#)]. 72
- [159] “Homepage of the HERWIG Event Generator.”
<http://hepwww.rl.ac.uk/theory/seymour/herwig/herwig65.html>. 72
- [160] S. Frixione and B. R. Webber, *Matching NLO QCD computations and parton shower simulations*, *JHEP* **06** (2002) 029, [[hep-ph/0204244](#)]. 72
- [161] “Homepage of the MC@NLO Event Generator.”
<http://www.hep.phy.cam.ac.uk/theory/webber/MCatNLO/>. 72
- [162] B. P. Kersevan and E. Richter-Was, *The Monte Carlo event generator AcerMC version 2.0 with interfaces to PYTHIA 6.2 and HERWIG 6.5*, [hep-ph/0405247](#). 72
- [163] “Homepage of the AcerMC Event Generator.” <http://borut.home.cern.ch/borut/>. 72
- [164] Q.-H. Cao and C. P. Yuan, *Combined effect of QCD resummation and QED radiative correction to W boson observables at the Tevatron*, *Phys. Rev. Lett.* **93** (2004) 042001, [[hep-ph/0401026](#)]. 72
- [165] “Homepage of the ResBos-A Event Generator.”
<http://hep.pa.msu.edu/people/cao/ResBos-A.html>. 72
- [166] C. Balazs and C. P. Yuan, *Soft gluon effects on lepton pairs at hadron colliders*, *Phys. Rev.* **D56** (1997) 5558–5583, [[hep-ph/9704258](#)]. 71, 72
- [167] “Homepage of the ResBos Event Generator.” <http://www.pa.msu.edu/~balazs/ResBos/>. 72

- [168] “Homepage of the WGRAD Event Generator.”
<http://ubpheno.physics.buffalo.edu/~dow/wgrad.html>. 72
- [169] U. Baur, O. Brein, W. Hollik, C. Schappacher, and D. Wackerroth, *Electroweak radiative corrections to neutral-current Drell-Yan processes at hadron colliders*, *Phys. Rev.* **D65** (2002) 033007, [[hep-ph/0108274](http://arxiv.org/abs/hep-ph/0108274)]. 72
- [170] “Homepage of the ZGRAD2 Event Generator.”
<http://ubpheno.physics.buffalo.edu/~dow/>. 72
- [171] A. Arbuzov *et. al.*, *One-loop corrections to the Drell-Yan process in SANC. I: The charged current case*, *Eur. Phys. J.* **C46** (2006) 407–412, [[hep-ph/0506110](http://arxiv.org/abs/hep-ph/0506110)]. 72
- [172] “Homepage of the SANC Event Generator.” <http://sanc.jinr.ru> or
<http://pcphsanc.cern.ch/>. 72
- [173] W. T. Giele, E. W. N. Glover, and D. A. Kosower, *Higher order corrections to jet cross-sections in hadron colliders*, *Nucl. Phys.* **B403** (1993) 633–670, [[hep-ph/9302225](http://arxiv.org/abs/hep-ph/9302225)]. 71
- [174] **ATLAS** Collaboration, *ATLAS computing: Technical design report*, *CERN-LHCC-2005-022*. 72, 73, 74
- [175] **ATLAS** Collaboration, “ATLAS Computing Workbook.”
<https://twiki.cern.ch/twiki/bin/view/Atlas/WorkBook>. 73, 74
- [176] G. Barrand *et. al.*, *GAUDI - The software architecture and framework for building LHCb data processing applications*, Prepared for International Conference on Computing in High-Energy Physics and Nuclear Physics (CHEP 2000), Padova, Italy, 7-11 Feb 2000. 73
- [177] G. Barrand *et. al.*, *GAUDI - A software architecture and framework for building HEP data processing applications*, *Comput. Phys. Commun.* **140** (2001) 45–55. 73
- [178] R. Brun and F. Rademakers, *ROOT: An object oriented data analysis framework*, *Nucl. Instrum. Meth.* **A389** (1997) 81–86. 73, 76, 82
- [179] “The ROOT System Homepage.” <http://root.cern.ch/>. 73, 76, 82
- [180] E. Richter-Was, F. Daniel, and P. Luc, *ATLFAST 2.0 a fast simulation package for ATLAS*, *ATL-PHYS-98-131* (October, 1998). 73
- [181] Cavalli, D and others, *Performance of the ATLAS fast simulation ATLFAST*, *ATL-PHYS-INT-2007-005*, *ATL-COM-PHYS-2007-012* (January, 2007). 73
- [182] “Atlfast homepage.” <http://www.hep.ucl.ac.uk/atlas/atlfast/>. 73
- [183] “Generator Services Subproject.” <http://lcgapp.cern.ch/project/simu/generator/>. 75
- [184] “CLHEP - A Class Library for High Energy Physics.”
<http://proj-clhep.web.cern.ch/proj-clhep/>. 75
- [185] M. Dobbs and J. B. Hansen, *The HepMC C++ Monte Carlo event record for High Energy Physics*, *Comput. Phys. Commun.* **134** (2001) 41–46. 75
- [186] **GEANT4** Collaboration, S. Agostinelli *et. al.*, *GEANT4: A simulation toolkit*, *Nucl. Instrum. Meth.* **A506** (2003) 250–303. 75
- [187] J. Allison *et. al.*, *Geant4 developments and applications*, *IEEE Trans. Nucl. Sci.* **53** (2006) 270. 75

- [188] M. A. Dobbs *et. al.*, *Les Houches guidebook to Monte Carlo generators for hadron collider physics*, [hep-ph/0403045](#). 77
- [189] F. Fayette and G. Stavropoulos, *Implementation of WINHAC inside the Athena framework*, October, 2006. <http://indico.cern.ch/materialDisplay.py?contribId=2&materialId=slides&confId=6357>. 77
- [190] F. Fayette and G. Stavropoulos, *Report on Winhac.i validations status*, October, 2006. <http://indico.cern.ch/materialDisplay.py?contribId=3&materialId=slides&confId=6872>. 77
- [191] D. Adams and others, *Track Reconstruction in the ATLAS Muon Spectrometer with MOORE*, *ATL-SOFT-2003-007*, *ATL-COM-MUON-2003-012* (2003). 78
- [192] D. Stump *et. al.*, *Inclusive jet production, parton distributions, and the search for new physics*, *JHEP* **10** (2003) 046, [[hep-ph/0303013](#)]. 143
- [193] S. Gieseke, M. H. Seymour, and A. Siódmok, *A model of non-perturbative gluon emission in an initial state parton shower*, *JHEP* **06** (2008) 001, [[arXiv:0712.1199](#)]. 145
- [194] **H1** Collaboration, D. Newton *et. al.* H1 Internal Note H1-8/90-145 (1990). 145
- [195] **ALEPH** Collaboration. ALEPH Handbook, Vol. 1 (1995). 145
- [196] M. W. Krasny, *Electron beam for LHC*, *Nucl. Instrum. Meth.* **A540** (2005) 222–234, [[hep-ex/0405028](#)]. 153

Index

A

Athena..... *see* ATLAS software
 ATLAS detector 47–62
 Calorimeters 49–52
 Electromagnetic 50–51
 Hadronic 52
 Forward detectors 49
 Luminosity 49
 Muon spectrometer 53–54
 Cathode Strip Chambers (CSC) 53
 Monitored Drift Tubes (MDT) 53
 Overview of the detector 47–49
 TDAQ 48
 Tracker 48, 55–62
 Misalignment/weak modes 60–62
 Pixel detector 57
 Semi-Conductor Tracker (SCT) 57–58
 Solenoid 56
 Transition Radiation Tracker (TRT) 58–59
 Trigger 48
 ATLAS software
 AOD 78
 Athena 73
 Simulation and reconstruction 73–76
 CBNT 78
 Data format 76
 Analysis Object Data (AOD) 73, 76
 CBNT 76
 Event Summary Data (ESD) 73, 76
 HepMC 76
 Hits 76
 Raw data 76
 Raw Data Object (RDO) 73, 75, 76
 TAG 73, 76
 ESD 75, 78
 Tiers 73

C

CDF detector 63–66, 146
 W in Drell–Yan event selection 132
 Tracker 64
 Tracker misalignment/weak modes ... 64–66
 W analysis 138
 W properties measurements ... *see* W boson

Charge asymmetry

Definition 23
 used for the extraction of M_W 134
 used for the extraction of $M_{W^+} - M_{W^-}$ 139–
 140, 148–154

Charged lepton from W decay

Helicity *see* Helicity
 Pseudo-rapidity 39–40, 93–100, 105, 108, 114,
 122
 Transverse momentum . 40, 93–100, 105, 108,
 114, 122, 134, 136, 139, 156–159, 161

Chi-2 (χ^2) likelihood analysis

Principle (based on the extraction of M_W)
 137–138
 Results 149, 151
 Results (detailed) 165, 167
 Used for the extraction of $M_{W^+} - M_{W^-}$ 138–
 140

D

Double charge asymmetry

Definition 135
 Used for the extraction of $M_{W^+} - M_{W^-}$ 140,
 148–150, 165, 170–171

Drell–Yan processes for W *see* W boson

Generalities 28–41

E

Electroweak 20, 25, 27

Chirality 27
 CKM matrix elements 18, 25–26, 90–92, 106,
 127, 152
 Radiative corrections in W in Drell–Yan . 32,
 145
 $V - A$ coupling ... 21, 24–25, 93, 95–98, 101,
 106, 110, 121, 145, 161

G

Generator level *see* Monte Carlo

H

Helicity 27–28

Definition 22
 In the high energy limit 27

- Of the colliding quarks and the decaying leptons 33, 93–102, 108–110
- Of the decaying leptons 27–28
- Of the W boson 25
- I**
- Improved leading order *see* QCD
- L**
- LEP collider 11, 20, 43
- LHAPDF *see* Parton Distribution Functions
- LHC 19, 43–46
- Energy of the colliding beams 43
- Experiments 46
- Alice 46
- CMS 46
- LHC-f 46
- LHCb 46
- TOTEM 46
- Luminosity *see* Luminosity
- Luminosity
- At the LHC (expected) 43, 45–46
- Integrated 45, 46, 133, 134
- Low 46, 177
- Nominal/High 45, 178
- Integrated
- Used in CDF II M_W analysis 21
- M**
- Monte Carlo 67–71, 143
- Event generator 69
- Generator/particle/true level 23
- Parton Shower 69
- PYTHIA *see* PYTHIA
- Random/pseudo-random numbers 69
- Unweighted events 69
- Weighted events 68
- WINHAC *see* WINHAC
- P**
- Particle level *see* Monte Carlo
- Parton Distribution Functions (PDFs)
- Behaviour (CTEQ6) 35–36
- CTEQ 35, 36, 88, 104, 105, 143
- Definition 29
- DGLAP 29
- LHAPDF 71, 75–77, 81–82, 175
- PHOTOS Monte Carlo
- Interfaced to PYTHIA 77–78
- Pile-up 46, 47, 73–75
- Pseudo-rapidity
- Definition 23
- Of the charged lepton from W decay *see* Charged lepton from W decay
- PYTHIA Monte Carlo event generator 69, 71, 72, 77, 88, 90, 92
- Interface to WINHAC 71, 77
- Interfaced with PHOTOS 77–78
- Use of LHAPDF routines 81–82
- Q**
- QCD
- Basics 16–17
- Corrections in W decay into quarks 26
- Hadronic cross section calculation 29–30
- Improved leading order 36
- Parton Distribution Functions (PDFs) *see* Parton Distribution Functions (PDFs)
- Quarks *see* Quarks
- QED
- Basics 15–16
- Radiative correction in single W production 32, 69, 71, 77, 78
- Quantum Field Theory 15
- Quarks
- Helicity *see* Helicity
- Intrinsic transverse momenta 38–39, 144–145, 151, 152, 167, 173
- At the Tevatron energies 39
- Generated by PYTHIA 88
- Sea quarks 35–36, 92, 97, 104
- $s - c$ asymmetry 90, 144, 151–154, 167, 176
- Transverse momenta in single W production 95–96, 127–128
- $u^{(v)} - d^{(v)}$ asymmetry 91, 92, 107, 143–144, 150–153, 167, 175
- Valence quarks 35–36, 90, 92, 97, 104, 143, 150–153, 167, 175
- R**
- Rapidity
- Definition 23
- Of the W boson *see* W boson
- Reconstructed level 23
- S**
- Sea Quarks *see* Quarks
- Smeared level 23
- SPS collider 11, 43, 44, 87, 88
- Standard Model 13–19
- Symmetry
- CP 21, 101, 107, 110
- CPT 11, 20

T

Tevatron
 Luminosity *see* Luminosity
 Tevatron collider ... 11–12, 19–22, 32, 38, 63, 177
 Partons intrinsic transverse momentum ... 39
 Tracker misalignment *see* ATLAS and CDF
 Transverse mass of the lepton pair ... 41, 42, 133
 Definition 40
 In CDF II M_W analysis 132
 Transverse momentum
 Definition 22
 Of the charged lepton from W decay *see*
 Charged lepton from W decay
 Of the quarks *see* Quarks
 Of the W boson *see* W boson
 Transverse momentum of the charged lepton .. 41
 True level *see* Monte Carlo

V

Valence Quarks *see* Quarks

W

W boson
 Breit-Wigner resonance 31
 Decay in pp collisions 93–100
 Decay in $p\bar{p}$ collisions 93, 96–97
 Hadronic cross sections in Drell–Yan 88
 LO expressions 90
 Helicity *see* Helicity
 Mass M_W 24, 31, 34
 At the LHC (prospects) 22
 At the Tevatron 21
 In CDF 20, 42, 63–66
 Link to the charged lepton p_T 40
 Link to the lepton pair transverse mass. 40
 Mass charge asymmetry $M_{W^+} - M_{W^-}$ 20–22,
 61, 90, 106, 115
 In CDF 20, 63–66
 Polarisation 26–28
 Longitudinal states 28, 94
 Transverse states .. 26–28, 94, 97, 104–106,
 108–110
 Production in dd collisions
 Detailed 121
 Production in pp collisions 89–92
 Detailed 113–116
 Production in $p\bar{p}$ collisions 88–89
 Detailed 107–112
 Production in pp or $p\bar{p}$ collisions without va-
 lence quarks contributions 105–106
 Rapidity 37–38, 88–92, 105, 108, 114, 122

Transverse momentum ... 38–39, 88–92, 105,
 108, 114, 122

Width Γ_W 24–26, 31, 40, 159
 Narrow width approximation 37

Weak modes

In ATLAS tracker 60–62, 146

In CDF tracker 64–66

WINHAC Monte Carlo event generator ... 70–71

Event generation in Athena 77–78

Generation framework for the analysis 81–82

Implementation inside Athena 76–83

WINHAC event example 85

Z

Z boson 11, 19

Properties extraction 131

To calibrate the leptons energy scale ... 134